Christoph Böhme

Dynamics of spin-dependent charge carrier recombination

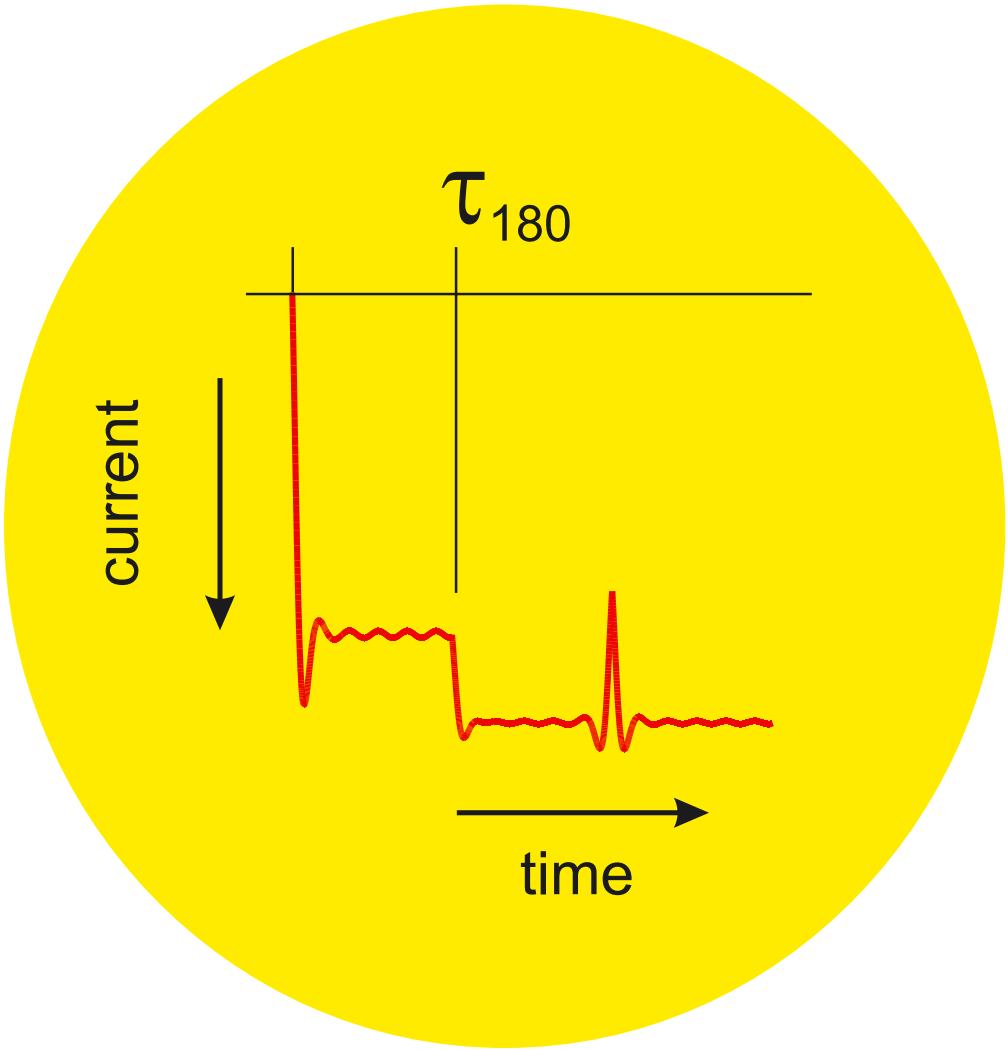

Dynamics of spin–dependent charge carrier recombination

Dissertation

zur
Erlangung des Doktorgrades
der Naturwissenschaften
(Dr. rer. nat.)

dem
Fachbereich Physik
der Philipps–Universität Marburg
vorgelegt

von
Christoph Böhme
aus Oppenau

Marburg/Lahn 2002

Bibliografische Information Der Deutschen Bibliothek
Die Deutsche Bibliothek verzeichnet diese Publikation in der Deutschen Nationalbibliografie; detaillierte bibliografische Daten sind im Internet über http://dnb.ddb.de abrufbar.
1. Aufl. - Göttingen : Cuvillier, 2003
Zugl.: Marburg, Univ., Diss., 2002
ISBN 3-89873-634-2

Vom Fachbereich Physik der Philipps–Universität Marburg als
Dissertation angenommen am: 17.12.2002

Erstgutachter:	Prof. Dr. W. Fuhs
Zweitgutachter:	Prof. Dr. S. Baranovski

Tag der mündlichen Prüfung: 13.01.2003

⊕ CUVILLIER VERLAG, Göttingen 2003
Nonnenstieg 8, 37075 Göttingen
Telefon: 0551-54724-0
Telefax: 0551-54724-21
www.cuvillier.de

1. Auflage, 2003
Gedruckt auf säurefreiem Papier

ISBN 3-89873-634-2

M.C. Escher's "Moebius Strip" © Cordon Art B.V. – Baarn – Holland. All rights reserved. [1]

"Never stop questioning." Albert Einstein

Contents

Summary

The study presented deals with the dynamics of spin–dependent charge carrier recombination between localised band–gap states in semiconductors. A general model is presented that takes influences of spin–dipole and spin–exchange interactions between the recombining charge–carrier spin pairs, spin relaxation and triplet recombination into account. A theoretical investigation based on this model predicts a variety of transient effects on the recombination rate due to the excitation with coherent electron spin resonance (ESR). These effects can be observed in the time domain of photocurrents. Depending on the coupling within the spin pairs, rapidly dephasing Rabi and Rabi–beat oscillation during the ESR excitation can occur, which is reflected by the magnitude of photocurrent decay transients. The dephased spin–pair ensembles can be rephased which causes an echo effect (Recombination echo). After the excitation, the charge carrier ensemble carries out dephasing Larmor and Larmor–beat oscillation. Also, a slow multiexponential relaxation of the photocurrent transients due to incoherence is predicted that is determined by the electronic transition probabilities and spin relaxation. An enhancement of the photocurrent due to non–negligible triplet recombination is possible.
A new experiment was designed and implemented technically, the time–domain measurement of spin–dependent recombination (TSR), which allowed the experimental verification of the effects that were predicted and described theoretically. A first demonstration of TSR was performed on hydrogenated microcrystalline silicon (μc-Si:H) which led to new insights about charge carrier recombination in this material: Spin–dependent recombination channels through dangling bond (db) centres are the dominant recombination paths of μc-Si:H. Two spin–dependent db recombination channels exist in μc-Si:H. A dominant db direct capture (dc) and a less dominant tunnelling transition of trapped conduction electrons (CE) to db states. Spin pairs of the dc channel are strongly coupled, their singlet- and triplet–recombination probabilities could be determined. The applicability of TSR could also be demonstrated on hydrogenated amorphous silicon. In addition, the ability of TSR to detect the spin coherence of recombining charge carriers allows the measurement of coherence times of spin quantum bits in semiconductor based spin–quantum computers.

Zusammenfassung

Die vorliegende Arbeit behandelt die Dynamik spinabhängiger Ladungsträgerrekombination zwischen lokalisierten Bandlückenzuständen in Halbleitern. Ein allgemeines Modell wird vorgestellt, in dem die Spin–Dipol und die Spin–Austauschwechselwirkungen zwischen den Paaren rekombinierender Ladungsträger, sowie Spin–Relaxationsprozesse und Triplettrekombination berücksichtigt werden. Eine theoretische Untersuchung, basierend auf diesem Modell, führt zur Vorhersage einer Vielfalt von Effekten auf die Rekombinationsrate nach Anregung durch kohärente Elektronenspinresonanz (ESR). Diese Effekte können in transient gemessenen Fotoströmen beobachtet werden. Je nach Kopplung innerhalb der Spinpaare kann es dabei zu schnell dephasierenden Rabi und Rabi–beat–Oszillationen während der ESR–Anregung kommen, welche von der Intensität der Fotostromtransienten reflektiert werden. Die dephasierten Spinpaarensembles können rephasiert werden, was einen Echoeffekt hervorruft (Rekombinationsecho). Nach der Anregung finden dephasierende Larmor- und Larmor–beat–Oszillationen statt. Darüber hinaus wird eine langsame, auf Inkohärenz zurückzuführende, multiexponentielle Photostromrelaxation vorhergesagt, welche von elektronischen Übergangsratenkoeffizienten und Spinrelaxation abhängt. Dabei ist eine Photostromerhöhung durch nichtvernachlässigbare Triplettrekombination möglich.
Ein neuartiges Experiment wurde konzipiert und technisch realisiert, die zeitaufgelöste Messung spinabhängiger Rekombination (TSR), mit welcher es möglich war, die theoretisch vorhergesagten Effekte experimentell zu verifizieren. Eine erste Demonstration von TSR wurde an wasserstoffabgesättigtem mikrokristallinem Silizium (μc-Si:H) durchgeführt, was zu neuen Einsichten über die Ladungsträgerrekombination in diesem Material führte: Spinabhängige Rekombinationsmechanismen an gebrochenen Bindungen (db) sind dominante Rekombinationspfade in μc-Si:H. Zwei spinabhängige db–Pfade existieren, der dominante db Direkteinfang (dc) und der weniger dominante Tunnelübergang von Leitungselektronen von lokalisierten Bandausläuferzuständen (CE) in db Zustände. Die Spinpaare des dc–Kanals sind stark gekoppelt, ihre Singulet- und Triplettrekombinationswahrscheinlichkeiten konnten bestimmt werden. Die Anwendbarkeit von TSR konnte auch für wasserstoffabgesättigtes amorphes Silizium demonstriert werden. Darüber hinaus konnte ausserdem noch gezeigt werden, dass die Fähigkeit der TSR–Methode, die Spinkohärenz von rekombinierenden Ladungsträgern zu detektieren, die Möglichkeit eröffnet, Kohärenzzeiten von Spinquantenbits in halbleiterbasierten Spinquantencomputern zu messen.

Chapter 1

Introduction

Recombination in semiconductors are energy loss transitions of electrons and holes that lead to a depletion of excess–charge carrier densities. Since recombination belongs to the determining factors for the electronic properties of semiconductors, the investigation and understanding of recombination has become one of the most important aspects of modern semiconductor research and development. Examples for the relevance of recombination for technological applications can be found in the fields of microelectronics and photovoltaics: The creation of materials with low recombination rates is the crucial task for the further improvement of solar cells since recombination is the most important origin of electronic losses and therefore a major factor for the limitation of solar cell efficiencies [2]. Progress in the field of microelectronics has always been marked by reduced scaling dimensions and an increased speed of thin film transistors [3]. The achievement of these goals depends to a large extend on the reduction of recombination activity at the interface between crystalline silicon and gate dielectric materials.

Obtaining experimental access to the physics of recombination is as difficult as it is important. Recombination can only be observed indirectly through macroscopic observables such as the photoconductivity or luminescence intensity. Moreover, in general, many different recombination paths contribute to a given observable, complicating the identification and characterisation of the different transitions. While standard lifetime measurements such as transient photoconductivity measurements can reveal electronic lifetimes and thus recombination rates, it is hardly possible to attribute the obtained quantitative data to distinct microscopic processes. Thus, other ways to gain a more detailed picture about the defect structure and the densities have been developed such as the capacitance–voltage method [4] or deep level transient spectroscopy [5]. These methods reveal information about different defect centres in a given material, but they still fail to give insight about the microscopic, local structure and most of all, the recombination activity of a certain defect.

Ways to investigate the microscopic environment of point defects are provided by magnetic resonance methods such as electron spin resonance (ESR) or nuclear magnetic resonance (NMR). The foundations of these methods go back mostly to the work of Felix Bloch who developed the theory of resonant nuclear induction [6] and carried out the first NMR experiments [7] in 1946. The first ESR spectrum was recorded by Zavoiski [8]. These first demonstrations were soon proceeded by coherent time–domain NMR experiments, which

revealed effects such as coherence decays, coherent dephasing and the existence of the nuclear spin echo, which was detected by Hahn [9] in 1950. After these initial discoveries, the research activity in the NMR field expanded dramatically and led to the development of many applications like different pulse sequences for structural analysis of chemical compounds or the magnetic resonant imaging applied for medical diagnostics. Unlike NMR, the development of time–domain ESR spectroscopy took place at a much slower pace due to the unavailability of fast detection electronics and the necessary strong coherent microwave sources [10]. After these technical challenges had been overcome in the early 1980s, the development of ESR techniques followed those of NMR in many regards, only with a 25 year delay. Time–resolved magnetic resonance spectroscopy is much superior in comparison to the original continuous wave (cw) experiments since it allows a fast high–resolution access to the resonance spectra (Fourier transform spectroscopy), it provides an easy and distinguishable access to the different relaxation and dephasing times and it allows the deconvolution between homogeneous and inhomogeneous line shapes which opens access to information about diffusion related phenomena and many other effects that have an influence on spin motion [10]. Nowadays, NMR experiments are carried out almost only in the time domain. ESR is still practised as cw ESR by many researchers which is due to cost constraints and the higher sensitivity of cw ESR.

While magnetic resonance methods allow access to microscopic information about paramagnetic defects, they still fail to reveal information about the recombination activity of a given defect centre. Because of this limitation, experimental methods have been developed that combine the microscopic sensitivity and selectivity of ESR with other methods such as photoconductivity or photoluminescence measurements. These combined methods take advantage of the spin dependency of many recombination processes in various semiconductor materials. Spin–dependent recombination of charge carriers is recombination through transitions whose probabilities are governed by spin–selection rules. Figure 1.1 illustrates how spin-conservation rules of electronic transitions can prohibit recombination of an electron through a paramagnetic defect. When the electron in the localised state and the defect are in a triplet spin–pair state, the spin of this pair would have to change from a triplet state ($S = 1$) to a singlet state ($S = 0$) during the transition. However, this is impossible when the spin is conserved due to the absence of spin–orbit coupling.

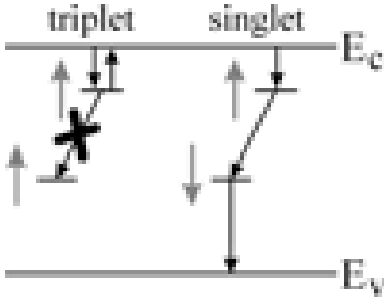

Figure 1.1: Spin–dependent recombination between localised bandgap states. Transitions between paramagnetic states are allowed only when the spin–pair state of the two electrons has singlet content.

The discovery of spin–dependent recombination processes goes back to the first optically detected magnetic resonance (ODMR) experiments carried out by Geschwind et al. in 1959 [11, 12]. In these experiments, spin configurations of excited electronic states were manipulated with ESR, which led to a rate change of recombination processes that could be observed by luminescence measurements. Since ODMR is also applicable to electronic transitions in atomic or molecular systems, it has become a versatile tool for the investiga-

tion of chemical reactions and due to the availability of fast and sensitive photo detectors, the development of transient ODMR has kept pace with pulsed-ESR. Many chemical reactions of radicals are spin–dependent electronic transitions similar to the charge carrier recombination in semiconductors. A time–resolved optical detection of the relative coherent spin motion of organic radical ion pairs has already been observed in 1976 by Klein and Voltz [13]. The reaction yield, proportional to the detected fluorescence intensity, oscillated with the Larmor–beat oscillation of the radical pair ensemble that was exposed to a constant magnetic field. Soon after this experiment, transient ODMR became a frequently utilised method for chemical reaction analysis and with the advent of pulsed-ESR in the early 1980s, optically detected electron spin echo techniques [14, 15, 16, 17] and optically detected Rabi–beat oscillations [18] were used for the investigation of atomic and molecular systems.

All of these developments in the ODMR community have had little impact on EDMR and semiconductor research. While cw ODMR has been used also for the investigation of charge carrier recombination, pulsed ODMR on semiconductors is difficult since longer wavelengths (near IR) are difficult to detect on fast time scales and the luminescence is weak in some materials. Moreover, ODMR intensities do not necessarily reflect the charge carrier recombination: Some radiative processes do not contribute to photoconductivity (geminate recombination) while other transitions that do contribute are not radiative.

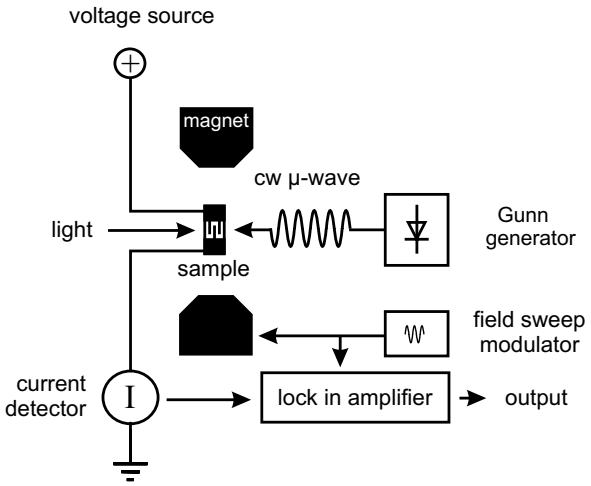

Figure 1.2: Experimental setup for the detection of spin–dependent recombination. Continuous wave EDMR as developed by Honig [19] is performed with continuous microwave radiation which is irradiated onto a semiconductor sample in which a constant current of excess–charge carriers (induced electrically or optically) flows. When the DC magnetic field is swept through an electron spin resonance, the current may be quenched due to an enhancement of recombination.

Alternatively to the detection of ESR by luminescence measurements, spin–dependent recombination of charge carriers in semiconductors can also be detected by resonant changes of the photoconductivity. This method is called electrically detected magnetic resonance (EDMR) or electrically detected electron spin resonance. The standard EDMR experiment, illustrated in fig. 1.2 and explained in greater detail in appendix B.2, is basically a continuous wave ESR experiment where the photoconductivity is measured instead of the radiation intensity in the microwave cavity. Its development followed the closely related ODMR method by about a decade and was started by Maxwell and Honig [19] who investigated the impact of ESR on spin–dependent scattering of charge carriers at impurities in 1966. The first spin–dependent recombination path was discovered by Lepine at the beginning of the 1970s [20, 21]. When Lepine equalised the densities of localised charge–carrier pairs in triplet states and the density of pairs with singlet content, an enhancement

of the singlet density and hence of the recombination took place. The latter was detected by photoconductivity measurements. Since these first experiments were carried out, various recombination paths in inorganic [22, 23, 24, 25, 26, 27, 28] and organic [29, 30, 31] semiconductors, semiconductor heterostructures [32, 33] and devices [34, 35, 36, 37], as well as interface systems [38], were investigated with EDMR and much insight into the nature of spin–dependent recombination has been gained.

While the development of time–resolved ESR and ODMR spectroscopy is delayed in comparison to NMR methods, a time–resolved EDMR, which reveals the influence of coherent spin motion on charge carrier recombination, had not even been demonstrated by the turn of the century, when the work presented in the following chapters was begun. The reasons why EDMR has always been limping behind both ESR and ODMR are related to the multiple challenges with regard to a sophisticated coherent ESR experiment that has to be carried out on a conducting (and therefore microwave absorbing) sample and an appropriate detection setup for the subtle current changes which occur on a short time scale. In addition to these technical problems, no theory about the effects and processes which could potentially become visible by "pulsed-EDMR" was existent. A first time–domain approach to standard cw EDMR had been carried out in 1999 by Hiromitsu et al. [30] who recorded the exponential relaxation of a photocurrent through a polymer–fullerene heterojunction during and after a resonant microwave radiation had been imposed on the material. In these experiments the microwave intensities and the time resolution were too low for the detection of coherent phenomena. Applied to other semiconductor systems, a transient measurement of cw EDMR can only reveal spin–relaxation rates — an information that can just as well be obtained by ESR.

The goal of the study presented in the following chapters was therefore to open up the experimental doors of EDMR to the world of coherent spin motion in order to make the wide range of effects utilised for pulsed ODMR and pulsed ESR available for semiconductor characterisation. Point of departure of this work was the theoretical investigation of the dynamics of spin–dependent recombination, a topic which had hardly been treated in the literature before. These theoretical considerations start out with a chapter that deals with the formulation of a general qualitative picture in which the essentials of many models developed in the past 30 years [20, 21, 39, 40, 41, 42, 43, 44, 45] are condensed down into a simple set of properties. The insight obtained from the theoretical descriptions will then lead to an assessment of the experimental feasibility of coherent spin motion measurements with recombination. An experiment, which will be referred to as time–domain measurement of spin–dependent recombination (TSR) is described. In this regard, it is important to point out that the study presented in this book does not deal with the time domain of spin–dependent transport processes, which represent a completely different class of ESR effects on conductivity and photoconductivity. Spin–dependent transport can be due to a variety of qualitatively completely different effects such as spin–dependent tunnelling [22] or spin–dependent scattering [46]. While cw EDMR line shapes due to transport and recombination are usually very similar, the transient behaviour could exhibit quite different features. Thus, all transport related processes have been excluded from the considerations in the following chapters. After the theoretical considerations and an introduction to the experimental foundations are made, first experimental results will be presented for two recombination paths in hydrogenated microcrystalline silicon (μc-Si:H). Based on this model

material, the range of experimental data accessible with TSR is demonstrated. It is shown that TSR is able to detect the influence of coherent spin motion on recombination such as the recombination–rate control by coherent dephasing of Rabi–beat oscillations within a spin–pair ensemble and a subsequent rephasing effect, which is referred to as recombination echo. It is then shown that the coherence decay due to incoherent processes such as recombination itself can be detected from these effects. This allows a direct measurement of the recombination dynamics in a distinct recombination path. After the discussion of the experimental observations, a chapter dealing with applications of the TSR method and its results follows. Therein, the data on μc-Si:H is discussed with regard to new insights about the material properties. Then, first experimental data on hydrogenated amorphous silicon (a-Si:H) is presented and potential benefits of TSR measurements in this material are discussed. The final part of this chapter deals with the discovery that coherent spin states can determine recombination processes itself: Based on this effect, a readout concept for spin–based solid–state quantum–computers as proposed by Kane [47, 48] is suggested. Thus, the insight about the dynamics of spin–dependent recombination gained in the study presented may have an impact on quantum computing research and development, which is presently one of the most active areas of physics research.

Chapter 2

Pictures of spin–dependent recombination

In the following, a brief review is given on the history of theoretical as well as experimental work done on spin–dependent recombination. Based on these previous studies, the attempt is undertaken to extract the underlying properties of the various models given in the literature in order to unify them into one general picture.

2.1 A brief history

After the first observation of conductivity related effects due to spin–dependent recombination by Lepine [20, 21] more than thirty years ago, the number of qualitative models for these mechanisms has risen continuously with the increasing experimental evidence in many semiconductor materials and devices. The original explanation given by Lepine is a simple thermal polarisation model for which it was assumed that any free excess electron in the system can recombine at a given time. In the presence of an external magnetic field B_0, the two energy eigenstates of all the unpaired, paramagnetic electrons and holes lose their degeneracy and a Zeeman energy split $\Delta E = g_{e,h}\mu_B B_0$ [1] separates the two levels of each charge carrier. An ensemble $\hat{\rho}$ of all the electrons and holes in a thermal equilibrium will be represented by the Boltzmann operator

$$\hat{\rho}_0 = \frac{\sum_{i=1}^{4} \exp\left(-\frac{E_i}{k_B T}\right) |i\rangle\langle i|}{\sum_{i=1}^{4} \exp\left(-\frac{E_i}{k_B T}\right)} \tag{2.1}$$

if it is in contact with a thermal bath of temperature T. The four energy levels E_i can be scaled to $E_1 = 0$, $E_2 = g_e\mu_B B_0$, $E_3 = g_h\mu_B B_0$ and $E_4 = (g_e + g_h)\mu_B B_0$. If a resonant microwave is switched on, the ensemble will be brought into a highly saturated non–equilibrium state

$$\hat{\rho}_{ESR} = \frac{1}{4}\sum_{i=1}^{4} |i\rangle\langle i| \tag{2.2}$$

[1] μ_B is Bohrs magneton and $g_{e,h}$ the effective Landé g-factor of electrons and holes.

which changes the average recombination probability by a change

$$\Delta R = r_S \mathrm{Tr}\{|S\rangle\langle S|\,(\hat{\rho}_{ESR} - \hat{\rho}_0)\} = \frac{r_S}{4}\left(\frac{1-e^{-\xi}}{1+e^{-\xi}}\right)\left(\frac{1-e^{-\xi}}{1+e^{-\xi}}\right); \quad \text{and} \quad \xi \approx \frac{g_e \mu_B B_0}{k_B T} \approx \frac{g_h \mu_B B_0}{k_B T} \tag{2.3}$$

under the assumption that triplet states can not recombine and pure singlet states recombine with a finite probability r_S. When the photoconductivity $\sigma_{ph} \propto \frac{1}{R}$ is anti proportional to the recombination and the recombination changes are sufficiently small ($\Delta R \ll R$), the equation

$$\Delta\sigma_{\mathrm{ph}} \approx \frac{\partial \sigma_{\mathrm{ph}}}{\partial R}\Delta R = -\frac{\sigma_{\mathrm{ph}}}{R}\Delta R \tag{2.4}$$

holds so that if the eq. 2.3 is expanded into a Taylor series up to the second order, the relative photocurrent change becomes

$$\frac{\Delta\sigma_{\mathrm{ph}}}{\sigma_{\mathrm{ph}}} = -\frac{g^2\mu_B^2}{16k_B^2}\frac{B_0^2}{T^2}. \tag{2.5}$$

Note that eq. 2.3 is independent from the chosen base of energy eigenstates. This means that the recombination change in Lepine's model would be absolutely independent from any exchange or dipole coupling between the electrons and holes, but due to eq. 2.5 quadratically dependent on the ratio of the applied magnetic field and the temperature. Moreover, at room temperature, an X-Band EDMR experiment which is carried out at $B \approx$ 345mT would show a relative recombination change of less than 10^{-6}. These predictions of Lepine's simple explanation were soon contradicted by experimental data [21, 28, 34] which could not confirm the quadratic dependence of the relative photocurrent changes from the B_0 field and the temperature and, more strikingly, the strength of the signal was more than two orders of magnitude stronger than predicted. Hence, polarisation effects, which may or may not have an influence as described above, are buried under a much stronger signal.

The realisation that a simple polarisation model could not account for spin–dependent recombination changes sparked the development of a series of other approaches throughout the 1970s. Initially, other polarisation models were developed, which attempted to take the huge signal into account by the assumption that (a) effective spins larger then $\frac{1}{2}$ could exist due to ferromagnetic exchange [39] that (b) clusters of paramagnetic centres, strongly coupled by exchange interaction, could exist [40] or that (c) multiphonon self trapping processes, which increase recombination through resonant heating [41]. However, all these models could not explain the absence of the T^{-2} dependence and the first non–polarisation models were developed: Wosinski and Figielski [42] attempted to explain the EDMR data by exchange coupled centres in dislocations. Mendz et al. [43, 44] described a picture where a combination of spin–dependent recombination and spin–dependent trapping would cause the observed behaviour. Again, both proposals also led to contradictive temperature dependences.

2.2 Intermediate pairs

In 1978 Kaplan, Solomon and Mott [45] developed another model of spin–dependent recombination (KSM model). In this proposal the qualitative properties were similar to those of the original simple model by Lepine. No coupling of the recombining charge carriers to any other spins or defects contained in the material was assumed: The spin dependency was solely based on spin conservation imposed by weak spin–orbit coupling as present for instance in crystalline silicon. The crucial difference to Lepine's model was the idea that intermediate pairs of charge carriers out of which a recombination of the two pair partners is possible would exist prior the the actual recombination transition. The important qualitative feature of the intermediate pair is its exclusivity: The two pair partners may or may not recombine at a given moment; however, before they can recombine with any other charge carrier not involved in the existing pair, the pair has to dissociate and new pairs with new partners have to form. In the KSM model, the exclusivity is the only defining property of a given pair system, which means pairs can be tightly bound electronic states such as excitons as well as electron–hole pairs trapped at two localised bandgap states which are in close proximity as illustrated in fig. 2.1. In the latter case, the exclusivity is given by the high transition probability between nearest neighbours. Even excited species of doubly occupied charged states as proposed by Xiong and Miller [49] can, in principle, form an exclusive spin pair.

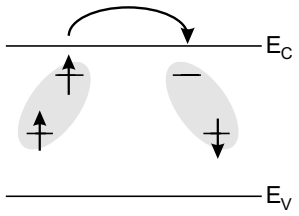

Figure 2.1: Illustration of the KSM model. The trapped electron can recombine only with a deep level state in sufficient proximity and when the spin state of the electron pair has singlet content. Before recombination with other deep levels is possible, the electron has to propagate to a different location. This process is described by pair dissociation and pair generation.

The advent of the pair model marked a strong advance in the understanding of spin–dependent recombination with regard to the large signal, the temperature and the magnetic field dependence. Its simplicity and generality make it easily applicable to many recombination systems and materials. While the idea of the intermediate pairs solved many questions about spin–dependent recombination, it also raised new ones such as of the existence of spin interactions within a pair or of interactions between different pairs. The assumption made by Kaplan et al. that the interaction between the pair partners is weak in any case can certainly not be generalised since spin–spin interaction is highly dependent on the nature of a given pair system. In addition, triplet recombination was assumed to be negligible as well, an assumption whose validity depends on whether spin–orbit coupling is negligible or not. Hence, after the proposal of the pair model, various other models followed dealing with these additional aspects of spin–dependent recombination, most of which, however, utilise the idea of intermediate pairs in one or the other way. In 1980, Movaghar et al. proposed a pair model in which a finite triplet recombination probability was introduced [50]. This assumption implies that ESR changes of spin–dependent recombination can actually lead to a quenching of recombination and hence, an enhancement of the photocurrent. The idea of triplet recombination was later pursued by Vlasenko et al. [51]. The question for the relevance of spin–spin interactions such as spin–exchange and spin–dipole coupling has been discussed in recent years by Fukui et al. [52] and Eick-

elkamp et al. [29]. Both studies outline how a base change of the four energy eigenstates of spin pairs can influence the recombination probabilities. Another important issue, especially for the understanding of EDMR line shapes, is the question for the influence of spin relaxation. A field that has been investigated in the early 1990s by Lips [53] and by Barabanov et al. [54, 55, 56].

2.3 Ingredients for a general model

Three decades of research spent on the formulation of models raises the question of an appropriate dynamical picture. The models discussed above have always been applied exclusively for a static case, the steady state recombination in presence or absence of cw ESR. Hence, in order to keep the results obtained for the dynamical case as general as possible and, therefore, applicable to as many different systems as possible, the attempt to take aspects of previous work as much as possible into account is made. Based on this approach, the model used in this book has the following qualitative properties:

1. Spin–dependent recombination takes place in the picture of Kaplan, Solomon and Mott: Before an electron and a hole annihilate in a single electronic state, an intermediate pair state is formed.

2. After intermediate pairs are generated, they can only be destroyed by recombination transitions or pair dissociation. In the latter case, the pair partners are not annihilated and can return to the charge carrier ensembles.

3. The charge carrier density and hence, the conductivity are considered to be in a steady state with pair generation, dissociation and recombination. Therefore, the dynamics of spin–dependent recombination is governed solely by the spin dynamics of the pair ensemble. This assumption is reasonable as long as the relative photocurrent changes are small[2] — a condition which is, to the knowledge of the author, fulfilled by all experimentally observed spin–dependent recombination paths.

4. The intermediate pairs are systems of two $S = \frac{1}{2}$ spins that have four spin eigenstates with respect to a given observable.

5. Within a pair, spin–spin interactions such as spin–exchange and spin–dipole interaction are possible and can have an impact on recombination. The interactions are determined by the nature of a given pair.

6. Spin–dependent recombination is caused by spin conservation due to weak but in general not negligible spin–orbit coupling. Hence, the possibility of triplet recombination has to be taken into account.

7. The interaction of a spin pair with its environment can cause spin relaxation. The impact of spin–phonon scattering (spin–lattice relaxation) and dipolar coupling to spins in the environment of a pair (spin–spin relaxation) can therefore also influence the transient behaviour of the recombination rate.

[2] small enough, such that second order effects are negligible

Chapter 3

Theoretical considerations

The aim of the theoretical study on the model presented in the previous section is to gain an understanding of possible effects present in the time domain as well as the time scales on which these effects appear. In addition, the questions whether and how disorder can affect these processes are raised and whether there is potential to obtain microscopic information about a given material from the measurement of these phenomena.

3.1 A quantum ensemble of spin pairs

With the qualitative assumptions given in the previous chapter, the evolution of the recombination at a certain time depends solely on the evolution of the spin pairs. This approach dramatically simplifies the creation of an appropriate equation of motion for the given many–particle system because the set of existing spin pairs at any given time can be considered as one entity, a quantum ensemble of equal systems. The evolution of this ensemble state is determined by the individual pairs whose evolutions depend on their pair Hamiltonian. External changes of the ensemble are due to the generation and recombination as well as the dissociation of pairs as illustrated in fig. 3.1. Mathematically, the dynamics of the pair ensemble can be described in terms of a stochastic Liouville equation

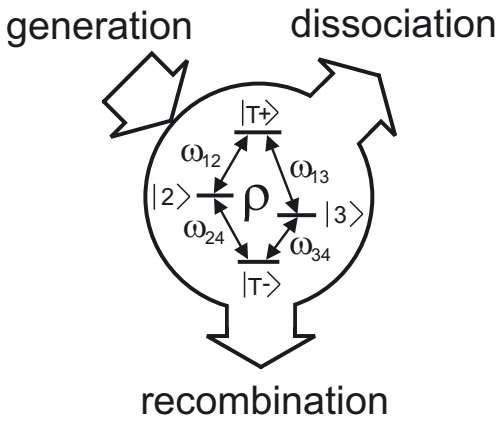

Figure 3.1: Ensemble of spin pairs ρ which is subjected to changes by recombination, dissociation and generation of pairs. The individual pairs have four eigenstates which depend on the nature of a given pair system.

$$\partial_t \hat{\rho} = \frac{i}{\hbar}\left[\hat{\rho}, \hat{H}\right]^- + \mathcal{S}\left[\hat{\rho}\right] + \mathcal{R}\{\hat{\rho} - \hat{\rho}_0\}, \qquad (3.1)$$

in which the state of the ensemble is represented by the density operator $\hat{\rho} = \hat{\rho}\,(t)$, as explained in appendix A.1. This operator describes a two spin $\frac{1}{2}$ system with four eigenstates that can be represented by a 4×4 matrix by choice of an arbitrary base set. The density operator in eq. 2.1 has the same mathematical form even though it represents a quite different physical reality.

While $\hat{\rho}$ represents in this section the ensemble of intermediate spin pairs, which means the ensemble of electrons in pairs with their respective hole partners, the density operator in eq. 2.1 represents all charge carriers present in the semiconductor. The difference of these two physical realities in mathematical terms lies in the form of different stochastic terms $\mathcal{S}[\hat{\rho}]$. The use of stochastic Liouville equations for the description of recombining spin pairs was originally developed by Haberkorn and Dietz [57] and applied to systems with non–negligible spin relaxation by Barabanov et al. [54, 55, 56]. In these studies, the Liouville equations were only solved for steady state systems as given in conventional EDMR experiments.

The Hamiltonian $\hat{H}$ in eq. 3.1 describes a single system while the stochastic operator $\mathcal{S}$ represents the external changes of the ensemble. The latter are creation and annihilation rates which are a source of incoherence for the ensemble state. This treatment of pair generation, recombination and dissociation is justified since these processes are spontaneous energy transitions in the system described. Finally, the operator $\mathcal{R}$ in the last term of eq. 3.1 describes influences of spin relaxation.

Once the time dependent solution $\hat{\rho}(t)$ of eq. 3.1 is found, the pair recombination, and thus, the photocurrent transients can be obtained directly due to assumption 3 on page 10. With assumption 6 of the same list, the recombination rate $R(t)$ becomes the sum of all singlet and triplet transitions

$$R(t) = r_S \mathrm{Tr}\left[|S\rangle\langle S|\hat{\rho}(t)\right] + r_T \sum_{i=-1}^{1} \mathrm{Tr}\left[|T_i\rangle\langle T_i|\hat{\rho}(t)\right] \tag{3.2}$$

which is dependent on the products of the transition probabilities r_i and the respective state densities. Since dissociation is assumed to be spin independent, its rate $D(t) = d\mathrm{Tr}\left[\hat{\rho}(t)\right]$ is just a simple product of the dissociation probability and the spin–pair density. Another consequence of assumption 3 on page 10 is that the generation rate G of spin pairs can be considered constant. Experimentally, a constant charge carrier generation rate is achieved by using a continuous wave (cw) light source. Note that this rate is not equal to the spin–pair generation–rate. The latter depends on the charge carrier densities that are to be changed due to recombination. Thus, the constance of G is true only to the first order; however, with relative charge carrier changes of less than 10^{-3}, the second order contributions are truly negligible. Hence, the changes of the electron density and hole density

$$\begin{aligned} \Delta n_e(t) &= \tau_L \Delta D(t) = \tau_L \left[D(t) - D_S\right] \\ \Delta n_h(t) &= -\tau_L \Delta R(t) = \tau_L \left[R_S - R(t)\right] \end{aligned} \tag{3.3}$$

are determined by the dissociation change $\Delta D(t)$ and the recombination change $\Delta R(t)$ that are the differences of the dissociation and recombination rates from their steady states values D_S and R_S, respectively. The lifetime τ_L of the charge carriers in eq. 3.3 is the average lifetime depending on all recombination processes that take place. Therefore, it can be considered constant for the same reasons as the pair generation rate G. Note that eq. 3.3 does also imply the neglect of the transition probability of an electron from the charged deep level state (which exits after the spin–dependent transition has occurred) into the hole state in the valence band (depicted as the last transition in the recombination

path of fig. 1.1). However, since this process is a capture transition of a charged defect centre, it is assumed to be fast and not rate limiting as well.

Since the conductivity σ depends on the charge carrier densities, the change of the transient photoconductivity due to the influence of the dynamics of a spin–dependent recombination mechanism becomes

$$\Delta\sigma_{ph}(t) = e\left[\Delta n_e(t)\,\mu_e + \Delta n_h(t)\,\mu_h\right] \tag{3.4}$$

wherein e is the elementary charge and μ_i the mobility of electrons and holes, respectively. The set of simple equations (eq. 3.2 to 3.4) provides a connection between the dynamics of spin–dependent recombination and an experimentally accessible parameter, the conductivity or the current of excess charge carriers. This will be utilised for the experiments discussed in chapter 4 and below.

3.1.1 Hamiltonian of a spin pair

The Hamiltonian $\hat{H}$ of an intermediate spin pair as given in eq. 3.1 can be split into a time–independent and a time–dependent contribution $\hat{H}(t) = \hat{H}_0 + \hat{H}_1(t)$ which represent the interactions of a pair system without the presence of an external radiation field and the radiation field, respectively. The interactions of the pair with the surrounding ensemble of many other pairs could actually be taken into account by a third contribution, a random fluctuation Hamiltonian. However, as explained in section 3.1.3 the latter has already been accounted for by the Redfield operator $\mathcal{R}$ in the Liouville equation. The first part

$$\hat{H}_0 = \mu_B g_a \hat{\mathbf{S}}_\mathbf{a}\cdot\mathbf{B} + \mu_B g_b \hat{\mathbf{S}}_\mathbf{b}\cdot\mathbf{B} - J\hat{\mathbf{S}}_\mathbf{a}\cdot\hat{\mathbf{S}}_\mathbf{b} - D^d\left[3S_a^zS_b^z - \hat{\mathbf{S}}_\mathbf{a}\cdot\hat{\mathbf{S}}_\mathbf{b}\right] \tag{3.5}$$

consists of the Zeeman interaction $g_i\mu_B\hat{\mathbf{S}}_\mathbf{i}\cdot\mathbf{B}$ of the respective pair partners, the exchange coupling with coupling constant J as well as the dipolar interaction with coupling constant D^d taken into account in the high field approximation ($|D^d| \ll |g_i\mu_B B|$) as explained in appendix A.2. Note that nuclear interactions of the two electronic spins are not considered in eq. 3.5. The latter may play a role when the spin–dependent recombination takes place in the vicinity of nuclear spins with $I \neq 0$ such as recombination through phosphorus donor states. A brief discussion of these hyperfine effects will take place in chapter 7. The unperturbed, time–independent Hamiltonian in eq. 3.5 is represented by a non–diagonal matrix in the product base $|\uparrow\uparrow\rangle$, $|\downarrow\uparrow\rangle$, $|\uparrow\downarrow\rangle$, $|\downarrow\downarrow\rangle$ that can be diagonalised by a unitary transformation

$$\tilde{U} = \begin{pmatrix} 1 & 0 & 0 & 0 \\ 0 & \cos(\phi) & \sin(\phi) & 0 \\ 0 & -\sin(\phi) & \cos(\phi) & 0 \\ 0 & 0 & 0 & 1 \end{pmatrix} \tag{3.6}$$

into the base of energy eigenstates $|T_+\rangle$, $|2\rangle$, $|3\rangle$ and $|T_-\rangle$ (indicated in fig. 3.1). Note that $\tilde{U}$ leaves the two states $|T+\rangle$ and $|T-\rangle$ unchanged. As the spin–spin interactions increase, the states $|2\rangle$ and $|3\rangle$ change continuously from product states with mixed symmetry properties into $|S\rangle$ and $|T_0\rangle$ states with purely antisymmetric and symmetric permutation behaviour. This can be seen from the expression for the argument

$$\phi = \frac{1}{2}\arcsin\left(\frac{J + D^d}{\hbar\omega_\Delta}\right) \tag{3.7}$$

of the transformation matrix which approaches $\frac{\pi}{4}$ as the spin interactions go to infinity. The Hamiltonian in the eigenbase becomes a diagonal matrix

$$\hat{H}_0 = \begin{pmatrix} \frac{\hbar\omega_0}{2} - J + D^d & 0 & 0 & 0 \\ 0 & -D^d + \hbar\omega_\Delta & 0 & 0 \\ 0 & 0 & -D^d - \hbar\omega_\Delta & 0 \\ 0 & 0 & 0 & -\frac{\hbar\omega_0}{2} - J + D^d \end{pmatrix} \tag{3.8}$$

whose elements represent the energy eigenvalues of the four states. In this form, the variable ω_Δ stands for the half of the frequency separation of the states $|2\rangle$ and $|3\rangle$

$$\omega_\Delta = \sqrt{\frac{J + D^d{}^2}{\hbar} + \frac{\Delta\omega^2}{4}} \tag{3.9}$$

and $\omega_0 = \omega_a + \omega_b$ and $\Delta\omega = \omega_a - \omega_b$ are the sum and the difference of the pair partners' Larmor frequencies. The latter correspond to the energy splits

$$\hbar\omega_i = g_i \mu_B B_0 \tag{3.10}$$

between the two spin states of each pair partner which are induced by an externally applied magnetic field B_0. Note that the Larmor frequencies are different in general due to the different effective Landé g factors of the two pair partners a and b. These effective g factors are due to the vacuum Landé factor of the electron ($g \approx 2.0023$) altered by the effect of local fields in the microscopic environments of a spin in a solid. The existence of effective Landé factors is the reason for the versatility of ESR: A certain type of defect has its own characteristic local field and therefore, the value of the g factor reveals information about the type of defect and its microscopic structure.

The second, time–dependent part $\hat{H}_1(t)$ of the Hamiltonian describes the electromagnetic radiation imposed on the pair as is the case, when an ESR microwave is used for the manipulation of the pair ensemble. The radiation at the location of the spin pair causes an oscillating magnetic field

$$\mathbf{B_1}(t) = \hat{\mathbf{x}} B_1 e^{(-i\omega t)} \tag{3.11}$$

with frequency ω and field amplitude B_1. In the frame of the rotating magnetic field, also called a rotating Bloch sphere representation (explained in appendix A.4), the radiation amplitude behaves like a constant magnetic field vector so that the Hamiltonian

$$\hat{H}_1 = g_a \mu_B \hat{\mathbf{S}}_\mathbf{a} \cdot \mathbf{B_1} + g_b \mu_B \hat{\mathbf{S}}_\mathbf{b} \cdot \mathbf{B_1} = \hbar\gamma B_1 \{\hat{\sigma}_a^x \otimes \mathbb{I}_b + \mathbb{I}_a \otimes \hat{\sigma}_b^x\} \tag{3.12}$$

becomes time independent as well. The term on the right hand side of eq. 3.12 implies the assumption that the g factor difference of the pair partners becomes negligible for the available radiation field strength[1] and that the radiation is polarised perpendicularly to the static magnetic field B_0. The operators of the two spin components are represented in a product space. The variable $\gamma = \frac{g\mu_B}{2\hbar}$ is the gyromagnetic ratio, a constant which unifies all the factors. Note that the Landé factor difference between g_a and g_b can be

[1] $\frac{B_1}{B_0} \leq 10^{-2}$ for pulsed X-Band applications with kW microwave intensities and $g \approx 2$

ignored in the expression for $\tilde{H}_1$ because of the weakness of the microwave field B_1. The g factor difference on the spin propagation about the $\mathbf{B_1}$ field causes oscillations in the sub kHz range which will turn out to be much slower than most of the incoherent processes in the experiments discussed. However, as shown in section 3.3, the impact of the Landé factor difference on the Hamiltonian $\hat{H}_0$ can not be neglected due to the strong B_0 field. With the neglect of the g-factor difference and the definition of γ, the microwave induced Hamiltonian in the product base representation becomes

$$\tilde{H}_1^{\uparrow\downarrow} = \hbar\gamma B_1 \begin{pmatrix} 0 & 1 & 1 & 0 \\ 1 & 0 & 0 & 1 \\ 1 & 0 & 0 & 1 \\ 0 & 1 & 1 & 0 \end{pmatrix} \tag{3.13}$$

and after a transformation $\tilde{U}\tilde{H}_1\tilde{U}^\dagger$ into the base of energy eigenstates, it can be added to eq. 3.8. The Hamiltonian discussed in this section contains all terms which are necessary for a detailed investigation of line shapes and resonant current changes of cw EDMR as well as time domain experiments. In order to find a solution for cw experiments, it is usually sufficient to treat the influence of H_1 as a weak perturbation. This approach is justified because of the weak microwave intensities used for such experiments. The requirement that a resonant radiation intensity has to be below the saturation limit of cw ESR, which means the induced spin oscillation (Rabi oscillation) has to take place slower than incoherent processes, implies the applicability for perturbation theory. Hence, from the matrix representation of $\hat{H}_1$ one can directly obtain the transition strength $\omega_{ij} = |\langle i|\hat{H}_1|j\rangle|$ of this perturbation which yields

$$\omega_{1,2} = \omega_{2,4} = \gamma B_1 \sqrt{1 + \frac{J + D^d}{\hbar\omega_\Delta}} \qquad \omega_{1,3} = \omega_{3,4} = \gamma B_1 \sqrt{1 - \frac{J + D^d}{\hbar\omega_\Delta}} \tag{3.14}$$

for the allowed ESR-transitions depicted in fig. 3.1. These transition strengths can be plugged into rate equations. For coherent, resonant experiments carried out on a short time scale, this approach does not work. In order to gain coherent spin motion, the microwave–induced oscillations have to be faster than any incoherent process. In this case, the field strength is so strong that many orders of perturbation theory have to be taken into account. However, this means, the complicated systems of differential equations as contained in eq. 3.1 must be solved analytically which can be difficult and sometimes impossible to do. Therefore, other approaches have to be utilised for the description of the spin dynamics as discussed in section 3.5.

3.1.2 Electronic transitions

As discussed in section 3.1, spin pairs recombine at different probabilities r_S and r_T out of pure singlet and triplet states, respectively. Due to the base change induced by spin–spin interaction, the recombination from the $|2\rangle$- and $|3\rangle$–energy eigenstates in fig. 3.1 will have different recombination probabilities

$$r_i = r_S|\langle i|S\rangle|^2 + r_T|\langle i|T_0\rangle|^2 \tag{3.15}$$

which, under consideration of eqs. 3.6 and 3.7, can be written as

$$\begin{aligned} r_{T+} &= r_T \\ r_2 &= \frac{r_S}{2}\left[1-\frac{J+D^d}{\hbar\omega_\Delta}\right]+\frac{r_T}{2}\left[1+\frac{J+D^d}{\hbar\omega_\Delta}\right] \\ r_3 &= \frac{r_S}{2}\left[1+\frac{J+D^d}{\hbar\omega_\Delta}\right]+\frac{r_T}{2}\left[1-\frac{J+D^d}{\hbar\omega_\Delta}\right] \\ r_{T-} &= r_T. \end{aligned} \tag{3.16}$$

Note that the two unchanged states $|\uparrow\uparrow\rangle = |T_+\rangle$ and $|\downarrow\downarrow\rangle = |T_-\rangle$ retain their recombination probability r_T, independently from the strength of spin–spin interactions. Equation 3.16 shows that recombination from spin pairs strongly depends on the spin interaction and the Larmor separation when $r_T \ll r_S$. With the introduction of these eigenstate recombination probabilities, the annihilation part $\mathcal{S}_{an}[\hat{\rho}(t)]$ of the stochastic term $\mathcal{S}[\hat{\rho}(t)] = \mathcal{S}_{an}[\hat{\rho}(t)] + \mathcal{S}_{cr}[\hat{\rho}(t)]$ in the Liouville eq. 3.1 simplifies drastically and in the base of energy eigenstates and under consideration of the recombination term as defined by Haberkorn and Dietz [57], its matrix elements become

$$\{\mathcal{S}_{an}[\hat{\rho}(t)]\}_{ij} = \left\{\sum_{k=1}^{4}\frac{r_k+d}{2}\left[|k\rangle\langle k|,\hat{\rho}\right]^+\right\}_{ij} = (r_i+r_j+d)\frac{\rho_{ij}}{2} \tag{3.17}$$

Similarly, the expression for the pair recombination rate (eq.3.2) simplifies to the term

$$R(t) = \sum_{i=1}^{4} r_i\rho_{ii} \tag{3.18}$$

which leads together with eq. 3.4 to a general expression

$$\Delta\sigma_{\mathrm{ph}}(t) = e\tau_L d\mu_e \sum_{i=1}^{4}\left[\rho_{ii}(t)-\rho_{ii}^S\right]\left(1-\frac{r_i}{d}\frac{\mu_h}{\mu_e}\right) \tag{3.19}$$

for the transient photocurrent change $\Delta\sigma_{\mathrm{ph}}$ induced by a resonant microwave field. This result reveals a quite new insight: The sign of the photoconductivity change induced by a change of the spin–pair ensemble out of its steady state $\hat{\rho}^S$ depends on the recombination and dissociation probability as well as the electron and hole mobilities. Therefore, the presence of a finite triplet recombination and spin–spin interactions can determine whether an ESR–excited spin–dependent recombination path causes a photocurrent enhancement or quenching. This is in contrast to the models described in refs. [45, 22, 53] in which the steady state of the pair recombination always marked a minimum and ESR–excited photocurrent changes could only introduce photocurrent quenching. A recombination quenching due to ESR interaction has been described before by Movaghar et al. [50]. However, this effect is solely due to the existence of non–negligible triplet recombination unlike the quenching effect described above.

3.1.3 Spin relaxation

The influence of spin relaxation on spin–dependent recombination has been treated by Barabanov et al. [54, 55, 56] and Eickelkamp et al. [29] in the past. In these studies, a relaxation term

$$-\frac{1}{\tau_S}\left(\hat{\rho}\left(t\right)-\hat{\rho}^0\right) \tag{3.20}$$

was added to a stochastic Liouville equation in the way it was done for eq. 3.1. In this expression, the relaxation time τ_S is a phenomenological constant, defined by the expression itself. In analogy to the definition of the spin relaxation times in Bloch's equations (see also appendix A.3), τ_S is supposed to equalise the density matrix elements at a rate proportional to the difference to their respective equilibrium values. As outlined in the following, this approach turns out to be false, due to the fact that, unlike components of Bloch's equations, the individual elements of the density matrix are not uncoupled observables and, hence, their relaxation must not necessarily be single exponential.

The theory of relaxation of quantum mechanical ensembles has been developed in the 1950s by Redfield [58, 59], who calculated the dynamics of a spin ensemble in the presence of a random fluctuation field caused by the ensemble itself. As explained in appendix A.5, Redfield used second order perturbation theory in order to express the influences of the complicated fluctuation Hamiltonian on a much simpler relaxation rate–coefficient matrix. Applied to the ensemble of spin pairs described above, the relaxation term in eq. 3.1 becomes

$$\left[\mathcal{R}\{\hat{\rho}\left(t\right)-\hat{\rho}_0\}\right]_{ij}=\sum_{k=1}^{4}\sum_{l=1}^{4}R_{ijkl}\{\rho_{kl}\left(t\right)-\rho_{kl}^0\} \tag{3.21}$$

in an arbitrary matrix representation. For a spin-$\frac{1}{2}$ pair, the Redfield matrix R_{ijkl} is a $4\times4\times4\times4$ matrix with 256 elements. The physical meaning behind these huge expressions is that the relaxation rate of each of the 16 given matrix elements is not only dependent on its own difference to its equilibrium value, but on the differences of all other elements as well. The complexity of the Redfield matrix requires simplification which can be achieved by the omission of matrix elements that have little impact on the pair system. The creation of expression 3.20 is an attempt to increase the zero density of the matrix R_{ijkl}. If we define

$$R_{ijkl}=\begin{cases}\frac{1}{\tau_S} & \text{if } i=k \text{ and } j=l,\\ 0 & \text{otherwise,}\end{cases} \tag{3.22}$$

the prefactor of eq. 3.20 turns out to have the same form as a Redfield matrix. However, note that since Redfield's theory is based on a perturbation theory of a fluctuation Hamiltonian $\hat{H}_{fl}$, one can show that the matrix elements are different functionals

$$R_{ijkl}=F_{ijkl}\left[\hat{H}_{fl}\right] \tag{3.23}$$

which are all dependent on the same operator, the Hamiltonian $\hat{H}_{fl}$ itself. Consequently many relations exist between these functionals, among which the equation

$$-R_{1111}=\sum_{i=2}^{4}R_{11ii} \tag{3.24}$$

is only one example. This equation contradicts definition 3.22 and thus, the term 3.20 can not be used for the description of spin relaxation in the ensemble of recombining spin pairs and a new approach has to be formulated.

The most simple system is a single $s = \frac{1}{2}$ spin whose relaxation is discussed for instance by Atherton [10]. The Redfield matrix of such a single spin contains 16 elements that can be identified via the functionals of eq. 3.23 with the spin–relaxation times T_1 and T_2 as defined by Bloch (see appendix. A.3). As explained in appendix. A.5, this identification reveals

$$R_{ijkl} = \begin{cases} \frac{1}{T_1} & \text{if } i = j = k = l, \\ -\frac{1}{T_1} & \text{if } i = j \text{ and } k = l \text{ and } j \neq k, \\ \frac{1}{T_2} & \text{if } i \neq j \text{ and } k \neq l \\ 0 & \text{otherwise} \end{cases} \tag{3.25}$$

which leads to a Relaxation matrix where only two constants appear and 8 of the 16 elements vanish.

The approach taken in the following is to create an expression for an appropriate Redfield matrix of the spin–pair ensemble which does not contradict the functional relations and is sufficiently simple at the same time, so that the stochastic Liouville equation remains solvable. The approach is simply based on the assumption that any of the two spin–pair partners relaxes as an isolated spin and that cross relaxation contributions are negligibly small. In this picture, relaxation of spin pairs

$$\mathcal{R}\{\hat{\rho} - \hat{\rho}_0\} = [\mathcal{R}_a \otimes \mathbb{I}_b] \{\hat{\rho} - \hat{\rho}_0\} + [\mathbb{I}_a \otimes \mathcal{R}_b] \{\hat{\rho} - \hat{\rho}_0\} \tag{3.26}$$

is just the sum of the two single spin contributions which can be combined into one single Redfield operator

$$\mathcal{R} = [\mathcal{R}_a \otimes \mathbb{I}_b + \mathbb{I}_a \otimes \mathcal{R}_b] \tag{3.27}$$

whose matrix elements can be associated with the longitudinal and transverse relaxation times T_1^a, T_1^b, T_2^a, T_2^b of the respective spin–pair partners. In the product base, this relaxation matrix leads to a very complex expression (displayed in table 3.1) in spite of the omission of cross relaxation; however, unlike expression 3.22, this matrix is in accordance with the requirements of Redfield's theory and therefore, it represents a much more realistic relaxation behaviour of the spin–pair ensemble. In tab. 3.1, seven other relaxation times

$$T_{3,4} = \frac{T_1^a T_1^b}{T_1^b \pm T_1^a} \qquad T_5 = -\frac{T_2^a T_2^b}{T_2^a + T_2^b} \qquad T_{6,7} = -\frac{T_1^a T_2^b}{-T_2^b \pm T_1^a} \qquad T_{8,9} = -\frac{T_2^a T_1^b}{T_1^b \pm T_2^a} \tag{3.28}$$

appear in this matrix beside the respective single spin–relaxation times T_1^i and T_2^i. These are combined relaxation times that depend on the single spin–relaxation terms only. In table 3.1, the index variables i and k define the rows and columns of the outer matrix while j and l address rows and columns of the inner matrices. Transformed by eq. 3.6 into the base of energy eigenstates, it can be added to the Liouville equation (eq. 3.1) which reveals an inhomogeneous system of first order ordinary differential equations for which it is still hard to obtain a reasonably short analytic solution. However, with proper choice of simplifications imposed on the relaxation times, some of the terms in eq. 3.28

$$
\begin{bmatrix}
\begin{pmatrix} \frac{1}{T_3} & \frac{1}{T_1^b} & \frac{1}{T_1^b} & -\frac{1}{T_4} \\ \frac{1}{T_1^b} & \frac{1}{T_1^b} & \frac{1}{T_8} & \frac{1}{T_8} \\ \frac{1}{T_1^b} & \frac{1}{T_8} & \frac{1}{T_1^b} & \frac{1}{T_8} \\ -\frac{1}{T_4} & \frac{1}{T_8} & \frac{1}{T_8} & \frac{1}{T_3} \end{pmatrix} & \begin{pmatrix} \frac{1}{T_1^b} & \frac{1}{T_1^b} & 0 & 0 \\ \frac{1}{T_1^b} & \frac{1}{T_1^b} & -\frac{1}{T_2^a} & -\frac{1}{T_2^a} \\ 0 & -\frac{1}{T_2^a} & \frac{1}{T_2^a} & 0 \\ 0 & -\frac{1}{T_2^a} & 0 & \frac{1}{T_2^a} \end{pmatrix} & \begin{pmatrix} 0 & 0 & -\frac{1}{T_1^a} & 0 \\ 0 & 0 & 0 & -\frac{1}{T_1^a} \\ -\frac{1}{T_1^a} & 0 & \frac{1}{T_1^a} & 0 \\ 0 & -\frac{1}{T_1^a} & 0 & \frac{1}{T_1^a} \end{pmatrix} & \begin{pmatrix} \frac{1}{T_4} & -\frac{1}{T_1^b} & -\frac{1}{T_3} \\ -\frac{1}{T_1^b} & \frac{1}{T_1^b} & \frac{1}{T_1^b} \\ -\frac{1}{T_1^b} & \frac{1}{T_1^b} & \frac{1}{T_1^b} \\ -\frac{1}{T_3} & \frac{1}{T_1^b} & \frac{1}{T_1^b} \end{pmatrix} \\
\begin{pmatrix} \frac{1}{T_1^a} & 0 & 0 & -\frac{1}{T_4} \\ 0 & \frac{1}{T_1^b} & \frac{1}{T_8} & \frac{1}{T_8} \\ 0 & \frac{1}{T_8} & \frac{1}{T_1^b} & \frac{1}{T_8} \\ -\frac{1}{T_4} & \frac{1}{T_8} & \frac{1}{T_8} & \frac{1}{T_1^b} \end{pmatrix} & \begin{pmatrix} \frac{1}{T_1^b} & 0 & 0 & -\frac{1}{T_2^a} \\ 0 & \frac{1}{T_1^b} & -\frac{1}{T_2^a} & \frac{1}{T_2^a} \\ 0 & -\frac{1}{T_2^a} & \frac{1}{T_2^a} & 0 \\ -\frac{1}{T_2^a} & \frac{1}{T_2^a} & 0 & \frac{1}{T_2^a} \end{pmatrix} & \begin{pmatrix} 0 & 0 & -\frac{1}{T_1^a} & 0 \\ 0 & 0 & 0 & -\frac{1}{T_1^a} \\ -\frac{1}{T_1^a} & 0 & \frac{1}{T_1^a} & 0 \\ 0 & -\frac{1}{T_1^a} & 0 & \frac{1}{T_1^a} \end{pmatrix} & \begin{pmatrix} \frac{1}{T_4} & -\frac{1}{T_1^b} & -\frac{1}{T_3} \\ -\frac{1}{T_1^b} & \frac{1}{T_1^b} & \frac{1}{T_1^b} \\ -\frac{1}{T_1^b} & \frac{1}{T_1^b} & \frac{1}{T_1^b} \\ -\frac{1}{T_3} & \frac{1}{T_1^b} & \frac{1}{T_1^b} \end{pmatrix} \\
\begin{pmatrix} \frac{1}{T_1^a} & 0 & 0 & -\frac{1}{T_4} \\ 0 & \frac{1}{T_1^b} & \frac{1}{T_8} & \frac{1}{T_8} \\ 0 & \frac{1}{T_8} & \frac{1}{T_1^b} & \frac{1}{T_8} \\ -\frac{1}{T_4} & \frac{1}{T_8} & \frac{1}{T_8} & \frac{1}{T_1^b} \end{pmatrix} & \begin{pmatrix} \frac{1}{T_1^b} & 0 & 0 & -\frac{1}{T_2^a} \\ 0 & \frac{1}{T_1^b} & -\frac{1}{T_2^a} & \frac{1}{T_2^a} \\ 0 & -\frac{1}{T_2^a} & \frac{1}{T_2^a} & 0 \\ -\frac{1}{T_2^a} & \frac{1}{T_2^a} & 0 & \frac{1}{T_2^a} \end{pmatrix} & \begin{pmatrix} 0 & 0 & -\frac{1}{T_1^a} & 0 \\ 0 & 0 & 0 & -\frac{1}{T_1^a} \\ -\frac{1}{T_1^a} & 0 & \frac{1}{T_1^a} & 0 \\ 0 & -\frac{1}{T_1^a} & 0 & \frac{1}{T_1^a} \end{pmatrix} & \begin{pmatrix} \frac{1}{T_4} & -\frac{1}{T_1^b} & -\frac{1}{T_3} \\ -\frac{1}{T_1^b} & \frac{1}{T_1^b} & \frac{1}{T_1^b} \\ -\frac{1}{T_1^b} & \frac{1}{T_1^b} & \frac{1}{T_1^b} \\ -\frac{1}{T_3} & \frac{1}{T_1^b} & \frac{1}{T_1^b} \end{pmatrix} \\
\begin{pmatrix} \frac{1}{T_3} & \frac{1}{T_1^b} & \frac{1}{T_1^b} & -\frac{1}{T_4} \\ \frac{1}{T_1^b} & \frac{1}{T_1^b} & \frac{1}{T_8} & \frac{1}{T_8} \\ \frac{1}{T_1^b} & \frac{1}{T_8} & \frac{1}{T_1^b} & \frac{1}{T_8} \\ -\frac{1}{T_4} & \frac{1}{T_8} & \frac{1}{T_8} & \frac{1}{T_3} \end{pmatrix} & \begin{pmatrix} \frac{1}{T_1^b} & \frac{1}{T_1^b} & 0 & 0 \\ \frac{1}{T_1^b} & \frac{1}{T_1^b} & -\frac{1}{T_2^a} & -\frac{1}{T_2^a} \\ 0 & -\frac{1}{T_2^a} & \frac{1}{T_2^a} & 0 \\ 0 & -\frac{1}{T_2^a} & 0 & \frac{1}{T_2^a} \end{pmatrix} & \begin{pmatrix} 0 & 0 & -\frac{1}{T_1^a} & 0 \\ 0 & 0 & 0 & -\frac{1}{T_1^a} \\ -\frac{1}{T_1^a} & 0 & \frac{1}{T_1^a} & 0 \\ 0 & -\frac{1}{T_1^a} & 0 & \frac{1}{T_1^a} \end{pmatrix} & \begin{pmatrix} \frac{1}{T_4} & -\frac{1}{T_1^b} & -\frac{1}{T_3} \\ -\frac{1}{T_1^b} & \frac{1}{T_1^b} & \frac{1}{T_1^b} \\ -\frac{1}{T_1^b} & \frac{1}{T_1^b} & \frac{1}{T_1^b} \\ -\frac{1}{T_3} & \frac{1}{T_1^b} & \frac{1}{T_1^b} \end{pmatrix} \\
\begin{pmatrix} \frac{1}{T_1^a} & 0 & 0 & -\frac{1}{T_4} \\ 0 & \frac{1}{T_1^b} & \frac{1}{T_8} & \frac{1}{T_8} \\ 0 & \frac{1}{T_8} & \frac{1}{T_1^b} & \frac{1}{T_8} \\ -\frac{1}{T_4} & \frac{1}{T_8} & \frac{1}{T_8} & \frac{1}{T_1^b} \end{pmatrix} & \begin{pmatrix} \frac{1}{T_1^b} & \frac{1}{T_1^b} & 0 & 0 \\ \frac{1}{T_1^b} & \frac{1}{T_1^b} & -\frac{1}{T_2^a} & -\frac{1}{T_2^a} \\ 0 & -\frac{1}{T_2^a} & \frac{1}{T_2^a} & 0 \\ 0 & -\frac{1}{T_2^a} & 0 & \frac{1}{T_2^a} \end{pmatrix} & \begin{pmatrix} 0 & 0 & -\frac{1}{T_1^a} & 0 \\ 0 & 0 & 0 & -\frac{1}{T_1^a} \\ -\frac{1}{T_1^a} & 0 & \frac{1}{T_1^a} & 0 \\ 0 & -\frac{1}{T_1^a} & 0 & \frac{1}{T_1^a} \end{pmatrix} & \begin{pmatrix} \frac{1}{T_4} & -\frac{1}{T_1^b} & -\frac{1}{T_3} \\ -\frac{1}{T_1^b} & \frac{1}{T_1^b} & \frac{1}{T_1^b} \\ -\frac{1}{T_1^b} & \frac{1}{T_1^b} & \frac{1}{T_1^b} \\ -\frac{1}{T_3} & \frac{1}{T_1^b} & \frac{1}{T_1^b} \end{pmatrix}
\end{bmatrix}
$$

Table 3.1: Redfield matrix R_{ijkl} of the spin pair without contributions from cross relaxation. In the notation, the outer matrix elements are addressed by the variables i and k, the inner matrix elements by j and l respectively.

vanish. One way to impose simplifications is to assume equal spin–lattice and spin–spin relaxation times $T_1^i = T_2^i$ which leads to the disappearance of some matrix elements. For low temperature cases, the T_1 terms may be omitted completely since spin–lattice relaxation times can become very long in semiconductors [60, 61].

3.1.4 Influence of polarisation

In the following, the influence of thermal spin polarisation on the pair model is discussed briefly. As mentioned in chapter 2, the thermal influences on spin–dependent recombination are negligible in comparison with the effects caused by the intermediate pair formation under certain conditions. Even though these conditions apply to most of the experiments discussed and presented in the following chapters, it is important to be aware when and where the thermal bath which embeds the spin–pair ensemble has to be taken into account. Polarisation effects need to be addressed with regard to the generation rate as well as the equilibrium value $\hat{\rho}^0$ that appears in the relaxation term 3.21. Since pair generation is a transition between energy eigenstates, it can simply be taken into account by a term

$$\{\mathcal{S}_{cr}\left[\hat{\rho}\left(t\right)\right]\}_{ij} = \langle i| \sum_{k=1}^{4} |k\rangle\langle k|G_k|j\rangle = \delta_{ij} G_i \tag{3.29}$$

which is to be added to the annihilation term $\mathcal{S}_{an}\left[\hat{\rho}\left(t\right)\right]$ in eq. 3.17. Note that both the equilibrium ensemble $\hat{\rho}^0$ in the relaxation term as well as the generation rate G_i are the only inhomogeneous contributions to the Liouville equation (eq. 3.1). At high temperatures, the generation of pairs in energy eigenstates G_i is equal $\frac{G}{4}$, one fourth of the net generation rate of all four states. At finite temperatures this has to be changed into the Boltzmann distribution given in eq. 2.1 multiplied by G.

With the discussion of thermal effects on the pair model of spin–dependent recombination, all aspects of the qualitative model, presented in the last chapter, have been expressed in terms of mathematical equations. All relevant contributions to the Liouville equation (eq. 3.1) are available and this central equation of motion can be solved. The latter is of course a separate challenge which can be done analytically only if simplifications are imposed on some of the terms. In following sections, the expression discussed so far will be used for the description of effects and phenomena that can be detected with time–resolved measurements of recombination rates after coherent ESR excitation. Before these solutions for the equation of motion discussed above are presented, a conceptual overview about the time–domain measurements of spin–dependent recombination (TSR) will be given first. This will enable the reader of this book to connect the results and theoretical predictions made in sections 3.3 to 3.6 with the way experiments are carried out and also with the experimental results that are presented in the following chapters.

3.2 The conceptual idea of the TSR experiment

In the past sections, equations were introduced which express the qualitative features of the model presented in chapter 2 in a mathematical form. Here, an overview is given about the TSR experiment and its underlying ideas. Readers who want to learn how the

TSR experiment works but do not whish do go into the theoretical details should read this section only and skip the following sections 3.3 to 3.6. In addition to the general explanation, technical terms and nomenclature used in the following sections and chapters are defined and explained and some qualitative features of quantum mechanics that are important for the understanding of the TSR experiment are reviewed briefly.

3.2.1 Coherence and incoherence

The mathematical foundation described above can be used for the calculation and the prediction of the transient behaviour of a spin–dependent recombination channel during and after a strong resonant microwave interaction. "Strong" in this regard means that the intensity, and hence, the radiation field B_1 of the resonant microwave is high enough such that a significant motion of a given spin pair can take place before a spontaneous ("incoherent") process occurs. Note that the existence of spontaneous processes, also called "collapse of the wave function", is one of the oddities of quantum mechanics: While the spin propagation is fully determined by Schrödinger's time evolution operators before a collapse occurs, the system remains in one of its energy eigenstates after the collapse. Figure 3.2 illustrates the two situations before and after such a collapse for an arbitrary spin vector. Initially, the system is in a state which can be represented by a linear combination of energy eigenstates. Such coherent superpositions that exist for one system will be referred to as "coherent states" in the following. In the presence of an appropriate interaction (e.g. magnetic fields) a continuous precession takes place. When the collapse of the wave function takes place due to an "incoherent process" such as spontaneous electron–photon scattering for instance, the spin is in one of its two eigenstates (when $S = \frac{1}{2}$), its original phase information is lost and no propagation takes place anymore. Note that a measurement process has to be an incoherent process since measurement always requires an exchange of energy. This implies that any observation of a system's propagation within the "coherence time," which means the time before the coherence of a system is lost, has to be done indirectly by repetition of a given experiment many times such that the measurement probabilities for the different eigenstates reveal the coherent superposition of the system before the incoherent process. This also explains why the spin propagation during a pulse ESR experiment has to be fast enough so that the spin state changes significantly before an incoherent process occurs: Slow changes alter the detection probabilities of eigenstates only marginally, and thus, the number of repetitions that reveal these small changes become unreasonably large.

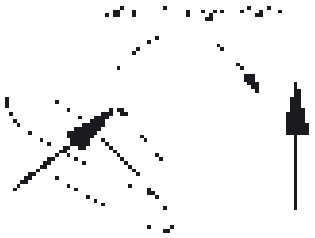

Figure 3.2: The propagation of a spin state (here illustrated by the thick arrow) takes place continuously (thin arrow) and is determined by Schrödinger's time evolution operator. It ends when the state collapses into an energy eigenstate. The collapse is completely random, and hence, undetermined.

The motivation for the observation of coherent spin motion lies in the range of information that can be obtained from it. Since observation implies incoherence, the decay of an observable that represents a coherent propagation reveals coherence times — in the case of recombination an important parameter.

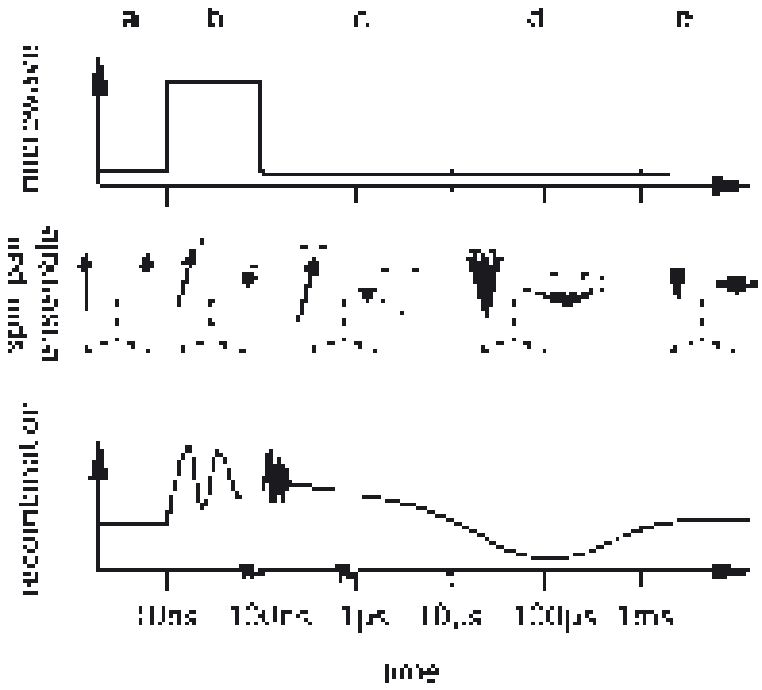

Figure 3.3: The sketch of the conceptual time line of the TSR experiment. A microwave pulse causes Rabi oscillation (b) that changes the pair ensemble from the steady state (a). Because of this, fast dephasing Larmor oscillation takes place after the pulse (c). When the spin ensemble is dephased, the recombination is solely determined by incoherent processes which lead to a change of the recombination increase right after the pulse into a temporary recombination quenching (d) before the ensemble relaxes back to its steady state (e). Note that the figure is just an illustration that does not reflect any experimental or simulated data.

3.2.2 The different time domains of TSR

The idea of the TSR experiment is to obtain information about recombination through certain defects in a given semiconductor material by measuring the excess charge carrier conductivity transient after an intensive microwave burst. Figure 3.3 illustrates the temporal development of the spin ensemble and the recombination during a TSR experiment on a logarithmic time scale. Note that the displayed plots neither represent experimental nor simulated data. They are intended to visualise the different processes that take place during and after a microwave pulse is imposed on one or both partners of a given spin–pair ensemble. The explanation of these processes and the proof of their existence is the central message of this book.

The point of departure for any TSR experiment is the presence of a steady state spin–pair ensemble which has to be obtained under continuous light irradiation, a constant magnetic field and an applied constant voltage which leads to a constant photo current and thus a steady state charge carrier recombination rate [see fig. 3.3(a)]. Since spin pairs are always generated in energy eigenstates (generation is an incoherent process in the sense of the definition given above), only a small set of different states will exist in the steady state, which can serve as defined initial conditions for the propagation during the microwave pulse. Note that the time which a given pair ensemble needs in order to develop

a steady state, is the parameter that poses a lower limit on the length of the shot repetition time between two consecutive experiments. The initial steady state of the photocurrent as well as the eigenstates of the spin–pair ensemble are illustrated in fig. 3.3(a) in the time domain, before the resonant microwave pulse begins.

When a microwave radiation with a frequency close to the Larmor frequencies of the two spin–pair partners is switched on, the two spins begin to precess about the net magnetic field consisting of the externally applied magnetic field $\mathbf{B_0}$ and the microwave field $\mathbf{B_1}$. This precession is called "Rabi oscillation". It is illustrated in fig. 3.3(b) and can be easily described in rotating reference frames as explained in appendix A.4. As already discussed in section 3.1.2, the observable of TSR experiments, the photocurrent, is fundamentally different than the observable of time–resolved ESR: The latter is always based on the measurement of microwave radiation produced by the polarisation of a precessing spin ensemble. Because the photocurrent in a TSR experiment reflects recombination and therefore singlet and triplet densities, only the symmetry state of the spin–pair ensemble becomes measurable and polarisation does not play an important role. Consequently, the relative spin motion of the two partners within a pair are of much greater importance than the absolute spin precession of any of the two spins itself. The relative periodic motion between two energy eigenstates, which means the coherent oscillation, is called a quantum–beat oscillation. Since the recombination rate is dependent on the relative motion between the two spin–pair partners, the recombination rate will reflect the beat oscillation of the two single precessions. Thus, when both partners carry out different Rabi oscillations, the frequency at which the permutation symmetry of the spin pair oscillates will be a beat frequency that is dependent on the two Rabi frequencies. In section 3.5 in which the theory of coherent spin propagation of the spin pairs is outlined in detail, this process is referred to as "Rabi–beat oscillation". The Rabi–beat oscillation can become equal to the Rabi oscillation of one pair partner, when a strong difference between the Larmor frequencies of the two pair partners is present and the microwave is in resonance with one partner only. The different Rabi precessions of the two spin–pair partners and the resulting oscillation of the recombination rate is illustrated in time domain (b) of fig. 3.3. It takes place as long as the microwave is switched on and it is a purely coherent process when the microwave pulse length is much shorter than the recombination time as well as the spin–relaxation times.

After the microwave burst the Rabi–oscillation stops and the pairs will no longer be in energy eigenstates. Because of this, the two spin–pair partners will precess about the constant magnetic field that remains applied throughout the experiment. This precession is called "Larmor oscillation". Due to the different Larmor frequencies of the pair partners, a "Larmor–beat oscillation" will take place that will be reflected by the recombination rate. As shown in section 3.3, Larmor–beat oscillation reflected in a recombination rate can be attenuated very fast by dephasing processes. Unlike incoherent transitions that also cause an attenuation, dephasing is a coherent process solely due to the inhomogeneity of the Larmor frequency difference within the ensemble that causes the macroscopically observed recombination rate. The Larmor–beat oscillation and the subsequent dephasing are depicted in the domain (c) of fig. 3.3. Once the dephasing has prevailed, no coherent spin motion can be reflected by the recombination rate anymore. Because of this the further evolution of the recombination rate is determined solely by incoherent processes: New spin

pairs are generated in eigenstates and the subensemble of spin pairs in non–eigenstates gradually disappears due to recombination and dissociation. Since the dephasing leads to a complete cancellation of all phase information, the description of these incoherent processes can be done with simple rate equations as shown in section 3.4. It is not surprising that the relaxation of the recombination rate back to the steady state turns out to be multiexponential. It is interesting however that the recombination change can become negative temporarily during this process (depicted in time domain (d) of fig. 3.3) and that all magnitudes of the different exponential functions turn out to be dependent on the spin state densities in the moment when the pulse interaction ends. It is this realisation that will pave the way to the measurement of coherent spin motion with recombination: For experiments where a small signal amplitude prohibits a time resolution in the nanoseconds time domain, the transient behaviour during the microwave pulse can be reconstructed from the spin pair propagation in the time domain of the incoherent processes (μs range).

In the following sections, the different processes illustrated in fig. 3.3 are discussed in a non–chronological order: First, the existence of rapidly dephasing Larmor–beat oscillation is shown in section 3.3. Since dephasing will also play an important role for the description of Rabi oscillation, the much less complex Larmor oscillation is discussed first. Thereafter, the possibility of echo experiments is discussed. The latter allow the rephasing of dephased ensembles by means of external interaction. The results of section 3.3 reveal that the dephasing cancels out phase information and thus, the recombination from a dephased spin–pair ensemble can be described by simple rate equations. These rate equations are then formulated and solved for the incoherent time domain in section 3.4. Therein, the impact of spin–spin interactions and non–negligible triplet recombination on the exponential relaxation and the influence of the ensemble state right after the microwave on the magnitude of the exponentials is discussed. Finally, the evolution during the microwave pulse is discussed in section 3.5. Even though this part comes first in the time line of fig. 3.3, it is presented at the end of the theoretical considerations since the reader will probably more easily develop an understanding of this mathematically complex section when he or she has gotten familiar with the connections of its results (states of the spin pair ensembles right after a microwave burst) and the predictions for actually measurable photocurrent transients.

3.3 Larmor–beat oscillation and Larmor–beat echoes

In the following, a first solution of the Liouville equation (eq. 3.1) is presented for a spin–pair ensemble that is in an arbitrary initial state $\hat{\rho}^1 \neq \hat{\rho}^S$, unequal the steady state. It is discussed with regard to the question of the presence of beat oscillation of spin pairs and whether the model discussed above could imply the possibility of coherent dephasing.

3.3.1 Solution of the Liouville equation

If polarisation effects, spin relaxation and triplet recombination are neglected and weak spin–spin interaction as well as the absence of resonant microwave radiation are assumed, equation 3.1 can be written as a linear and inhomogeneous system of ordinary first order

differential equations

$$\partial_t \tilde{\rho}(t) = \tilde{M}\tilde{\rho}(t) + \tilde{G} \tag{3.30}$$

with

$$\tilde{M} = \begin{pmatrix}
\eta & 0 & 0 & 0 & 0 & 0 & 0 & 0 & 0 & 0 & 0 & 0 & 0 & 0 & 0 & 0 \\
0 & \alpha_2 & \frac{r_S}{4} & 0 & 0 & 0 & 0 & 0 & 0 & 0 & 0 & 0 & 0 & 0 & 0 & 0 \\
0 & \frac{r_S}{4} & \beta_2 & 0 & 0 & 0 & 0 & 0 & 0 & 0 & 0 & 0 & 0 & 0 & 0 & 0 \\
0 & 0 & 0 & \epsilon_2 & 0 & 0 & 0 & 0 & 0 & 0 & 0 & 0 & 0 & 0 & 0 & 0 \\
0 & 0 & 0 & 0 & \alpha_1 & 0 & 0 & 0 & \frac{r_S}{4} & 0 & 0 & 0 & 0 & 0 & 0 & 0 \\
0 & 0 & 0 & 0 & 0 & \xi & \frac{r_S}{4} & 0 & 0 & \frac{r_S}{4} & 0 & 0 & 0 & 0 & 0 & 0 \\
0 & 0 & 0 & 0 & 0 & \frac{r_S}{4} & \nu_1 & 0 & 0 & 0 & \frac{r_S}{4} & 0 & 0 & 0 & 0 & 0 \\
0 & 0 & 0 & 0 & 0 & 0 & 0 & \beta_2 & 0 & 0 & 0 & \frac{r_S}{4} & 0 & 0 & 0 & 0 \\
0 & 0 & 0 & 0 & \frac{r_S}{4} & 0 & 0 & 0 & \beta_1 & 0 & 0 & 0 & 0 & 0 & 0 & 0 \\
0 & 0 & 0 & 0 & 0 & \frac{r_S}{4} & 0 & 0 & 0 & \nu_2 & \frac{r_S}{4} & 0 & 0 & 0 & 0 & 0 \\
0 & 0 & 0 & 0 & 0 & 0 & \frac{r_S}{4} & 0 & 0 & \frac{r_S}{4} & \xi & 0 & 0 & 0 & 0 & 0 \\
0 & 0 & 0 & 0 & 0 & 0 & 0 & \frac{r_S}{4} & 0 & 0 & 0 & \alpha_2 & 0 & 0 & 0 & 0 \\
0 & 0 & 0 & 0 & 0 & 0 & 0 & 0 & 0 & 0 & 0 & 0 & \epsilon_1 & 0 & 0 & 0 \\
0 & 0 & 0 & 0 & 0 & 0 & 0 & 0 & 0 & 0 & 0 & 0 & 0 & \beta_1 & \frac{r_2}{4} & 0 \\
0 & 0 & 0 & 0 & 0 & 0 & 0 & 0 & 0 & 0 & 0 & 0 & 0 & \frac{r_S}{4} & \alpha_1 & 0 \\
0 & 0 & 0 & 0 & 0 & 0 & 0 & 0 & 0 & 0 & 0 & 0 & 0 & 0 & 0 & \eta
\end{pmatrix} \tag{3.31}$$

and

$$G_i = \begin{cases} \frac{G}{4} & \text{if } i\text{=1,6,11,16} \\ 0 & \text{otherwise} \end{cases}. \tag{3.32}$$

The coefficient matrix in eq. 3.31 has a high zero density and diagonal elements

$$\begin{aligned}
\alpha_{1,2} &= \pm i\omega_a - d - \frac{r_S}{4} \\
\beta_{1,2} &= \pm i\omega_b - d - \frac{r_S}{4} \\
\epsilon_{1,2} &= \pm i\omega_a + i\omega_b - d - \frac{r_S}{4} \\
\nu_{1,2} &= \pm i\omega_a - i\omega_b - d - \frac{r_S}{4} \\
\xi &= -d - \frac{r_S}{4} \\
\eta &= -d.
\end{aligned} \tag{3.33}$$

In this expression, d and r_S represent the pair dissociation and the singlet recombination probabilities, G is the pair generation rate and ω_i are the Larmor frequencies of the two pair partners. Note that the simplifications imposed on equation 3.30 are not a strong confinement of the generality with regard to the point that is to be made in this section which is to show that any coherent Larmor oscillation which takes place after the pair ensemble is excited into a non–eigenstate will eventually dephase: When the spin–spin interactions become stronger and thus, the spin eigenstates become more symmetric, the Larmor oscillation will reduce and therefore, the attenuation of an oscillating recombination rate will be even faster. It is also assumed that spin relaxation takes place on a

time scale slower than the dephasing process. Due to the absence of the radiative part $\hat{H}_1$ in the Hamiltonian, the coefficient matrix of the ODE in eq. 3.30 is constant, which allows the calculation of a solution with a straight forward algorithm as outlined in appendix A.6. First, an arbitrary solution of the inhomogeneous case has to be found which, for simplicity, is chosen to be the steady state case

$$\rho^S = \begin{pmatrix} \frac{G}{4d} & 0 & 0 & 0 \\ 0 & \frac{G\left(8[\omega_a-\omega_b]^2+4r_S d+r_S^2+4d^2\right)}{8\left(r_S^2 d+3d^2 r_S+4[\omega_a-\omega_b]^2 d+2[\omega_a-\omega_b]^2 r_S+2d^3\right)} & \frac{i\left(2[\omega_a-\omega_b]Gr_S-2idGr_S-ir_S^2 G\right)}{8\left(r_S^2 d+3d^2 r_S+4[\omega_a-\omega_b]^2 d+2[\omega_a-\omega_b]^2 r_S+2d^3\right)} & 0 \\ 0 & -\frac{i\left(2[\omega_a-\omega_b]Gr_S+2idGr_S+ir_S^2 G\right)}{8\left(r_S^2 d+3d^2 r_S+4[\omega_a-\omega_b]^2 d+2[\omega_a-\omega_b]^2 r_S+2d^3\right)} & \frac{G\left(8[\omega_a-\omega_b]^2+4r_S d+r_S^2+4d^2\right)}{8\left(r_S^2 d+3d^2 r_S+4[\omega_a-\omega_b]^2 d+2[\omega_a-\omega_b]^2 r_S+2d^3\right)} & 0 \\ 0 & 0 & 0 & \frac{G}{4d} \end{pmatrix}$$

that can be obtained from eq. 3.30 when the left hand side is set to zero. Note that the steady state $\hat{\rho}^S$ is in general different from the equilibrium state $\hat{\rho}^0$ mentioned above. When the pair partners have separated Landé factors ($g_a \neq g_b$), and the constant magnetic field is sufficiently strong, the condition $|\omega_a - \omega_b| \gg r \gg d$ is fulfilled and the steady state approaches

$$\hat{\rho}^S = \frac{G}{2d}\begin{pmatrix} \frac{1}{2} & 0 & 0 & 0 \\ 0 & 0 & 0 & 0 \\ 0 & 0 & 0 & 0 \\ 0 & 0 & 0 & \frac{1}{2} \end{pmatrix} \tag{3.34}$$

which reflects the short lifetime of the states with singlet content. The matrix of eq. 3.34 represents an incoherent mixture of $|T+\rangle$ and $|T-\rangle$ states that is completely unpolarised since thermal influences are disregarded. A characteristic equation of the coefficient matrix of eq. 3.30 reveals a set of eigenvectors

$$\begin{aligned}
\tilde{v}_1 &= [0,0,0,0,0,0,0,0,0,0,0,0,1,0,0,0]\,, & \lambda_1 &= i\xi_4 - d \\
\tilde{v}_2 &= [0,0,0,1,0,0,0,0,0,0,0,0,0,0,0,0]\,, & \lambda_2 &= -i\xi_4 - d \\
\tilde{v}_3 &= [0,0,0,0,0,1,\xi_1,0,0,\xi_2,1,0,0,0,0,0]\,, & \lambda_3 &= 2\xi_5 - d - r/2 \\
\tilde{v}_4 &= [0,0,0,0,0,1,-\xi_2,0,0,-\xi_1,1,0,0,0,0,0]\,, & \lambda_4 &= -2\xi_5 - d - r/2 \\
\tilde{v}_5 &= [0,0,0,0,\xi_1,0,0,0,1,0,0,0,0,0,0,0]\,, & \lambda_5 &= \xi_4 + \xi_5 - d - r/2 \\
\tilde{v}_6 &= [0,0,0,0,0,0,0,0,0,0,0,0,0,0,\xi_2,1,0]\,, & \lambda_6 &= \xi_4 + \xi_5 - d - r/2 \\
\tilde{v}_7 &= [0,0,0,0,0,0,0,0,0,0,0,0,0,0,-\xi_1,1,0]\,, & \lambda_7 &= \xi_4 - \xi_5 - d - r/2 \\
\tilde{v}_8 &= [0,0,0,0,-\xi_2,0,0,0,1,0,0,0,0,0,0,0,0]\,, & \lambda_8 &= \xi_4 - \xi_5 - d - r/2 \\
\tilde{v}_9 &= [0,\xi_2,1,0,0,0,0,0,0,0,0,0,0,0,0,0,0]\,, & \lambda_9 &= -\xi_4 + \xi_5 - d - r/2 \\
\tilde{v}_{10} &= [0,0,0,0,0,0,0,0,\xi_1,0,0,0,1,0,0,0,0]\,, & \lambda_{10} &= -\xi_4 + \xi_5 - d - r/2 \\
\tilde{v}_{11} &= [0,0,0,0,0,0,0,-\xi_2,0,0,0,1,0,0,0,0]\,, & \lambda_{11} &= -\xi_4 - \xi_5 - d - r/2 \\
\tilde{v}_{12} &= [0,-\xi_1,1,0,0,0,0,0,0,0,0,0,0,0,0,0,0]\,, & \lambda_{12} &= -\xi_4 - \xi_5 - d - r/2 \\
\tilde{v}_{13} &= [0,0,0,0,0,0,0,1,0,0,-1,\xi_3,0,0,0,0,0]\,, & \lambda_{13} &= -d - r/2 \\
\tilde{v}_{14} &= [0,0,0,0,0,0,1,0,0,0,0,-1,0,0,0,0,0]\,, & \lambda_{14} &= -d - r/2 \\
\tilde{v}_{15} &= [0,0,0,0,0,0,0,0,0,0,0,0,0,0,0,0,1]\,, & \lambda_{15} &= -d \\
\tilde{v}_{16} &= [1,0,0,0,0,0,0,0,0,0,0,0,0,0,0,0,0] & \lambda_{16} &= -d
\end{aligned} \tag{3.35}$$

as well as their respective eigenvalues λ_i. The variables ξ_k in this expression correspond to

$$\begin{aligned}\xi_{1,2} &= \frac{\xi_5 \pm i\,(\omega_a - \omega_b)}{r} \\ \xi_3 &= \frac{-2i}{r}\,(\omega_a - \omega_b) \\ \xi_4 &= \frac{i}{2}\,(\omega_a + \omega_b) \\ \xi_5 &= \frac{1}{4}\sqrt{r^2 - 4\,(\omega_a - \omega_b)^2}. \end{aligned} \tag{3.36}$$

With the results given above, it is possible to calculate the evolution of a spin–dependent recombination rate after the pair ensemble was brought into an initial state $\hat{\rho}^1$ by an ESR excitation. In the following, a notation for microwave pulses is used, where a (ϕ_a, ϕ_b) pulse describes a single microwave pulse, whose length, frequency and intensity are chosen, such that spin a turns by an angle ϕ_a and spin b by an angle ϕ_b. This behaviour of the exciting pulse can only be achieved if the two pair partners have a sufficient separation of their Landé g-factors. Due to the shortness of the pulse, the two spins then experience different field strength from the microwave radiation at their respective resonances and oscillate therefore at different Rabi frequencies. A symmetric $\left(\frac{\pi}{2}, \frac{\pi}{2}\right)$ pulse excitation of the spins can be expressed as a transformation $\hat{V}_1$ that is represented in the product base by a matrix

$$\tilde{V}_1 = \frac{1}{2}\begin{pmatrix} 1 & -i & -i & -1 \\ -i & 1 & -1 & -i \\ -i & -1 & 1 & -i \\ -1 & -i & -i & 1 \end{pmatrix}. \tag{3.37}$$

Transformation $\hat{V}_1$ brings the spin ensemble into a state $\hat{\rho}^1 = \hat{V}_1^\dagger \hat{\rho}^S \hat{V}_1$ which is a mixture of a $\frac{1}{\sqrt{2}}\left(|T_+\rangle - |T_-\rangle\right)$ and a $|T_0\rangle$ state, while an antisymmetric $\left(\frac{\pi}{2}, \frac{3\pi}{2}\right)$ pulse, which can be described by a transformation

$$\tilde{V}_2 = \frac{1}{2}\begin{pmatrix} 1 & -i & i & 1 \\ -i & 1 & 1 & i \\ i & 1 & 1 & -i \\ 1 & i & -i & 1 \end{pmatrix}, \tag{3.38}$$

leads to a mixture of the $\frac{1}{\sqrt{2}}\left(|T_+\rangle + |T_-\rangle\right)$ and a $|S_0\rangle$ state. In a similar way, double selective pulses could bring the steady state into a mixture of a coherent superposition of the $|T_+\rangle$ and $|T_-\rangle$ states and an arbitrary coherent linear combination of the $|S_0\rangle$ and the $|T_0\rangle$ states. The origin of the expressions 3.37 and 3.38 will be explained in section 3.5 where the evolution of a pair ensemble during the presence of resonant radiation is discussed.

With the initial condition $\hat{\rho}^1$ for the evolution of the spin pair after the pulse interaction given, one can now calculate a solution for this evolution from the eigenvectors and eigenvalues of the coefficient matrix as given in eq. 3.35. Since only singlet recombination is considered, the recombination rate change $\Delta R\,(t) = R\,(t) - R_S$ as defined in eq. 3.3 can

be obtained from the density matrix by the equation

$$R(t) = r_S \mathrm{Tr}\left[|S\rangle\langle S|\hat{\rho}(t)\right] = \frac{r_2}{2}\left[\rho_{33}(t) + \rho_{22}(t) - \rho_{32}(t) - \rho_{23}(t)\right]. \tag{3.39}$$

With the solution $\rho_{ij}(t)$ calculated as explained in appendix A.6, the evolution of the recombination change after the microwave pulse

$$\begin{aligned}\Delta R(t) = &-\frac{r_S}{2\left(r_S^2 - 4\Delta\omega^2\right)} \exp\left(-\left[d + \frac{r_S}{2}\right]t\right)\Bigg[4\Delta\omega^2\left(\Delta\rho_{22}^1 + \Delta\rho_{33}^1\right) \\ &+ \left(\left(r_S^2 - 4\Delta\omega^2\right)\left(\Delta\rho_{23}^1 + \Delta\rho_{32}^1\right) - r_S^2\left(\Delta\rho_{22}^1 + \Delta\rho_{33}^1\right)\right)\cosh\left(\frac{\sqrt{r_S^2 - 4\Delta\omega^2}}{2}t\right) \\ &+ \sqrt{r_S^2 - 4\Delta\omega^2}\, r_S\left(\Delta\rho_{22}^1 + \Delta\rho_{33}^1 - \Delta\rho_{23}^1 - \Delta\rho_{32}^1\right)\sinh\left(\frac{\sqrt{r_S^2 - 4\Delta\omega^2}}{2}t\right)\Bigg]\end{aligned} \tag{3.40}$$

is obtained, with

$$\begin{aligned}\Delta\omega &= \omega_a - \omega_b \\ \Delta\rho_{ij}^1 &= \rho_{ij}^1 - \rho_{ij}^S.\end{aligned} \tag{3.41}$$

Note that eq. 3.40 depends on the pair annihilation contributions r_S and d but not on the generation rate G that is contained in the inhomogeneous part of the Liouville equation (eq. 3.30). Generation impacts only the steady state and, therefore, the magnitude of ΔR but not the shape of its transient. Another remarkable aspect of the recombination transient is that it depends solely on the Larmor–frequency difference but not on their absolute values. This confirms the assumption expressed above that only the relative spin motion within one spin pair determines recombination. In the following, the result in eq. 3.40 is discussed for three limiting cases which will illustrate the qualitative properties of the spin pair motion after a certain microwave pulse preparation.

(A) Strong incoherence due to fast recombination
In case of strong recombination ($\frac{r_S}{2} \gg \Delta\omega \gg d$), the solution eq. 3.40 becomes

$$\Delta R(t) = \frac{r_S}{2}\left(\Delta\rho_{22}^1 + \Delta\rho_{33}^1 - \Delta\rho_{23}^1 - \Delta\rho_{32}^1\right)\exp\left(-r_S t\right). \tag{3.42}$$

From a steady state $\hat{\rho}^S$ any given microwave interaction will lead to $\Delta\rho_{ij}^1 > 0$ for any of the matrix elements in eq. 3.42. This means when recombination is strong, a resonant increase of the recombination rate during the pulse will be followed by an exponential relaxation of the recombination rate after the pulse whose time constant will be determined by the recombination probability.

(B) Asymptotic case
When the recombination time of a spin pair approaches the Larmor–beat frequency ($\frac{r_S}{2} \approx \Delta\omega \gg d$), the evolution of recombination after a resonant excitation becomes

$$\Delta R(t) = \frac{r_S}{2}\left(\Delta\rho_{22}^1 + \Delta\rho_{33}^1\right)\exp\left(-\frac{r_S}{2}t\right). \tag{3.43}$$

which is still an exponential decay that is half as fast as in case (A), however.

(C) Weak incoherence due to slow recombination
In the case of slow recombination ($d \ll \frac{r_S}{2} \ll \Delta\omega$), $r_S^2 - 4\Delta\omega^2$ becomes negative and its square root purely imaginary, which turns the hyperbolic function of eq. 3.40 into periodic functions. Thus, recombination

$$\Delta R\left(t\right) = \frac{r_S}{2}\left(\Delta\rho_{22}^1 + \Delta\rho_{33}^1 - \left[\Delta\rho_{23}^1 + \Delta\rho_{32}^1\right]\cos\left(\Delta\omega t\right)\right)\exp\left(-\frac{r_S}{2}t\right) \tag{3.44}$$

has an oscillating transient whose frequency depends on the Larmor–frequency difference within the spin pairs. This oscillation is damped by the recombination process. Equation 3.44 shows that a coherent beat oscillation within the ensemble of spin pairs can control the recombination rate. Note that the recombination probability of the spin–dependent process has to be sufficiently weak, such that the oscillation is damped weakly. However, this means that beat–oscillation processes will actually be detectable only in a certain recombination range since the signal has to be also strong enough in order to be detectable at all.

3.3.2 Dephasing and rephasing

Before eq. 3.44 can be applied to a material with disorder, another aspect has to be taken into account: Recombination through localised band gap states is caused by point defects which exhibit in many cases an inhomogeneity of structure or microscopic environment. The latter may cause an inhomogeneous broadening of the defect's paramagnetic resonances which means a distribution of the g factor within the entity of defects. In the description of spin–dependent recombination as discussed so far, inhomogeneous broadening has not been considered. In order to do this, one can describe the ensemble of spin pairs as an ensemble of many ensembles of spin pairs: Within a given subensemble, the Larmor–frequency differences are all equal and the model as discussed can be applied. The distribution $\Phi\left(\Delta\omega\right)$ of Larmor–frequency differences given in a material is then described by different Larmor–frequency differences that exist in the different subensembles. Since all systems contribute to the net recombination according to their occurrence, the recombination rate

$$\Delta R_{net}\left(t\right) = \int_{-\infty}^{\infty}\Phi\left(\Delta\omega\right)\Delta R\left(t\right)d\Delta\omega \tag{3.45}$$

is the integral of the distribution $\Phi\left(\Delta\omega\right)$ over the recombination transients of the different subensembles. In the following, a simulation of the spin–dependent recombination through a material with a distribution of Larmor–frequency differences is discussed for the two $\hat{V}_1$ and $\hat{V}_2$ preparations mentioned in eqs. 3.37 and 3.38. With these pulse preparations, one can obtain from eqs. 3.44 and 3.45 an expression

$$\frac{\Delta R_{\mathrm{net}}^{\hat{V}_1,\hat{V}_2}\left(t\right)}{\Delta R_{max}} = \frac{1}{2}\int_{-\infty}^{\infty}\Phi(\Delta\omega)\left[1 \pm \cos\left(\Delta\omega t\right)\right]e^{-\frac{r_S}{2}t}d\Delta\omega. \tag{3.46}$$

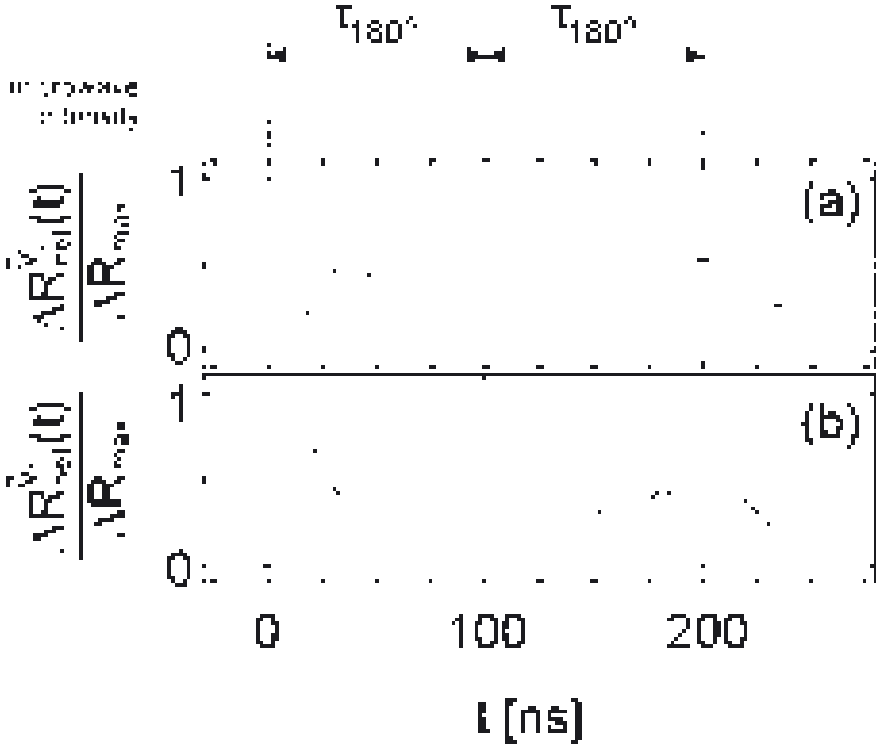

Figure 3.4: Simulation of quantum–beat recombination–echoes for a $\left(\frac{\pi}{2}, \frac{3\pi}{2}\right) - \tau - (\pi, \pi)$ pulse sequence (a) and a $\left(\frac{\pi}{2}, \frac{\pi}{2}\right) - \tau - (\pi, \pi)$ pulse sequence (b). The timing of the pulses is sketched in the upper part of the figure. The dotted lines in (a) and (b) illustrate the beat envelopes. For further details see text.

for the recombination change, normalised to the maximum recombination change ΔR_{max}. The parameters of this simulation were obtained from a line shape analysis of EDMR measurements on recombination between shallow trap states (CE) and dangling bond states (db) [23] in intrinsic hydrogenated microcrystalline silicon (μc-Si:H). The value for the singlet recombination probabilities was chosen to be $r_S = 3 \times 10^6\ s^{-1}$ which is within the range estimated by Kanschat [46]. The same reference estimated a negligible dissociation probability which would fulfill the assumption made above. Both the CE and db resonances exhibit broad inhomogeneous peaks. The distribution of the Larmor–frequency differences is the convolution of the distribution of the Larmor frequencies of the two pair partners. Therefore, for $\Phi(\Delta\omega)$ an even broader Gaussian distribution with a maximum at 25MHz and a width of 40MHz was assumed. The latter corresponds to a phase conservation time of T_M=25 ns. Figure 3.4a shows the recombination transient when the ensemble is subjected to a $\left(\frac{\pi}{2}, \frac{3\pi}{2}\right)$ pulse. During the pulse, the ensemble changes as discussed above and increases its $|S_0\rangle$ content from the minimum to the maximum which maximises the recombination rate after the pulse at $t = 0$. Right after the pulse (t=0), the ensemble starts to beat between $|S_0\rangle$ and $|T_0\rangle$ states. Due to the Larmor–frequency inhomogeneity, the beat oscillations dephase within the phase conservation time T_M. This phase loss is illustrated by the dotted line in Fig. 3.4. Once it has prevailed ($t \approx 50$ ns), the $|S_0\rangle$ and $|T_0\rangle$ densities are equalised and the intermediate recombination rate slowly relaxes exponentially towards the steady state. This relaxation process is determined by

incoherent transitions. If singlet recombination is faster than spin relaxation, the decay reflects the singlet recombination probability. Figure 3.4b illustrates the transient after a symmetric $\left(\frac{\pi}{2}, \frac{\pi}{2}\right)$ preparation pulse. The beat oscillation is now phase shifted because the ensemble maximises only its $|T_0\rangle$ content during the pulse. Note that the recombination remains unchanged during the pulse since the singlet content has not been changed. The spin pairs in $|T_0\rangle$ states can now precess towards the $|S_0\rangle$ state leading to an increase of the recombination rate.

The transients of fig. 3.4 illustrate the difficulty in distinguishing between a coherent dephasing of the ensemble and incoherence due to the recombination transitions. This is always the case when the width of the distribution and the incoherent processes are of the same order of magnitude. In the case of rapid dephasing (width of $\Phi(\Delta\omega)$ is larger than transition probabilities of incoherent processes), a measurement of the coherence decay can only be carried out by introduction of a phase reversal process that removes the dephasing but leaves the incoherence unchanged. In the literature such temporary phase reversal effects are referred to as echo effects, which have been reported for a variety of other physical systems. Hahn [9] first reported spin echoes for nuclear spin ensembles before Kurnit et al. [62] observed photon echoes. Only recently, Niggemeier et al. [63] described a current echo effect for one dimensional conducting structures. Echoes can be produced through the reversal of the phase loss process in initially coherent systems. Reversible dephasing occurs whenever a macroscopic observable is dependent on the phase between oscillating systems whose eigenfrequencies have a certain time independent distribution [9]. When the dephasing process is reversed through resonant excitation at a certain time τ_{180°, an echo can be detected at time $2\tau_{180^\circ}$. This is explained in greater detail in appendix A.4. A rephasing of the Larmor–beat oscillations can be introduced in a similar way as for the polarisation of single spins (see appendix A.4). The calculation of the pair response to a second microwave pulse (π–π pulse), imposed at time τ_{180° after the first pulse, reveals a recombination

$$\frac{\Delta R_{\mathrm{net}}^{\hat{V}_1,\hat{V}_2}\left(2\tau_{180^\circ}\right)}{\Delta R_{max}} = \frac{1}{2}\left[1 \pm 1\right] e^{-r_S \tau_{180^\circ}} \tag{3.47}$$

at time $2\tau_{180^\circ}$. Equation 3.47 is independent of $\Delta\omega$, indicating that a phase recovery has taken place. Thus, echo experiments on spin–dependent recombination centres in disordered semiconductors, in which microwave pulses stimulate the phase recovery of oscillating spin pairs, are possible. Note that the echo has a different sign for the two pulse preparations illustrated in fig. 3.4. In the moment of rephasing, the spin ensemble returns to the initial state right after the pulse, which makes the echo as dependent on the preparation pulse as the transient before the dephasing prevails.

In the following, the effect described above is referred to as "quantum–beat recombination–echo" or, abbreviated, "recombination echo". The simulations and calculations shown indicate how coherent spin motion experiments on recombination mechanisms could give new insights into semiconductor materials: In contrast to conventional incoherent field domain spin–dependent recombination experiments, it is possible to determine parameters such as r_S, T_M, $\Delta\omega$ or the inhomogeneity $\Phi\left(\Delta\omega\right)$ of defects participating in recombination. In addition, the general nature of distant pair recombination and the validity of the recombination model by Kaplan, Solomon and Mott can be further explored. Note that the description of the pulse preparation in eqs. 3.37 and 3.38 neglects any dephasing of

the spin ensemble during the pulse interaction. Thus, the Larmor–echo experiment can only take place as described above, when the pulse interaction is sufficiently fast so that dephasing is small. However, this implies that the pulse sequences are carried out with extraordinary high microwave intensities. For the given simulation and its parameters, microwave intensities would be necessary that are beyond state of the art spectrometers. Thus, for real experiments the dephasing during the pulse has to be taken into account as it is done in the discussion of Rabi oscillation during microwave irradiation in section 3.5.

3.4 Incoherence

The results presented in the previous section illustrate that coherent spin motion can govern recombination. While the simplifications made with regard to spin–spin interaction and triplet recombination are of minor relevance with regard to the existence of Larmor–beat oscillations, the results presented in eqs. 3.46 and 3.47 are not accurate with regard to the decay of the recombination rate after dephasing has prevailed. Moreover, it is important to keep in mind that the pair–recombination rates as expressed in eqs. 3.46 and 3.47 are not equal to the actual photocurrent transients that can be measured experimentally. Therefore, the influence of incoherent processes on the charge carrier densities is discussed in the following. This leads to an expression that shows how long–term contributions to the photoconductivities of both the electron and the hole densities allow the access to coherent experiments. In spite of the simplified model used in section 3.3, eq. 3.46 demonstrates the general behaviour of the pair ensemble long[2] after a resonant microwave pulse has moved the spin–pair ensemble from the steady state. When dephasing has prevailed, the ensemble is completely mixed and an equal number of symmetric $|T_0\rangle$ and antisymmetric $|S\rangle$ pair states exist at any given time. The relaxation of the recombination rate towards the steady state is only determined by incoherent influences and therefore exponential. In section 3.3.2, the distribution of Larmor–frequency differences $\Delta\omega$ was taken into account by an integration over a continuity of many ensembles. Since eq. 3.19 depends linearly on the different matrix elements, we can move the integral in eq. 3.45

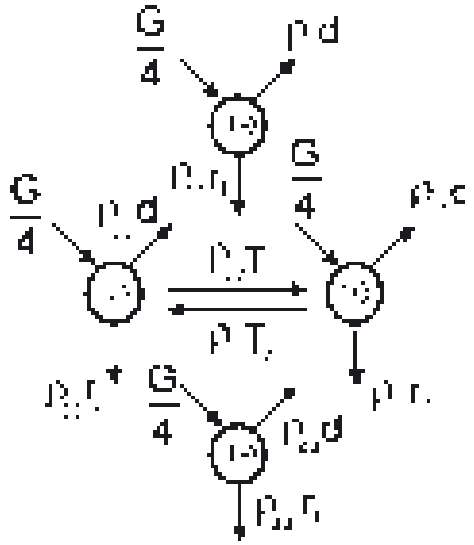

Figure 3.5: Sketch of different incoherent processes that can influence the densities of the 4 spin–pair configurations T+, T-, 2 and 3. For details see text.

[2]longer than the dephasing time

right before the density matrix elements which yields an equation

$$\Delta\sigma_{\mathrm{ph}}(t) = e\tau_L d\mu_e \sum_{i=1}^{4} \left[\rho_{ii}^{net}(t) - \rho_{ii}^{S}\right] \left(1 - \frac{r_i}{d}\frac{\mu_h}{\mu_e}\right)$$

$$\text{with} \qquad \rho_{ii}^{net}(t) = \int_{-\infty}^{\infty} \Phi(\Delta\omega)\, \rho_{ii}^{\Delta\omega}(t)\, d\Delta\omega \tag{3.48}$$

for the photoconductivity changes. The matrix element $\rho_{ij}^{\Delta\omega}$ in the integral symbolises a matrix element of the subensemble with Larmor–frequency difference $\Delta\omega$. Expression ρ_{ij}^{net} in eq. 3.48 is highly inconvenient for calculations in the coherent time domain since it can not be plugged into the Liouville equation. However, when dephasing has occurred, the equalisation of symmetric and antisymmetric states diagonalises the matrix that represents the net density matrix $\tilde{\rho}^{net}(t)$ in its energy eigenbase and therefore, the whole problem reduces to a simple set of rate equations that describe transitions between energy eigenstates.

Figure 3.5 illustrates this simple rate picture. Herein, singlet as well as triplet recombination is considered according to eq. 3.18 and the spin–spin interactions are taken care of by the shifted energy eigenbase. The densities of the respective pair states are represented by ρ_{ii} in conjunction with the nomenclature of the previous section.

3.4.1 Influence of relaxation

In the rate picture of fig. 3.5, no spin–lattice relaxation has been taken into account. Since spin–lattice relaxation is a phonon–scattering process [10], it can be controlled in most material systems by the temperature at which an experiment is carried out. Most of the experiments presented in the following chapters where performed at very low temperatures such that the spin–lattice relaxation processes did not play a role at all. The absence of spin–lattice transitions reduces the number of incoherent processes that influence the recombination transients. This simplifies the data interpretation of experiments and also the theoretical considerations presented in this chapter.

Spin–spin relaxation–transitions can not be neglected. In general, they are faster than spin–lattice processes and moreover, they are much less temperature dependent and therefore less controllable by experimental conditions. As illustrated in fig. 3.5, spin–spin relaxation causes transitions between states $|2\rangle$ and $|3\rangle$ only. This can be deduced from the structure of the Redfield matrix displayed in table 3.1: When the spin–lattice relaxation times $T_1^{a,b}$ are assumed to be infinite and, for simplicity, the spin–spin relaxation times of both pair partners are assumed to be equal (T_2^a=T_2^b=T_2), the Redfield matrix (tab. 3.1) has the rank two, which means the row and column vectors are highly linear dependent. If this Redfield matrix is then plugged into eq. 3.21, the contribution of the Redfield term to the Liouville equation $\delta\rho_{ij} = \left[\mathcal{R}\{\hat{\rho}(t) - \hat{\rho}_0\}\right]_{ij}$ leads to a set of equations

$$\begin{aligned}
\delta\rho_{11} &= 0 \\
\delta\rho_{22} &= -\left(\delta\rho_{12} + \delta\rho_{13} + \delta\rho_{23} + \delta\rho_{32} + \delta\rho_{33} + \delta\rho_{42} + \delta\rho_{43}\right) && (3.49)\\
\delta\rho_{33} &= -\left(\delta\rho_{21} + \delta\rho_{31} + \delta\rho_{32} + \delta\rho_{23} + \delta\rho_{22} + \delta\rho_{24} + \delta\rho_{34}\right) && (3.50)\\
\delta\rho_{44} &= 0
\end{aligned}$$

that relate the different Redfield contributions under cancellation of the actual relaxation matrix elements, the T_2 relaxation times. From the two conditions 3.49 and 3.50 and the Hermiticity that $\delta\tilde{\rho}$ is known to have, one can show that

$$\begin{aligned} \mathfrak{Im}\left[\delta\rho_{12}+\delta\rho_{13}+\delta\rho_{42}+\delta\rho_{43}\right]&=0\\ \mathfrak{Im}\left[\delta\rho_{21}+\delta\rho_{31}+\delta\rho_{24}+\delta\rho_{34}\right]&=0 \end{aligned} \tag{3.51}$$

as well as

$$\begin{aligned} \mathfrak{Re}\left[\delta\rho_{12}+\delta\rho_{13}+\delta\rho_{42}+\delta\rho_{43}\right]&=0\\ \mathfrak{Re}\left[\delta\rho_{21}+\delta\rho_{31}+\delta\rho_{24}+\delta\rho_{34}\right]&=0. \end{aligned} \tag{3.52}$$

Thus, when a dephasing has taken place, and $\mathfrak{Re}\left[\delta\rho_{23}\right]=\mathfrak{Re}\left[\delta\rho_{32}\right]=0$, eqs. 3.49 and 3.50 become a single expression

$$\delta\rho_{22}=-\delta\rho_{33}. \tag{3.53}$$

This shows that in absence of spin–lattice relaxation and under the assumption of equal spin–spin relaxation of both pair partners, mutual transitions between pairs in the states $|2\rangle$ and $|3\rangle$ take place only. This result obtained from the Redfield matrix is not surprising: Unlike spin–lattice relaxation which is an energy transfer process where energy from phonons is absorbed into Zeeman levels or vice versa, spin–spin relaxation processes are rather phase–relaxation processes which is why they are also called transverse relaxation processes. Since only the states $|2\rangle$ and $|3\rangle$ have close energy levels, the T_2 processes are limited to the mutual transitions between these states.

3.4.2 Influence of recombination and dissociation

From the rate picture given in fig. 3.5, an ODE system

$$\begin{pmatrix}\dot{\rho}_{11}\\ \dot{\rho}_{22}\\ \dot{\rho}_{33}\\ \dot{\rho}_{44}\end{pmatrix}=\begin{pmatrix}-d-r_T & 0 & 0 & 0\\ 0 & -d-r_2-\frac{1}{T_2} & \frac{1}{T_2} & 0\\ 0 & \frac{1}{T_2} & -d-r_3-\frac{1}{T_2} & 0\\ 0 & 0 & 0 & -d-r_T\end{pmatrix}\begin{pmatrix}\rho_{11}\\ \rho_{22}\\ \rho_{33}\\ \rho_{44}\end{pmatrix}+\frac{G}{4}\begin{pmatrix}1\\1\\1\\1\end{pmatrix} \tag{3.54}$$

can be formulated which has a constant coefficient matrix similar to the ODE system obtained from the Liouville equation (eq. 3.30) of section 3.3. Therefore, the solution can also be obtained with the algorithm outlined in appendix A.1. The steady state solution

$$\begin{aligned} \rho^S_{11,44} &= \frac{G}{4}\frac{1}{d+r_T}\\ \rho^S_{22,33} &= \frac{G}{4}\frac{2/T_2+d+r_{3,2}}{d^2+r_2d+2d/T_2+r_3d+r_2r_3+r_3/T_2+r_2/T_2} \end{aligned} \tag{3.55}$$

is indicative of the non–equilibrium situation that exists, when different recombination probabilities are present. As expected, when $r_S \gg r_T, d$, the ratio between the densities of states with and without singlet content becomes small ($\rho_{22,33}/\rho_{11,44} \ll 1$), independently

of the strength of the spin–spin relaxation rate. The general solution of the homogeneous part of the ODE in eq. 3.54 can be obtained from the eigenvectors and eigenvalues

$$\begin{aligned}
\tilde{v}_1 &= [1,0,0,0]\,, & \tau_{\mathrm{s}}^{-1} &= -\left(d + r_T\right)\\
\tilde{v}_2 &= \left[0, \frac{T_2}{2}\left(r_3 - r_2 + \xi\right), 1, 0\right], & \tau_{\mathrm{m}}^{-1} &= -\frac{1}{T_2} - d - \frac{r_2}{2} - \frac{r_3}{2} + \frac{\xi}{2},\\
\tilde{v}_3 &= \left[0, 1, \frac{T_2}{2}\left(r_3 - r_2 - \xi\right), 0\right], & \tau_{\mathrm{f}}^{-1} &= -\frac{1}{T_2} - d - \frac{r_2}{2} - \frac{r_3}{2} - \frac{\xi}{2}\\
\tilde{v}_4 &= [0,0,0,1]\,, & \tau_{\mathrm{s}}^{-1} &= -\left(d + r_T\right)
\end{aligned} \tag{3.56}$$

with

$$\xi = \sqrt{\frac{4}{T_2^2} + \left(r_3 - r_2\right)^2}$$

of the constant coefficient matrix. From the eigenvalues, it becomes immediately clear that the photocurrent transient in the incoherent time domain is determined by a multiexponential decay with three time constants[3] $\tau_{\mathrm{f,m,s}}$, independently of the spin–spin relaxation strength. Since the dissociation probability d is assumed to be low, it does not play a determining role for any of the three time constants. Thus, when spin–spin relaxation is weak, the time constants of the three exponentials are determined by the three recombination probabilities. When it is strong, the three time constants are the triplet recombination probability ($\tau_{\mathrm{s}} \approx r_T$), the average of the recombination probabilities 2 and 3 ($\tau_{\mathrm{m}} \approx \frac{1}{2}(r_2 + r_3)$) and the spin–spin relaxation probability ($\tau_{\mathrm{f}} \approx \frac{2}{T_2}$), respectively.

3.4.3 Pulse length dependence of recombination decay

In order to illustrate the qualitative behaviour of the recombination transient in the incoherent time domain after the pair ensemble gets excited by a coherent, resonant pulse with length τ, an example is discussed in the following were $r_3 \gg \frac{1}{T_2} \approx r_2 > r_T \gg d$. According to eq. 3.55, the initial steady state of the pair ensemble, before the pulse is imposed, is

$$\tilde{\rho}^S = \begin{pmatrix} \frac{G}{4r_T} & 0 & 0 & 0\\ 0 & 0 & 0 & 0\\ 0 & 0 & 0 & 0\\ 0 & 0 & 0 & \frac{G}{4r_T} \end{pmatrix} =: \begin{pmatrix} \rho^S & 0 & 0 & 0\\ 0 & 0 & 0 & 0\\ 0 & 0 & 0 & 0\\ 0 & 0 & 0 & \rho^S \end{pmatrix}, \tag{3.57}$$

under these conditions. The pulse interaction does not change the absolute number of spin pairs, if pair generation, recombination and dissociation during the few nanoseconds of the pulse are negligible. Thus, when $\omega_a - \omega_b \ll \gamma B_1$, the triplet densities $\rho_{11,44}$ are reduced equally by a relative density change

$$-\Delta\left(\tau\right) := \frac{\rho_{11,44}\left(\tau\right) - \rho^S_{11,44}}{\mathrm{Tr}\left[\rho^S\right]}, \tag{3.58}$$

[3] here, “s” stands for slow, “m” for medium and “f” for fast

and the 2,3-densities $\rho_{22,33}$ are enhanced by relative changes

$$\frac{\rho_{22,33}(\tau) - \rho^S_{22,33}}{\mathrm{Tr}\left[\rho^S\right]} = \left(1 \pm \frac{J + D^d}{\hbar\omega_\Delta}\right)\Delta(\tau), \tag{3.59}$$

which depend on the spin–spin interaction. Equations 3.58 and 3.59 as well as an expression for $\Delta(\tau)$ will be derived in section 3.5 where a detailed explanation of the ensemble changes during the microwave excitation is given. Note that the sum of the relative density increases of ρ_{22} and ρ_{33} are equal to the density decreases of the ρ_{11} and ρ_{44}, which confirms the conservation of the spin pair due to the absence of incoherent processes during the microwave pulse. Based on the definition of the relative density change $\Delta(\tau)$ as well as the conditions mentioned above, the transient photoconductivity given in eq. 3.48 becomes

$$\begin{aligned}\Delta\sigma_{ph}(t) = \frac{e\tau_L d\mu_e G}{2r_T}\Bigg[\quad & 2 \quad \left(\frac{r_T}{d}\frac{\mu_h}{\mu_e} - 1\right) e^{-(r_T+d)t} \\ & - \quad \left(\frac{r_2}{d}\frac{\mu_h}{\mu_e} - 1\right)\left(1 + \frac{J + D^d}{\hbar\omega_\Delta}\right) e^{-\left(d + \frac{1}{T_2} + \frac{r_2}{2}\right)t} \\ & - \quad \frac{r_3}{d}\frac{\mu_h}{\mu_e}\left(1 - \frac{J + D^d}{\hbar\omega_\Delta}\right) e^{-r_3 t}\Bigg]\Delta(\tau)\end{aligned} \tag{3.60}$$

which is an multiexponential decay that reflects the decay rates of the different spin–pair states. Note that the prefactors of the exponential functions can be positive and negative, which means that the photoconductivity transient can have values below (recombination enhancement) and above (recombination quenching) its steady state value. This is an important realisation: The quenching of spin–dependent recombination by means of ESR has often been attributed to spin–dependent transport processes only [22, 46] — eq. 3.60 shows that a recombination quenching can also be due to a spin–dependent recombination–process. Note that the recombination probabilities r_2 and r_3 depend on the spin–spin interactions according to eq. 3.16. This means however that when $r_T < r_2 \ll r_3$ (as assumed above), the spin–spin interaction must be relatively large ($\frac{J+D^d}{\hbar\omega_\Delta} \approx 1$) which reduces the prefactor of the last, fast exponential decay in eq. 3.60.

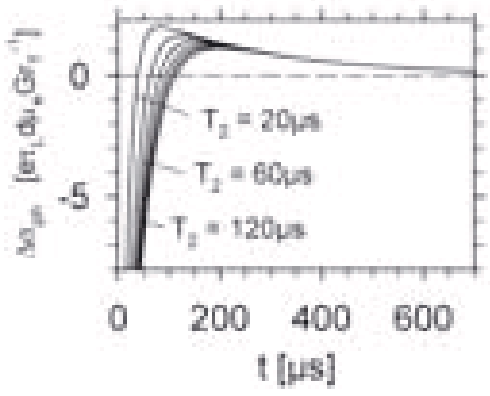

Figure 3.6: Simulation of incoherent time–domain transients for spin–spin relaxation times $T_2 = 20\mu$s to 120μs. The fast exponential part is so small that it is not recognisable. The medium and slow exponential part contribute as quenching (negative) and enhancing (positive) signals, respectively.

Figure 3.6 illustrates a series of transients where T_2 is varied between 20μs and 120μs, $r_T = 4 \times 10^3\mathrm{s}^{-1}$, $r_S = 3 \times 10^6\mathrm{s}^{-1}$, $\frac{d\mu_e}{\mu_h} = 10^3\mathrm{s}^{-1}$, and $\frac{J+D^d}{\hbar\omega_\Delta} = 0.98$. The combination of quenching and enhancing signals after a resonant pulse excitation is due to the relative enhancement and depletion of states

with high and low singlet content, respectively. The density of triplet states $|T+\rangle$, $|T-\rangle$ is high in the steady state (see eq. 3.55) and, therefore, it is reduced during the pulse excitation. States with singlet content $|2\rangle$, $|3\rangle$ have a low steady state density which is increased during the pulse. Even though the decrease of the triplet state density equals the increase of the density of states with singlet character, the net recombination change is positive right after the pulse due to the different recombination probabilities. The different recombination probabilities do also have an impact on the way the ensemble relaxes back to its steady state: When the singlet state density has returned to its steady state, the enhancement signal has not due to the slower triplet recombination.

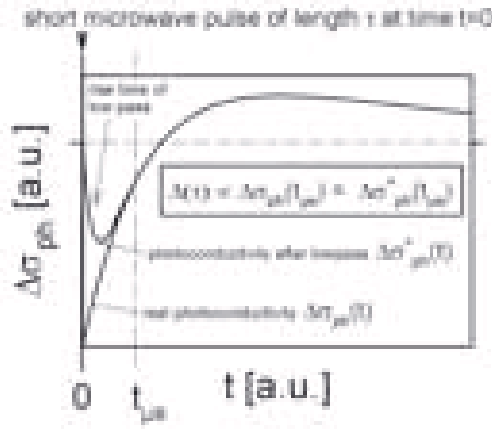

Figure 3.7: Calculated photocurrent response after a microwave pulse at time t=0 assuming an ideal and a realistic detection setup. When the time resolution of the experiment is unable to resolve the photocurrent during the pulse, an indirect access is possible by measurement of the pulse length dependence of either of the three exponential decay functions of eq. 3.60.

Expression 3.60 for the transient photocurrent change after a pulse excitation not only explains the possible existence of resonantly excited photocurrent enhancing and quenching, but also shows that the photoconductivity at any given time after the pulse[4] is proportional to the relative state density change $\Delta(\tau)$. This opens up an experimental possibility: If the experimentally available time resolution for the current transients is beyond the ns range on which coherent spin effects take place, but within the μs range on which the incoherent effects discussed in this section are detectable, the evolution of the state densities ρ_{ii} during the nanosecond pulse can be obtained from long–time transient–measurements (μs range) recorded after resonant pulses of different pulse length. Figure 3.7 illustrates such a case: The two plots represent the simulation of a photocurrent transient after a short microwave pulse with and without a low pass filter that could be posed by the experimental current detection setup. Since the exponential decay function of the photocurrent change $\Delta\sigma_{\mathrm{ph}}$ after a pulse of length τ is proportional to $\Delta(\tau)$, the filtered photocurrent change $\Delta\sigma^{*}_{\mathrm{ph}}$ is proportional after the rise time of the low pass. Thus, experimentally, a measurement of the photocurrent at an arbitrary time $t_{\mu\mathrm{s}}$ after the rise time of a given current detection setup as a function of the pulse length of a given microwave radiation reveals the dynamics of $\Delta(\tau)$ on a time scale whose resolution is only determined by the pulse length resolution of the microwave pulse generator.

Figure 3.8 shows a two dimensional plot where simulated photocurrent transients are plotted for different microwave pulse lengths. A damped oscillation of $\Delta(\tau)$ is reflected by the different amplitudes of the transients. The measurement of the photocurrent change at

[4]and also after the subsequent dephasing that is assumed to have taken place in eq. 3.60

a certain time $t_{\mu s}$ after the end of the resonant pulse allows the reconstruction of $\Delta(\tau)$. According to eq. 3.60, an indirect measurement can also be carried out by an integration

$$\Delta(\tau) \propto \int_0^\infty \Delta\sigma_{ph}(t)\, dt \tag{3.61}$$

of the entire photocurrent transient between the end of the pulse and the relaxation back to the steady state. Such a measurement would oppress low frequency noise and hence increase the signal to noise ration.

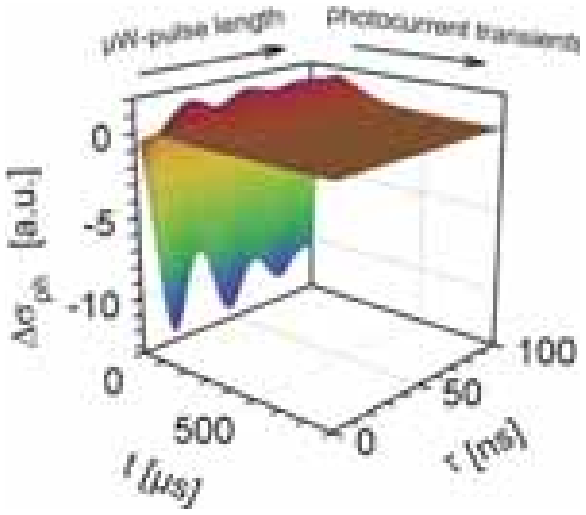

Figure 3.8: The plot shows simulated photocurrent transients on a microsecond time scale excited by resonant radiation pulses of different lengths (in ns-range). The τ dependence exhibits for any given t the function $\Delta(\tau)$ and hence, its shows the dynamics of the spin pair ensemble on a nanosecond times scale. The oscillations on the τ axis are due to Rabi oscillation as discussed in section 3.5.

Equations 3.60 and 3.61 show how time resolved measurements of recombination changes after a short coherent ESR excitation of spin–pair ensembles can reveal information about different recombination probabilities, spin–relaxation times and even the dynamics during the pulse on a nanosecond time scale. A complete description of a pulsed EDMR experiment still requires a discussion of the pulse interaction itself. The variable $\Delta(\tau)$ depends on the pulse length, the microwave frequency and intensity as well as the magnetic field and the Landé g factors of the respective pair partners. All of this will be explained in the following section. In addition, an understanding of the line shape of the photocurrent transients, which means their dependence on the externally applied magnetic field, is developed. Finally, the existence of dephasing Rabi–beat oscillations during resonant pulses and rephasing (echo) experiments on pulsed–ESR excited photocurrent transients are discussed.

3.5 Rabi oscillation

The motion of a spin–pair ensemble in presence of a microwave is described by the general solution of the Liouville equation (eq. 3.1) when the perturbation Hamiltonian $\hat{H}_1$ of eq. 3.12 is included. This leads to an inhomogeneous system of ODEs whose coefficient matrix has a low zero density and is highly non–diagonal making the calculation of an analytic solution as obtained for the off–resonant case in section 3.3 extremely tedious. Therefore, a different approach is undertaken in the following, wherein the change of the ensemble is described solely by its coherent propagation and spontaneous transitions are considered to be non–existent. When the time range on which the microwave–induced spin–pair propagation takes place is sufficiently short in comparison to the recombination and relaxation times, this approach is highly accurate. For the recombination processes considered in the chapters on the first TSR experiments (chapters 5 and 6), it will be

shown that this condition is fulfilled. The negligence of incoherent transitions has the advantage that time–domain solutions of the Liouville equation can be obtained without solving a complicated system of differential equations. One way to find such a solution is to use the Liouville equation in its integrated form

$$\hat{\rho}\left(\tau\right) = \exp\left(-\frac{i}{\hbar}\hat{H}\right)\hat{\rho}^{S}\exp\left(\frac{i}{\hbar}\hat{H}\right), \tag{3.62}$$

which is simply the initial state $\hat{\rho}^S$ transformed by the Schrödinger operator $\exp\left(-\frac{i}{\hbar}\hat{H}\right)$. The latter is an exponential series that contains the Hamiltonian $\hat{H} = \hat{H}_0 + \hat{H}_1$, which under consideration of eqs. 3.5 and 3.13, can be represented by a matrix

$$\tilde{H} = \begin{pmatrix} \frac{\hbar}{2}\omega_0 - J + D^d & \hbar\gamma B_1 & \hbar\gamma B_1 & 0 \\ \hbar\gamma B_1 & \hbar\omega_\Delta - D^d & -J - D^d & \hbar\gamma B_1 \\ \hbar\gamma B_1 & -J - D^d & -\hbar\omega_\Delta - D^d & \hbar\gamma B_1 \\ 0 & \hbar\gamma B_1 & \hbar\gamma B_1 & \frac{\hbar}{2}\omega_0 - J + D^d \end{pmatrix} \tag{3.63}$$

in the base of product states. The variables in eq. 3.63 correspond to the Larmor separation as well as the spin–dipolar and the spin–exchange interactions as defined in section 3.1. An analytic expression for the exponential functions in eq. 3.62 can be found by diagonalisation of the Schrödinger operator which can be done by the transformation of eq. 3.62 into the base of $\hat{H}$ eigenvectors and a subsequent matrix multiplication. The resulting analytic solutions are as messy as the mathematical approach seems simple, which makes the derivation of predictions and simulations of experiments extremely difficult and highly awkward. Moreover, while these solutions represent the correct physical reality of the coherent spin–pair motion, it is hardly possible to draw an illustrative insight and understanding about the spin–pair behaviour during the pulse excitation from these complicated terms. Therefore, another, different approach to the description of the coherent spin motion is taken in the following: The idea is to take advantage of the circumstance that the entire coherent motion of the two spins is a complicated precession about the oscillating magnetic field of the microwave radiation and the applied constant magnetic field. Thus, the changes in the spin ensembles can be described by unitary rotation transformations that depend on the different magnetic fields. The idea behind this approach is to use the relation between the group of geometrical rotations in a vector space $\mathbb{R}^3$, the orthogonal group $O(3)$ and the special unitary group $SU(2)$ which represents these rotations on a unitary space $\mathbb{C}^2$, the Hilbert space representation of a spin-$\frac{1}{2}$ system. The theory of rotation operators, also called drehtransformations, is outlined in many textbooks about quantum mechanics such as the book by Sakurai [64].

The description of the evolution of the spin–pair ensemble by time evolution operators and the description by rotations induced by the magnetic fields are two completely different approaches to an almost equivalent situation. The only difference between the two pictures is the neglect of the mutual spin interactions in the precession picture. While the rotations due to constant and oscillating external fields can be put in mathematical terms with unitary transformations, the consideration of interactions between the pairs would require the use of differential equations which would be even more complicated than the original approach with Liouville equations. The omission of the spin–spin interaction in eq. 3.63 would not simplify the solution of eq. 3.62 significantly.

However, for the approach with unitary drehoperators, the absence of spin–spin interaction (an already inherent property of this picture) simplifies the resulting expressions sufficiently enough for useful applications. The neglect of the spin–spin interactions in the precession picture raises the question whether this is a realistic simplification, especially since spin–spin interactions have turned out to be of great importance for instance for recombination (see eq. 3.16) or the eigenbase of the spin–pair system (see eqs. 3.6 to 3.7). In most of the experimental situations, the spin–spin interactions are weak in comparison to the Zeeman interactions ($(D^d + J) \ll \omega_{a,b}$), and since the experiments for which the considerations in the following sections are made are carried out with strong microwave radiation, one can assume that the spin–spin interactions are weak even in comparison to the microwave fields ($(D^d + J) \ll \hbar\gamma B_1$). Because of this, the field–induced precession will always be much more relevant than the interaction related precession and hence, the assumptions made above are correct for the spin motion. Note that the negligible impact of spin–spin interaction on the absolute spin motion does not imply that the impact on the relative spin motion between the two spins is negligible as well. The latter will become important for the calculation of Rabi–beat oscillation as shown in section 3.5.1.

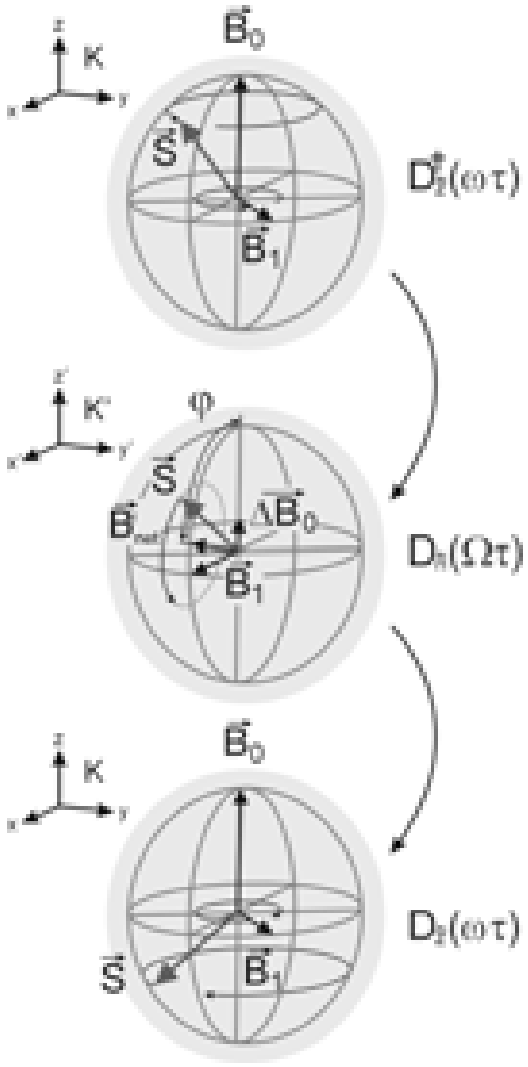

Figure 3.9: The Illustration of the motion of a spin **S** exposed to a constant magnetic field $\mathbf{B_0}$ and a microwave $\mathbf{B_1}$ in the observer frame K and the the rotating frame K', and the necessary drehtransformation. For details see text and appendix A.4.

As explained in appendix A.4, both the $\mathbf{B_0}$ field induced Larmor oscillations and the $\mathbf{B_1}$ field induced Rabi oscillations involve spin rotations. When the operator

$$\mathcal{D}_{\hat{\mathbf{n}}}(\phi) = \exp\left(-\frac{i}{\hbar}\mathbf{S}\cdot\hat{\mathbf{n}}\phi\right) = \mathbb{I}\cos\left(\frac{\phi}{2}\right) - i\sigma\cdot\hat{\mathbf{n}}\sin\left(\frac{\phi}{2}\right) \tag{3.64}$$

represents a rotation of a spin-$\frac{1}{2}$ by an angle ϕ about an axis $\hat{\mathbf{n}}$, the impact of a microwave pulse of length τ and frequency ω on a spin-$\frac{1}{2}$ with Larmor frequency ω_a is equivalent to the transformation

$$\mathcal{D}(\tau,\omega,\omega_a) = \mathcal{D}_{\hat{\mathbf{z}}}(\omega\tau)\,\mathcal{D}_{\hat{\mathbf{n}}_\Omega}(\Omega\tau)\,\mathcal{D}^\dagger_{\hat{\mathbf{z}}}(\omega\tau) \tag{3.65}$$

in which

$$\Omega = \sqrt{\frac{(\gamma B_1)^2}{\hbar^2} + (\omega - \omega_a)^2} \tag{3.66}$$

is the Rabi frequency and

$$\hat{\mathbf{n}}_{\mathbf{\Omega}} = \cos(\varphi)\,\hat{\mathbf{z}} + \sin(\varphi)\,\hat{\mathbf{x}} = \frac{\omega - \omega_a}{\Omega}\hat{\mathbf{z}} + \frac{\gamma B_1}{\Omega}\hat{\mathbf{x}} \tag{3.67}$$

is the rotation axis of the Rabi precession in the rotating frame K'. Note that $\mathcal{D}(\tau, \omega, \omega_a)$ actually consists of three rotations: The transformation into and out of the rotating frame and the Rabi precession about the net magnetic field $\mathbf{B_{net}}$, which is tilted away from the $\hat{\mathbf{z}}$ axis by the angle φ. Figure 3.9 illustrates this sequence of drehoperations for the geometric space.

For a pair of spins $\mathbf{S_a}$ and $\mathbf{S_b}$ with different Larmor frequencies ω_a and ω_b, the representing Hilbert space has to be extended into a product space $\mathbb{C}^4 = \mathbb{C}^2 \times \mathbb{C}^2$ and hence, the transformation

$$\mathcal{D}(\tau, \omega, \omega_a, \omega_b) = \mathcal{D}_a(\tau, \omega, \omega_a) \otimes \mathcal{D}_b(\tau, \omega, \omega_b) \tag{3.68}$$

is a product of the two single spin motions. The evolution of a spin–pair ensemble which has a state $\hat{\rho}^S$ at time t=0 during the pulse can then be obtained from a transformation

$$\hat{\rho}(\tau) = \mathcal{D}^\dagger \hat{\rho}^S \mathcal{D}. \tag{3.69}$$

This expression is a simple multiplication of 4×4 matrices which requires much less computational power than finding the solution of a complicated system of ODEs. The different Rabi oscillations of the two pair partners cause an oscillation of the pairs symmetry similar to the Larmor precession described in section 3.3. This Rabi–beat oscillation is reflected in the ensemble state $\hat{\rho}(\tau)$ after the microwave pulse (see fig. 3.10). Note again that the description of the spin–pair motion by unitary transformations implies the negligence of any incoherent process which is a realistic assumption for the experiments discussed in the following chapters, since the applied microwave pulse lengths are in a nanosecond time range and the fastest incoherent processes are in a lower microsecond range. Thus, the results obtained from the calculation with drehoperators are highly accurate.

For the simulation of the spin ensemble's motion during a resonant excitation, the inhomogeneity of the Landé factors has to be taken into account since the drehtransformation in eq. 3.69 depends on both ω_a and ω_b. This can be done in a similar way as discussed in section 3.3: When the entire ensemble

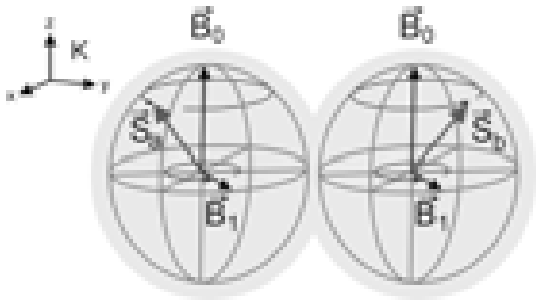

Figure 3.10: Sketch of the motion of two spins a and b induced by the magnetic fields $\mathbf{B_0}$ and $\mathbf{B_1}$. Both spins have different g factors which causes a difference of the two Rabi precessions.

of spin pairs is considered to be an ensemble of ensembles which have infinitely narrow resonances, the net density operator can be calculated by an integration

$$\hat{\rho}^{net}(t) = \int_{-\infty}^{\infty}\!\!\int \Phi_a(\omega_a)\,\Phi_b(\omega_b)\,\mathcal{D}^{\dagger}(\tau,\omega,\omega_a,\omega_b)\,\hat{\rho}^{S}\mathcal{D}(\tau,\omega,\omega_a,\omega_b)\,d\omega_a d\omega_b \tag{3.70}$$

wherein the distributions of the two partner's Landé factors are represented by $\Phi_a(\omega_a)$ and $\Phi_b(\omega_b)$. Under consideration of eq. 3.64, the matrix representation of eq. 3.68 in the product base has the form

$$\mathcal{D}(\tau,\omega,\omega_a,\omega_b) = \begin{pmatrix} \xi^a\xi^b & -\xi^a\zeta^b & -\zeta^a\xi^b & \zeta^a\zeta^b \\ \xi^a\overline{\zeta^b} & \xi^a\overline{\xi^b} & -\zeta^a\overline{\zeta^b} & -\zeta^a\overline{\xi^b} \\ \overline{\zeta^a}\xi^b & -\zeta^a\overline{\zeta^b} & \overline{\xi^a}\xi^b & -\overline{\xi^a}\zeta^b \\ \overline{\zeta^a}\zeta^b & \overline{\zeta^a}\overline{\xi^b} & \overline{\xi^a}\zeta^b & \overline{\xi^a}\overline{\xi^b} \end{pmatrix} \tag{3.71}$$

in which the constants represent

$$\begin{aligned} \xi^{a,b} &= \cos\left(\frac{1}{2}\Omega_{a,b}\tau\right) + i\sin\left(\frac{1}{2}\Omega_{a,b}\tau\right)\cos(\varphi_{a,b}) \\ \zeta^{a,b} &= \sin\left(\frac{\Omega_{a,b}\tau}{2}\right)e^{-i\omega\tau}\sin\varphi_{a,b} \\ \text{wherein} \qquad \cos\varphi_{a,b} &= \frac{\omega-\omega_{a,b}}{\Omega_{a,b}} \qquad \text{and} \qquad \sin\varphi_{a,b} = \frac{\gamma B_1}{\Omega_{a,b}}. \end{aligned} \tag{3.72}$$

This expression can now be plugged into eq. 3.69 in order to calculate the evolution of a pair ensemble which propagates from a steady state $\hat{\rho}^S$ before a pulse of length τ into a non–steady state $\hat{\rho}(\tau)$ after at the end of the pulse. For simplicity, $\hat{\rho}^S$ is assumed to be the same as in eq. 3.57, as defined in section 3.4.3. The result of this triple matrix product leads to a matrix

$$\hat{\rho}(\tau) = \rho^S \begin{pmatrix} |\xi^a\xi^b|^2 + |\zeta^a\zeta^b|^2 & \xi^b\zeta^b\left(|\xi^a|^2 - |\zeta^a|^2\right) & \xi^a\zeta^a\left(|\xi^b|^2 - |\zeta^b|^2\right) & 2\xi^a\xi^b\zeta^a\zeta^b \\ \overline{\xi^b\zeta^b}\left(|\xi^a|^2 - |\zeta^a|^2\right) & |\xi^a\zeta^b|^2 + |\zeta^a\xi^b|^2 & 2\xi^a\overline{\xi^b}\zeta^a\overline{\zeta^b} & \xi^a\zeta^a\left(|\zeta^b|^2 - |\xi^b|^2\right) \\ \overline{\xi^a\zeta^a}\left(|\xi^b|^2 - |\zeta^b|^2\right) & 2\overline{\xi^a}\xi^b\overline{\zeta^a}\zeta^b & |\xi^a\zeta^b|^2 + |\zeta^a\xi^b|^2 & \xi^b\zeta^b\left(|\zeta^a|^2 - |\xi^a|^2\right) \\ 2\overline{\xi^a\xi^b\zeta^a\zeta^b} & \overline{\xi^a\zeta^a}\left(|\zeta^b|^2 - |\xi^b|^2\right) & \overline{\xi^b\zeta^b}\left(|\zeta^a|^2 - |\xi^a|^2\right) & |\xi^a\xi^b|^2 + |\zeta^a\zeta^b|^2 \end{pmatrix} \tag{3.73}$$

that leads to useful analytic expressions for various cases that are considered in the next section.

3.5.1 Spin–spin interactions

The matrix $\hat{\rho}(\tau)$ represents the coherent spin motion of a spin–pair ensemble for the product base, which means for a base of energy eigenstates that exist in absence of any spin–spin interaction. The assumed initial steady state (eq. 3.34) of the pair ensemble on which the pulse transformation (eq. 3.68) is imposed, is independent of the eigenbase shift (eq. 3.6) caused by spin–spin interactions. Thus, in order to obtain the eigenstate density

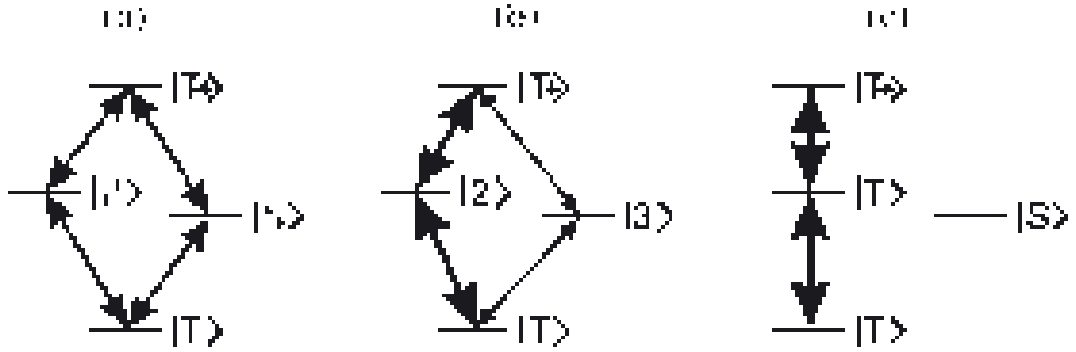

Figure 3.11: Sketch of the four energy levels of the spin pair and allowed Rabi oscillation induced changes between them for the three cases of (a) the absence of spin–spin interactions ($J + D^d = 0$), (b) medium spin–spin interaction ($J + D^d \approx \hbar\Delta\omega$), (c) strong spin–spin interaction ($J + D^d = \hbar\omega_\Delta$). The thickness of arrows indicates transition probabilities. For more details see text.

matrix $\tilde{\rho}^{\mathrm{E}}$ after a resonant pulse under consideration of the spin–spin interaction, one has to carry out a transformation

$$\tilde{\rho}^{\mathrm{E}}(\tau) = \tilde{U}(\phi)\,\tilde{\rho}(\tau)\,\tilde{U}^{\dagger}(\phi) \tag{3.74}$$

in which the matrix $U(\phi)$ depends on the spin–exchange and spin–dipole interactions J and D^d respectively, according to eqs. 3.6 and 3.7. This transformation yields for the diagonal elements in the eigenbase the form

$$\begin{aligned}
\rho^E_{11} &= \rho^S \Delta^u(\tau) \\
\rho^E_{22} &= \rho^S \Delta^v(\tau) + \rho^S \frac{J + D^d}{\hbar\omega_\Delta} \Delta^w(\tau) \\
\rho^E_{33} &= \rho^S \Delta^v(\tau) - \rho^S \frac{J + D^d}{\hbar\omega_\Delta} \Delta^w(\tau) \\
\rho^E_{44} &= \rho^S \Delta^u(\tau)
\end{aligned} \tag{3.75}$$

wherein the constants $\Delta^u(\tau)$, $\Delta^v(\tau)$, $\Delta^w(\tau)$, stand for three pulse length dependent parameters that determine the amplitudes of the incoherent decay transients. Equation 3.74 reveals for these constants the expressions

$$\begin{aligned}
\Delta^u(\tau) &= |\xi^a \xi^b|^2 + |\zeta^a \zeta^b|^2 \\
&= \left[\cos^2\left(\frac{\Omega_a \tau}{2}\right) + \sin^2\left(\frac{\Omega_a \tau}{2}\right)\cos^2(\varphi_a)\right]\left[\cos^2\left(\frac{\Omega_b \tau}{2}\right) + \sin^2\left(\frac{\Omega_b \tau}{2}\right)\cos^2(\varphi_b)\right] \\
&+ \sin^2\left(\frac{\Omega_b \tau}{2}\right)\sin^2\left(\frac{\Omega_a \tau}{2}\right)\sin^2(\varphi_a)\sin^2(\varphi_b)
\end{aligned} \tag{3.76}$$

$$\begin{aligned}
\Delta^v(\tau) &= |\xi^a \zeta^b|^2 + |\zeta^a \xi^b|^2 \\
&= \left[\cos^2\left(\frac{\Omega_a \tau}{2}\right) + \sin^2\left(\frac{\Omega_a \tau}{2}\right)\cos^2(\varphi_a)\right]\sin^2\left(\frac{\Omega_b \tau}{2}\right)\sin^2(\varphi_b) \\
&+ \left[\cos^2\left(\frac{\Omega_b \tau}{2}\right) + \sin^2\left(\frac{\Omega_b \tau}{2}\right)\cos^2(\varphi_b)\right]\sin^2\left(\frac{\Omega_a \tau}{2}\right)\sin^2(\varphi_a)
\end{aligned} \tag{3.77}$$

and

$$\begin{aligned}\Delta^w(\tau) &= 2\mathfrak{Re}\left(\xi^a\overline{\xi^b}\zeta^a\overline{\zeta^b}\right)\\ &= 2\sin\left(\frac{\Omega_a\tau}{2}\right)\sin\left(\frac{\Omega_b\tau}{2}\right)\cos\left(\frac{\Omega_a\tau}{2}\right)\cos\left(\frac{\Omega_b\tau}{2}\right)\sin(\varphi_a)\sin(\varphi_b)\\ &+ 2\sin^2\left(\frac{\Omega_a\tau}{2}\right)\sin^2\left(\frac{\Omega_b\tau}{2}\right)\cos(\varphi_a)\cos(\varphi_b)\sin(\varphi_a)\sin(\varphi_b). \qquad (3.78)\end{aligned}$$

Equation 3.75 shows how the spin–spin interactions can govern the Rabi oscillation induced changes between the energy eigenstates of the spin pairs. When spin–spin interaction is weak and the spin pairs have the product base as energy eigenstates ($J + D^d = 0$), the Rabi oscillation can propagate the $|T+\rangle$ and $|T-\rangle$ into the $|2\rangle = |\uparrow\downarrow\rangle$ and $|3\rangle = |\downarrow\uparrow\rangle$ states with equal probability ($\rho^E_{22} = \rho^E_{33}$, see fig. 3.11(a)). When spin–spin interaction is very strong ($J + D^d \approx \hbar\omega_\Delta$), the state densities of state $|2\rangle$ and $|3\rangle$ become unequal. As shown below, state $|2\rangle$ becomes a triplet $|T_0\rangle$ and its density will become twice as strong as without spin–spin interaction. In contrast, state $|3\rangle$ which now becomes a pure singlet state $|S\rangle$, will remain unchanged during Rabi oscillation (see fig. 3.11(c)). In any other case in between these two extremes, the density increases of the states $|2\rangle$ and $|3\rangle$ will increase and decrease, respectively with increasing spin–spin interaction. The underlying principle behind this shift of the energy eigenbase and the density changes caused by Rabi oscillation becomes clear with the graphic illustration given in fig. 3.11: The Rabi oscillation caused by the microwave radiation can only rotate spin states with $S \neq 0$. With regard to the spin pairs which are two spin–$\frac{1}{2}$ systems, this means that triplet states can be rotated while singlet states remain unchanged by any microwave radiation. Thus, when the eigenbase is a set of three triplet and one singlet state, the transitions involving the singlet state are forbidden. When the eigenbase is the product base, the states $|2\rangle$ and $|3\rangle$ have equal singlet and triplet content. Consequently Rabi oscillation from and to these states are equally strong. In the case of medium interaction (see fig. 3.11(b)), the Rabi oscillation from and to the states $|2\rangle$ and $|3\rangle$ is unequal according to the singlet and triplet content of the two states. In the following, the evolution of the state densities given in eqs. 3.75 to 3.78 are discussed for the limiting cases of small and strong Larmor separation between the pair partners:

(A) Rabi–beat oscillation due to small Larmor separation ($\omega_a - \omega_b \ll \gamma B_1$)

When the two resonances are very close, the Larmor frequencies approach a common value ω_L and thus, the state density oscillations depend only on a single Rabi frequency $\Omega = \sqrt{\gamma^2 B_1^2 + (\omega - \omega_L)^2}$ at which both spin systems oscillate similarly. Under this assumption, eq. 3.72 becomes

$$\begin{aligned}\cos\varphi_a &\approx \cos\varphi_b \approx \frac{\omega - \omega_L}{\Omega}\\ \sin\varphi_a &\approx \sin\varphi_b \approx \frac{\gamma B_1}{\Omega}. \qquad (3.79)\end{aligned}$$

and therefore, eqs. 3.76 to 3.78 become

$$\begin{aligned} \Delta^v(\tau) = \Delta^w(\tau) &= \sin^2(\Omega\tau)\,\frac{\gamma^2 B_1^2}{\Omega^2} + 2\sin^4(\Omega\tau)\,\frac{\gamma^2 B_1^2(\omega-\omega_L)^2}{\Omega^4} =: \Delta(\tau) \\ \Delta^u(\tau) &= 1 - \Delta^v(\tau) = 1 - \Delta^w(\tau) =: 1 - \Delta(\tau). \end{aligned} \tag{3.80}$$

When the results of eq. 3.80 are plugged into eq. 3.75 the relative density changes can be calculated under consideration of the steady state $\tilde{\rho}^S$ as defined in eq. 3.57. This leads to an expression

$$\frac{\rho_{11,44}(\tau) - \rho^S_{11,44}}{\mathrm{Tr}\,[\tilde{\rho}^S]} = -\Delta(\tau) \tag{3.81}$$

for the triplet state densities and

$$\frac{\rho_{22,33}(\tau) - \rho^S_{22,33}}{\mathrm{Tr}\,[\rho^S]} = \left(1 \pm \frac{J + D^d}{\hbar\omega_\Delta}\right)\Delta(\tau) \tag{3.82}$$

for the 2,3-densities. These are exactly the forms that were already introduced in eqs. 3.58 and 3.59 of section 3.4.3. Along the way, the analytic form of the relative density change $\Delta(\tau)$ has been deduced as well: If the microwave frequency is in the vicinity of the spin resonance ($\omega - \omega_L \ll \gamma B_1$), the relative density change

$$\Delta(\tau) = \frac{1}{2}\frac{\gamma^2 B_1^2}{\Omega^2}\left[1 - \cos(2\Omega\tau)\right] \tag{3.83}$$

is an oscillating function whose frequency is twice the Rabi frequency. This indicates that both spin partners are moving and the observable depends on a beat oscillation, a "Rabi–beat oscillation". However, note that this nomenclature is just a matter of interpretation: Alternatively, one could also say that due to the strong spin–spin coupling, the spin pair is just an $S = 1$ system and, as a result, its Rabi frequency is twice as high as the Rabi frequency of an $S = \frac{1}{2}$ system.

The interpretation as Rabi–beat oscillation becomes more plausible when another aspect is taken into account: As mentioned above, in the description of the spin–pair evolution by precession in the rotating–frame Bloch–sphere picture the influence of the spin–dipolar interaction on the relative motion of the two pair partners is neglected. This influence, generally negligibly small, becomes relevant when the two pair partners move in an absolute identical manner, as it is the case, when both have the same Larmor frequency and are exposed to the same external magnetic field and the same microwave radiation. Thus, in order to find an expression for the dependence of the Rabi–beat oscillation in eq. 3.83, one has to go back to the description of the spin motion by Schrödinger's time evolution operator as shown in eqs. 3.62 and 3.63. While it is difficult to obtain a solution for the time evolution (for reasons mentioned in the first paragraph of this section), it is quite feasible to calculate the oscillation frequencies of the precession. Therefore, the Rabi frequency that has been defined by equation 3.66 becomes

$$\Omega = \sqrt{\gamma^2 B_1^2 + \left(\frac{3D^d}{4\hbar}\right)^2} \tag{3.84}$$

for the case of small Larmor separation and in the vicinity of the resonance condition ($\omega-\omega_a, \omega-\omega_b \ll \frac{D^d}{\hbar}$). This insight plays a role for dephasing processes that are discussed in section 3.5.3. Dephasing will not only be determined by Larmor frequency and B_1–field inhomogeneities but also by the distribution of spin–dipolar coupling within the pair ensemble.

(B) Rabi oscillation due to large Larmor separation ($\omega_a - \omega_b \gg \gamma B_1$)

When the Larmor separation of the two spin partners becomes large, an evolution of the spin–pair ensemble takes place when the microwave frequency ω is in the vicinity of either ω_a or ω_b. Due to the symmetry of these two cases, we can discuss without confinement of generality, the first of these two cases which implies that $\omega-\omega_b \gg \gamma B_1$. Thus, $\Omega_b = \omega-\omega_b$ and therefore, eq. 3.72 becomes

$$\begin{aligned} \cos\varphi_b &= 1 \\ \sin\varphi_b &= 0. \end{aligned} \tag{3.85}$$

which causes eqs. 3.76 to 3.78 to attain a form

$$\begin{aligned} \Delta^w(\tau) &= 0 \\ \Delta^v(\tau) &= \frac{\gamma^2 B_1^2}{\Omega_a^2}\sin^2\left(\frac{\Omega_a\tau}{2}\right) =: \Delta(\tau) \\ \Delta^u(\tau) &= 1-\frac{\gamma^2 B_1^2}{\Omega_a^2}\sin^2\left(\frac{\Omega_a\tau}{2}\right) = 1-\Delta(\tau). \end{aligned} \tag{3.86}$$

When the results of eq. 3.86 are plugged into eq. 3.75 the relative density changes can be calculated in a similar way as for the case of small Larmor separation (case A). For large Larmor separation, this leads to an expression

$$\frac{\rho_{11,44}(\tau)-\rho^S_{11,44}}{\mathrm{Tr}\left[\tilde{\rho}^S\right]} = -\Delta(\tau) \tag{3.87}$$

for the triplet state densities and

$$\frac{\rho_{22,33}(\tau)-\rho^S_{22,33}}{\mathrm{Tr}\left[\rho^S\right]} = \Delta(\tau) \tag{3.88}$$

for the $|2\rangle$,$|3\rangle$ densities. Again, a form similar to the expression used in eqs. 3.58 and 3.59 of section 3.4.3 has been obtained and an analytic form of the relative density change $\Delta(\tau)$ is derived. However, note that in opposite to the case of small Larmor separation, there is no influence of the spin–spin interactions on the density changes of the states $|2\rangle$ and $|3\rangle$. Thus, the brackets containing the spin–spin interaction terms in eq. 3.60 would have to be removed, if eqs. 3.87 and 3.88 were to be used for the predictions of the pulse length dependence of TSR transients. Similar to case A discussed above, the relative density change

$$\Delta(\tau) = \frac{1}{2}\frac{\gamma^2 B_1^2}{\Omega_a^2}\left[1-\cos\left(\Omega_a\tau\right)\right] \tag{3.89}$$

is an oscillating function. Unlike the oscillation in eq. 3.83, the frequency in eq. 3.89 is just the Rabi frequency Ω_a. This indicates that only one spin partner is moving about the B_1 field and that the observable depends on a single "Rabi oscillation".

3.5.2 The line shape of TSR transients

The dependence of the photocurrent transients after microwave pulses on the pulse length as well as the applied external magnetic field can be explained with the expressions for the relative density change $\Delta(\tau)$ in eqs. 3.83 and 3.89. Both expressions consist of an oscillation factor that depends on the Rabi or Rabi–beat frequency and a prefactor $\frac{\gamma B_1}{\Omega}$ which, if considered as a function whose argument is the microwave frequency, is an expression for a Lorentzian with line width B_1. Since both factors depend on the Larmor frequencies of one or both pair partners, one has to convolute the density change with the Larmor–frequency distributions Φ_a and Φ_b in order to obtain realistic line–shape predictions. As discussed already at the begin of this section (sec 3.5), this leads to the expression 3.70. For the case of large Larmor separation, the one distribution that is out of resonance with the microwave frequency integrates to a factor 1 and vanishes. For the case of small Larmor separation, one has to distinguish two cases: When the g factor inhomogeneity is smaller than the microwave field ($\omega - \omega_L \ll \gamma B_1$ for all ω_a, ω_b), the inhomogeneity is negligible anyway since the B_1–induced Lorentz–broadening determines the line shape. In the second case, when the distribution is broader than the B_1 field but not the Larmor separation within a given pair, only one distribution exists for both pair partners.

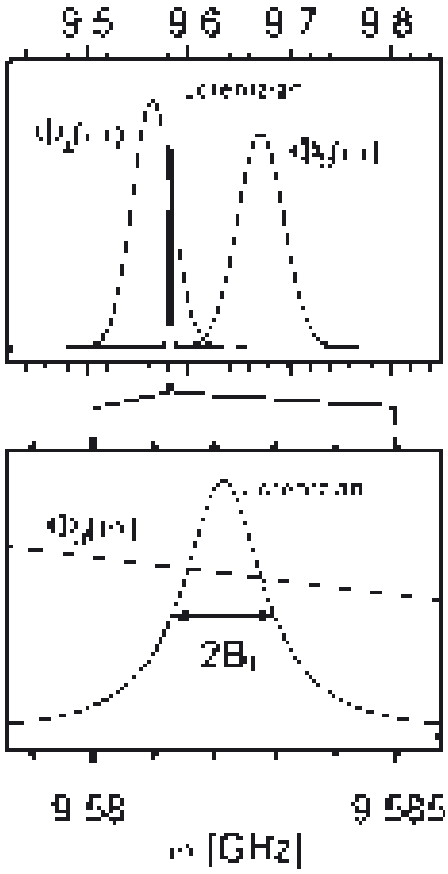

Figure 3.12: An illustration, why a TSR experiment reveals purely inhomogeneous broadening, with a resolution determined by B_1. The distributions Φ_a, Φ_b of the two pair partners are much broader than $2B_1$ so that they can be considered constant within the range were the Lorentzian function becomes large. Note the different frequency scales for the two plots.

In any case, the two integrals of eq. 3.70 reduce to a single integral and the effective relative density change $\Delta^{\text{eff}}(\tau)$ that takes g factor inhomogeneities into account becomes

$$\Delta^{\text{eff}}(\tau) = \int_{-\infty}^{\infty} \Phi(\omega_L) \frac{\gamma^2 B_1^2}{\gamma^2 B_1^2 + (\omega - \omega_L)^2} \sin^2\left(\kappa \sqrt{\gamma^2 B_1^2 + (\omega - \omega_L)^2}\,\tau\right) d\omega_L, \qquad (3.90)$$

in which κ represents a parameter that is $\frac{1}{2}$ and 1 in the cases of large and small Larmor separation, respectively. Equation 3.90 is a convolution of the inhomogeneous g factor distribution $\Phi(\omega_L)$ and a Lorentzian line shape, whose width can be influenced by choice

of the applied microwave radiation. When the distribution $\Phi(\omega_L)$ is smooth in the range of B_1, which means $\partial_{\omega_L}\Phi(\omega_L)\gamma B_1 \ll \Phi(\omega_L)$, the state density change

$$\Delta^{\text{eff}}(\tau) = \gamma B_1 \Phi(\omega)\, T(\gamma B_1 \tau) \tag{3.91}$$

reduces to a product of the value of the inhomogeneous distribution at the microwave frequency ω and a general transient function

$$T(\alpha) = \int_{-\infty}^{\infty} \frac{\sin^2\left(\alpha\sqrt{1+x^2}\right)}{1+x^2} dx \tag{3.92}$$

in which $\alpha = \kappa\gamma B_1 \tau$. The line shape of the recombination transient can be obtained from eq. 3.91, which is obviously proportional to the g–factor distributions $\Phi(\omega)$. This shows one of the crucial advantages of the time–domain measurement of spin–dependent recombination with short and strong pulses in comparison to the conventional EDMR method which employs weak steady–state radiation. The line shape of the pulsed experiment reveals directly and without any incoherent influences on the broadening the distribution of Landé factors, which is of importance for the characterisation of recombination active defects. Figure 3.12 illustrates how this measurement principle works in a less mathematical way. The width of the Lorentzian corresponds to a microwave intensity of $B_1 \approx 0.04$mT which is a frequency width of about 1.1MHz, while the inhomogeneous distributions of the two recombination centres whose shapes were assumed to be Gaussian, are much broader. Thus, the amplitude of the recombination changes depends only on a small cutout of the g–factor distribution and hence, changes of the resonant frequencies due to a magnetic field sweep of the B_0 field can reveal the shape of the respective pair distributions. In this regard it is important to mention that the low B_1–field strength used for standard EDMR experiments would in principle reveal an even better resolution then strong field strength used for TSR. However, since radiation is imposed continuously onto the spin pairs in an EDMR experiment, broadening increases dramatically due to spontaneous transitions that take place and the advantage of the low microwave intensity is more than compensated.

3.5.3 Dephasing of TSR transient

The integral in eq. 3.92 is a general function, which can not be calculated analytically. Since its only parameter is α, $\Delta^{\text{eff}}(\tau)$ of eq. 3.91 is stretched anti proportional to B_1 on the time axis. The parameter α itself can be considered as the turning angle that is induced by B_1 while $T(\alpha)$ is a function representing the recombination response of the sample. Figure 3.13(a) displays a plot of $T(\alpha)$ for α=0–40. The influence of the Rabi oscillation is clearly visible. Due to the integration over a distribution of oscillators, a dephasing takes place that is fast at first but eventually slow so that the oscillation does not vanish completely.

In addition, two other influences on $\Delta^{\text{eff}}(\tau)$, which are important for the dephasing in TSR experiments, have to be taken into account: One, as mentioned above, is the influence of a distribution of spin–dipolar coupling. The latter can become relevant in the case of small Larmor separation. The second influence has an experimental origin: Any TSR sample has to be connected to a current detection setup with wiring and an appropriate contact

system. As discussed in greater detail in chapter 4, this contact system can be quite complex and, thus, the quality factor of the microwave resonator is altered. For TSR experiments, this effect is even stronger than for conventional cw EDMR, since the fill factor of the cavity is high. Hence, the same metallic contact system of a sample will have a much stronger influence on the Q factor and the B_1 inhomogeneities than in an cw EDMR experiment that uses a cw resonator. For the description of $T(\alpha)$, the microwave field distribution has to be taken into account as well. An exact simulation for a given sample system is highly complex and would require the calculation of the different microwave eigenmodes that develop between the contact grids. Thus, for the demonstration that the presence of a B_1 inhomogeneity can lead to an additional acceleration of the dephasing process, a plot of an effective function

$$T_{\text{eff}}(\alpha) = \int_0^{B_1^{max}} T(B_1\tau)\,\frac{dB_1}{B_1^{max}} \qquad (3.93)$$

is displayed in fig. 3.13(b), for which a constant probability distribution $\frac{1}{B_1^{max}}$ was assumed up to the maximum irradiated field B_1^{max} and whose argument is $\alpha = \kappa\gamma B_1^{max}\tau$. The plot shows how the Rabi oscillation reflected in $T_{\text{eff}}(\alpha)$ has practically vanished within less than two oscillation cycles.

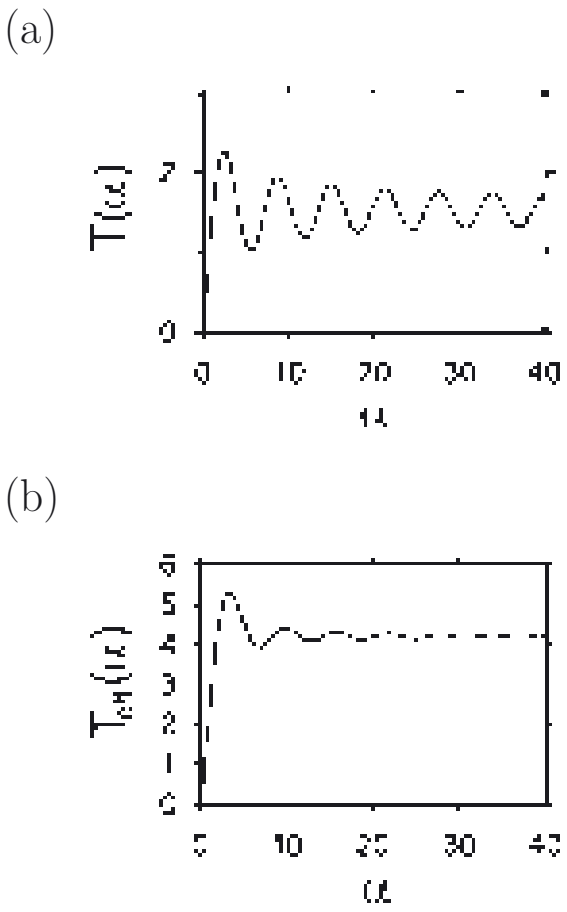

Figure 3.13: (a) The plot displays numerically obtained values for the function $T(\alpha)$. The amplitude of the Rabi oscillation reduces gradually due to the distribution of the Rabi frequencies. (b) The plot displays numerically obtained values for the function $T_{\text{eff}}(\alpha)$ under the additional consideration of B_1–field inhomogeneities which lead to much stronger dephasing.

3.6 Rabi echoes

The fast and highly complex dephasing of the Rabi oscillation reflected by the recombination rate makes it difficult to obtain coherence decay times from experimental data measured under the conditions that are assumed for the simulations presented above. In order to reflect a coherence decay in the recombination rate, a rephasing of the Rabi oscillators must be introduced, similar to the Larmor–echo experiment suggested and described theoretically in section 3.3. However, in opposite to the Larmor–echo experiment, resonant microwave pulses can not be used for the preparation of the spin–pair ensemble before the dephasing begins, nor can they be used for the spin reversal, since

the pulse induced Rabi oscillation is the driving force for the dephasing process itself. Therefore, a different approach to an echo experiment is undertaken in the following, where the rephasing of the Rabi oscillation due to a 180^o change of the direction of the B_1 polarisation in the rotating Bloch sphere is investigated. The basic idea of this approach is illustrated in fig. 3.14. After a resonant microwave has been irradiated onto a pair ensemble for a time τ_{180^o}, the B_1 field polarisation is shifted by 180^o without change of the field strength. The dephased spins then precess into the opposite direction, but at the same speed as before the polarisation change. Thus, the faster spins move behind the slower spins until they catch up with them at the time τ_{180^o} after the polarisation change. Therefore, at the time $t = 2\tau_{180^o}$ after the radiation is switched on, a phase recovery takes place. Since the pulse excitation begins when the pair ensemble has high triplet content, a triplet recovery occurs and therefore, a recombination quenching at $2\tau_{180^o}$. This temporary quenching is a recombination–echo effect similar to the Larmor–recombination echo discussed above. Experimentally, the change of the microwave field polarisation can be implemented easily.

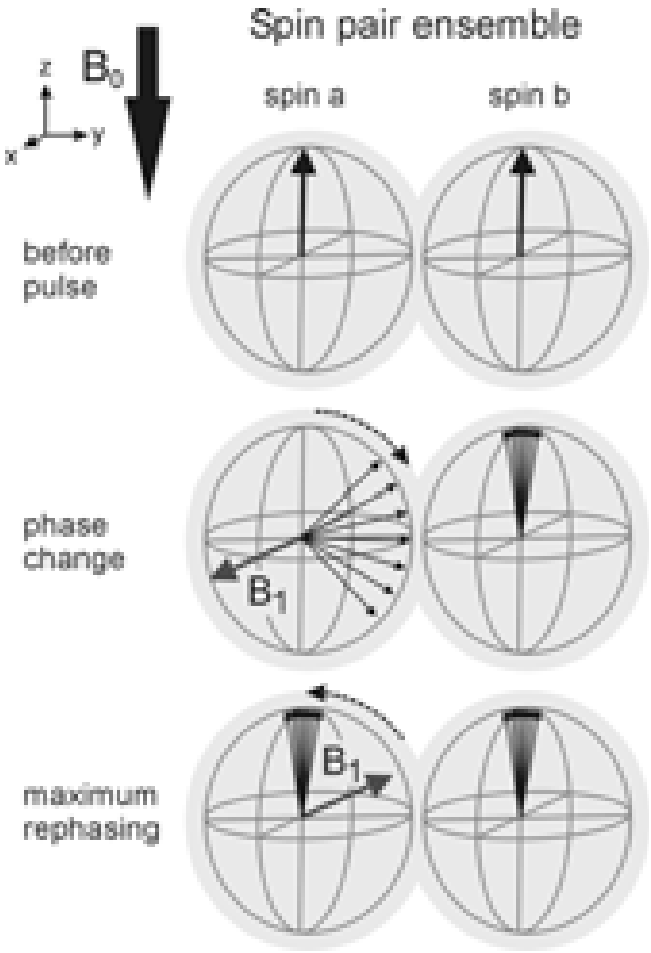

Figure 3.14: The propagation of a spin–pair ensemble with large Larmor separation during a Rabi–echo experiment illustrated with Bloch spheres in the rotating frame. The three sketches correspond to the steady state, the moment prior to the phase reversal at a time $t = \tau_{180^o}$ after the pulse begins and the moment of phase recovery $t = 2\tau_{180^o}$.

An echo experiment can be described mathematically with unitary transformations, similar to the description of the Rabi oscillation discussed above. In the moment of the phase change, which is assumed to take place instantly[5], the direction of the B_1 field is reversed. This means the direction of the Rabi oscillation $\hat{\mathbf{n}}_{\mathbf{\Omega}} = \hat{\mathbf{n}}^+_{\mathbf{\Omega}}$ as defined in eq. 3.67 right after the pulsed radiation begins, turns to a new direction

$$\hat{\mathbf{n}}^-_{\mathbf{\Omega}} = \cos(\varphi)\,\hat{\mathbf{z}} - \sin(\varphi)\,\hat{\mathbf{x}} = \frac{\omega - \omega_a}{\Omega}\hat{\mathbf{z}} - \frac{\gamma B_1}{\Omega}\hat{\mathbf{x}}. \tag{3.94}$$

Therefore, the spin pair that propagates according to the transformation $\mathcal{D}\left(\tau, \hat{\mathbf{n}}^+_{\mathbf{\Omega}}\right) = \mathcal{D}_+$

[5]experimentally, the change takes place on a time scale of less than 500ps

(see eq. 3.68) before the phase change, changes its motion according to the transformation $\mathcal{D}\left(\tau, \hat{\mathbf{n}}_{\mathbf{\Omega}}^{-}\right) = \mathcal{D}_{-}$ after the phase change and thus, the evolution

$$\hat{\rho}\left(\tau_{+}+\tau_{-}\right) = \mathcal{D}_{-}^{\dagger}\left(\tau_{-}\right)\mathcal{D}_{+}^{\dagger}\left(\tau_{+}\right)\hat{\rho}^{S}\mathcal{D}_{+}\left(\tau_{+}\right)\mathcal{D}_{-}\left(\tau_{-}\right) \tag{3.95}$$

of the density operator during the consecutive pulses with opposite phase and respective lengths of τ_{+} and τ_{-} can be calculated. Equation 3.95 leads to a highly complicated and lengthy expression, even under consideration of a simple $|T_{+}\rangle$, $|T_{-}\rangle$ mixture as initial condition $\hat{\rho}^{S}$. Moreover, this expression has to be convoluted with the g–factor distributions as shown in eq. 3.70. The latter increases the complexity even further, without giving any new insight since the line shape of the recombination signal after a pulse sequence with phase change is just as dependent on inhomogeneous broadening as without the phase change. Therefore, without a confinement of the generality, one can dramatically simplify the expression of eq. 3.95 by considering only the two cases, where either one or both pair partners are in the resonance range $\pm B_1$ about the applied microwave frequency ω. The actual line shape can then be obtained from the subsequent convolution of one or both pair partner's g–factor distribution with the calculated recombination transient.

(A) Rabi–beat echoes due to small Larmor separation ($\omega_a - \omega_b \ll \gamma B_1$)

When small Larmor separation is present, the Rabi frequencies $\Omega_{a,b}$ approach the same value Ω. The angle $\varphi_{a,b}$ between the externally applied magnetic field B_0 and the direction of the Rabi oscillation becomes 90^o for both partners. Thus, the expressions for the two transformations

$$\mathcal{D}_{\pm}\left(\tau_{\pm}\right) = \begin{pmatrix} \cos^2\left(\frac{\Omega\tau_{\pm}}{2}\right) & \mp\eta e^{i\omega\tau_{\pm}} & \mp\eta e^{i\omega\tau_{\pm}} & \sin^2\left(\frac{\Omega\tau_{\pm}}{2}\right)e^{2i\omega\tau_{\pm}} \\ \pm\eta e^{-i\omega\tau_{\pm}} & \cos^2\left(\frac{\Omega\tau_{\pm}}{2}\right) & -\sin^2\left(\frac{\Omega\tau_{\pm}}{2}\right) & \mp\eta e^{i\omega\tau_{\pm}} \\ \pm\eta e^{-i\omega\tau_{\pm}} & -\sin^2\left(\frac{\Omega\tau_{\pm}}{2}\right) & \cos^2\left(\frac{\Omega\tau_{\pm}}{2}\right) & \mp\eta e^{i\omega\tau_{\pm}} \\ \sin^2\left(\frac{\Omega\tau_{\pm}}{2}\right)e^{-2i\omega\tau_{\pm}} & \pm\eta e^{-i\omega\tau_{\pm}} & \pm\eta e^{-i\omega\tau_{\pm}} & \cos^2\left(\frac{\Omega\tau_{\pm}}{2}\right) \end{pmatrix}$$

with

$$\eta := \sin\left(\frac{\Omega\tau_{\pm}}{2}\right)\cos\left(\frac{\Omega\tau_{\pm}}{2}\right) \tag{3.96}$$

become simple enough to be plugged into eq. 3.95, which leads to a relative density change

$$\begin{aligned} \Delta(\tau_{+},\tau_{-}) &= F\left[\tau_{+},\tau_{-},\Omega,\omega\right]\cos\left(\omega\left[\tau_{+}-\tau_{-}\right]\right) \\ &+ 12\left[\cos^4\left(\frac{\Omega\tau_{+}}{2}\right)\cos^2\left(\frac{\Omega\tau_{-}}{2}\right)+\cos^2\left(\frac{\Omega\tau_{+}}{2}\right)\cos^4\left(\frac{\Omega\tau_{-}}{2}\right)\right] \\ &- 12\left[\cos^4\left(\frac{\Omega\tau_{+}}{2}\right)\cos^4\left(\frac{\Omega\tau_{-}}{2}\right)+\cos^2\left(\frac{\Omega\tau_{+}}{2}\right)\cos^2\left(\frac{\Omega\tau_{-}}{2}\right)\right] \\ &- 2\left[\cos^4\left(\frac{\Omega\tau_{+}}{2}\right)-\cos^4\left(\frac{\Omega\tau_{-}}{2}\right)+\cos^2\left(\frac{\Omega\tau_{+}}{2}\right)+\cos^2\left(\frac{\Omega\tau_{-}}{2}\right)\right] \end{aligned} \tag{3.97}$$

after the pulse sequence. The first contribution to these matrix elements reflects the influence of Larmor oscillation which is of the order of 10GHz for the experiments discussed in

the following sections and therefore much faster than the time ranges where recombination transitions and even state of the art current detection takes place. Therefore, the cosine function averages out on the experimentally available time resolution and the first line of eq. 3.97 can be neglected. Note that the function $F[\tau_+, \tau_-, \Omega, \omega]$ vanishes when either $\tau_+ = 0$ or $\tau_- = 0$. This is the reason why contributions due to Larmor oscillation did not appear in the last section about the Rabi oscillation (section 3.5) even though the same initial conditions were used. When the Larmor oscillation F is neglected, the relative density change can be written as

$$\Delta(\tau_+, \tau_-) = \frac{5}{8} - \frac{2}{16}\cos(2\Omega\tau_+) - \frac{2}{16}\cos(2\Omega\tau_-) - \frac{3}{16}\cos(2\Omega[\tau_+ + \tau_-]) - \frac{3}{16}\cos(2\Omega[\tau_+ - \tau_-]). \tag{3.98}$$

From equation 3.98, one can directly obtain the effective relative density change by multiplication with the line shape factor and subsequent integration over the Larmor–frequency distributions. The result

$$\Delta^{\text{eff}}(\tau_+, \tau_-) = \gamma B_1 \Phi(\omega)\, T_{\text{eff}}^{\text{echo}}(\alpha_+, \alpha_-) \tag{3.99}$$

is similar to eq. 3.91. The dimensionless function $T_{\text{eff}}^{\text{echo}}(\alpha_+, \alpha_-)$ is defined to be

$$T_{\text{eff}}^{\text{echo}}(\alpha_+, \alpha_-) = \int_0^{B_1^{max}} \int_{-\infty}^{\infty} \Phi_{\mu\text{w}}(B_1) \frac{\Delta(x\alpha_+, x\alpha_-)}{1 + x^2} dB_1 dx \tag{3.100}$$

which takes Rabi–frequency distributions due to g–factor and B_1–field inhomogeneities into account. The variable $\alpha_\pm := \gamma B_1 \tau_\pm$ is defined in analogy to the definitions in sections 3.5.2 and 3.5.3. For the B_1 distribution, an arbitrary function $\Phi_{\mu\text{w}}(B_1)$ is assumed. Note that both $\tau_- = 0$ and thus $\alpha_- = 0$ as long as $\tau_+ \leq \tau_{180^o}$.

Equation 3.98 shows that Rabi–beat echoes can exist: When eq. 3.98 is convoluted with the Rabi–frequency distributions as done in eq. 3.100, the first three oscillating terms will dephase with increasing τ_+ and τ_-. Dephasing occurs for the fourth term, the $\cos(2\Omega[\tau_+ - \tau_-])$ as well; however, when $\tau_+ = \tau_-$, which means in the case when the second pulse with opposite phase is as long as the first pulse, a rephasing occurs. Note that the recombination echo effect caused by Rabi–beat oscillation is much smaller than the signal itself - thus, the echo amplitude can be at the most one third of the signal amplitude.

For a better understanding of the qualitative behaviour of the Rabi–beat oscillation–echo, the function $T_{\text{eff}}^{\text{echo}}(\alpha)$ is plotted in fig. 3.15. This plot, whose argument $\alpha := \alpha_+ + \alpha_-$ is the sum of the two pulse lengths variables[6], displays essentially the function in eq. 3.98 under consideration of dephasing due to B_1- and g–factor inhomogeneities similar to the assumptions of section 3.5. The plot reveals another interesting qualitative feature of the Rabi–beat oscillation echo–sequence: Due to the second term of eq. 3.98, a second dephasing process starts right after the phase change is introduced which gives the entire function a step like shape. With the result of the calculated evolution of the spin–pair ensemble plotted in fig. 3.15, it is important to note that the graphical Bloch–sphere

[6] $\alpha_- = 0$ as long as $\tau_+ \leq \tau_{180^o}$

illustration of the Rabi–echo experiment in fig. 3.14 has some inaccuracies: This sketch shows neither why the second dephasing process occurs right after the microwave phase change, nor illustrate why the echo is smaller than the initial signal. The difference between the illustration of the Rabi–echo experiment and the result of the calculation in eq. 3.98 is that the different Rabi frequencies which are due to a distribution of Larmor frequencies (because of the Landé–factor inhomogeneity) do not only cause a vertical dephasing in the $\hat{\mathbf{z}}$–$\hat{\mathbf{y}}$ plane of the Bloch sphere as shown in fig. 3.14, but also a horizontal dephasing about the $\hat{\mathbf{z}}$ axis which is neglected in fig. 3.14. The latter can not be rephased due to the microwave phase change, which is the reason why the echo amplitude is smaller than the signal itself. Note that the result in eq. 3.98 is based on the assumption that no incoherence is present, which means the entire spin motion described takes place without the loss of a single spin pair. In a real experiment, recombination will take place, making the echo smaller the longer the microwave pulses become. Hence, a two pulse Rabi–beat echo–experiment repeated for different phase change times τ_+ is an excellent way to measure the coherence decay of recombining charge carriers. As long as spin relaxation is sufficiently slow, this coherence decay will reflect the recombination probability of the charge carriers trapped within the spin pairs.

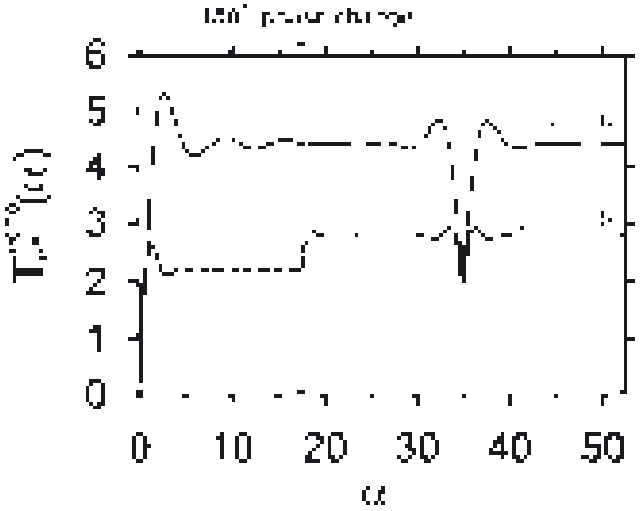

Figure 3.15: The two plots illustrate the evolution of $T_{\text{eff}}^{\text{echo}}$ as a function of the parameter α (that is proportional the pulse length). At α_{180}=17 a phase change of 180^o is introduced leading to a Rabi echo (upper case) and a Rabi–beat echo (lower case) echo at α=2α_{180}. Both plots were obtained under the assumption of a fast dephasing due to a strong Rabi–frequency distribution. Because of non–rephasable Larmor dephasing, the echo amplitudes are smaller than the signals at the begin of the precession after $\alpha = 0$. An important qualitative difference between the Rabi–oscillation echo and the Rabi–beat oscillation echo–sequence is the additional dephasing right after the microwave phase change.

(B) Rabi–oscillation echoes due to large Larmor separation ($\omega_a - \omega_b \gg \gamma B_1$)

When large Larmor separation is present, the Rabi frequencies $\Omega_{a,b}$ are different. While the angle φ_a between the externally applied magnetic field B_0 and the direction of the Rabi oscillation of the arbitrarily chosen spin a becomes perpendicular, the angle φ_b of the other spin vanishes, which means its Rabi frequency reduces to $\Omega_b = \omega_b - \omega$, the difference between the microwave frequency and its Larmor frequency. Therefore, the expressions for the two transformations turn into the form

$$\mathcal{D}_{\pm}(\tau_{\pm}) = \begin{pmatrix} \mu e^{\frac{i}{2}(\omega_b-\omega)\tau_{\pm}} & 0 & \mp\eta e^{\frac{i}{2}(\omega_b+\omega)\tau_{\pm}} & 0 \\ 0 & \mu e^{-\frac{i}{2}(\omega_b-\omega)\tau_{\pm}} & 0 & \mp\eta e^{-\frac{i}{2}(\omega_b-3\omega)\tau_{\pm}} \\ \pm\eta e^{\frac{i}{2}(\omega_b-3\omega)\tau_{\pm}} & 0 & \mu e^{\frac{i}{2}(\omega_b-\omega)\tau_{\pm}} & 0 \\ 0 & \pm\eta e^{-\frac{i}{2}(\omega_b+\omega)\tau_{\pm}} & 0 & \mu e^{-\frac{i}{2}(\omega_b-\omega)\tau_{\pm}} \end{pmatrix} \quad (3.101)$$

with $\eta = \sin\left(\frac{\Omega_a \tau_\pm}{2}\right)$ and $\mu = \cos\left(\frac{\Omega_a \tau_\pm}{2}\right)$. When these terms are plugged into eq. 3.95, the diagonal matrix elements of $\hat{\rho}$ reveal the same spin–spin interaction independent form as in eqs. 3.87 and 3.88 and thus, the relative density change becomes

$$\begin{aligned}\Delta(\tau_+, \tau_-) &= \frac{1}{2}\left[1 - \frac{1}{2}\cos(\Omega_a[\tau_+ - \tau_-]) - \frac{1}{2}\cos(\Omega_a[\tau_+ + \tau_-])\right] \\ &\quad -\frac{1}{2}\sin(\Omega_a\tau_+)\sin(\Omega_a\tau_-)\cos(\omega[\tau_+ - \tau_-]). \end{aligned} \tag{3.102}$$

Equation 3.102 is only dependent on the Rabi oscillation of spin a which is not surprising, since spin b is far out of resonance with the microwave radiation. An echo effect is completely due to the rephasing of an ensemble consisting of only one of the two pair partners and, hence, it is a Rabi–oscillation echo and not a Rabi–beat oscillation–echo as discussed above. In this regard it is also important to mention that the dephasing oscillation has a frequency Ω_a, the Rabi frequency of the oscillating pair partner. The Rabi–beat oscillation described in eq. 3.98 oscillates at 2Ω, which is due to the relative motion of both pair partners.

An expression that is indicative of Larmor oscillation appears in eq. 3.102, similar to eq. 3.98. This expression can be neglected as well and just two oscillation terms that depend on the difference and the sum of the pulse lengths τ_+ and τ_- remain. Convoluted with the B_1- and g–factor inhomogeneities, both lead to dephasing oscillations among which the one that depends on the pulse–length difference is rephasable. When $\tau_+ = \tau_-$, the contribution of $\cos(\Omega_a[\tau_+ - \tau_-]) = 1$ for arbitrary values of Ω_a and thus an echo effect takes place, similar as for the case of small Larmor separation. Since the pair partner b that is out of resonance does not contribute to the oscillation, the net recombination change

$$\Delta(\tau_+, \tau_-) = \gamma B_1 \Phi_a(\omega)\, T_{\text{eff}}^{\text{echo}}(\alpha_+, \alpha_-) \tag{3.103}$$

depends only on the g–factor distribution of spin a and the convolution of the oscillation function $\Delta(\tau_+, \tau_-)$ with the B_1–field inhomogeneities. The latter is represented by $T_{\text{eff}}^{\text{echo}}(\alpha)$ whose dimensionless parameter has already been defined above. $T_{\text{eff}}^{\text{echo}}(\alpha)$ is illustrated in the second plot of fig. 3.15. Similarly to the Rabi–beat oscillation sequence, an echo effect is possible that is smaller than the signal itself. However, in opposite to the Rabi–beat oscillation, only one dephasing process right at the beginning of the pulse sequence is present and no second dephasing takes place right after the phase change is introduced. This is a major qualitative difference between the two pulse sequences, which makes a distinction of Rabi and Rabi–beat oscillation effects and therefore a distinction between small and large Larmor separation possible.

The purely theoretical and also very general view on the dynamics of spin–dependent charge carrier recombination that has been developed in the course of this chapter revealed a variety of phenomena which can be expected from transient photoconductivity measurements of semiconductor systems that contain spin–dependent recombination channels through localised band gap states. This insight will be crucial for the understanding and the interpretation of the experimental observations presented in the following chapters, where most of the phenomena discussed so far will be shown to exist in real semiconductor materials.

Chapter 4

Experimental foundations

For the detection of the previously discussed effects an experimental setup was used, whose development is outlined and described in the following. Point of departure is the traditional EDMR setup as explained in chapter 1 and illustrated in fig. 1.2, whose sensitivity is achieved by employment of lock–in amplifier technology. For the detection of resonant changes in the steady state photocurrent under continuous light and microwave irradiation of the semiconductor sample, the magnetic field is simultaneously swept and modulated and the detected photocurrent changes are then coupled into the lock–in filter. For the high speed transient measurement of the photocurrent, a lock in approach is not feasible anymore and thus, the whole challenge that lies in the experimental detection of the effects discussed in the past chapters is to achieve a sufficient time resolution and current sensitivity at the same time, even though one of these two requirements deteriorates always when the other one is improved.

4.1 Pulsed EDMR

It is important to keep a clear nomenclature with regard to the terms used for the different kinds of magnetic resonance experiments in order to express the fundamental differences between the principles behind these methods: In analogy to the "continuous wave" and "pulsed" ESR experiments, the label "pulsed" does not only stand for a time–domain measurement of ESR but a time–domain measurement within the coherent times: Note that cw ESR as well as cw EDMR can also be carried out as a "pulsed" experiment when the microwave is modulated (usually chopped) instead of the magnetic field. This however is not referred to as "pulsed" in the following because it is a time–domain measurement on a time scale beyond the coherence times. Hence, in this work, the expression "cw" is always referred to an experiment carried out on a time scale beyond the slowest incoherent process, while a "pulsed" experiment always describes a measurement where the excitation is faster than the fastest incoherent process. In the following, the pulsed EDMR experiment will also be called time–domain measurement of spin–dependent recombination (TSR), in order to prevent confusion with time–domain measurements of spin–dependent transport that could also be considered as pulsed EDMR. In general, the experiments will be called "pulsed EDMR" when experimental details are discussed, and TSR when the observed recombination is emphasised.

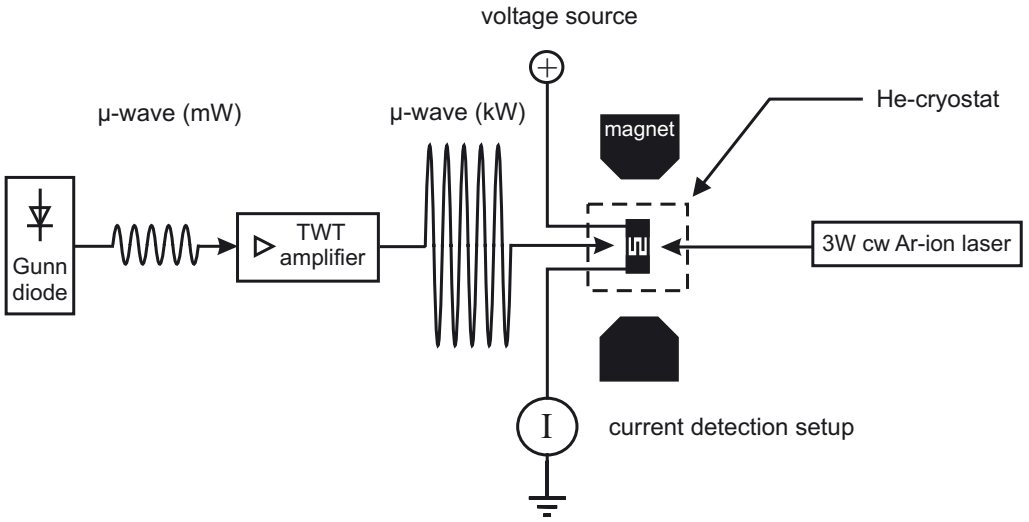

Figure 4.1: The experimental setup for pulsed EDMR. The principle idea is rather simple. It consists of a standard pulsed ESR spectrometer as well as a strong light source, a cryostat system and a transient current detection unit. Sensitivity and time resolution of the latter impose the challenges and limitations on this experiment.

Figure 4.1 illustrates the setup used for the experiments discussed in the following chapters. It consists of a commercial X-Band ($\nu \approx$10GHz) Bruker E580 FT-EPR spectrometer which is used for the generation of the magnetic field as well as the short microwave pulse sequences. The microwave pulses are amplified by a 1kW travelling wave tube (TWT) amplifier made by Applied Systems Engineering which carries out a coherent amplification of the microwave intensity by stimulated emission of radiation. During the experiments, the semiconductor sample was located in the centre of a cylindrical dielectric resonator that was installed in an Oxford CF 935 continuous He-flow cryostat. The resonator used for all experiments was a Bruker ER4118XMD5W1 probe head, a dielectric X-Band pulse cavity that is equipped with an optical window which consists of an array of metal grids that allow light radiation to propagate into the cavity but prevent microwave radiation from propagating out of the cavity (see fig. 4.2). At low temperature, the constant He-flow was brought about the sample by injection through a hole in the cavity bottom. The sample itself was fixed at the tip of a sample rod, which also served as a tube for the electrical wiring between the sample contacts and the outside of the cryostat where they are connected to the current detection setup that is described in detail in the next section.

For the light injection of excess charge carriers, an irradiation by an intensive light source is necessary. Thus, a Coherent Innova 90 continuous wave Ar^+-ion laser was used for the experiments presented, which is able to radiate continuously at up to 10W in multi mode operation and up to 1W in single–mode operation at λ =514nm. For all experiments, the laser was used in single mode operation. The beam was reflected by two mirrors directly onto the sample without employment of additional optics which illuminated the sample with a circular spot that was 2.3mm in diameter.

The magnetic field of the Bruker E580 spectrometer was measured with a Hall probe. This has the advantage that fast and accurate relative measurements can be carried out.

The drawback of the Hall sensor is that it can not measure absolute values with high accuracy. This means, an offset on the measured value can exist, which may be in a range of several Gauss and which can drift in the course of a measurement session. Thus, for the determination of the absolute Hall probe offset, an additional measurement of the magnetic field was carried out with a Teslameter. A Teslameter is based on a nuclear magnetic resonance experiment carried out on protons with a known, very narrow NMR resonance. When a certain, very accurate radio frequency is imposed and an absorption can be measured, a highly accurate magnetic field determination is possible. Since Teslameter measurements take much time (several seconds), the continuous B_0 field measurement during a magnetic field sweep experiment is not possible. Thus, for most of the experiments presented, a Teslameter measurement was carried out before and after the sweep in order to determine the Hall–probe offset and drift, while the field during the sweep was determined by the Hall sensor only. Note that most of the displayed data exhibits the raw scaling as obtained from the Hall probe. However, for the determination of all the Landé factors presented, the magnetic field offset given from the Teslameter was taken into account. The microwave frequency was measured by an internal frequency counter.

Figure 4.2: Photo of the pulse probe head used for the experiments. In the lower left corner, an enlargement of the cavity is shown clearly showing the laser window.

The microwave intensity was controlled through an attenuator that was placed before the input of the TWT amplifier. Even though the microwave power irradiated into the cavity can be calculated from a given attenuation, the measurement of the microwave field strength B_1 within the sample is difficult since it is determined by the cavity and sample geometry as well as the fill factor and the distribution of conducting material (contacts and wires) within the cavity. Thus, for a given sample the scaling has to be determined by means of a measurement where the field–induced Rabi frequency is scaled versus the squareroot of the applied microwave power. How to obtain such a scaling by means of pulsed EDMR is outlined in section 5.5.1.

4.1.1 Time resolution and current sensitivity

The experimental challenge of pulsed EDMR is the fast measurement of relative current changes as small as $\frac{\Delta I}{I} = 10^{-7}$ in small semiconductor samples at low temperatures where the photoconductivity and hence the offset sample currents are low. In order to keep noise as low as possible and to gain fastest current amplification (short amplifier rise times), the absolute sample resistance has to be kept at a minimum. This poses a significant problem

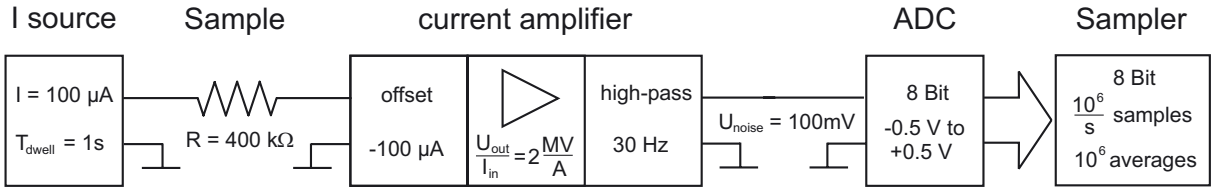

Figure 4.3: Block diagram of the detection setup for transient photoconductivity changes. A current source with long dwell time compensates drift changes of the photoconductivity due to laser and temperature fluctuations. The current amplifier separates the fast and subtle current changes from the large offset signal.

since the sample size is confined by the size of the microwave field in the resonator (length about 10mm, diameter about 4mm), and the photoconductivity is reduced due to the low temperature. Thus, a geometrical reduction of the sample resistance has to be done by lateral micrometer sized interdigited contact grids as explained in the section 4.2 about sample preparation. The actual size and the distance of the grids depends on the value of the photoconductivity and has to be chosen for the given detection setup, such that the sample photoresistance is at least of the order of $10^5\Omega$. The thickness of the grid should be sufficiently high such that contact resistance does not play a role, but thin enough so that the contact volume does not decrease the quality factor of the microwave resonator and attenuate the microwave intensity too much.

For the induction of the sample photocurrent, a Keithley 220 PCS programmable current source was used. Note that a constant current source was employed even though the photoconductivity changes were detected by measurements of current changes in the sample. This was done in order to keep the sample offset current independent from slow photoconductivity changes due to laser and temperature drift. Thus, a long dwell time (T_{dw} ≈1-10s) had to be chosen such that the current changes due to the actual spin–dependent recombination changes were not filtered away. The constant current was chosen such that the voltage necessary for its induction did not exceed the breakdown level of the sample contacts. For instance, at grid distances of 50μm the breakdown voltage is at about 150V, given of a safety factor of 3 that takes geometrical inhomogeneities into account, the maximum is $U_{max} = 50V$.

For the current detection, a Stanford Research SR570 high speed current amplifier was used for most of the experiments. The entire photocurrent detection setup is illustrated in fig. 4.3. Therein, the constant photocurrent offset was compensated before the actual pulsed current changes were amplified. Finally, before the amplified current signals were coupled into a digitiser, they were filtered by a second high pass (the first is the current source) in order to compensate the small drift between the constant current source and the constant current offsets. For some experiments, a Femto high speed current amplifier DLPCA-200 was employed, whose time resolution is for any given sensitivity range by about an order of magnitude faster then the SR570. However, the drawback of this advantage is the worse ability of the Femto amplifier to compensate current offset. Thus, the SR570 was preferred for most of the experiments, since it provided an already sufficient time resolution.

For the sampling as well as the real time averaging of the recorded transients, an 8 Bit Bruker SpecJet digitiser and transient recorder was used. This device, developed and built into the pulsed-ESR spectrometer for the fast real time recording of microwave pulses in the ns range turned out to be crucial for the detection of pulsed EDMR signals. For the measurements on the sample discussed in this book, the signal to noise ratio (SNR) at the output of the amplification setup hardly exceeded 10^{-2} since the transient measurements did not allow the use of lock-in filters for noise reduction. Therefore, at least 10^4 to 10^6 averages had to be collected and averaged before a transient could be obtained, since the SNR increases proportional to the squareroot of the number of averaged data sets. Thus, in order to keep the collection times of the current transient in a reasonable time frame, the experiment had to be repeated immediately after a system had relaxed back to its steady state (ms-range), which means, the recorded transients had to be averaged at the same time as they were collected.

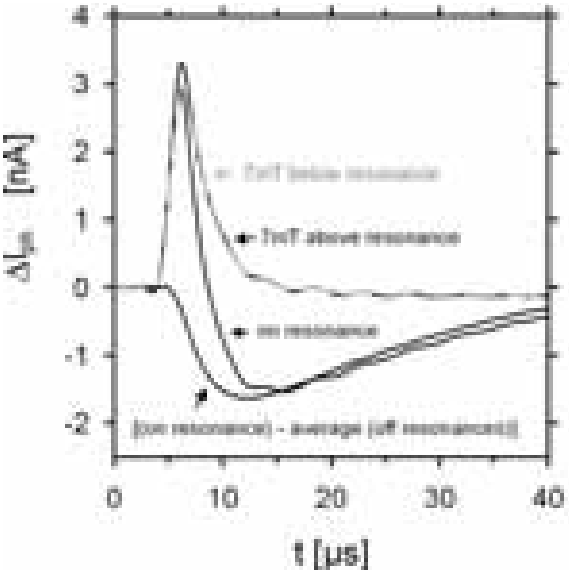

Figure 4.4: Raw data of photocurrent transients after 320ns long microwave pulses in hydrogenated microcrystalline silicon on and 7mT away from the dangling bond resonance. The data was obtained from the average of about 1.1 million transients. The off–resonance transients are identical which allows a straight forward subtraction of the non–resonant current background from the on–resonant transient. (I=50μA, T=10K, $P_{\mu W}$=8W (21db), τ=320ns)

When the photoresistance of a sample is below 100kΩ, the current detection setup as described above is able to collect real time transients at a time resolution of up to 2μs and a sensitivity of 10pA in presence of an offset current of I=10μA. This is a major achievement: Under the assumption that the relaxation of a current transient is close to the time resolution and the induced current changes are close to the sensitivity limit, the detection of recombination changes in the range of only 100 electron–hole pairs is possible.

4.1.2 Microwave–induced currents

Unlike the weak continuous–wave microwave radiation used for conventional EDMR, the strong radiation of the coherent pulses used for pulsed EDMR induces non-negligible sample currents that can have magnitudes much higher than the current contributions of spin–dependent recombination. For a given transient, the undesired background caused by microwave induction has to be subtracted. Figure 4.4 displays the raw data of three current transients recorded in a μc-Si:H sample. One of the transients was recorded at a magnetic field B_0=346,79mT, which for the applied microwave frequency corresponds to a Landé factor of the dangling bond [65] defect ($g \approx$2.0054(4)). The other two transients were recorded at 7mT above and below this resonance. The latter overlap indistinguishably on the plot. The features of these off–resonance current transients is solely due to microwave–induced

currents.
A fourth plot of fig. 4.4 shows the subtraction of the average of the two off–resonant transients from the on–resonant signal. It exhibits a quenching of the sample current after a certain time that is determined by the amplifier time constant of about 5μs.

The example displayed in Fig. 4.4 shows that microwave–induced currents impose a second offset on top of the offset due to the constant photocurrent. The subtraction can be done from off–resonant transient collected at magnetic fields far away from any magnetic resonance that may occur in a given sample. Note that this procedure may lead to an error due to a magnetic–field dependence of the current. Such a dependence could arise from a magnetoresistance effect of the photoconductivity. Therefore, it is important to know whether such effects exist in a given sample so that they be be taken care of[1].

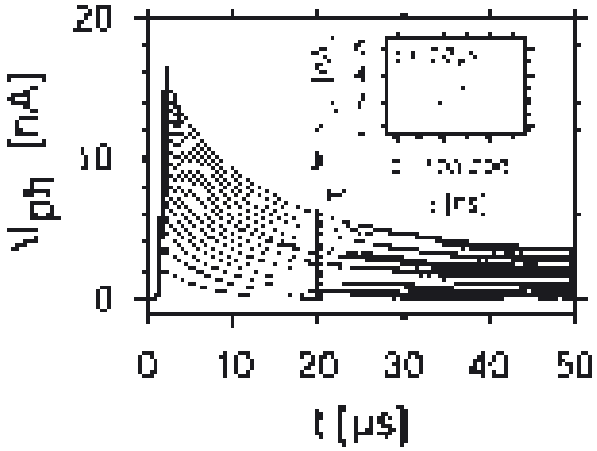

Figure 4.5: Photocurrent changes after microwave pulses of lengths between τ=16ns and τ=256ns. The data was collected at a magnetic field of B_0=341.8mT, far away from any electron spin resonance. The inset shows the magnitude of the microwave induced current change at t=20μs after the end of the pulse as a function of the pulse length τ. (T=10K, P=63W (12db), I=100μA).

The existence of microwave–induced currents poses a significant constraint on the measurement of photocurrent transients and their dependence on the pulse length τ, which, as discussed in section 3.4.3, can reveal a spin–pair propagation during the pulse excitation. The magnitude of this offset signal increases almost linearly with increasing pulse length. Figure 4.5 exhibits this dependence for transients recorded under the same conditions but with increasing microwave pulse length. The inset displays the dependence of the photocurrent changes at an arbitrary time t=20μs after the pulse as a function of the pulse length τ. One can clearly recognise the linear dependence. A comparison of fig. 4.5 with fig. 4.4 also shows that an increasing microwave intensity also increases the offset signal. The magnitude of the signal after a 63W pulse with length τ=256ns (fig. 4.5) is larger than the magnitude of the signal after a 8W pulse with length τ=320ns (fig. 4.4). Since a decrease of the signal–to–noise ratio with increasing microwave induced currents is inevitable, the range in which pulse length dependencies of the spin–dependent recombination can be measured depends strongly on the used microwave intensity. In the following, only background corrected transients are discussed.

[1]for instance by subtraction of an averaged off–resonant transient that is obtained from off resonant transients measured above and below the resonance line

4.2 Sample and contact design

The current detection setup that is described above can only achieve required sensitivity when the photoresistance of a given semiconductor sample does not exceed a range of $10^5\Omega$ to $10^6\Omega$. For quasi undoped thin film silicon at low temperatures, this requirement becomes a significant experimental problem. In addition to the low resistance between the sample contacts, the overall volume of conducting material in the microwave resonator (wires, contacts, sample substrates) has to be as low as possible since conducting volumina impose short circuits onto the microwave radiation, which means the radiation intensities can be attenuated dramatically. These requirements seem to contradict each other and given the fact that the overall size of a sample has to be confined to the volume, where the microwave field modes bulge into a maximum, the sample design becomes one of the significant challenges of a pulsed EDMR experiment. Figure 4.6 displays the picture of a hydrogenated microcrystalline silicon sample. The material, whose properties and deposition procedures will be discussed in chapter 5, was deposited directly onto a 1737 corning glass substrate. After this deposition, the grid system had to be made, which was done by

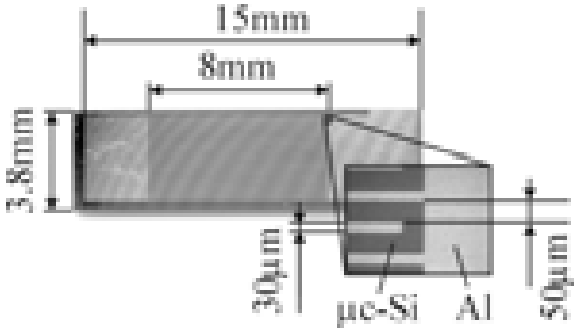

Figure 4.6: The design of a pulsed EDMR sample. The photo displays a thin 2.7μm thin layer of hydrogenated microcrystalline silicon deposited on a glass substrate. The 48 interdigited contact grids were etched out of a 300nm thin magnetron sputtered Al-layer.

(i) the removal of a possible thin oxide layer that can form on silicon surfaces due to the exposure of the deposited thin film to atmospheric oxygen. This was done by a wet chemical treatment in which the sample was exposed to a 2% solution of hydrofluoric acid (HF) for 30s.

(ii) The deposition of a thin layer (300nm) aluminium by physical vapour deposition. This was done by a magnetron sputtering process in an excited argon plasma.

(iii) The etch of the grid structure out of the thin Al layer was done with an Al–standard etch solution after a positive resist layer had been developed by photo lithography.

The absolute net contact lengths that can be accommodated on a given sample is limited by the electric fields that can be applied to a given material. As long as the grid system is on top of the semiconductor sample, the grid gap is limited by the breakdown voltage of the vacuum only, which is much lower than the breakdown voltages of most semiconductor materials. Therefore, under consideration of a safety factor of 3, the minimum allowed grid gap is 50μm when the contact system is supposed to sustain voltages of $U \approx 50$V [2]. This leads to an effective contact length of 384mm. However, when the contact grid

[2]Breakdown voltage under vacuum is $\approx 3\frac{\text{kV}}{\text{mm}}$

is covered by another layer which is a dielectric insulator with high breakdown voltage, much smaller grid distances of down to 1μm can be used in principle that make effective contact lengths of several meters possible.

In order to prevent inhomogeneities within the photolayer for the lithography process, it is crucial to keep the area used for the contact at least 3 mm apart from sample edges. Therefore, the photolithography has always to be carried out on substrates that are much larger than the final sample size (at least 20×20mm). After the lithography step, the samples have then to be brought into their final shape: With crystalline substrates such as c-Si or quartz it is generally possible to cleave the appropriate size. However, for glass substrates where cleaving leads to random shapes (the sample breaks), the desired shape has to be sawed by a precision diamond saw.

4.3 Timing of the experiment

The timing of the entire pulsed EDMR experiment is controlled by the Bruker ESR spectrometer. The latter controls the pattern jet pulse generator as well as the data recording and real time averaging by the spec jet transient recorder. For standard ESR measurements, Bruker offers a large variety of software which requests only experimental parameters from the user and carries out the experiment mostly self contained. However, for new experiments such as pulsed EDMR, a new customised software has to be written, which takes the special requirements of this method (pulse sequences, timing of data recording) into account. The Bruker Xepr control software allows the integration of customer designed pulse sequences by "Pulse Spell", a script language specially developed for magnetic resonance applications.

For the time–domain measurement of spin–dependent recombination (TSR), three main routines were utilised, which are listed and documented in appendix B.3. Therein, the first and second routine are designed for the control and the recording of the real time transients after a given microwave pulse and for the pulse length dependence measurements respectively. Both measurement routines are able to repeat the experiment automatically for various magnetic fields which allows the measurement of line shapes and resonance distributions. The third routine is a combination of the first two: It allows the measurement of the pulse length dependence of real time transients.

Chapter 5

Experimental results for microcrystalline silicon

In the following sections, the feasibility of the TSR experiment is illustrated for recombination processes in hydrogenated microcrystalline silicon (μc-Si:H). This material was chosen because of the high degree of understanding that exists about spin–dependent recombination processes therein. In order to achieve greatest possible reproducibility and comparability between the different experiments, all measurements were made on samples which came from the same deposition run; in fact many measurements were even carried out on one single sample. After a brief introduction to the general properties of microcrystalline silicon and the particular properties of the material that was used for the experiments, a series of TSR scans is presented which shows that the effects predicted and described in chapter 3 can be detected for the chosen recombination paths.

5.1 Properties of the used material

The structure and morphology of hydrogenated microcrystalline silicon (μc-Si:H) has been discussed in various studies [46, 61, 66] which led to a picture that is illustrated in fig 5.1. Herein, columns of crystalline silicon, grown perpendicular to the substrate surface are separated by disordered regions similar to an amorphous silicon (a-Si:H) phase. The latter is assumed to contain hydrogen atoms and dangling bond (db) defects just as bulk a-Si:H [61]. The columns consist of many small (5-30nm) crystallites which are separated by dislocations. The morphology of μc-Si:H, which appears in many regards to be a mixture of an amorphous and a crystalline silicon material, leads to a density of states that has also properties from both a-Si:H and c-Si: While the band gap of μc-Si:H is the same as in crystalline silicon (E_g $\approx$1.1eV), a series of localised states can be found within the band gap similar to a-Si:H. Above the valence band and below the conduction band, high densities of shallow trap states are present. The trap states close to the conduction band (CE centres) were identified by ESR spectroscopy. The latter exhibit a resonance at g=1.998 [46, 61, 66] when the tail states are singly occupied by excess charge carriers due to sample illumination (LESR). The uncharged db states have energies right below the middle of the band gap. Due to their positive correlation energy, they

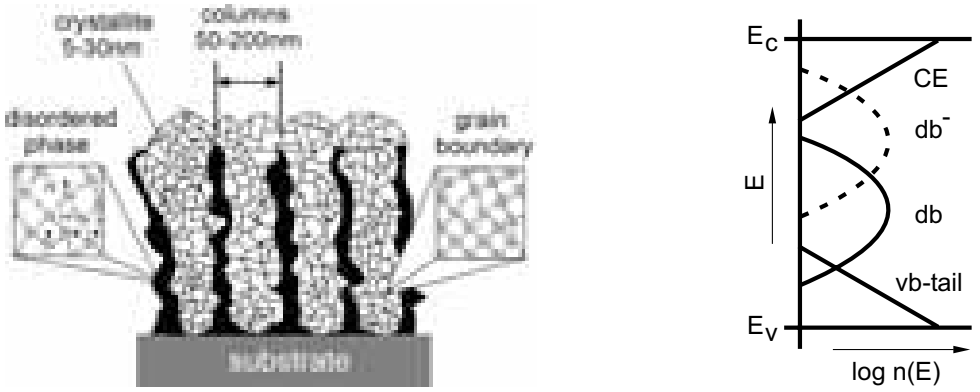

Figure 5.1: Sketch of the morphology of microcrystalline silicon (left). A density of states diagram (right) reflects the complexity of the material. Dangling bond (db) states exist close to the middle of the band gap, shallow trap states exist close to the conduction band (CE centres) and valence band edges.

are paramagnetic in an equilibrium state and thus detectable by ESR at Landé factors of about $g \approx 2.005$. The detection of the valence band traps is not as easy with LESR due to the huge line width of these centres [46]. Due to the high densities of localised states in the band gap of μc-Si:H, recombination processes through traps and dangling bonds are likely to be the dominant recombination channels of μc-Si:H. Kanschat et al. [67, 23, 46] have shown properties of some of these recombination channels such as the CE–db recombination for instance. Figure 5.2 displays data from Kanschat's studies [46]: The comparison of an ODMR and an EDMR plot, obtained from the same light irradiated μc-Si:H sample at the same conditions, shows the involvement of CE and the db centres in non–radiative recombination processes. Note that the CE- and db peaks of the ODMR spectrum have equal integrated intensities which is evidence that the observed CE and db signals actually belong to the same process. This is different for the EDMR plot in which the db peak has a much stronger integrated intensity which raises the question of whether a second recombination path could exist in addition to the CE-db path. As shown by Kanschat, the ratio between the integrated db- and CE peak intensities can vary significantly between different samples and tem-

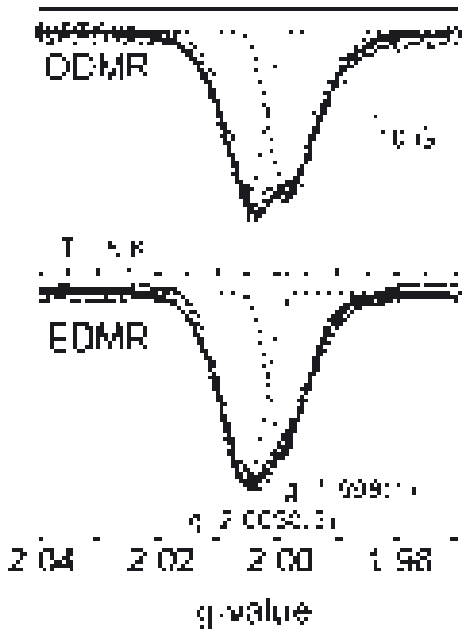

Figure 5.2: The ODMR and EDMR spectra of illuminated, intrinsic μc-Si:H as measured by Kanschat et al. [67, 23, 46]. The ODMR spectrum is measured in the integral photoluminescence intensity. It shows equally strong quenching peaks at the resonances of CE and db centres. The EDMR exhibits photocurrent quenching at the same peaks. Here, the db resonance is stronger than the CE resonance.

peratures. The origin of this "pure db" signal has not been resolved so far since no second recombination partner has been found. One explanation for the missing partner could be that it has a g factor so close to the db such that the two peaks with their strong inhomogeneous broadening are not resolvable in the EDMR spectrum. Such a pair could be formed by excited, negatively charged db^- states, for instance. Even though this configuration could explain the identity of the g factors of both pair partners, it has remained unconfirmed so far [46, 23, 67].

The properties of microcrystalline silicon make it an excellent candidate for the experimental verification of the effects and phenomena discussed in chapter 3. Recombination between CE and db centres consists of tunnelling processes between localised electronic states. Thus, nearest neighbour transitions have a contribution to recombination and the exclusive pair model as outlined in chapter 2 is fulfilled. Moreover, for X-band microwave frequencies used ($\nu \approx$10GHz), a Larmor separation $\omega_a - \omega_b \approx 340\text{mT} \times (2.0055 - 1.998)\,\mu_B \approx 40\text{MHz}$ is present. Therefore, due to the large Landé factor separation between CE and db, excellent conditions for possible spin–beat experiments and also selective resonance experiments are given. Moreover, as one can learn from chapter 3, TSR is an excellent method to distinguish wide from narrow Larmor separation within recombining charge carrier pairs. Thus, it should be possible to reveal information about the contribution of the strong db peak to the EDMR signal and, therefore, the possible existence of a second recombination channel can be investigated. Finally, another property of nominally undoped microcrystalline silicon makes it a good candidate for a first TSR experiment: The material exhibits photoconductivities which are suitable for the achievement of the required sample photoresistance [68], so that a sufficient time resolution is achievable.

5.1.1 Material deposition

The material used in the following experiments has been deposited by electron cyclotron resonance chemical vapour deposition (ECR–CVD) which is a low temperature remote plasma deposition process. The general idea behind plasma deposition is to produce a highly non–equilibrium state in a given reactant gas were the electron temperature can exceed the equilibrium temperature within the gas by many orders of magnitude. Thus, a high reaction yield can be achieved for the chemical vapour deposition of one or several reactant gases into a desired solid state. Remote plasma deposition processes such as ECR–CVD have a spatial separation between the plasma zone, which is where the plasma is made by resonant excitation of a non–reactant gas (e.g. an inert gas) and the reaction zone, where the reactant gases grow into the solid through reactions that are enhanced by collisions with excited species of the non–reactant gas. The advantage of a remote plasma process is the improved control of the sample growth in comparison to direct plasma processes for which no separation of the plasma and the reaction zone exists: When the excited non–reactant gas atoms or molecules leave the plasma zone, an immediate decay of all the excited states takes place except of the metastable species. Because of this, the number of possible interactions with reactant atoms or molecules and thus the variety of possible reactions at the sample surface are strongly reduced. The plasma of an ECR–CVD process is generated by electron cyclotron resonance which

base pressure:	4.5×10^{-7}Torr	deposition time:	180min
substrate temperature:	325°C	microwave power:	1000W
chuck level:	95%	chuck temperature:	550°C
current of window magnet:	180A	current of exit magnet:	120 A
RF bias:	-15 V	chamber pressure:	7mTorr
excitation gas:	H_2	excitation gas flow:	80 sccm
process gas:	SiH_4	process gas flow:	4 sccm
sample thickness:	2.7μm		

Table 5.1: Deposition parameters of the NTi085 sample series, deposited by an ECR–CVD process.

takes advantage of the propagation of charged species on circular trajectories through the plasma zone due to the external application of a magnetic field. When a radiation whose frequency corresponds to the rotation frequency of the charged particles, the so called cyclotron frequency is applied and a resonant absorption of energy takes place that eventually leads also to an excitement of electronics states due to collisions of gas particles.

The samples used for the experiments were taken from the NTi085 series deposited at the Hahn–Meitner–Institut, Berlin on June, 2nd 1999. The deposition parameters used for this deposition run are illustrated in tab. 5.1. After the deposition, the samples were stored in air until the contact structure that is described in the last chapter was created in April 2001.

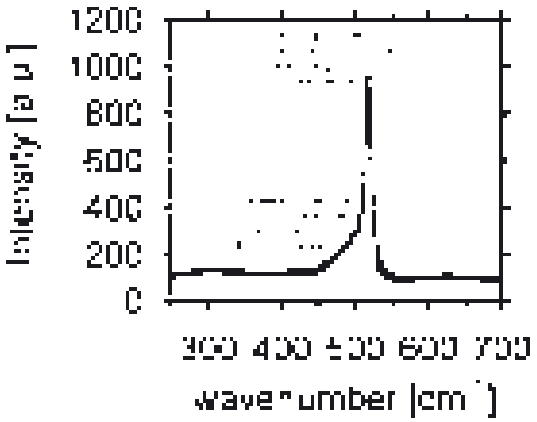

Figure 5.3: Raman spectrum of the sample NTi085b-2. The fit displays a peak that can be deconvoluted into a strong homogeneous peak (Lorentzian) at about $k \approx 520cm^{-1}$ and a weak inhomogeneous peak (Gaussian) at $k \approx 480cm^{-1}$.

5.1.2 Material characterisation

In order to confirm that the thin films grown in the NTi085 series have the properties of hydrogenated microcrystalline silicon, a variety of standard characterisation methods was used. After 180min of deposition, the sample thickness had reached 2.7μm, as confirmed by a KLA-Tencor P10 surface profilometer measurement. The characterisation of the conductivity was done by a Hg–four point–probe measurement under atmospheric conditions, 47 hours after the sample had been removed from the deposition reactor, revealing an ohmic behaviour between applied voltages of $\pm 100V$, a dark resistivity of $2.6 \times 10^3\Omega$cm and a photoresistivity of $1.37 \times 10^3\Omega$cm. This corresponds to a low relative photo sensitivity of 1.9, which is not indicative of low photoconductivity (compared to other literature values [68]) but a relative high dark conductivity. The latter may be due to unwanted

impurities such as oxygen which can play the role of a thermal donor in crystalline silicon [2]. The degree of crystallinity was investigated by Raman spectroscopy. A scan obtained from the shift of a HeNe–laser line is illustrated in fig. 5.3. It clearly depicts a strong asymmetric line which was fit by a combination of a Lorentzian and a Gaussian function. The fit shows that a strong homogeneously broadened line exists at $k \approx 520cm^{-1}$ and a weak inhomogeneously broadened line at $k \approx 480cm^{-1}$. These two resonances are typically found in the Raman spectra of crystalline and amorphous Si spectra, respectively. The fraction of the integrated peak intensities of $\frac{I_{520}}{I_{480}} = 7.5$ is a typical value for a microcrystalline silicon morphology in which the crystalline volume fraction is dominant [69, 70].

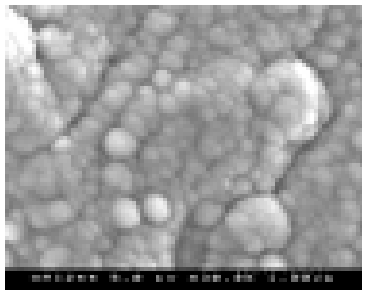

Figure 5.4: SEM image of the surface of μc-Si:H.

A more direct approach to the characterisation of a material's microscopic morphology can be taken by scanning electron microscopy (SEM). Figure 5.4 displays the SEM scan of one of the samples of the NTi086 series, deposited under similar[1] deposition parameters as the NTi085 series. In this scan, cauliflower–like structures are recognisable on the sample surface. These structures correspond to the tops of the crystalline columns. The cauliflower–like structures itself exhibit a fairly inhomogeneous texture with subtle substructures that are not recognisable on the resolution of the picture. These substructures are due to the small crystallites that form the columns.

5.1.3 ESR measurements

For the preparation of the first TSR experiment, a verification of the presence of CE and db centres in the given material is crucial. Naturally, the standard method of choice is ESR spectroscopy. At first, a cw-ESR experiment was carried out in order to get an estimate on the defect densities. The experiment was carried out without illumination and at room temperature. More details about standard cw-ESR spectroscopy are outlined in appendix. B.1. The experiment was carried out in an optical continuous wave resonator which was connected to a He–flow cryostat. The result of the ESR scan is displayed in fig. 5.5. The db resonance at $g \approx 2.005$ is clearly visible but the noise level is still recognisable. The db resonance is so weak such that the weak artifact signals due to cavity contamination and E' centres of the quartz substrate are of the same magnitude. A deconvolution of the

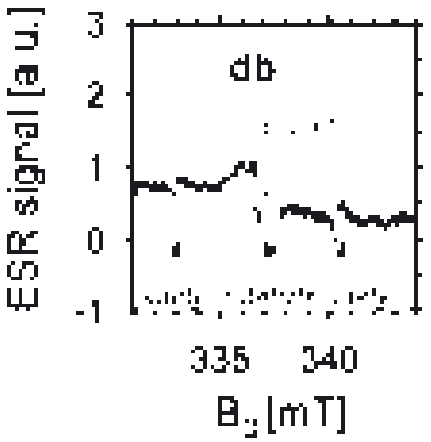

Figure 5.5: The dark cw-ESR spectrum of the NTi085 sample at room temperature. (97 scans; field modulation: f=100kHz; microwave frequency: ν=9.45435GHz; microwave power: $P_{\mu W} = 628.441\mu$W; time constant of the receiver lock in: 40.96ms; modulation amplitude: 0.6mT; receiver amplification: 106db)

[1] All parameters were equal except the RF bias

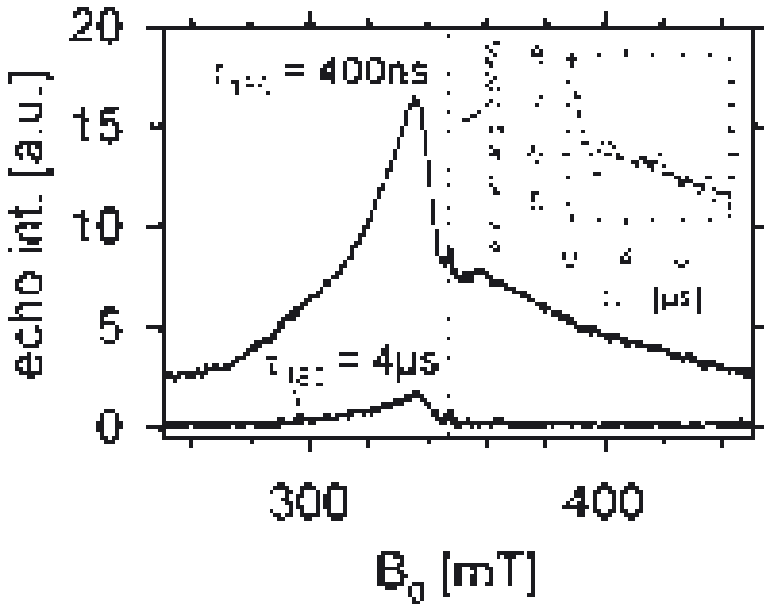

Figure 5.6: The magnetic field dependence of the echo intensity in a Hahn spin–echo experiment with pulse separation $\tau_{180} = 400$ns and $\tau_{180} = 4\mu$s. The microwave pulses where τ=16ns and 32ns long which corresponded at the given microwave intensity of about 250W to a $\frac{\pi}{2} - \pi$ sequence. The experiment was carried out at $T = 10$K and under an illumination with $P = 400$mW intensity. The broad peak is due to cavity artifacts. The inset displays the echo decay measured at $g \approx 2.005$.

different signals followed by the comparison of the db peak intensity with the spectrum of a db reference sample (a-Si:H) that was measured under the same conditions, reveals an absolute db density of $5(3) \times 10^{16}$. This value is close to the lower limit in the range of db densities that can be obtained for microcrystalline silicon films (10^{16}–10^{20}cm^{-3}, [46, 71]). Even though fewer db centres imply less recombination and hence fewer spin pairs, the low number of db centres makes the given material to a good model system nevertheless: Less recombination implies a higher photoconductivity which improves the time resolution of the experiment (see chapter 4) and the higher average distance between spin pairs reduces the interaction between different pairs and thus, it enhances coherence times.

A series of Hahn–spin echo–experiments was carried out with the sample NTi085b-2 in order to investigate the coherence times of the CE and db centres. The experiments were carried out under the same conditions as some of the TSR experiments discussed below, which allows a comparison with coherence times obtained for recombination–echo experiments. The sample was measured at T=10K which ensures that the spin–lattice relaxation time T_1 of any of the two centres is far beyond the microsecond time range [61]. The sample illumination led to a sample resistance of R=396kΩ. The Hahn–echo sequence as explained in appendix A.4, reveals the transverse relaxation time T_2, which, since T_1 is very long, is the shortest coherence time in the given ensemble as long as other sources of incoherence such as recombination do not exist [10]. The comparison of the coherence decay of spin–echo and recombination–echo experiments will show that the latter is a reasonable assumption since only a small fraction of the paramagnetic db and CE centres contribute at any given time to the recombination process. Figure 5.6 shows

the shape of the magnetic field dependence of the Hahn echo which exhibits a broad resonance due to cavity background and a weak, narrow peak around g=2 due to the db and CE signals. Similar to the cw ESR experiment discussed above, the low spin density together with the small sample volume lead to such a low absolute number of paramagnetic centres contained in the cavity that cavity artifacts impose a significant offset to the measured signal. Note that the E' centres do not play a role for any of the displayed measurements. Apparently, their coherency decay is so strong that all spins have already collapsed after $2\tau_{180}$=800ns. Unlike the ESR signals of μc-Si:H, the cavity background is very short lived, too. It has almost disappeared in the echo plot after a sequence with $2\tau_{180}$=8μs. The inset of fig. 5.6 shows the τ_{180} dependence of the echo intensity at a magnetic field corresponding to g ≈2.005. It clearly shows that a strong initial signal (the cavity artifact) decay is fast and that the remaining db signal decay takes place slowly. The measured function is highly non–exponential which makes the determination of a single T_2 time for the entire db ensemble difficult. However, one can clearly recognise that any db–coherence time would be well beyond 10μs.

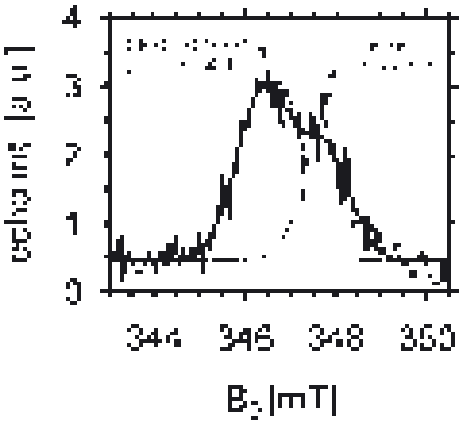

Figure 5.7: The magnetic field dependence of the echo intensity measured under the same experimental conditions as in fig. 5.6 with τ_{180} = 4μs.

This result is also confirmed by another experiment, whose data is plotted in fig. 5.7: It shows the echo intensity after a Hahn–echo sequence that was carried out with τ_{180}=4μs and a much higher magnetic field resolution in a field range about the resonances of CE and db centres and with all other parameters identical to the experiments of fig. 5.6. The plot clearly exhibits the resonances of both spin ensembles, CE and db centres whose coherence decay appears to be equally slow even after a time $2\tau_{180}$=8μs. The estimates for the T_2 times of CE and db centres will be of great benefit for the interpretation of the different time constants which appear in the TSR measurements. They will allow the identification of the relaxation related influences and thus, a reduction of the number of unknown parameters will be possible.

5.1.4 EDMR measurements

A cw EDMR experiment was carried out in order to confirm the expected CE and db involvement in recombination. In order to ensure a maximum comparability the EDMR was carried out in the Bruker ER4118 dielectric resonator used for the pulsed ESR and TSR experiments. The coupling of this pulse resonator was tuned to a very high value in order to achieve a maximum quality factor (Q-factor[2]). The measured spectrum as displayed in fig. 5.8 was obtained by microwave–field modulation. The microwave modulation is advantageous in comparison to the magnetic field modulation since it does

[2] $Q \gg$ for cw experiments since narrow frequency range necessary, $Q \ll$ for pulse experiments where broad frequency range necessary for pulse spectrum.

not introduce an artifact broadening into the measured EDMR spectrum and moreover, the determination of the modulation phase is independent from the applied modulation frequency. The spectrum in fig. 5.8 depicts the relative changes of the photocurrent due to resonant microwave irradiation versus the externally applied magnetic field B_0. One can clearly recognise the quenching of the photo current about the two Landé factors that correspond the db and CE resonances. Figure 5.8 also displays the result of a fit with two pseudo–Voigt distributions. A Voigt distribution is the convolution of a Gaussian distribution with the Lorentzian distribution. Voigtians have to be used for the fit of EDMR–line shapes in μc-Si:H due to the inhomogeneous distribution of the Landé factors and the homogeneous broadening due to incoherent influences [46]. For convenience, the fit in fig. 5.8 was done with pseudo Voigtians, linear combinations of Gaussians and Lorentzians, since the real Voigt–distribution function is not displayable analytically and thus, a numerical fit becomes highly complex. Note that the intensity of the db resonance is much stronger than the intensity of the CE centre. As explained above, the spin–dependent recombination path observed in the experiment described would be purely due to CE–db transitions, if both peaks appeared equally strong in the EDMR quenching signals. Thus, the measurement conditions that lead to a spectrum as shown in fig. 5.8 are ideal for the investigation of a possible second recombination path that exists parallel to the well known CE–db path.

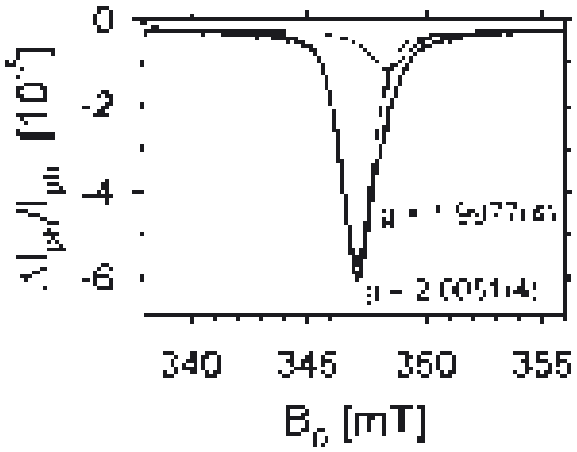

Figure 5.8: EDMR spectrum of sample NTi085. The spectrum is fitted with two pseudo–Voigtian lines whose g factors are given in the graph. (T=10K; laser: P=400mW; R=394kΩ; $P_{\mu w}$=200mW, modulated at f=2260Hz.)

In conclusion, the data presented in this section shows that the material produced in the NTi085 deposition run exhibits all properties known for hydrogenated microcrystalline silicon and, thus, it fulfills all the requirements for a model semiconductor that can be used for a TSR experiment. In the following sections, the results of the first TSR measurements conducted on the NTi085b-2 sample are presented and discussed and in the course of this, it is shown that the effects and properties of the time domain of spin–dependent recombination as discussed in chapter 3 can be detected.

5.2 Detection of the TSR signal

First TSR experiments were carried out on the NTi085b-2 sample using the experimental setup described in chapter 4. The results are displayed in fig. 5.9. It is based on the photocurrent transient (TSR transient) measurement versus the magnetic field B_0. The

length of the microwave pulse (τ=320ns) corresponds to an excitation width of less than 1G. On the μs-time scale shown in the plot of fig. 5.9, the resonant pulse ended at about $t = 0$. Note that the displayed time range does not include the first 15μs after the pulse. This time range has been skipped in order to omit the artifact signal produced by the limited time resolution of the current detector that is discussed in chapter 4. The data displayed in fig. 5.9 shows how a short coherent ESR interaction leads to a decrease of the photocurrent due to the enhancement of the singlet content within a given spin–pair ensemble. The photocurrent quenching gradually relaxes back towards its steady state; however, before the signal vanishes, a temporary photocurrent enhancement becomes visible, which will be discussed in section 5.3. The time scale on which the photocurrent relaxes back to its steady state is orders of magnitudes longer than the duration of the resonant interaction. Clearly, the B_0 dependence of the recombination rate is due to a resonant process. Note that the data depicts the dynamics of spin–dependent recombination in the absence of any ESR radiation. It can be detected solely due to the fact that the spin–pair ensemble of CE–db pairs has not relaxed to its steady state. For the verification that the observed resonant quenching is due to the db and CE centres, the line shape of the transients has to be determined. With the three dimensional set of the data given in fig. 5.9, the question arises, from which time slice, the magnetic field dependence has to be taken. A measurement during or right after pulse is not possible due to the limitations imposed by the experimental time constants. However, as discussed in theory in section 3.4.3, the relaxation transients after the pulse are exponential and thus, for any given magnetic field B_0, proportional to their value right after the pulse. This proportionality, which will be proven experimentally in section 5.3 is the reason why the time of the line shape measurement is irrelevant and one can choose the time slice where the best signal to noise ratio can be obtained.

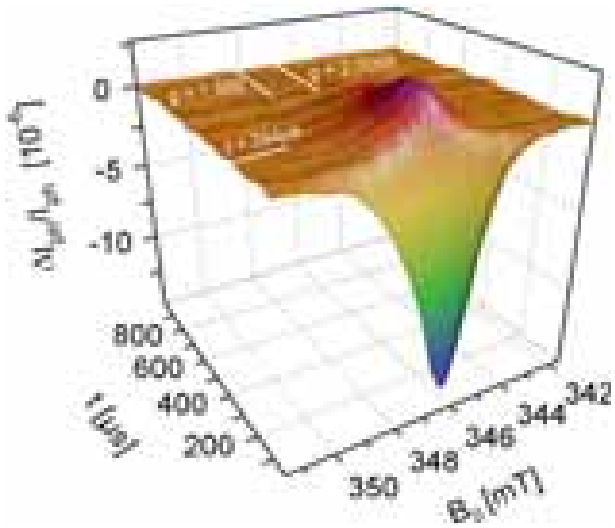

Figure 5.9: The magnetic field dependence of TSR transients during the first ms after a 320ns long microwave burst. One can clearly recognise how a photocurrent quenching right after the pulse takes place that changes into an enhancement before it relaxes back towards its steady state. (laser: P=300mW, λ=514nm; microwave: $P_{\mu W}$=4W (24db), ν=9.746438GHz, τ=320ns; T=40K, I=200μA; 128 fields, 65536 averages)

For the verification of the resonances contained in the magnetic field dependence of a TSR measurement (TSR spectrum), a comparison was made of the EDMR data presented in fig. 5.8 and a TSR spectrum recorded under similar experimental conditions. Fig. 5.10 shows normalised plots of the EDMR and TSR spectrum. Note that the resolution of the TSR spectrum is limited due to the magnitude and the excitation width of the microwave

radiation during the pulse excitation. Transients were recorded at much fewer magnetic fields in comparison to the EDMR measurement. The two plots in fig. 5.10 agree within their respective noise levels. Since TSR, unlike EDMR, displays inhomogeneous broadening only, it can be concluded that the homogeneous broadening of the EDMR spectrum is smaller than the resolution of the TSR spectrum ($\approx 1G$). Thus, the incoherent processes such as recombination and dissociation of spin pairs or spin–relaxation processes seem to be slower than $\frac{2\pi\hbar}{g\mu_B \times 1G} \approx 350ns$. However, note that the estimation of this upper limit is highly problematic: Due to the pulse length of τ=320ns, any process faster than this would influence both EDMR and TSR spectra. Slower processes would broaden the EDMR line but not the TSR line, and hence, are not recognisable due to the limitations of the resolution. This example shows the dilemma with regard to the quantitative measurement of time constants from EDMR–line shapes which is difficult and highly inaccurate. It is this what makes direct time–domain measurements necessary and valuable as it will be shown in the following sections and the next chapter.

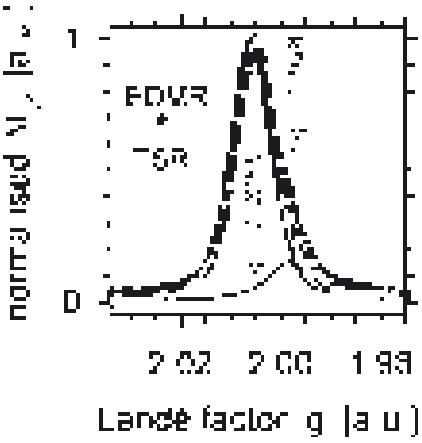

Figure 5.10: Normalised line shapes of an EDMR and TSR spectrum obtained under comparable conditions. The solid lines are pseudo Voigtians used to fit the resonances and their g factors are indicated. (P=400mW, λ=514nm, T=10K, I=100μA; $t_{\mu s}$=18μs)

5.2.1 Microwave intensity dependence of the TSR spectrum

In the theoretical picture presented in section 3.5.2, the TSR spectrum is described as a convolution of a Lorentzian line whose width is determined by $2B_1$ with that of an inhomogeneous line that is determined by the structure of the material. Thus, the widths of the TSR lines have to increase with decreasing microwave attenuation. Figure 5.11 depicts two TSR spectra recorded at two different microwave intensities. The measured data clearly reveals an increase of the line width with increasing microwave intensity. For a quantitative comparison, fits with two pseudo Voigtian peaks were carried out for both data sets. These fits are plotted along with the fit results for the db peaks of each data set. The full width at half maximum of the db resonance turned out to be $\Delta H = 3.8(2)$mT in the 6db measurement and $\Delta H = 1.64(6)$mT in the 24db measurement. At this point, a scaling for the B_1 field strength has not been introduced. However, on the B_1 scale obtained from the cycle duration of Rabi–beat oscillation as discussed in section 5.5 (displayed in fig. 5.22), we obtain B_1=1.6mT at 6db and B_1=0.2mT at 24db. If it is assumed that the width of the convoluted Voigtian line shape $\Delta H_{\mathrm{V}} = \sqrt{\Delta H_{\mathrm{L}}^2 + \Delta H_{\mathrm{G}}^2}$ is the geometrical sum of the widths of the Gaussian and the Lorentzian lines, the fitted db-line width in conjunction with the known B_1 scale reveals an inhomogeneous broadening of the db line of $\Delta H_{\mathrm{G}} \approx$1.6mT

for both data sets. This shows how homogeneous broadening determines the line shapes at 6db while at 24db the line shape is determined mostly by the inhomogeneous broadening.

5.3 Photocurrent enhancement

The fact that a TSR signal is found proves that the photocurrent transient takes place on a time scale that is directly accessible experimentally. The plot in fig. 5.9 shows that the increase of the recombination observed by the decrease of the photocurrent right after the resonant pulse is imposed, is followed by a temporary enhancement of the photocurrent before the system returns to its steady state. An ESR induced photocurrent enhancement has been reported many times before in the literature and is summarised by Stutzmann and Brandt [22]. Such effects have often been attributed to hopping transport but not to recombination. Thus, it is important to check if a similar origin accounts for the photocurrent enhancement signal of fig. 5.9. The enhancements of spin–dependent transport transitions in hydrogenated microcrystalline silicon has been observed by Kanschat [46] who identified the enhancement of the dark conductivity under resonance of the CE centre with a phonon assisted, spin-dependent hopping process that takes place between shallow trap states with energies close to the conduction band. Kanschat showed that the resonant enhancement of the dark conductivity did occur for the CE resonance only. The resonances of dangling–bond centres would not appear in the dark EDMR since these db-energies are too low within the band gap to become a part of an electron transport path.

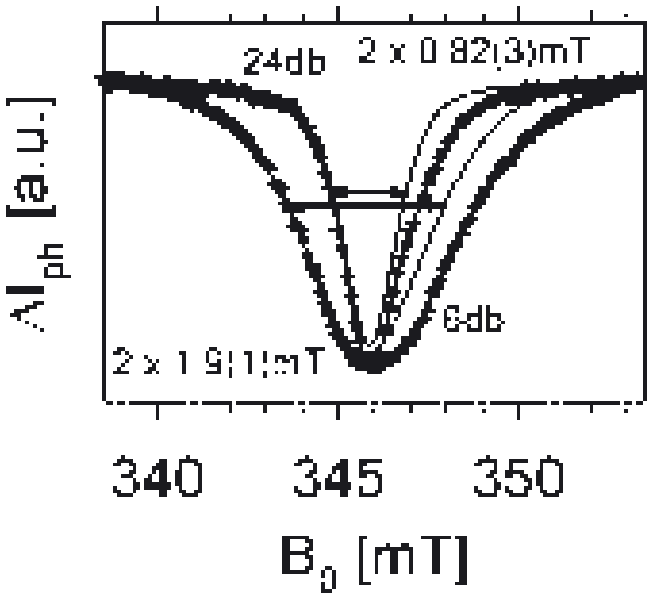

Figure 5.11: Plot of two TSR spectra at different microwave intensities. The experimental data is represented by the crosses. The solid lines are the results of a fit of two pseudo–Voigtian line shapes. The fit functions as well as the fit for the db resonances are also plotted in solid lines for both data sets. (T=10K, I=100μA; laser: λ=514nm, P=350mW; microwave: $P_{\mu W}$=250W (6db) and 4W (24db), ν=9.725100 GHz, τ=300ns and 900ns; 128 magnetic fields, 338.97mT$\leq B_0 \leq$353.97mT)

Figure 5.12 displays two TSR spectra taken from the two dimensional data in fig. 5.9 at $t_{\mu s}$=34μs and at $t_{\mu s}$=244μs. Both plots were normalised to their minimum and maximum, respectively. These times were chosen, such that comparison of the spectra in the quenching and the enhancing regimen was possible. Note that the relative noise of the enhancement signal is stronger since the magnitude of the absolute signal is smaller. Remarkably, these normalised spectra do not reveal any difference within the given noise levels. Both signals are asymmetric and can be fit with a convolution of two pseudo–Voigtian lines that are centred at the db and the CE resonances. The possibility that two qualitatively

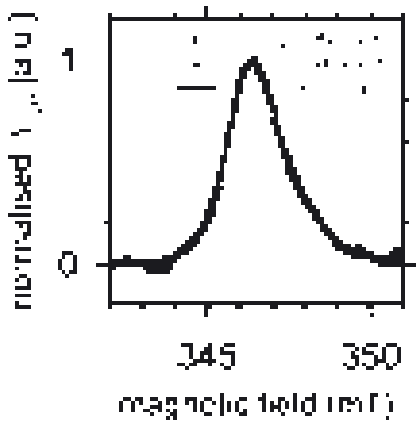

Figure 5.12: Comparison of the normalised TSR spectra of the quenching (△) and the enhancing signals (□) taken at $t_{\mu s}$=34μs and $t_{\mu s}$=244μs, respectively.

different processes cause identical line shapes in which two different resonances are contained with equal proportions is rather unlikely. Thus, only one conclusion seems to be reasonable: The quenching and the enhancing signal are two different effects caused by one and the same process. Moreover, this single process must be a recombination transition. This conclusion must be made due to the strong presence of the db resonance in the given spectra and since no transport process is known that could cause photocurrent quenching. Note that the identity of the two normalised spectra in fig. 5.12 shows that the magnetic field dependence of the TSR transient after the resonant pulse excitation remains proportional to its value right after the pulse. This confirms that the assumptions made for the model presented in chapter 3.4.3 are appropriate.

The independence of the line shapes on the time slice as shown above implies that the transients for any given magnetic field are proportional to each other as well. The experimental verification of this independence is depicted in fig. 5.13, which contains 10 plots of transients recorded at magnetic fields about the CE and db resonances. The displayed data sets were normalised to their respective maxima in order to ensure comparability of the transient shapes. Since the absolute magnitudes of the transients recorded at the edges of the magnetic field range were significantly smaller than the magnitude of those in the centre (see fig.5.8), the relative SNR of these transients was lower. A comparison of the transients reveals an overall identity within the given noise levels. Most surprisingly, the data can be fitted with only two exponential decay functions and the result of the fit is independent of the magnetic field were the data is collected. The fit results of the data displayed in fig. 5.13 are shown in table 5.2. It shows again that the data presented in fig. 5.9 displays different features that seem to belong to one and the same process. The identity of the time constants throughout the ensemble of traps and dangling bonds that produced the signals displayed in fig. 5.9, leads to the question why the disorder of the used material is not reflected in a strong distribution of transition frequencies. Tunnelling transitions

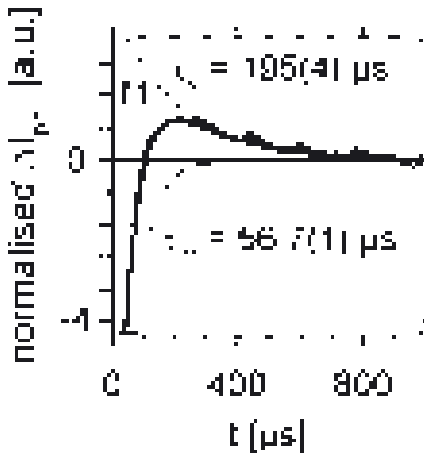

Figure 5.13: Comparison of the normalised photocurrent transients recorded at 10 different magnetic fields between B_0=345.335mT and 348.169mT. This interval includes both db and CE resonances.

$a_2 =$	$-15(1)$	$a_3 =$	$4(1)$
$\tau_{\mathrm{m}} =$	$56(1)\mu$s	$\tau_{\mathrm{s}} =$	$195(4)\mu$s

Table 5.2: Fit results of the photocurrent transients displayed in fig. 5.13. The fit was carried out with a double–exponential fit function $\frac{\Delta I}{\Delta I_{\max}}(t) = a_2 e^{-\frac{t}{\tau_{\mathrm{m}}}} + a_3 e^{-\frac{t}{\tau_{\mathrm{s}}}}$.

between traps and dangling bonds are highly dependent on the distance between these localised states [72]. However, the almost perfect exponential shape of the functions shown above indicates a rather sharp distribution of the observed processes. Thus, the observed signal appears to be mostly dependent on a recombination process other than the CE–db transition. A conclusion that is already confirmed by the weak CE-signal that is almost buried under the strong db peak at the measurement conditions given when the data in fig. 5.9 was recorded.

Note that the photocurrent transients displayed in fig. 5.13 exhibit a striking similarity to the simulated data of the photoconductivity shown in fig. 3.6 obtained from the assumption of a non–negligible triplet recombination. Thus, the fit results will be discussed in chapter 6 in terms of the model for the incoherent time domain outlined in section 3.4. Therein, it was assumed that the charge carriers in the spin pairs had a narrow Larmor separation and therefore non–negligible spin–spin interaction as well as non–negligible triplet recombination.

5.4 Rabi–beat oscillation

With the detection of photocurrent transients induced by short ESR excitation of CE and db spin states in μc-Si:H, the predictions made for the dependence of the photocurrent on the Rabi and Rabi–beat oscillation as made in section 3.5 can be tested. Crucial for the reconstruction of the dynamics of the spin–pairs through a measurement of the pulse length dependence (in the following referred to as PLD) is the reproducibility at any given measurement time. In addition, is has to be shown experimentally that PLD determines the amplitude of a photocurrent transient, but not the time constants of the multiexponential decay. The underlying principle behind PLD is outlined in section 3.4.3. Figure 5.14 illustrates this graphically. The Rabi oscillation during a ns-range pulse of length τ leads to change $\Delta(\tau)$ of the recombination rate thereafter. The relative value of $\Delta(\tau)$ can be obtained from the TSR transient recorded during such a single shot experiment even if the time resolution of the current detector is much lower then the time range of the pulse length since the TSR transient is proportional to $\Delta(\tau)$ at any given time. Thus, as explained in the caption of fig. 5.14, by repetition of the experiment for different τ the dynamics of $\Delta(\tau)$ can be obtained for the ns–time range.

5.4.1 PLD of photocurrent transient

Figure 5.15 shows a set of TSR transients recorded in the NTi085b-2 μc-Si:H sample as a function of the applied pulse lengths τ. The shape of the TSR transients in fig. 5.15

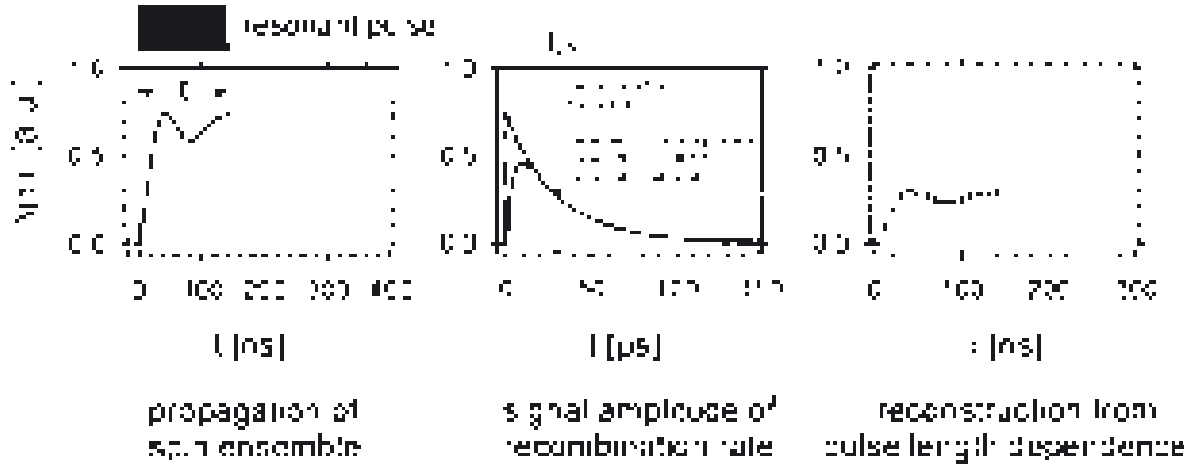

Figure 5.14: Illustration of the measurement principle of the pulse length dependence (PLD). The plot on the left hand side exhibits an arbitrary evolution of the spin ensemble on the ns–time range due to Rabi oscillation during the microwave pulse. After the pulse, the spin ensemble dephases immediately and the relaxation of the recombination rate is purely exponential as depicted by the centre plot. Thus, by measurement of the exponential transient on a time scale longer than the time resolution of a current detector (for instance by measuring the photocurrent at an arbitrary time $t_{\mu s}$ after the end of the pulse), the change of the spin ensemble $\Delta(\tau)$ as defined in chapter 3 can be determined. The evolution during the pulse can be obtained by repetition of the experiment with different pulse lengths τ.

shows the same behaviour as already depicted in fig. 5.13: It consists of two exponential decay functions, a fast decrease followed by a slower increase of the photocurrent. The difference between the different functions lies in the different magnitudes. At very short pulses ($\tau < 15$ns), the amplitudes increase with increasing pulse length. At longer pulse lengths ($\tau > 15$ns) the amplitudes appear to remain constant and are hardly changed with increasing pulse length.

If the theoretical assumptions made in section 3.5 are correct, the shape of the photocurrent transients is determined by the time constants of the two exponential decays only. Hence, they should be independent from the pulse length since the short pulse interaction can only change the state of the pair ensemble but not the way it relaxes back to its steady state. Figure 5.16(a) proves this pulse length independence of the decay constants: It depicts 22 different photocurrent transients recorded after pulse lengths between τ=6ns and τ=50ns. The data is normalised to the

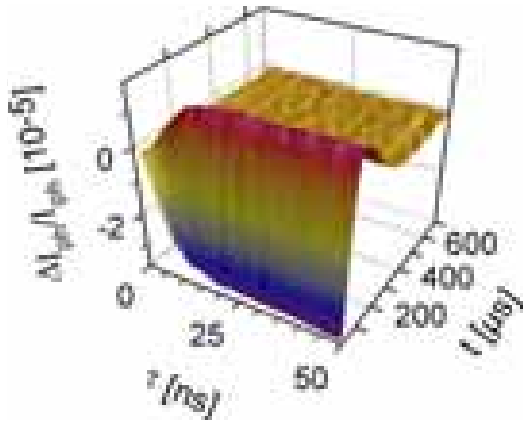

Figure 5.15: The PLD in μc-Si:H: The plot shows the photocurrent responses as a function of the pulse length τ. (T=30K, I=100μA; laser: λ=514nm, P=300mW; microwave: $P_{\mu W}$=250W (6db), ν=9.746516 GHz, τ=2ns to 50ns; magnetic field corresponds to the db-resonance at $g = 2.0055$)

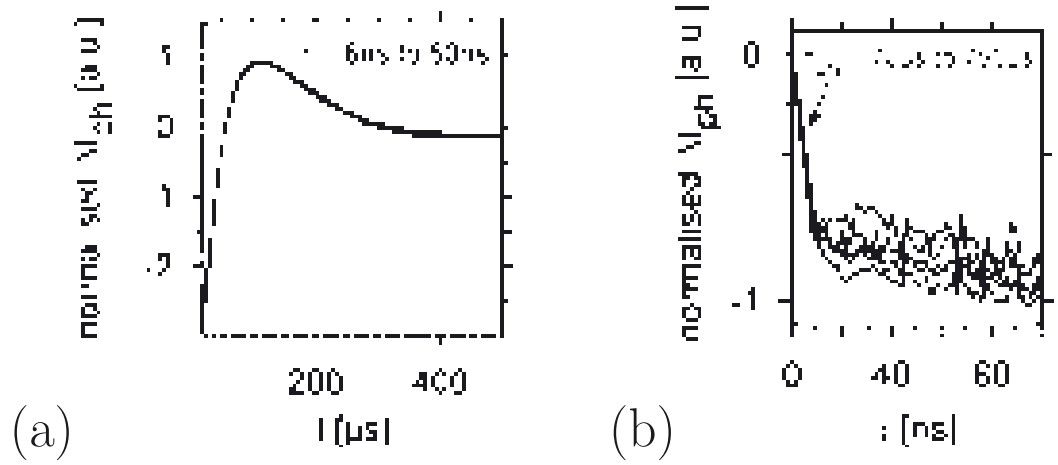

Figure 5.16: (a) Plot of 22 photocurrent transients taken from fig. 5.15 which were recorded after different pulse lengths. The normalised data reveals a reproducibility within the given noise levels; (b) Comparison of the PLD of the photocurrent measured at 6 different times $t_{\mu s}$ after the end of the pulses. Again, the plot of the normalised data reveals reproducibility.

maximum value of each transient. Within the given noise fluctuations, a convincing agreement of all transients is present. Thus, the assumption that the decay of the photoconductivity after the short ESR excitation is characteristic for the inherent time constants that determine a given recombination path in a given material can be made. Moreover, the pulse length dependence of the photocurrent that is solely contained in the amplitudes of the decay functions reproduces in the photocurrent at any given time after the end of the pulse as proven experimentally in fig. 5.16(b): Here, the pulse length dependence of the relative photocurrent change measured at different times after the end of the microwave pulses is depicted. For comparability, the data was normalised. Again, an agreement of the shape is revealed within the noise levels. Note that an equal absolute noise for all data sets leads to different relative noise levels in the normalised functions.

5.4.2 Rapid dephasing Rabi oscillation of db centres

From the PLD of the photocurrent as depicted in fig. 5.16(b), it is not possible to prove an oscillation during the pulse as predicted in section 3.5. However, the initial fast decrease of the PLD that takes place within less than 15ns and after which the amplitudes remain constant may be caused by an oscillation with a dephasing time faster than one oscillation cycle. As previously explained, dephasing can be caused by Larmor–frequency distribution (g–factor distribution), B_1 inhomogeneities and a distribution of spin–dipolar coupling. These factors are all expected to be present in the μc-Si:H and therefore, they can lead to a fast attenuation of the function $T_{\text{eff}}(\alpha)$ that was introduced in section 3.5. Note that the dimensionless argument $\alpha = \kappa\gamma B_1\tau$ of $T_{\text{eff}}(\alpha)$ as defined in eq. 3.92 depends on the two fixed constants κ and γ as well as the two variables B_1 and τ, which can be influenced experimentally by choice of the pulse length and pulse intensity. Thus, when the experimental PLD of the photocurrent is identical with $T_{\text{eff}}(\alpha)$, it has to scale proportionally with the inverse of the microwave field strength B_1. Figure 5.17 shows a PLD series measured

on resonance with the db centres at $g \approx 2.005$. While the shape of these plots is qualitatively equal in every case, one can see that the initial decay becomes slower with increasing microwave attenuation. In addition, the data sets reveal that after the initial strong decrease a minimum is reached after which the amplitude increases slightly before a complete dephasing has taken place. This small wiggle shifts equally on the time scale with increasing or decreasing microwave intensity. This is another hint that the measured pulse length dependence actually illustrates a very strong attenuated Rabi oscillation.

A final proof is given in the inset of fig. 5.17. It shows how the pulse length $\tau_{1/2}$, defined as the time at which the signal amplitudes has decreased by 50% depends on the microwave field. Note that any point on the pulse length dependence function could have been chosen for the proof that this function stretches with increasing microwave attenuation. However, at the half maximum point is the deepest slope, which reduces the measurement error strongly. As one can see in the inset, $\tau_{1/2}^{-1}$ depends linearly on B_1. A linear fit that passes through the origin shows excellent agreement with the data points which means that the product τB_1 is constant and the theoretical predictions in section 3.5 are confirmed. The fit displayed in the inset graph represents a linear function without offset. Note that, at this point, the fit results are only constants that fit an arbitrarily chosen scale since $\tau_{1/2}$ was chosen arbitrarily as well and the absolute magnitude of B_1 is not known.

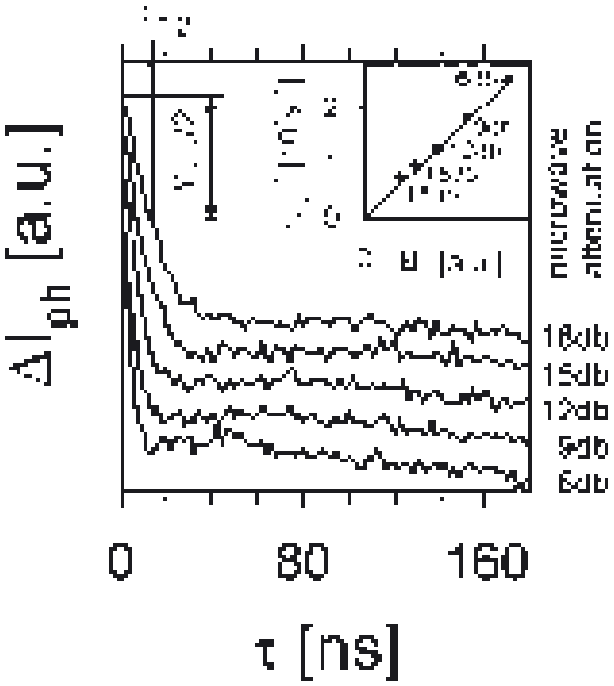

Figure 5.17: The PLD of the photocurrent transients after pulses with attenuation between 6db and 18db. The inset shows how the inverse of the half time $\tau_{1/2}$, which is defined in the plot is proportional to the microwave field B_1. The plots where shifted vertically by an arbitrary value so that they can be distinguished visually. (T=10K, I=100μA; laser: λ=514nm, P=600mW; microwave: $P_{\mu W}$=15W (18db) to 250W (6db), ν=9.750439GHz, τ=2 to 200ns in 2ns steps; magnetic field corresponding to the db-resonance at g = 2.0055; $t_{\mu s}$=17μs)

5.4.3 Rabi oscillation of CE centres

The detection of the rapidly dephasing oscillation of the db centre raises the question of the origin of this effect: Since the strong signal may be due to two recombination channels, the CE–db channel and the hypothetical db direct–capture process as proposed as proposed by Kanschat [46] and outlined in section 5.1.4, the oscillation could be a Rabi or Rabi–beat oscillation in the sense of the definitions given in sections 3.5 and 3.6. Due

to the small contribution of the CE peak (see figs 5.8 and 5.10), the contribution of the CE oscillation right at its resonance could be buried under the strong db signal. As one can see in the EDMR plot of fig. 5.8, a magnetic field range above the CE resonance exists, where the signal due to the strong db peak becomes weaker than the CE contribution whereas the latter is weak but still detectable. A PLD measurement for this magnetic field range is plotted in fig. 5.18. Note that the weak signal to noise ratio as well as the limit of the pulse length resolution (2ns) imposed strong noise contributions onto the data. Nevertheless, an oscillation is detectable for several cycles and thus it is of much different nature than the fast dephasing oscillation that causes the strong signal close to the db resonance. A comparison of the data set recorded at the different magnetic fields shows how the oscillation intensity decreases and the frequency increases with increasing distance of the magnetic field B_0 from the resonance with the CE-centre at B_0=348.533mT. This behaviour meets the prediction made for the Rabi frequency and the oscillation amplitude made in eqs.3.66 and 3.89, respectively. Unfortunately, the data for the cycle duration dependence on the B_0 field as depicted in the inset of fig. 5.18 is insufficient for a reasonable fit with eq. 3.66. The narrow magnetic field range in which the oscillation is visible, the large separation of this range from the CE resonance, as well as the low SNR cause unreasonable error margins for the B_1 field strength obtained from such a fit. Thus, a scaling of the B_1 field strength with the logarithm of the microwave attenuation is not possible. However, with a B_1 scaling from Rabi–echo experiments as it will be introduced in section 5.5.1, one can simulate the expected values of the cycle duration $\tau_{\min}$ of the oscillation for the experimental parameters used. The result of this simulation displayed by the solid line in the inset of fig. 5.18 exhibits an agreement with the experimental value within the noise range.

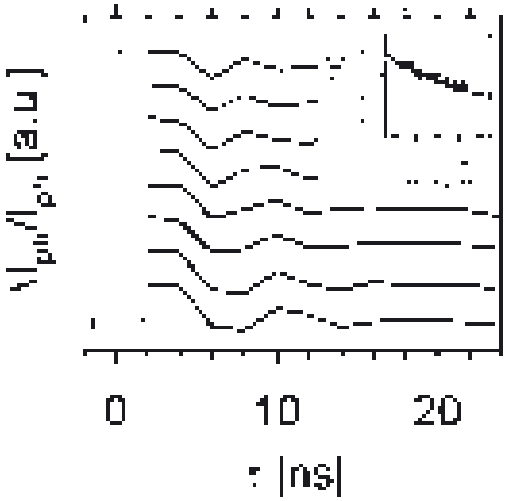

Figure 5.18: PLD transients for different positions of the magnetic fields B_0. The dotted lines are guides to the eye that indicate the decrease of the cycle duration with increasing magnetic field. The time of the first minimum of the oscillation , $\tau_{\min}$, is plotted as a function of the magnetic field in the inset graph. The solid line therein is a simulation that was based on the experimental parameters. (T=30K, I=100μA; laser: λ=514nm, P=300mW; microwave: $P_{\mu W}$=126W (9db), ν=9.746516 GHz; 8 magnetic field positions corresponding to g factors between 1.9660 and 1.9823; $t_{\mu s}$=20μs)

In spite of this insufficiency with regard to a quantitative interpretation of the CE–db recombination path, the data displayed in fig. 5.18 is evidence that the CE–db path has only a small contribution to the larger signal centred about the db resonance at ($g \approx 2.0055$). Thus, the largest part of this signal has to be due to a different process, which, as it will be proven in section 5.5, is due to the fast dephasing of a Rabi–beat oscillation.

$a = 1.45(9) \times 10^{-4}$	$b = 44(6)$ns	$c = 1.32(7) \times 10^{-4}$	$\tau_{\mathrm{f}} = 1.1(1)\mu$s	$Y_0 = -2.6(1) \times 10^{-4}$

Table 5.3: Fit results of the PLD data displayed in fig. 5.19. The fit was carried out with a double–exponential fit function $\frac{\Delta I_{\mathrm{ph}}}{I_{\mathrm{ph}}} = Y_0 + ae^{-\frac{\tau}{b}} + ce^{-\frac{\tau}{\tau_{\mathrm{f}}}}$.

5.4.4 Incoherence during the microwave pulse

The experimental PLD data presented so far (sections 5.4 to 5.4.3) was collected after excitation by very short pulse lengths ($\tau < 200$ns). On this time scale, no spontaneous electronic transitions or spin–relaxation processes are assumed to take place. Note that up to this point, this is only an assumption. However, a proof will be given in section 5.5. Because of these long coherence times, the PLD is assumed to be constant once the oscillation is damped by dephasing and hence, the densities of different spin pair states will not change since no pair creation and annihilation takes place. This changes when the pulse length is increased to a time scale where incoherence can not be neglected anymore as shown in fig. 5.19. The microwave pulse intensity was chosen to be weak so that the long pulse duration would not induce too strong microwave currents that diminish the SNR (explained in chapter 4). The graph shows that after the initial, a second, slower decay takes place which is due to the approach of the pair ensemble to the on–resonant steady state.

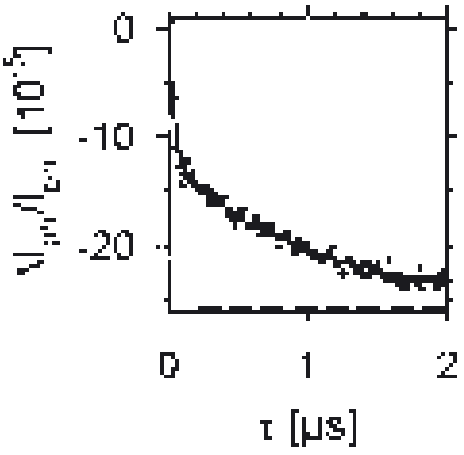

Figure 5.19: The PLD measured at the db resonance with long pulses. The solid line represents a double exponential fit whose results are plotted in tab 5.3. The dotted lines represent the two single exponential functions. (T=10K, I=200μA; laser: λ=514nm, P=575mW; microwave: $P_{\mu\mathrm{W}}$=8W (21db), ν=9.745277GHz, τ=20ns to 2μs in 20ns steps; the magnetic field corresponded to db resonance at $g \approx 2.005$; $t_{\mu\mathrm{s}}$=20μs)

The spin–pair annihilation rate of the on–resonant steady state is always higher than in the off–resonant steady state when no microwave radiation is present. This can be explained in a simple rate equation picture [65, 73]: In the presence of microwave radiation, any spin pair that is generated (no matter in which energy eigenstate) starts to precess immediately. Hence, when the pair precession is much faster then the recombination, all spin pairs have an equal lifetime, a value determined by the highest recombination probability. Consequently, the time constant contained in the second decay function of the PLD reveals the transition probability of the fastest spontaneous transition process. The data in fig. 5.19 is fit with a double exponential decay function. The fit function and results are shown in tab. 5.3. The first decay is due to the coherent dephasing of Rabi oscillation that was discussed above. Therefore, an exponential decay function for its description is actually not correct. However, since this inaccuracy does not have an impact of the fit of the second exponential decay, it is done

for simplicity, nevertheless. The fit result for the second decay reveals a time constant $\tau_{\mathrm{f}} = 1.1(1)\mu$s. This value is more than one order of magnitude faster than the processes responsible for the coherence decay obtained from electron spin echo experiments presented in section 5.1.3. Thus, the processes responsible for the electron spin echo decay have to be different than those that determine the time constant measured in the PLD. Since the Hahn–echo sequence used in section 5.1.3 reveals the spin–spin relaxation rate coefficient $\frac{1}{T_2}$, the other, faster decay constant of the PLD has to be due to an electronic transition such as recombination.

The PLD have shown how TSR experiments open access to new phenomena and information about recombination processes. The existence of dephasing Rabi–beat oscillation during the microwave interaction appears to take place and a fast spontaneous electronic transition exists in addition to the slower time constants that have already been detected in the μs–time domain of the photocurrent. The fact that the oscillating signal due to the CE centre is different than the strong fast dephasing signal at the db resonance strengthens the hypothesis that two different recombination channels exist. In spite of these new insights, the analysis, especially the quantitative analysis of the measured data has nevertheless been difficult and inaccurate. The fast dephasing diminishes the possibility to distinguish between coherent and incoherent processes. Since the origin of the dephasing is highly complex and dependent on many influences that can not be deconvoluted with the data available, echo experiments as proposed in section 3.6 are necessary. Along the way, the confirmation of the theoretical prediction of recombination echoes will be the final and conclusive proof that the interpretation of the observations presented above as coherently dephasing Rabi oscillation are correct.

5.5 The recombination echo

In order to prove the recombination echo as explained theoretically in section 3.6, a PLD transient was collected for which a 180^o phase change was introduced at a phase reversal time τ_{180^o}=200ns. The result of this experiment is depicted in the plot of fig. 5.20. It shows that before the phase change is introduced, the data resembles the fast dephasing Rabi–beat oscillation as discussed above. After the phase change, a second, fast decline takes place which has the same shape as the initial dephasing process but a clearly smaller amplitude. At $\tau = 2\tau_{180^o} = 400$ns, a temporary increase of the photocurrent can be seen — the experimental verification of the recombination echo.

According to the theoretical prediction made in sections 3.6, the step like behaviour of the photocurrent right after the dephasing strongly suggests that a large portion of the observed signal is due to a Rabi–beat oscillation of spin pairs whose partners have a narrow Larmor separation ($\omega_a - \omega_b \ll \gamma B_1$). Because of this the data was fit with the function that was simulated for this case and shown in fig. 3.15. The fit was only based on two parameters, the width of the Rabi–frequency distribution and a scaling factor for the magnitude of the fit function. Thus, all the proportionalities such as the ratio between the magnitudes of the echo intensity and the initial dephasing or the ratio between the magnitudes of the initial and the second dephasing were kept constant. The fit reveals an

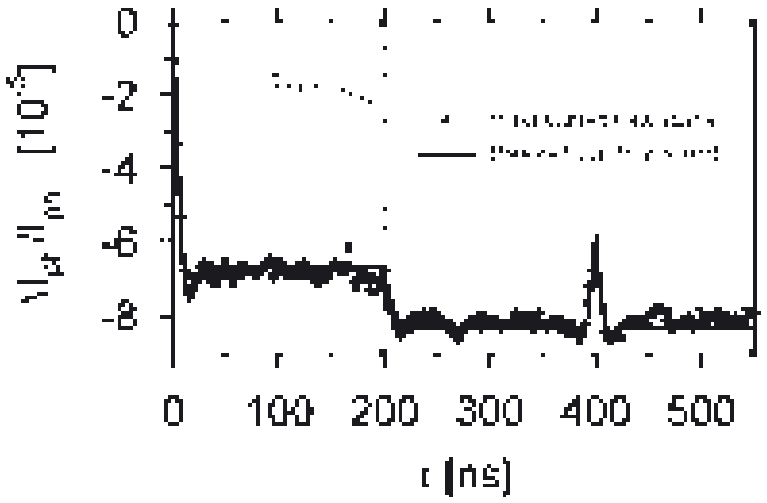

Figure 5.20: The PLD experiment on resonance with the db centre confirming the recombination echo. The microwave phase change at τ_{180°=200ns leads to a second dephasing. At $\tau = 2\tau_{180^\circ}$, a partial rephasing takes place. The solid line shows the fit with the simulated function as shown in fig. 3.15. It shows an excellent agreement with the measured data. (T=10K, I=100μA; laser: λ=514nm, P=600mW; microwave: $P_{\mu\mathrm{W}}$=100W (10db), ν=9.751972GHz, τ=2ns to 600ns in 2ns steps; $t_{\mu\mathrm{s}}$=20μs)

excellent match with the experimental data. This is strong evidence for the correctness of the theoretical approach that was taken in chapter 3.

The strong agreement of the data in fig. 5.20 with the simulation of Rabi–beat echoes of an ensemble of spin pairs with small Larmor separation confirms the assumption that the strong db contribution observed in the EDMR spectrum of fig. 5.8 is not due the CE–db recombination since the resonances of these two centres are far apart ($\omega_{\mathrm{db}} - \omega_{\mathrm{CE}} \approx 2\mathrm{mT}$) in comparison to the applied microwave field ($B_1 \approx 1\mathrm{mT}$). This confirms the hypothesis that a second spin–dependent transition is responsible for the photocurrent changes, a transition between two localised electronic pair states whit their Landé factors being very close to the db resonance at $g \approx 2.005$.

5.5.1 Dependence on microwave intensity

In order to show that the recombination echo effect displayed above is actually caused by a rephased Rabi oscillation, the microwave field–intensity dependence was investigated. Figure 5.21 shows the results obtained from a series of experiments that were performed under similar conditions as the echo experiment shown in fig. 5.20. The microwave attenuation was changed between 6db and 18db in 3db steps. The data clearly reveals how the echo width increases with decreasing microwave power as predicted theoretically. The solid lines in fig. 5.21 are the results of fits with a depasing oscillation

$$\frac{\Delta I_{\mathrm{ph}}}{I_{\mathrm{ph}}} = Y_0 + a\cos\left(\left[\tau - 2\tau_{180}\right]c\right)\exp\left(-\frac{\left[\tau - 2\tau_{180}\right]^2}{2b}\right) \tag{5.1}$$

for which a Gaussian distribution[3] of the Rabi frequencies had been assumed. Note that the minima before and after the echo indicate the dephasing of the Rabi–beat oscillation. Therefore, according to eq. 3.98 of chapter 3, the fit constant c of eq. 5.1 can be identified with the Rabi oscillation $c = 2\Omega = \frac{g\mu_B}{\hbar} B_1$ and a scaling of B_1 is possible. Figure 5.22 shows a plot containing the fit results for the oscillation frequencies obtained from the data in fig. 5.21 as a function of the B_1 field strength. The data shows an excellent agreement with the linear function that stretches through the origin. Again, the behaviour expected from a rapidly dephasing Rabi–beat oscillation is confirmed and hence, the PLD exhibits the coherent spin motion of the recombining spin pairs during a resonant microwave pulse.

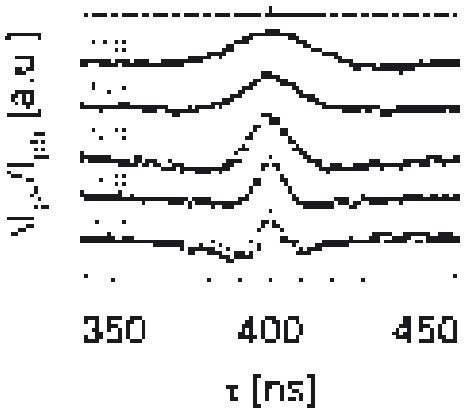

Figure 5.21: The dependence of the echo shape on the microwave intensity. With increasing attenuation, the shape of the echo broadens. A fit of the data with the dephasing oscillation as described by eq. 5.1 shows an excellent agreement with the experimental data. (T=10K, I=100μA; laser: λ=514nm, P=600mW; microwave: $P_{\mu W}$=251W (6db) to 16W (18db) in 3db steps, ν=9.751972GHz, τ=2ns to 600ns in 2ns steps; magnetic field corresponded to db resonance at g ≈2.005; $t_{\mu s}$=20μs)

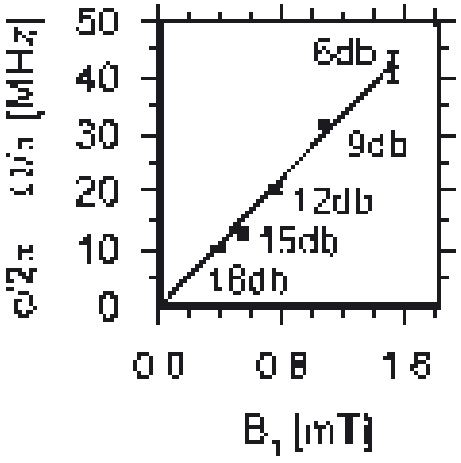

Figure 5.22: The values for the frequency obtained from fit parameter c in eq. 5.1. The solid line is a linear fit. The attenuations of the respective microwave field strength are given in the plot, and, using eq. 3.98, an absolute scaling of the B_1 field is possible.

At this point, another property of the microwave intensity dependence of the photocurrent transients as made by the theoretical calculation in chapter 3 needs to be addressed: As one can see from eq. 3.91, the magnitude of a given photocurrent transient is also proportional to the microwave field B_1. This proportionality is clearly not reproduced by the PLD at different microwave powers as displayed in figs. 5.17 and 5.21. The data exhibits a monotonous increase of the signal amplitudes with increasing microwave intensity which, however, is highly non–linear. This apparent contradiction of eq. 3.91 is due to the fact that the assumption that the microwave field B_1 is much smaller than the inhomogeneous Larmor broadening ($\partial_{\omega_L}\Phi(\omega_L)\gamma B_1 \ll \Phi(\omega_L)$) as made for the theoretical predictions is not met. As one can see from the EDMR spectrum in fig. 5.8, the db as well

[3]For simplicity, the complex influences of Larmor–frequency, B_1–field and Dipolar–coupling distributions are assumed to lead to a Gaussian distribution of the Rabi frequency Ω

as the CE resonances have a homogeneous broadening which is of the order of B_1. At attenuations below 6db, B_1 becomes even higher than the Larmor broadening.

5.5.2 Coherence decay

The experimental verification of the recombination echo has confirmed that coherent spin motion of localised charge carrier pairs is able to govern the recombination rate. This effect can be used to determine spontaneous transition probabilities such as recombination rates. Figure 5.23(a) shows a series of echo experiments which were carried out under similar conditions as in the echo experiments discussed above. The PLD was recorded in the range of ±50ns about the echo maximum at $\tau = 2\tau_{180^o}$ and the phase reversal time τ_{180^o} was varied between 150ns and 400ns. As expected, the amplitude of the echo decreases with increasing τ_{180^o} reflecting the loss of spin pairs out of the propagating ensemble due to spontaneous processes. The data set in fig. 5.23(a) was fit with eq. 5.1. The fit result for the echo amplitude (fit parameter a) is proportional to the echo intensity ΔI_{echo}, defined as the peak hight of the echo. The reference level for this amplitude was chosen far away from the time when the echo occurs. The fit results displayed in fig. 5.23(b) clearly show the decay of the echo with increasing phase reversal time. This decay was fit by a single exponential decay function. The fit result revealed a decay constant $\tau_{\mathrm{f}} = 1.2(3)\mu$s, a value that is in agreement with the decay constant f of tab. 5.3, which represented the influence of incoherent processes on the dephased PLD. However, unlike for the fit to which the values of tab. 5.3 correspond (displayed in fig. 5.19), the measurement of incoherence by means of the coherence decay has the advantage that the constant obtained is known to be the fastest transition rate that can influence the spin–pair ensemble. If any faster process were present, the rephasing could not take place.

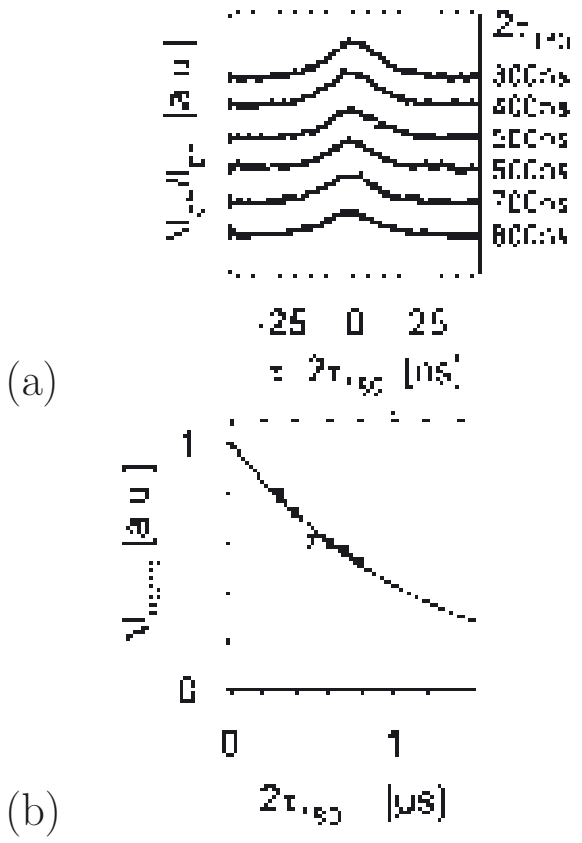

Figure 5.23: With increasing phase reversal time τ_{180^o}, the echo amplitude reduces due to the coherence decay in the spin–pair ensemble. (a) PLD plots of recombination echoes after different phase reversal times. The data sets are shifted vertically for a better visualisation. The solid lines are fits with eq. 5.1. (b) The echo intensities ΔI_{echo} obtained from the fit variable a of the fits in graph (a) as a function of $2\tau_{180}$. The process responsible for the echo decay is the fastest incoherent transition. A single exponential fit (solid line) shows excellent agreement and reveals a fast decay constant $\tau_{\mathrm{f}} = 1.2(3)\mu$s. ($T$=10K, I=200μA; laser: λ=514nm, P=600mW; microwave: $P_{\mu\mathrm{W}}$=32W (15db), ν=9.750428GHz, τ=2τ_{180}-50ns to 2τ_{180}+50ns in 2ns steps; magnetic field corresponded to db resonance at g ≈2.005; $t_{\mu\mathrm{s}}$=17μs)

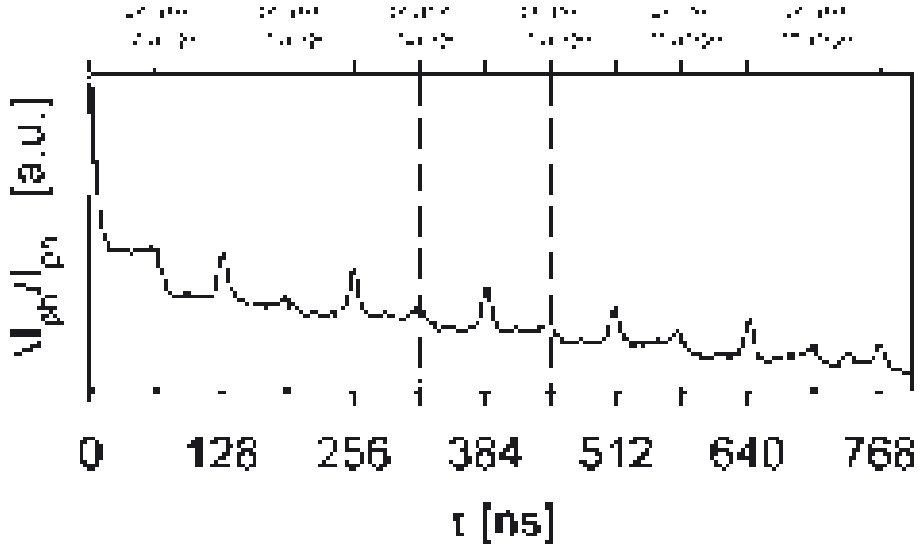

Figure 5.24: The PLD plot at the db resonance for microwave pulses with repeated phase changes indicated by the vertical dashed lines is the experimental proof for the existence of echo echoes. The coherence decay reduces the echo amplitudes with increasing lengths of the microwave pulse. Note that the dephasing after the first phase change at τ=64ns does not repeat when the other phase changes are introduced. (T=10K, I=100μA; laser: λ=514nm, P=600mW; microwave: $P_{\mu\mathrm{W}}$=126W (9db), ν=9.751972GHz, τ=2ns to 800ns in 2ns steps; $t_{\mu\mathrm{s}}$=20μs)

5.5.3 Echo echoes

Beside the single echo decay experiment, the coherence decay of the spin–pair ensemble can also be measured with echo–echo experiment. Herein, the first phase reversal that causes the rephasing and immediate dephasing is followed by a second phase change which forces the dispersed spins to move along their original direction. Hence, after a time that corresponds to the time between the first echo and the second phase reversal, a second rephasing can take place which is followed by a second recombination echo. This scheme can be repeated arbitrarily often such that a series of echo echoes is formed. Since spontaneous processes will reduce the coherence within the spin ensemble, the echo amplitudes will decrease with an increasing number of echoes that are produced. Thus, measurement of the echo–echo decay is another way to determine the time constant of transition rates. Figure 5.5.3 shows the experimental evidence of echo echoes. The experiment was carried out under similar conditions as the experiments plotted in figs. 5.20 and 5.21. Note that the dephasing after the first microwave phase change does

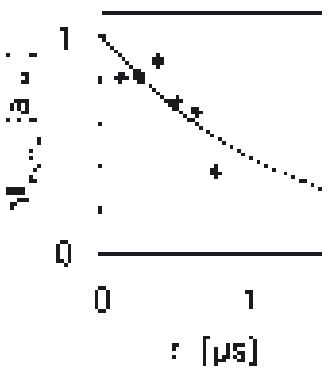

Figure 5.25: The coherence decay can also be measured from the series of echo echoes. The plot shows the intensity of the echo echoes versus the pulse length where they occur. The fit represents a single exponential decay. The decay constant is $\tau_{\mathrm{f}} = 1.3(5)\mu$s.

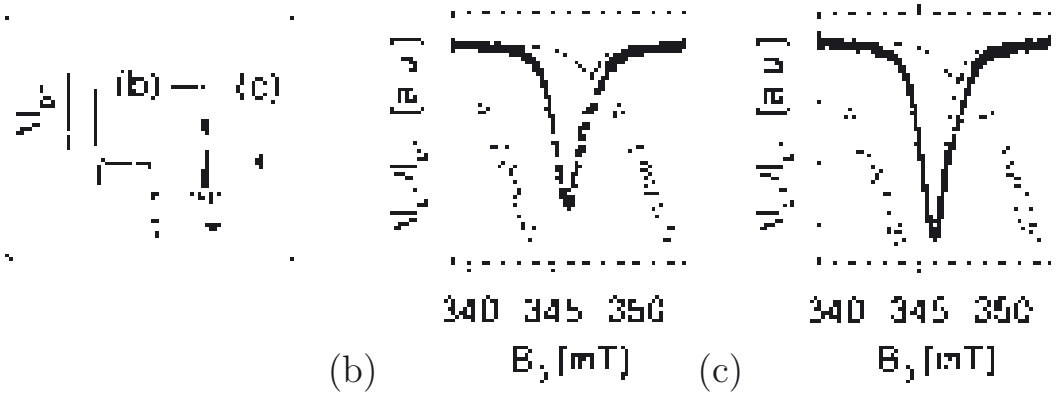

Figure 5.26: (a) Illustration of two pulse lengths τ where the PLD spectra depicted in (b) and (c) were recorded: (b) At the peak of the recombination echo and (c) after the dephasing of the signal. The arbitrary scale for the photocurrent changes is equal in both plots. The solid lines are fits of the data with two pseudo–Voigtian functions. Both plots resemble the peaks of db and CE centres. (T=10K, I=100μA; laser: λ=514nm, P=350mW; microwave: $P_{\mu\mathrm{W}}$=4W (24db), ν=9.755100GHz, τ=600ns (b) and 900ns (c), phase change at τ_{180}=300ns; 128 magnetic field steps; $t_{\mu\mathrm{s}}$=15μs)

not repeat after the following phase changes. Apparently, the signal is determined by spin pairs that can be rephased and by spin–pairs that can not be rephased. Once the latter are dephased completely (after the first phase change) no additional dephasing takes place anymore. The echo amplitudes as determined from fig. 5.5.3 are plotted in fig. 5.25 as a function of the pulse lengths where they occur.

The decrease was fit by a single exponential decay which revealed a decay constant of $\tau_{\mathrm{f}} = 1.3(5)\mu$s, a value that is in agreement with the value obtained from the coherence decay of the single echo experiment in section 5.5.2 as well as decay in the long time PLD as shown in section 5.4.4.

5.5.4 Magnetic field dependence of recombination echo

As explained in section 3.6 and illustrated in fig. 3.15, the recombination echoes from spin–pair ensembles with higher Larmor separation are significantly stronger than the recombination echoes obtained from pair ensembles with small Larmor separation such as spin pairs involving two db centres for instance. Thus, with the detection of the recombination echo in the PLD, the question arises whether the effects presented above are similar for the db and CE lines. All the echo data shown above was collected only at the dangling bond resonance at $g \approx 2.005$. Therefore, a magnetic field sweep of the echo amplitude was carried out. In order to prevent the B_1 field from swallowing the inhomogeneous broadening, a weak microwave intensity was used so that a slow Rabi dephasing and rephasing took place on a long time scale (τ_{180}=300ns, pulse length up to τ=900ns). As indicated by the sketch in fig. 5.26, the photocurrent was measured at τ=600ns, when the echo occurred, and at τ=900ns, when the ensemble was fully dephased again. The results of these two sweep experiments are displayed in plots (b) and (c) of fig. 5.26, respectively. Note that the arbitrary scale of the photocurrent was chosen to be equal for both plots. The comparison of the two data sets shows that the magnitude of lines depicted of the

first plot (b) are smaller than the magnitudes in the second plot (c) which reflects the reduction of the recombination quenching due to the rephasing of the spin–pair ensemble. The difference of both data sets represents the portion of the measured signal that changes due to the recombination echo. This difference is plotted in fig. 5.27.

All plots shown in figs. 5.26 and 5.27 were fit with a combination of two pseudo–Voigtain line shapes. As expected, they reveal the two resonances of the db ($g \approx 2.005$) and the CE centre ($g \approx 1.998$). A comparison of the fit results for the dephased TSR signal (plot (c) of fig. 5.26) and the echo sweep (fig. 5.27) revealed that the fraction q between the amplitude of the CE and the db peak may be different: While this fraction yielded a value of $q_{\mathrm{TSR}} = 0.22(1)$ for the entire signal, a value $q_{\mathrm{echo}} = 0.27(4)$ was found for the echo sweep. Unfortunately, the low SNR of the echo spectrum in fig. 5.27 does not allow a higher accuracy. However, a stronger appearance of the CE centre in the echo effect would confirm the theoretical predictions for Rabi echoes that are expected from spin pairs with strong Larmor separation such as CE–db pair for instance.

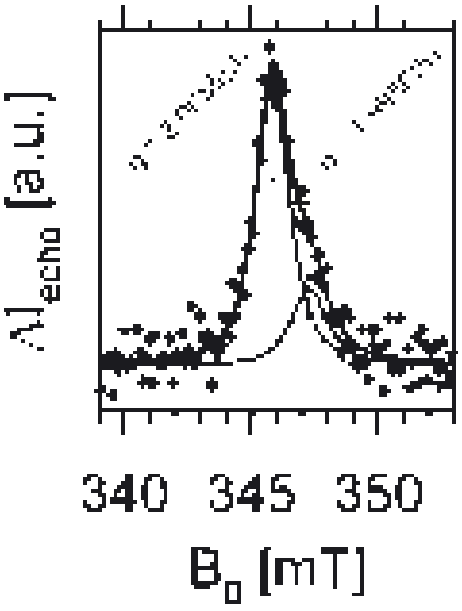

Figure 5.27: The magnetic field dependence of the recombination echo intensity as obtained from the difference of the data sets shown in fig. 5.26(b) and (c). The solid lines are fits of the data with two pseudo–Voigtian functions.

Chapter 6

Recombination properties of disordered silicon

In the previous chapters theoretical and experimental evidence has been presented for a variety of effects that can be explained by spin–dependent recombination transitions of charge carriers between localised band gap states. An experimental method was introduced that allows the detection of these ns range phenomena (PLD) as well as ways to distinguish incoherence and coherent dephasing (recombination echo). Subject of the following sections is to show how TSR measurements can be used for the investigation of electronic properties of silicon thin film materials. In principle, TSR should be applicable to all materials and devices where EDMR has been applied to in the past. Thus, the real potential of TSR will not be known until it is applied beyond the few materials and samples investigated in the course of this study.

6.1 Hydrogenated microcrystalline silicon

Hydrogenated microcrystalline silicon (μc-Si:H) was used for experiments discussed in the last chapter. In the following, these observations are discussed with regard to the material itself. As outlined in the introduction of chapter 5, conductivity, transport, and the structures of electronically active defects in μc-Si:H have been studied extensively in past [23, 67, 66, 61, 74, 68, 46]. From these studies, some open questions remained such as:

- Why do EDMR lines of CE and db centres have such different integrated peak intensities? In other words, is the stronger db intensity due to a second spin–dependent recombination path, for instance the direct capture (dc) recombination as proposed by Kanschat [46]?

- What is the paramagnetic pair partner of the db if the dc channel does exist? As explained by Kanschat, spin–dependent recombination that causes signal intensities as observed has come from intermediate pair formation. When a direct capture of conduction electrons takes place, what are the intermediate pairs?

- Are the recombination channels observed by EDMR and TSR really dominant recombination channels? Do the small relative recombination changes induced by ESR (maximum 10^{-4}) not indicate that stronger recombination channels exist which are not spin dependent?

- What are the spin–spin interactions within the paramagnetic defects centres? Do they have much influence on the recombination rate?

- Does the assumption that spin–orbit coupling is negligible in c-Si [75] imply the same for μc-Si:H? If not, how strong is singlet and triplet recombination?

- What are the recombination probability and the recombination cross section of the db centre?

- Does the dissociation of the charge carrier pairs play a role?

In the following, the TSR data presented in chapter 5 as well as the light- and temperature dependence of the time constants detected within the observed photocurrent transients are discussed with regard to these questions.

6.1.1 Triplet recombination and spin–spin coupling

The experimental data presented in fig. 5.13 of section 5.3 showed that processes are involved in the spin–dependent recombination through the db centre with time constants τ_{m} (medium) and τ_{s} (slow) that are in the range of $10^3\mathrm{s}^{-1}$ to $10^4\mathrm{s}^{-1}$. The qualitative agreement of this data with the simulated TSR transients displayed in fig. 3.6 of section 3.4.3 confirms the assumptions of non–negligible triplet recombination and strong spin–spin coupling under which the simulation was made. The model of section 3.4.3, illustrated in fig. 3.4, actually predicts a triple exponential decay constant with three different decay constants (see eq. 3.56) τ_{s}, τ_{m} and τ_{f} that dependent on the three recombination probabilities r_T, r_2 and r_3, the spin–spin relaxation time T_2 and the pair–dissociation probability d. The fastest time constant τ_{f} could not be confirmed in the TSR transients as expected from the model prediction. It could be detected from PLD measurements as discussed in section 5.4.4. Its value is about two orders of magnitude faster than the two slower processes, which is a hint for very strong spin–spin coupling. Section 3.4 explains, how the three time constants are dependent on as many as five completely different types of electronic transitions such as the three recombination probabilities r_T, r_2 and r_3 as well as the pair dissociation d and the transverse spin relaxation T_2^{-1}. Thus, the determination of the five transition rates by means of the three time constants measured is complicated and only possible by careful consideration of the different properties of the transitions that are involved. Note that there must not be three different recombination times of spin pairs in any case: When spin–spin interaction is very weak or very strong and triplet recombination is non–negligible or when triplet recombination is negligible and spin–spin interaction strong[1], only two recombination probabilities can exist. This circumstance, a

[1] $\hbar\omega_\Delta < J + D^d$ but J, D^d small enough so that a spin–dependent signal does not vanish completely

consequence of the model presented in section 3.4, makes the interpretation of the observed time constant even more difficult.

Thus, while the constants τ_{m} and τ_{s} are clearly due to recombination from two different spin–pair eigenstates, the origin of constant τ_{f} has to be confirmed by additional information. The pair dissociation constant d as well as the transverse relaxation coefficient T_2^{-1} are both due to processes which do not contribute to the recombination but to the incoherence of the spin–pair ensemble. Thus, if τ_{f} were due to any of these processes, the densities of at least two different spin eigenstates would by equalised on the time scale of τ_{f} and on the time scales of τ_{m} and τ_{s}, no signal would be detectable. Therefore, the fastest source of incoherence, the τ_{f} process, must be due to a third recombination time, the recombination from a spin–pair state with the highest singlet content. This implies that three distinct recombination times for the spin pairs exist. Moreover, it can also be concluded that the remaining incoherence sources, T_2 relaxation and pair dissociation d, have to be in the time range of τ_{m} and τ_{s} or slower. In summary, one can conclude for the spin–dependent recombination channel through db-centres:

- The model of recombination from spin pairs outlined in chapters 2 and 3 describe the observed TSR transients accurately.
- The triplet recombination r_T of the spin pairs is not negligible.
- The sum of the spin–dipolar as well as the spin–exchange coupling ($J + D^d$) is strong in comparison to the Larmor separation of the spin pairs but weak enough so that a photocurrent signal is still detectable.
- The recombination channel consists of three different, distinct recombination processes due to the recombination from pure triplet ($|T+\rangle$, $|T-\rangle$) states, and from the states $|2\rangle$ and $|3\rangle$, as defined in chapter 3.
- The TSR transients are determined by three time constants τ_{f}, τ_{m} and τ_{s} which correspond to the definitions made for the eigenvalues in eq. 3.56.
- Since it was found experimentally that $\tau_{\mathrm{f}}^{-1} \gg \tau_{\mathrm{m}}^{-1}, \tau_{\mathrm{s}}^{-1}, T_2^{-1}$, one can identified τ_{f}^{-1} with r_3 directly, according to eq. 3.60. For a laser illumination of P=300mW and a temperature of T=40K (the conditions under which the data in fig. 5.13 was recorded), this leads to $r_3 = 8.4(2) \times 10^5 \mathrm{s}^{-1}$.

With this insight, the question remains whether the contributions by T_2 and d are weak enough so that the time constants τ_{m}^{-1} and τ_{s}^{-1} can be identified with r_2 and r_T. Now, four unknown parameters dependent on two experimentally known values which appears to be insufficient for their determination. For the solution of this problem, one has to refer to the additional data provided by the prefactors of the multiexponential function given in eq. 3.60. The latter depend on some of the rate coefficients that determine the exponential decays and thus, enough information is available to obtain estimates for the constants d and T_2. In the following, this is done for the TSR transient displayed in fig. 5.13 whose data was fit by a biexponential decay as outlined in tab. 5.2.

First, an estimate is given for the strength of the spin–spin interactions which means the ratio $\frac{J+D^d}{\hbar\omega_\Delta}$. From eq. 3.60 we can conclude that

$$\tau_{\mathrm{m}}^{-1} = \frac{r_2}{2} + d + \frac{1}{T_2} > \frac{r_2}{2} \tag{6.1}$$

and similarly, one can conclude that

$$\tau_{\mathrm{s}}^{-1} = r_T + d > r_T. \tag{6.2}$$

From these equations and together with the fact that $r_3 = \tau_{\mathrm{f}}^{-1}$, one can estimate $\frac{J+D^d}{\hbar\omega_\Delta}$ from eq. 3.16. Therein, the subtraction of the equation in line 2 from the equation in line 3 leads to an expression

$$\frac{J + D^d}{\hbar\omega_\Delta} = \frac{r_3 - r_2}{r_S - r_T} > \frac{\tau_{\mathrm{f}}^{-1} - 2\tau_{\mathrm{m}}^{-1}}{r_S - r_T} \tag{6.3}$$

whereas their addition leads to

$$r_S - r_T = r_2 + r_3 - 2r_T = \tau_{\mathrm{f}}^{-1} + 2\tau_{\mathrm{m}}^{-1} - 2d - 2T_2^{-1} - 2\tau_{\mathrm{s}}^{-1} + 2d < \tau_{\mathrm{f}}^{-1} + 2\left[\tau_{\mathrm{m}}^{-1} - \tau_{\mathrm{s}}^{-1}\right]. \tag{6.4}$$

From eq. 6.4 and the values obtained from the fit, a range for the coupling strength

$$1 \geq \frac{J + D^d}{\hbar\omega_\Delta} > 0.93(3) \tag{6.5}$$

can be determined. This shows that the db signal originates from spin pairs with strong spin–spin interactions. This result is an important realisation: As explained in section 3.5.1, under strong spin–spin coupling, the signal has to be due to a change of the $|T+\rangle$ and $|T-\rangle$ densities towards the $|2\rangle \approx |T_o\rangle$ density while the $|3\rangle \approx |S\rangle$ density does not change. Therefore, the signal is solely due to a change of the triplet recombination. Since triplet recombination is weak, the net change of the photocurrent is small even though the changed recombination channel may be dominant. From the estimate of $\frac{J+D^d}{\hbar\omega_\Delta}$, an estimate of the pure singlet recombination rate r_S can be made. From eq. 3.16 and the knowledge that $r_T < \tau_{\mathrm{s}}^{-1} \ll r_3 < r_S$, the singlet recombination rate is

$$r_S \approx r_3 \frac{2}{1 + \frac{J+D^d}{\hbar\omega_\Delta}} \tag{6.6}$$

and hence can be estimated to lie in the range

$$r_3 = 8.4(2) \times 10^5 \mathrm{s}^{-1} < r_S < 8.7(3) \times 10^5 \mathrm{s}^{-1}. \tag{6.7}$$

The weak influence of the singlet recombination on the measured signal can also be seen from eq. 3.60. With the value for $\frac{J+D^d}{\hbar\omega_\Delta}$ given, the last exponential function in eq. 6.5 becomes smaller than the detection limit and the measured photocurrent transient is only a biexponential decay function whose decay constants τ_{m} and τ_{s} are determined by eqs. 6.1 and 6.2 respectively while the prefactors are

$$a_2 = \left(\frac{r_2\mu_{\mathrm{h}}}{d\mu_{\mathrm{e}}} - 1\right) \qquad \text{and} \qquad a_3 = \left(\frac{r_T\mu_{\mathrm{h}}}{d\mu_{\mathrm{e}}} - 1\right). \tag{6.8}$$

Thus, the overall recombination rate, which is dominated by the large singlet recombination, is only weakly changed under ESR influence since most of the recombination changes are due to changes of the weak triplet recombination rates. Equation 6.8 can be used to estimate d and T_2. Therein, the ratio of the macroscopic hole and electron mobility is required to be known. Finding a value for this fraction appears to be difficult since standard measurement techniques such as Hall-effect measurements or time of flight measurements are either complicated and can not be applied to a TSR sample for technical reasons or they reveal values for majority charge carriers only. A comparison with literature values [76, 77, 78] shows that both electron and hole mobilities of μc-Si:H are spread across a wide range depending on the material, doping and the temperature. However, in the various sets of literature values available, the ratio $\frac{\mu_\mathrm{h}}{\mu_\mathrm{e}}$ never exceeds 0.5, which is therefore assumed as an upper limit. This turns out to be a sufficient constraint for a reasonable estimate of the spin–spin relaxation time T_2 as well as the dissociation probability d. From eqs. 6.8, 6.1 and 6.2, one can deduce the equation

$$d = \frac{\frac{\mu_\mathrm{h}}{\mu_\mathrm{e}}}{a_2 - a_3 + \frac{\mu_\mathrm{h}}{\mu_\mathrm{e}}} \left(2\tau_\mathrm{m}^{-1} - \tau_\mathrm{s}^{-1} - \frac{1}{T_2} \right) \tag{6.9}$$

from which an upper limit of d can be estimated. Considering that T_2 is limited by T_1 ($\frac{1}{T_2} > \frac{1}{T_1} > 10^3\mathrm{s}^{-1}$, see ref. [61]) and that $\frac{\mu_\mathrm{h}}{\mu_\mathrm{e}} < \frac{1}{2}$, we find

$$d < 1.2(2) \times 10^3\mathrm{s}^{-1} \tag{6.10}$$

for the fit data given in tab. 5.2. Note that the real value of d will probably be much smaller since the assumption on $\frac{\mu_\mathrm{h}}{\mu_\mathrm{e}}$ has been quite conservative. Thus, the pair dissociation probability d has only a weak impact on the measured time constants and hence, the narrow range

$$5.1(1) \times 10^3\mathrm{s}^{-1} = \tau_\mathrm{s}^{-1} > r_T > 3.9(2) \times 10^3\mathrm{s}^{-1} \tag{6.11}$$

for the value of r_T is yielded. Finally, an estimate for T_2 and r_2 has to be made which can be obtained from eqs. 6.8, 6.1 and 6.2 in a similar way. This leads to

$$\frac{1}{T_2} = \tau_\mathrm{m}^{-1} - \frac{a_2 + 1}{a_3 + 1}\frac{\tau_\mathrm{s}^{-1}}{2} + d\left[\frac{1}{2}\frac{a_2 + 1}{a_3 + 1} - 1\right] \tag{6.12}$$

that reveals under consideration of eq. 6.10 a range

$$7.8(2) \times 10^3\mathrm{s}^{-1} < \frac{1}{T_2} < 10.5(2) \times 10^3\mathrm{s}^{-1} \tag{6.13}$$

and therefore a range of 90μs to 130μs for the spin–spin relaxation time T_2. This result confirms the estimates made about T_2 from the spin echo decay measurements presented in section 5.1.3. It also allows the identification of τ_m^{-1} and r_2 since $\tau_\mathrm{m}^{-1} \approx \frac{r_2}{2} + T_2^{-1}$ under neglect of d. This leads to an estimate

$$20(4) \times 10^3\mathrm{s}^{-1} < r_2 < 15(4) \times 10^3\mathrm{s}^{-1} \tag{6.14}$$

for the recombination probability from state $|2\rangle$. This again confirms strong spin–spin coupling as well as the assumption that spin–spin relaxation and r_2 lie in the same time

spin–spin relaxation probability:	$7.8(2) \times 10^3\mathrm{s}^{-1} < \frac{1}{T_2} < 10.5(2) \times 10^3\mathrm{s}^{-1}$
relative coupling strength:	$1 \geq \frac{J+D^d}{\hbar\omega_\Delta} > 0.93(3)$
pair–dissociation probability:	$d < 1.2(2) \times 10^3\mathrm{s}^{-1}$
$\|T+\rangle$, $\|T-\rangle$–recombination probability:	$5.1(1) \times 10^3\mathrm{s}^{-1} > r_T > 3.9(2) \times 10^3\mathrm{s}^{-1}$
$\|2\rangle$–recombination probability:	$20(4) \times 10^3\mathrm{s}^{-1} < r_2 < 15(4) \times 10^3\mathrm{s}^{-1}$
$\|3\rangle$–recombination probability:	$r_3 = 8.4(2) \times 10^5\mathrm{s}^{-1}$

Table 6.1: Estimates for time constants from signals detected at $g \approx 2.005$ (db resonance) in μc-Si:H at T=40K and laser irradiation of P=300mW, λ=514nm.

range, which was made for the derivation of eq. 3.60 in the example of section 3.4.3. In conclusion, the quantitative interpretation of the photocurrent transients as recorded for fig. 5.13 can be summarised:

- An estimate for the relative strength of the spin–spin interactions of the spin pairs was possible. It reveals that strong spin–spin interactions are present which could be indicative of small Larmor separation. Because of this, the recombination change under ESR excitation is mostly due to triplet transitions.

- An upper limit for the pair dissociation probability d could be obtained. The low value makes it questionable whether tunnel processes between trap states are responsible for the pair dissociation.

- Estimates for the three recombination probabilities, the pure singlet recombination probability as well as for the spin–spin relaxation time could be obtained.

A summarisation of these value is given in table 6.1.

6.1.2 Temperature and light dependence of time constants

In the last section is was shown that the data of ESR excited photocurrent transients provides enough information for the determination of recombination probabilities, spin–spin interaction, spin–spin relaxation, and pair dissociation. In the following, the temperature and light–intensity dependencies of the three time constants τ_f, τ_m and τ_s are discussed which will lead to additional insight about the nature of the recombination channels that are involved in the detected signal. Most importantly, statements about the dominance of the recombination paths involved in the observed signals for the net recombination rate will be possible. Note that a qualitative interpretation of the light–intensity and temperature dependencies of the observed time constants is possible even without a quantitative deconvolution of the three experimental values into the five time constants that describe TSR transients. Common for all data points obtained is that the dissociation constant d has such little impact that the slowest time constant τ_s^{-1} can be identified with the triplet recombination probability and that τ_m^{-1} represents the average of the spin–spin relaxation rate T_2^{-1} and the recombination coefficient r_2. The high recombination probability r_3 is

represented by the fast time constant τ_{f}^{-1}, which is very close to the value of the pure singlet recombination probability r_S due to the high spin–spin interaction.

The temperature dependence of the photocurrent transients measured at a fixed laser intensity and the three time constants τ_{s}^{-1}, τ_{m}^{-1} and τ_{f}^{-1} that were extracted from these plots by means of a fit and the PLD transients, respectively, are displayed in figs 6.1(a) to (d). The time constant τ_{f}^{-1} of the pulse lengths dependence turned out to be completely temperature independent in the measured temperature range. A temperature independence can also be seen for the slower time constants τ_{m}^{-1} and τ_{s}^{-1}, but only in the low temperatures range. Beyond T=50K, a sharp increase of these constants takes place.

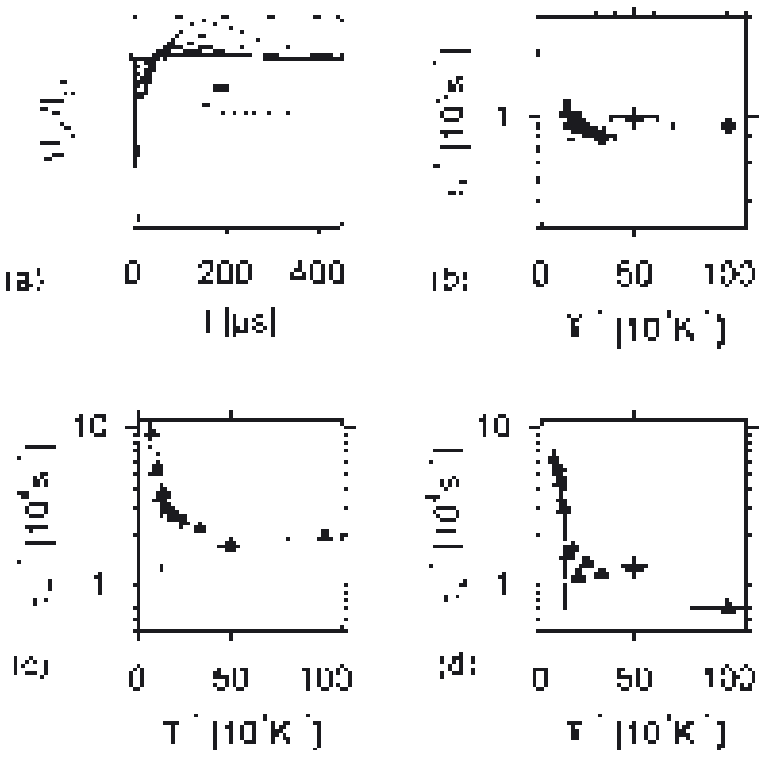

Figure 6.1: (a) Photocurrent transients measured a g ≈2.005 at various temperatures show that the recombination processes become faster with increasing temperature. The results of the double exponential fit are plotted for the decay times τ_{m} (c) and τ_{s} (d) as a function of T^{-1}. The constant τ_{f} determined from the PLD data exhibits no temperature dependence (b). (T=10K to 80K in 10K steps, 100K, 140K, I=20μA, 50μA, 100μA, 200μA, 1mA; laser: λ=514nm, P=300mW; microwave: $P_{\mu\mathrm{W}}$=8W (21db), ν=9.746947GHz, τ=320ns

The temperature dependencies of the three time constants can be discussed for the two temperature regions in which the slow time constants show a qualitatively different behaviour: These time constants are unaffected by temperature increases up to the point where spin–lattice relaxation processes become relevant. The influence of the spin–lattice or spin–phonon relaxation had not been treated explicitly in the theoretical considerations of chapter 3 since the spin lattice relaxation time T_1 was considered long and therefore negligible for most of the experiments. For the discussion of the high temperature measurements of fig. 6.1, this is not the case anymore [61]. Since spin–lattice relaxation is due to scattering of phonon and spin states, an exchange of energy is possible which means, T_1 processes equalise the densities of all four spin pair eigenstates. When spin–lattice relaxation becomes faster than any of the slow recombination times τ_{m} and τ_{s}, the decay of the TSR transient is determined by τ_{m} only. The temperature dependence of the T_1 of db and CE centres in μc-Si:H has been studied extensively by Zhou et al. [61] who showed that T_1 times of db centres follow a T^{-4} power law, which passes the 100μs limit at temperatures beyond T=50K. Now, T_1 becomes shorter than the two recombination

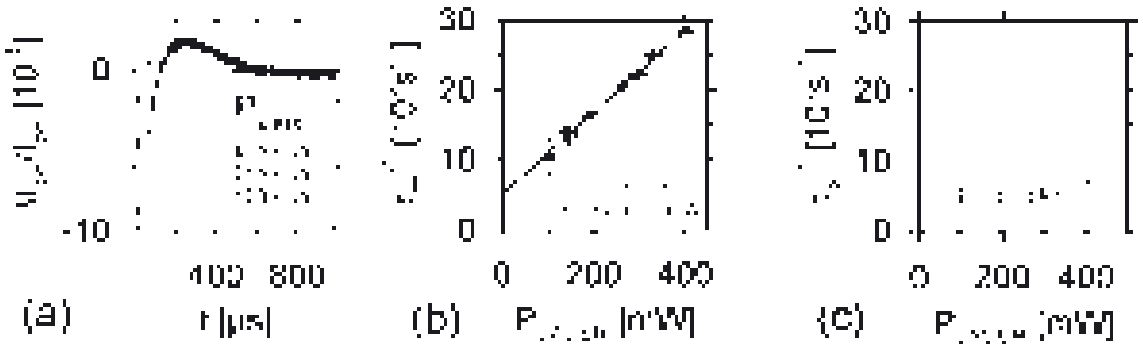

Figure 6.2: (a) TSR transients measured at $g \approx 2.005$ at different laser intensities. Biexponential fits were carried out as shown in fig. 5.13. The fit results for τ_{m}^{-1} (b) shows a linear increase with the light intensity while τ_{s}^{-1} (c) displays a light intensity independence. (T=10K, I=2μA, 5μA, 10μA, 10μA, 20μA, 20μA, 50μA; laser: λ=514nm, P=103mW, 142mW, 190mW, 265mW, 295mW, 330mW, 405mW; microwave: $P_{\mu\mathrm{W}}$=8W (21db), ν=9.745277GHz, τ=320ns)

probabilities r_T and r_2 and τ_{m}^{-1} and τ_{s}^{-1} are determined dominantly by T_1 processes leading to the strong increase with increasing temperature. In this temperature range, the ESR based T_1 measurements by Zhou et al. [61] are confirmed by the two constants τ_{m} and τ_{s} which approach each other with increasing temperature. While $\frac{\tau_{\mathrm{s}}}{\tau_{\mathrm{m}}} \approx 4$ at T=5K, this fraction decreases to 1.3 at T=100K. Moreover, note that the fast time constant τ_{f} remains unchanged throughout the measured temperature range. Since τ_{f} is about two orders of magnitude smaller than τ_{m} and τ_{s}, the spin–lattice relaxation does not exceed τ_{f} in the scanned temperature range.

With the realisation that the recombination probabilities are temperature independent at low temperatures, no new insight has been gained about the question whether the observed db transition is of distant–pair nature or a direct capture (dc) process. In both cases, a temperature independence would be expected for the low temperature range. Thus, for a distinction of the two cases, a light–intensity and therefore charge–carrier generation–rate dependence is necessary. While tunnelling processes are expected to become exponentially faster when more excess charge carriers are present and therefore the average distances are smaller [72, 79], a dc process would not change the transition probability or only within a narrow range.

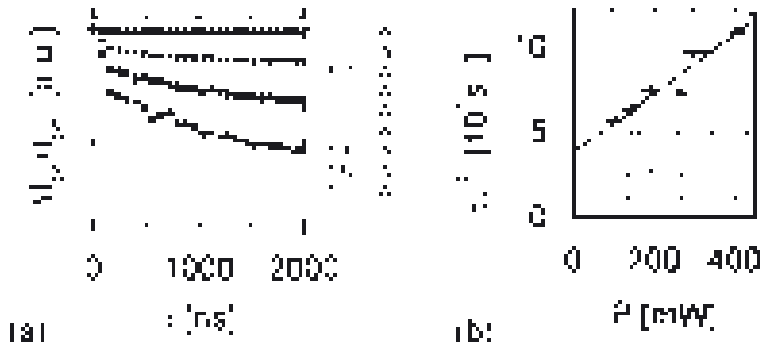

Figure 6.3: (a) The PLD transients after long (μs-range) microwave pulses measured at different light intensities. (b) The fit results for the τ_{f}^{-1} reveal a proportionality to the light intensity. The measurement was performed under the same conditions as the TSR transients shown in fig. 6.2.

Figure 6.2(a) displays a series of TSR transients recorded at different light intensities but equal conditions otherwise. All transients were fit by biexponential decay functions. The light–intensity dependence of the fit parameters τ_{m} and τ_{s} are plotted in fig. 6.2(b) and (c), respectively. The plots reveal that while the slow process τ_{s} displays the light–intensity independence, the faster process τ_{m}^{-1} exhibits a proportionality to the light intensity. This is quite unexpected for a tunnelling process. However, it is not in contradiction to a db direct capture process. The PLD measurements made for the determination of the time constant τ_{f} are displayed in fig. 6.3(a). The data points therein where obtained under identical conditions as the data shown in fig. 6.2. The fit results for the decay constant of the single exponential fit are plotted versus the applied laser intensity in fig. 6.3(b). Even though τ_{f}^{-1} is about two orders of magnitude larger than τ_{m}^{-1} a similar proportional behaviour can be seen. As one can see from the fit results that are plotted in fig. 6.3(b) and 6.2(a), both τ_{f}^{-1} and τ_{m}^{-1} are not only proportional, they also have a constant offset.

For an understanding of the linear light–intensity dependence, it is helpful to consider the charge carrier recombination rate induced by the laser light

$$G_{\mathrm{eh}} = \frac{P\lambda\epsilon}{hcA_{\mathrm{l}}f_{\mathrm{th}}}\left(1 - e^{f_{\mathrm{th}}\alpha}\right) \tag{6.15}$$

which depends on the area of the laser spot on the sample A_{l}=0.042(7)cm^2, the fraction $\epsilon = 0.5$ of light shielded by the cavity window[2], the wave length λ=514nm, the film thickness f_{th}=2.7×10^{-4}cm and the absorption of μc-Si:H, whose value depends on the material and is reported in the literature to lie in a range of α=5×10^3 to 5×10^4cm^{-1} for the given wavelength [80]. Thus, an estimate for the generation rate $G_{\mathrm{eh}} = \xi P$ is possible with a proportionality factor

$$6 \times 10^{22}\mathrm{cm}^{-3}\mathrm{s}^{-1}\mathrm{W}^{-1} \leq \xi \leq 12 \times 10^{22}\mathrm{cm}^{-3}\mathrm{s}^{-1}\mathrm{W}^{-1}. \tag{6.16}$$

The linear dependence of the generation rate on the illumination power raises the question whether the proportionality of the recombination probabilities $\tau_{\mathrm{f}}^{-1} = r_3$ and $\tau_{\mathrm{m}}^{-1} = r_3/2 - T_2^{-1}$ are related to the generation rate. As shown in fig. 6.3(b), the light intensity dependence of these time constants can be fit accurately with linear functions

$$\tau_{\mathrm{f}}^{-1} = \xi_{11} + \xi_{12}P \qquad \text{and} \qquad \tau_{\mathrm{m}}^{-1} = \xi_{21} + \xi_{22}P \tag{6.17}$$

with $\xi_{11} = 3.8(6) \times 10^5 s^{-1}$, $\xi_{12} = 1.7(2) \times 10^6 s^{-1}W^{-1}$, $\xi_{21} = 5.0(5) \times 10^3 s^{-1}$ and $\xi_{22} = 5.9(2) \times 10^4 s^{-1}W^{-1}$. TSR experiments are always carried out under steady state conditions, which implies that the net recombination rate R of the semiconductor sample is equal to the charge carrier generation rate G_{eh}. Thus, with the recombination rate of charge carriers given, a striking realisation can be made: For high light intensities, the product

$$n_{\mathrm{db}}r_3 = n_{\mathrm{db}}\left(\xi_{11} + \xi_{12}P\right) \approx \xi P = G_{\mathrm{eh}} \tag{6.18}$$

of the fast recombination probability $r_3 = \tau_{\mathrm{f}}^{-1}$ with the density of db centres $n_{\mathrm{db}} = 5(3) \times 10^{16} cm^{-3}$ as known from ESR measurements reported in section 5.1.3, is within

[2]the cavity window consists of an array of metal bars with distances below the wavelength of the microwave radiation that shield half of the window area

the error range of the fit variables in agreement with the recombination rate. At low light intensities, this agreement does not hold due to the presence of the constant offset ξ_{11}. In other words, if, at high generation rates, all the db centres present in the material are in a pair state with a charge carrier, almost the entire recombination takes place through db centres. However, this implies that when a change of the laser intensity and therefore of the generation and the recombination rates takes place, the recombination probability of the process observed by TSR has to change since the number of db centres n_{db} is a fixed constant. At low generation rates, the recombination probability r_3 remains constant, since not all db centres are charged with electrons anymore and generation changes change the db occupancy only.

This assumption, which would explain the proportionality between the laser power and the time constants τ_{f} and τ_{m}, can by verified by the following arguments: When dissociation of spin pairs is small (as it was shown above) and the observed db process is a dominant recombination path, the generation rate of spin pairs corresponds to the recombination rate under steady state conditions and thus, to the charge–carrier pair–generation rate ($g_{\mathrm{i}} \approx G$). In this case, the densities

$$\rho_{22,33} = \frac{g_{2,3}}{4\tau_{\mathrm{m,f}}^{-1}} \tag{6.19}$$

of the different spin pair eigenstates ρ_{ii} can be calculated for the off resonant steady state according to eq. 3.55 that was derived in section 3.4.2. Figure 6.4 shows the product $G_{\mathrm{eh}}\tau_{\mathrm{f}}$ as a function of the laser power, which according to eq. 6.19 corresponds to $\frac{\rho_{33}}{4}$. The plot shows that ρ_{33} is close to the density of db centres in the measured intensity range. With increasing laser power more dangling bonds are charged with a second electron. However, since ρ_{33} is limited by the absolute number of db centres present in μc-Si:H, it can grow with increasing laser light intensity only until up to the db density n_{db}. Once the generation rate exceeds the product $n_{\mathrm{db}}r_3$, the recombination rate can only follow the generation rate when the recombination probabilities r_i increase. The observation displayed in fig. 6.4 strongly suggests that the db line observed by EDMR and TSR originates from a dominant recombination process. This is also confirmed by the fact that the overall lifetime of charge carriers in μc-Si:H is found in the literature [81, 82, 83] to be similar to the fast time constant τ_{f}.

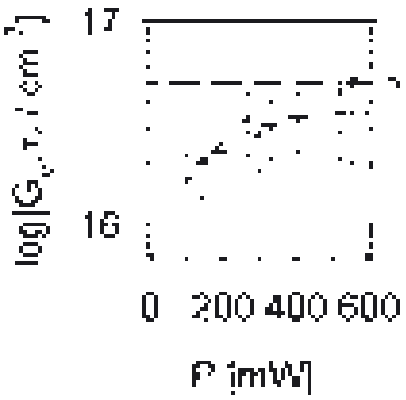

Figure 6.4: The light–intensity dependence of the product $G_{\mathrm{eh}}\tau_{\mathrm{f}}$ which corresponds to the number of db centres occupied with two electrons. The dashed line indicates the db density n_{db} of the sample. The solid line is a guide to the eye.

In conclusion, the results of the light–intensity and temperature–dependence measurements of the various time constants can be summarised as followed:

- Under the given experimental conditions, recombination at dangling bonds are the dominating recombination processes in hydrogenated microcrystalline silicon.
- The recombination probability at db centres is at high charge–carrier generation rates

(high light intensity) determined by the generation rates. Thus, a linear dependence between the generation and recombination probabilities exists.

- The recombination probabilities r_T of the non–dominant recombination probabilities (Triplet recombination) are not affected by this effect: They remain constant at any light intensity.
- There is no T dependence of the three recombination probabilities at low temperatures.
- At higher temperatures, the TSR transients are dominated by spin–lattice relaxation.

6.1.3 Trap–dangling bond recombination versus direct capture

With the new information obtained by TSR experiments, the question about the qualitative properties for the dominant recombination process in μc-Si:H can be discussed. It has been shown that the recombination processes connected to the ESR resonance at $g \approx 2.005$ are the life time determining transitions. Thus, the question that remains is whether this process is due to a tunnelling transition with a yet unidentified spin pair partner or a direct capture process. direct capture path (db–dc) that was described by Peter Kanschat [46]. Figure 6.5 contains a sketch that illustrates the qualitative features of the two different recombination mechanisms on the energy diagram in the region of the μc-Si:H band gap. Here the tunnelling mechanism is explained on the example of the well known CE–db process. As depicted, both recombination channels are due to spin–dependent transitions between localised band gap states, which makes the description of spin–dependent recombination as outlined in the chapters 3 and 2 applicable.

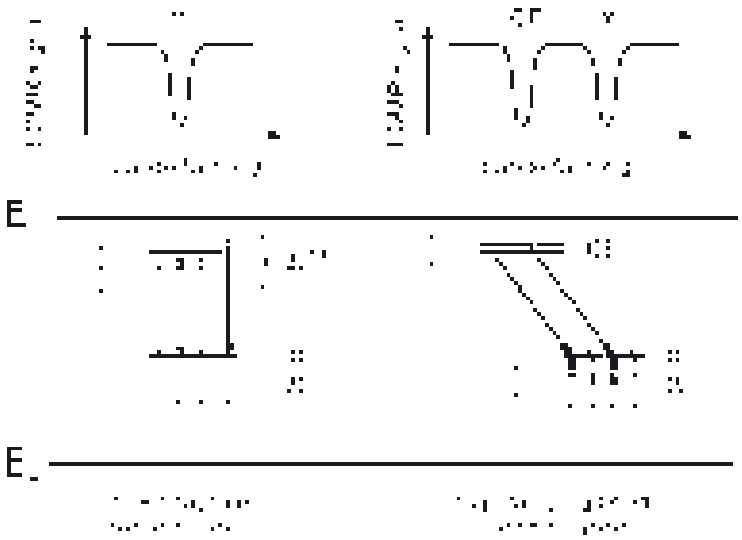

Figure 6.5: Sketch of a direct capture process (left) through dangling bonds and a tunnelling transition between the shallow trap state (CE) and dbs (right) in μc-Si:H. In addition, the expected cw EDMR spectra are depicted for both cases.

The transitions on the left hand side in fig. 6.5 illustrate the dc process at the db resonance. Therein, a charge carrier pair is formed between the electron contained in the paramagnetic db state and a second electron from the conduction band or a localised conduction tail state with an energy close to the conduction band. The conduction electron becomes localised in an excited charged db state (db^{-*}), which, unlike the db^- ground

state does not necessarily form a singlet spin pair with the second electron. When the charged, excited db state is sufficiently close to the conduction band, a dissociation of the spin pair can take place or a transition of the db^{-*} pair into a db^{-} ground state. The latter can only take place under spin conservation. It is this, what makes the entire recombination path spin–dependent. Once the electron pair is in the deep ground state, no emission of one electron into the conduction band is possible anymore and the db^{-} will be discharged by recombination with a hole. Note that the localisation of the two electrons in the db–dc model can be identical and that the wave functions of both electrons can also have similar shapes (e.g. 1s and 2s orbital if these states have hydrogenic character). Therefore, a very small g factor separation is possible which would cause a strong spin–spin coupling within the existing spin pairs. Important for the understanding that there is only one resonance in the EDMR and TSR spectrum is the fact that the strong spin–spin coupling give the spin pair a behaviour of a spin S=1 particle with one single Landé factor at $g \approx 2.005$. The right hand side of fig. 6.5 illustrates the qualitative nature of the CE–db process: Here, the spin–dependent transition is a distant pair tunnel process that takes place between a localised CE centre whose energy is close to the conduction band and a deep db centre. Since both defects stem from a well distinguishable environment and are localised at different places, distinct g factors and a weak spin–spin coupling exist.

Many data sets and plots obtained from the measurements presented in chapters 5 and 6 have already been discussed with regard to indications for the dominance of the dc process observed at the db resonance. The following list summarises briefly the arguments coming from these observations:

- The resonance at $g \approx$2.005 is much stronger than the resonance at $g \approx$1.998. Thus, when the resonances of CE and db centres correspond to the CE–db path equally, a second spin–dependent recombination process must existent whose spin pairs involve db centres but not CE centres.

- The PLD measurement reveals recombination–echo transients whose echo intensity as well as the presence of a second dephasing right after the phase change indicate that spin–pairs with a Larmor separation smaller than the B_1 field strength exist. Thus, the recombination of pairs takes place whose partners have both Landé-factors of $g \approx$2.005.

- The photocurrent transients exhibit three spin–dependent recombination probabilities, whose values are indicative of strong spin–spin coupling leading to a single resonance

- The time constants of the three exponential decay processes are independent of the magnetic field which means, there is hardly any distribution of the recombination times within the ensemble of existing spin pairs. This observation is hardly reconcilable with the large distribution of recombination probabilities that is expected from distant pair processes such as the CE–db step. However, it is not in contradiction to recombination through excited and charged db states.

- The light–intensity and temperature dependencies of the recombination probabilities are in contradiction with distant pair recombination. With increasing light irradi-

ation, the inter pair distance should decrease and the recombination probabilities therefore strongly (and highly non–linearly) increase.

- The transition probabilities of distant pair transitions should be distributed broadly. However, the measured time constants are distributed narrowly.

The facts listed above are compelling evidence that the dominant recombination paths of μc-Si:H is due to a dc process at db centres. However, this does not imply that the CE–db process is non–existent. The most compelling proof for the existence of this path has already been given by Peter Kanschat who showed that the CE and db resonance have identical integrated peak intensities in ODMR spectra. Moreover, the TSR measurements carried out in the course of this study have contributed additional evidence for the existence of this second, less dominating recombination channel:

- The existence of the CE peak in the EDMR and TSR spectra is a clear indication that CE centres also participate to recombination processes.

- When recombination involving CE-centres also involves db centres, a large g factor and thus a broad Larmor separation must exist. This was confirmed by detection of the Rabi oscillation of CE centres as explained in section 5.4.3.

- As outlined in section 3.6, the ratio q between the magnitude of the TSR transient and the echo is different for Rabi echoes and Rabi–beat echoes. The comparison of the TSR spectrum and the recombination echo spectrum discussed in section 5.5.4 showed that there could be a difference for the q values at the db and the CE centre. Thus, a weak Rabi echo due to weakly coupled CE–db pairs appears be buried under the strong Rabi–beat echo of the db centres.

In conclusion, it can be stated that charge carrier recombination in μc-Si:H for the given experimental conditions is mostly due to direct capture recombination at dangling bonds. in addition, the trap dangling bond channel exists even though it is less dominant. Thus, with the confirmation of the qualitative picture as outlined in fig. 6.5, a comprehensive and experimentally verified model of the lifetime limiting processes of μc-Si:H exists. Quantitatively, the dissociation and recombination probabilities that determine the dynamics of the dc channel could be determined. It has been shown that recombination can not only take place from spin pairs with high singlet content but also from triplet states. The only remaining drawback is that the widths and the proximity of the CE and the db resonances does not allow the determination of quantitative information about the dynamics of the CE–db path. This drawback of minor relevance, since the CE–db channel does not play a major role for recombination in the sample studied.

6.2 Outlook on hydrogenated amorphous silicon

The detailed investigation of μc-Si:H presented above raises the question about the transferability of the gained knowledge to similar materials such as hydrogenated amorphous silicon (a-Si:H), a highly disordered solid whose structure is very similar to the disordered

phase that exists between the columns of μc-Si:H. Historically, the investigation of recombination mechanisms and defect centres of was done first for a-Si:H and then for μc-Si:H, a development that was parallelled by the systematic investigation of spin–dependent recombination channels that was carried out first for a-Si:H [53] and then for μc-Si:H [46]. For a detailed review of the properties of photoconductivity, transport and recombination in a-Si:H as well as the differences of a-Si:H and μc-Si:H, one can refer to an abundance of literature that has been produced within the past 25 years [84, 85, 86, 87, 26, 72]. One of the remarkable properties of a-Si:H is the decay of its photoconductivity with increasing light irradiation length and time, which is referred to as Staebler–Wronski effect [84]. This decay is reversible which means the anneal of a degraded sample at appropriate temperatures can lead to a full recovery of the photoconductivity. Stutzmann et al. [86, 88] and Dersch et al. [89] have shown that the decrease of the photoconductivity correlates to a light–induced increase of the dangling bond density within the silicon matrix. During the irradiation, an almost linear dependence exists between the db density and the product $\mu\tau$ of the charge carrier mobility and lifetime. However, when the sample is annealed, the development of the $\mu\tau$ product is highly non–proportional [90, 91] which may be indicative of two defects, the db and the prime recombination (pr) centre as suggested by Heck and Branz [90]. Alternatively, the observed degradation and anneal behaviour could just as well be explained by the db centre only: When dbs are created with a constant recombination probability but annihilated during the anneal by changing the recombination probability first, the existence of the pr centre is not imperative. A judgement on whether the db- or the db–pr mechanism is responsible for the anneal behaviour is possible only when experimental methods are available that can provide information about recombination cross sections and probabilities. The

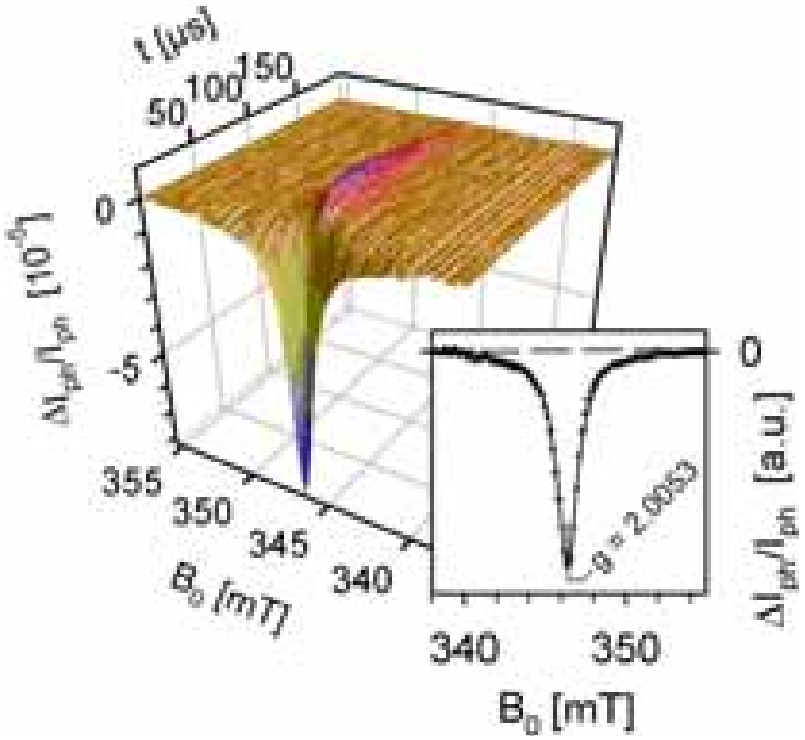

Figure 6.6: Photocurrent transients measured in a-Si:H after a coherent excitation of the db resonance. Similar to the TSR spectra of μc-Si:H an initial quenching followed by an enhancing takes place. The fit of the magnetic field dependence with a single pseudo Voigtian line is depicted in the inset and shows that only one resonance can be detected at g=2.0053. Thus, direct capture of db centres appears to be responsible for the observed transients. (T=70K, I=5μA; laser: λ=514nm, P=650mW; microwave: $P_{\mu W}$=4W (24db), ν=9.740283GHz, τ=1μs)

detailed study of the degradation and anneal behaviour by means of TSR goes far beyond the scope of this book and must be carried out in a separate study. However, as shown in the following, the transients of photocurrent changes caused by short and coherent ESR excitation of charge carriers and defect states in a-Si:H are sufficiently slow such that their measurement is possible. This shows the feasibility of TSR on a-Si:H and, thus, it shows recombination in this material can be investigated by means of TSR.

For this first demonstration, a nominally undoped intrinsic sample with 1μm thickness, deposited by hot wire chemical vapour deposition was used. For the TSR experiment, the a-Si:H film H556-d, deposited and provided by the National Renewable Energy Laboratory, USA, was contacted with a 300nm Al-grid system as described in chapter 4 and sawed into a size suitable for the microwave resonator. Since the used grid geometry was the same as for the μc-Si:H samples, the overall sample resistance turned out to be much higher since the low temperature photoconductivity of the a-Si:H material was significantly lower than the photoconductivity of the μc-Si:H sample. This made the current detection as well as noise oppression extremely difficult. A problem which prohibited the PLD measurements and thus, the verification or falsification of coherent spin motion effects. Moreover, in order to have a reasonable sample resistance at all, an extremely high laser intensity and a relatively high temperature T=70K had to be applied so that a sample resistance of R_{sam}=8.7MΩ could be achieved — a value barely low enough for the measurement of small current changes on a μs–time scale. This shows that for a systematic investigation of a-Si:H by means of TSR, a new contact grid design has to be developed.

Figure 6.6 shows the results of photocurrent transient measurements. The three dimensional plot of fig. 6.6 shows an ESR induced decay at the Landé factor of dangling bonds (db) at $g \approx 2.0053$. Similarly to μc-Si:H, an initial strong photocurrent quenching takes place that is followed by a temporary photocurrent enhancement. Unlike the TSR spectra of μc-Si:H films, no resonance at $g \approx$1.998 can be detected. As shown by the two dimensional magnetic field dependence plot of fig. 6.6, a single pseudo–Voigtian line–fit can reproduce the experimental data very accurately. This is an indication that db recombination in a-Si:H works in a similar way as the db–dc process of μc-Si:H. This hypothesis is also supported by the homogeneity of the two time constants contained in photocurrent transients.

Chapter 7

Readout concept for Si–based quantum computers

The classical computer technologies are rapidly approaching their physical limits as the dimensions of metal oxide semiconductor logic are minimised to scales at which quantum effects such as tunnelling currents or spatial quantisation determine device properties. While these natural limitations of classical electronics are the dead end for the development of conventional electronics as predicted and described by Moore [3], they open up possibilities for new alternative concepts such as spintronics and quantum computing (QC) [92].

7.1 Kane's silicon–based quantum computer

A silicon quantum computer as proposed by Kane [47, 48] is a semiconductor based solid state quantum computer (QC), in which the actual qubits are the spins of ^{31}P–donor nuclei and the donor electrons are used to negotiate a coupling between two qubits by means of hyperfine and exchange interaction. Presently, Kane's concept appears to be among the most promising candidates for a successful implementation of solid–state quantum computing. It combines the advantages of conventional semiconductor technology with regard to the high degree to which this technology has been developed and the fundamental concepts of QC, the massive parallel processing of information by coherent quantum states of microscopic systems. Technologically, it is based on the well established

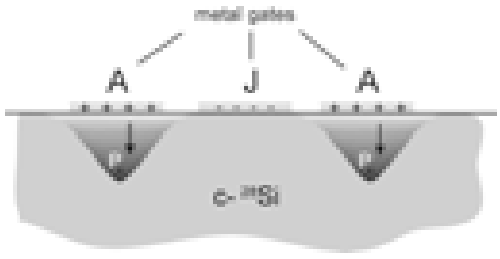

Figure 7.1: The hyperfine and exchange coupling controlled by electric fields of A and J gates. When the A gates are charged, the electron wave functions have little overlap with the ^{31}P nuclei. When the A gates are uncharged and the J gates are charged positively, a wavefunction containing the two donor electrons smears out across the two atoms, which couples the nuclear spins.

silicon technology that has been developed during the past fifty years of intensive research by thousands of scientists and engineers. The idea of Kane's QC is to take advantage of the two nuclear–spin energy eigenstates of ^{31}P-donor nuclei which can be used as well isolated (long relaxation times) quantum bits (qubits) as long as they are embedded in a nuclear spin free crystalline ^{28}Si matrix.

Figure 7.1 illustrates two quantum bits (qubits) as proposed: Interaction between these nuclear spin qubits can be controlled by electric fields from charged metal gates above and between the donor atoms, which can selectively increase the hyperfine interaction between the localised electron and nuclear states as well as the exchange interaction between donor electron states of different ^{31}P atoms [47, 48]. The exchange coupling between two adjacent ^{31}P donor electrons is controlled by an electric field of the J gate which increases or decreases the electron wavefunction overlap. Thus, with increasing J, the eigenbase of the electron pair changes from a product base into the singlet–triplet base. As illustrated in fig. 7.2, the symmetry (singlet or triplet) state of the electron pair after a J increase depends on the spin state of one nucleus when hyperfine coupling is switched on and the electron spins are in the ground state, initially. The hyperfine coupling can be controlled by the the electric field of an A gate above the respective qubit atom since the donor electron wave function has its maximum overlap with the ^{31}P nucleus only when it is undistorted by an applied electric field.

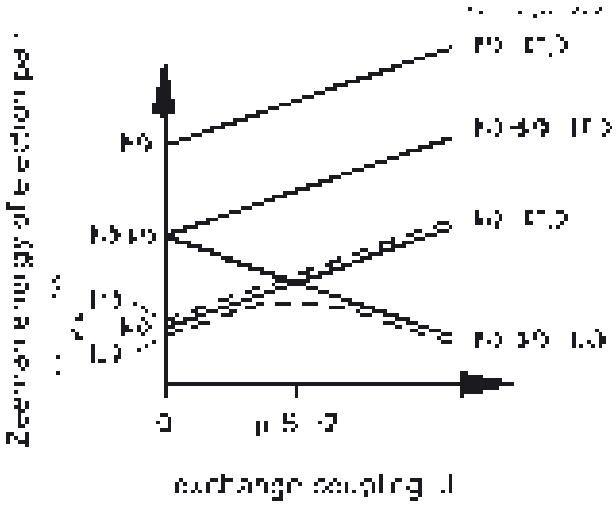

Figure 7.2: Zeeman energy of electron pair as a function of the exchange coupling J. In the presence of hyperfine coupling with a ^{31}P nucleus, the two electrons and one qubit nucleus form eight energy eigenstates. With increasing exchange interaction between the electrons, the electron–pair state changes from the product base into either singlet or triplet states, depending on the nuclear state.

Before an implementation of the silicon based spin QC is possible, many technological challenges have to be overcome such as the accurate placement of the ^{31}P donors within the ^{28}Si matrix [93], which is particularly difficult since the exchange coupling between two adjacent donor atoms in silicon is not only highly dependent on their mutual distance but also on the surrounding crystal orientation [94]. Another unresolved challenge of the Si based solid state QC is the problem of a single–spin readout: In the original proposal [47], the readout of nuclear–spin states is done by charge measurements of the qubit's electronic shell which can contain one or two donor electrons from adjacent ^{31}P atoms, depending on the electron's spin states and hence, due to hyperfine interaction, depending on the atoms nuclear–spin state. Recently, other proposals for the measurement of a single nuclear spin state have been made utilising single electron transistors [95] or spin transport in combination with spin refrigeration/spin–readout devices [48]. Common to all these readout concepts is that they utilise the possibility that the adiabatic

increase of the exchange coupling as shown in 7.2, encodes a nuclear–spin state into the permutation–symmetry state of an electron pair without changing the coherence of the nuclei. Once the information contained in the coherent nuclear–spin state has been cloned into the electron–pair state, one can isolate the two systems (electron pair and nucleus) by switching off the hyperfine coupling and measure the electron–spin state with an incoherent process. Beside the readout by means of charge–carrier measurement as proposed in the literature [48, 95], the permutation–symmetry state of an electron pair can also be obtained by means of recombination measurements as outlined in the previous chapter. Whenever an electronic transition between a donor level and an energetically deeper level is spin dependent, recombination, which means the refill of the two states that were charged by the transition with charge carriers will induce a measurable change of the excess charge carrier conductivity.

7.2 Readout with recombination

This principle, applied to Kane's quantum computer concept leads to a proposal of a recombination based readout device as illustrated in fig. 7.3. Therein, three ^{31}P qubits are drawn with their respective A gate electrodes above and two J gate electrodes in between. For the readout of the centre qubit, an additional readout device is drawn, consisting of a paramagnetic deep–level point defect centre (dl) in close proximity to the qubit donor as well as two additional gate electrodes above the dl centre (A) and between the donor qubit and the dl centre (R). The latter is referred to as "readout gate" or "R gate" in the following. As long as the R gate is charged negative, the wave–function overlap between the ^{31}P–donor electron and the dl centre is small which minimises the tunnelling transition probability between the two states and keeps the spin exchange negligibly small as well.

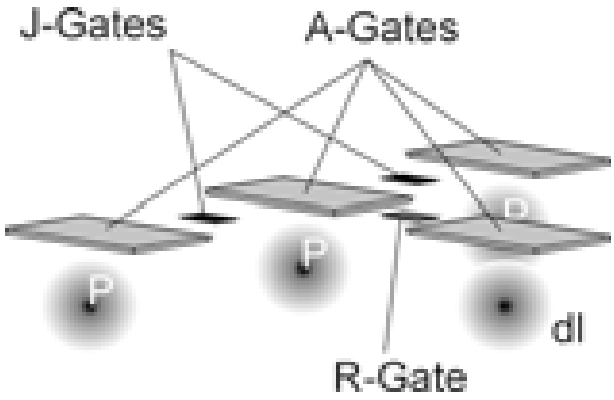

Figure 7.3: Concept of a recombination based readout mechanism of a silicon–based solid–state quantum computer. In the vicinity of the ^{31}P qubit is a point defect, which induces a localised, paramagnetic, deep–level (dl). A readout gate (R gate) controls the exchange between the ^{31}P donor and the dl and thus the possibility of a spin–dependent recombination transition.

When the R gate is charged positive, such that the wave function overlap between the ^{31}P and the dl centres is sufficiently large, exchange interaction increases. If this increase is introduced slowly, an adiabatic change of the spin pair's energy eigenstates can take place from an uncoupled product base into a set of singlet and triplet states. At low temperatures ($T \leq 100$mK), the uncoupled pair is polarised in a $|T-\rangle$ state as long as the coupling is absent. When the exchange is increased slowly, this $|T-\rangle$ state remains either unchanged or shifts into an $|S\rangle$ state, depending on the orientation of the ^{31}P nucleus.

Note that in presence of a second nuclear spin at the site of the dl state, the A gate above the deep level state would have to be charge positively in order to minimise hyperfine coupling. After the R gate has been "opened", an electronic transition can take place which charges the deep level state (see fig, 7.4); however, this transition is only possible when prior to the transition the electronic pair has singlet content and thus, the charging of the dl depends on the nuclear state of the phosphorus qubit. When the R gate is "closed" after the P-dl transition time, the electronic configuration remains unchanged until excess charge carriers which may be generated by a short laser pulse refill the positively charged donor and the negatively charged deep level state with an electron and a hole, respectively.

The sketch of the transitions and the timing during a readout sequence are displayed in figs. 7.4 and 7.5, respectively. As long as quantum operations on the qubit take place, no light is imposed on the sample and the R gate is charged negatively so that no electronic transitions can destroy the information contained in the qubits. When the readout sequence begins at a time t_0, the bias of the A gate above the ^{31}P donor atom that is to be read is slowly decreases such that hyperfine coupling maximises after a time τ_{hyper} later. Thereafter, the bias of the R gate is slowly inverted towards a positive voltage. Once exchange coupling is established a time τ_{slope} later, the hyperfine coupling is switched off. Now, the nucleus is isolated from the electrons even though its spin state is coded in the electron symmetry. The exchange coupling remains unchanged until the actual recombination transition has taken place. The time necessary for this transition is of the order of the electronic–pair state's lifetime τ_{life}, after which the exchange interaction is switched off again. By then, the nuclear spin state of the ^{31}P donor is coded into the donor and the deep level charge state. A short and weak[1] laser pulse imposed on the sample will then increase the photoconductivity (photoconductivity = 0 before pulse) through generation of a few pairs of excess electrons and holes. If the donor and the dl state are not charged (no transition), a slow decrease of the photoconductivity will follow, which is determined by slow band–band recombination in the ultra pure ^{28}Si. If the two states are charged (transition has occured), a fast decay of the photoconductivity will take place since charge carriers will be trapped in the charged states. Thus, the level of the photoconductivity a time τ_{decay} after the end of the laser pulse will reveal the result of the readout process. Note that the readout process itself automatically neutralises the two states such that a new series of operations can take place after its completion.

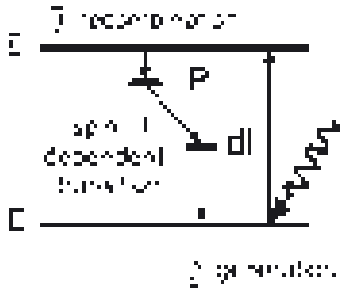

Figure 7.4: The electronic transitions of a single–qubit recombination readout process.

The implementation of the recombination readout presented depends on whether an appropriate ^{31}P–dl system will be found, that can be made with sufficient geometrical accuracy, and which provides a spin–dependent transition that can be influenced by ^{31}P–hyperfine coupling. Such nuclear–spin state–governed recombination has already been proven experimentally by Spaeth et al. who observed a fine structure of ^{31}P in EDMR

[1] τ_{flash} in ns Range; intensity in nW range

spectra [24]. Thus, the only condition for the feasibility of a readout of coherent spin states with recombination processes that has yet to be fulfilled is the ability of a given transition to reflect the coherence of the spin states involved. This implies that the pair states that determine whether a recombination transition takes place or not must not collapse into one of their four eigenstates before a second transition, the actual electronic transfer, takes place. In the previous chapters it was shown that a coherent spin motion can determine recombination rates of charge carriers. The coherence times of a given recombination path can be measured by the TSR experiment. The approach taken with this experiment, which is to extract coherence times of spin pairs by means of Rabi oscillation that induces changes in the spin–dependent electric currents, is similar to the proposal made by Burkard and Loss for coherence time measurements of spin qubits based on charge carrier transport through single–spin quantum dots [92, p. 256ff.].

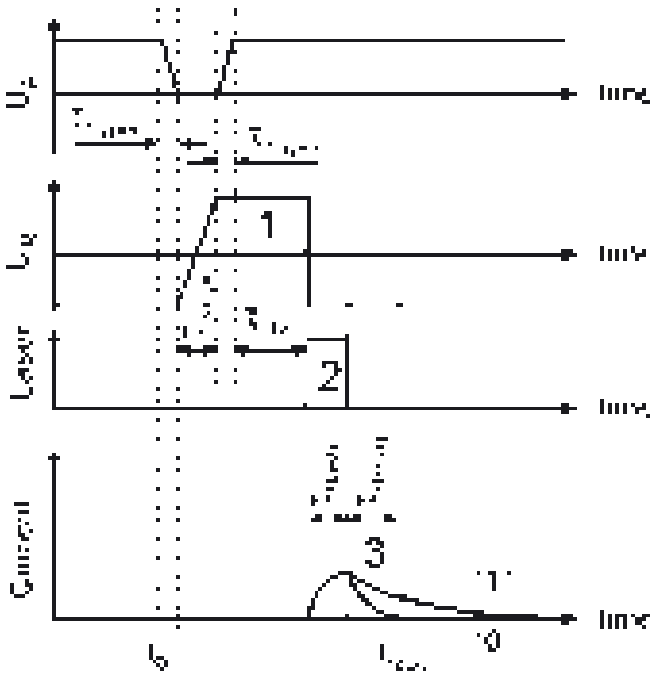

Figure 7.5: The timing of a single qubit recombination readout process. First, the hyperfine coupling between the donor nucleus and the electron is switched on. Then, the exchange between donor electron and deep level is increased where after the hyperfine coupling is switched off again. After this sequence, the nuclear state is coded into the symmetry state of the electron pair. This symmetry state can then be read by measurement of an excess charge–carrier current that will be influenced by means of a spin–dependent recombination process.

Thus, only TSR will be able to provide the information necessary to decide whether a ^{31}P–dl transition is suitable for a recombination readout or not. When a ^{31}P–dl pair is found by means of TSR in which coherent ^{31}P–dl transitions can be detected electronically and the coherence is limited by electronic transitions and not by spin relaxation, it could be used as a setup for a recombination readout as illustrated in fig. 7.3.

7.3 Deep donor candidates

With a tool given that allows the characterisation of suitable readout–recombination channels, potential candidate systems can be discussed. The implementation of singly occupied deep level states will depend on its properties with regard to the control of its location, its charge carrier–capture cross sections and the given transition times of the system. The dangling bond in amorphous and microcrystalline silicon would be an ideal system with regard to the latter properties (see chapter 6). The transitions times are in the order of

one microsecond [65], both the charged as well as the uncharged db state lies energetically below the P donor state and broken bonds in a ^{28}Si matrix are free of hyperfine interaction with any nuclear spin. However, due to the high disorder in the microcrystalline morphology of silicon and since there has no process been established which allows the creation of a single db with $\mathring{A}$ accuracy, a different way of deep level implementation must be chosen in a QC device.

Various impurities in crystalline silicon provide required deep levels, some of which are listed in the following:

- **Gold** has a deep level donor at E_v+290meV and an acceptor at E_c-54meV [96]. The one Au-isotope existent has a nuclear spin I=3/2 [97], which would require an oppression of the hyperfine coupling by an additional A gate.

- **Potassium** has deep level donors at E_v+350meV and E_c-260meV [96]. All three existent Isotopes have $I \neq 0$ [97].

- **Strontium** has deep level donors at E_c-280meV and E_v+500meV [96]. Its naturally most abundant Isotope (^{88}Sr, 82.58%) has no nuclear spin [97].

- **Chromium** is a deep donor at E_c-410meV whose most abundant isotope (^{52}Cr, 83.8%), [97] is nuclear spin free as well.

- **Hydrogen–oxygen:** Proton implanted c-Si have shown to provide two associated energy states at E_c-320meV and E_v+270meV which are an acceptor and a donor state respectively [98]. The microscopic origin of these levels appear to be H saturated stable VO configurations.

- **Interstitial carbon oxygen** (C_iO_i) centre, also referred to as C(3) centres [98] show a deep donor state at E_v+350meV which is stable up to 300^{o}C.

Which of these defects may be suitable as readout recombination centre will mostly depend on whether they can be implemented as isolated centres and in a controlled microscopic distance to the ^{31}P–donor. This will be especially challenging for the centres consisting of vacancies and two other atoms.

An alternative for the use of recombination for nuclear spin readout as described above could be interface recombination. Surface recombination at c-Si/SiO_2 interfaces has shown to have spin–dependent paths [38] and could be beneficial for a recombination–readout mechanism.

7.4 Challenges for an implementation

The TSR experiments presented in the previous chapters are the motivation for the QC readout concept proposed — many other questions will have to be answered experimentally before an actual proof of this concept can be given. Aside from the proper implementation of the dl state as discussed in the last section, several other issues remain to be

investigated: One challenge of a recombination readout is to keep the readout error[2] below 10^{-4} [99]. Clearly, a single qubit readout that is based on the annihilation of a single charge carrier pair could never reach this error probability since the process illustrated in fig. 7.4 consists of four completely random, spontaneous transitions. However, note that several subsequent readout processes can be carried out on one and the same qubit since the qubit content is not destroyed by the the recombination itself. Hence, under the assumption that the standard deviation of the number of recombined electrons that is counted from a conductivity measurement scales with $\sqrt{n}$ when the sequence in fig. 7.4 is carried out n times, the quantiles which would represent a readout error below 10^{-4} would be reached for $n > 44$. Thus, the readout of a single qubit by means of 50 or 60 recombination sequences would diminish the readout error and, moreover, it would make the detection by means of conductivity measurements easier: As shown in chapter 4, it is possible to detect 30 charge carrier pairs with TSR, even when the experiment is carried out in the presence of a strong constant photocurrent offset. For the readout as proposed, a measurement without offset would be made and the detection would be even more sensitive. A laser pulse of 1ns length and 3.2nW intensity would produce 10 electron–hole pairs if the internal quantum efficiency is assumed to be 100%. Thus, the detection of these 10 charge carrier pairs would require a pA–current measurement on a microsecond scale which does not pose a problem.

From this consideration, two additional issues arise that question the feasibility of the recombination readout: First, the number n of recombination sequences can not be extended infinitely. The changes of the hyperfine and exchange coupling are adiabatic only when they take place on an infinite time scale. A finite time for the change of these parameters induces incoherence. The chance of a spontaneous destruction of the information contained in the qubit rises with decreasing manipulation times τ_{hyper} and τ_{slope}. However, this means that for every readout system a maximum n_{max} exists that can not be exceeded without loosing more coherence than quantum error correction algorithms can compensate. Secondly, with increasing n, the overall readout time of a qubit increases as well. However, the latter has to be significantly shorter than the coherence times of the qubits which are limited by the nuclear spin–relaxation times. For ^{31}P qubits this means, that the overall readout time should not exceed a lower microsecond range.

Finally, another important aspect has to be addressed: When the ^{31}P deep level transition takes place, the charged donor as well as the charged dl state get discharged by excess charge carriers. The latter may not necessarily be in a spin–ground state since they are generated by a non–equilibrium process (light excitation). Since relaxation is slow at low temperatures, a non–equilibrium polarisation could pose a problem. This problem may be solved by spin–polarised injection of excess carriers instead of light injection.

[2]the sum of the probability that a qubit has a state “1” and readout reveals “0” plus the probability of the opposite case

Chapter 8

Conclusions and Outlook

A variety of new information about the nature of spin–dependent recombination has been gained in the course of this study. Theoretically, the description of the dynamics of spin–dependent recombination processes was built on a general foundation which will be applicable to many other recombination channels in semiconductor materials and devices. One of the important insights is that the traditional EDMR experiment has some principle limitations than can only be overcome if pulsed EDMR is performed.

The theoretical description of the dynamics of spin–dependent recombination has shown that a coherent ESR excitation of paramagnetic states can have a variety of effects on the transient behaviour of the photocurrent. The most promising features are the Rabi and Rabi–beat oscillations, that are predicted to determine the signal amplitude. The photocurrent transients after a coherent ESR excitation dependent a sum of different recombination processes such as singlet and triplet recombination or recombination from energy eigenstates with mixed symmetries. Consequently, an ESR excited photocurrent change may not only cause a current quenching but also a current enhancement. The current detected Rabi–oscillation can dephase quickly due to inhomogeneities of the Rabi–frequencies within a given charge carrier pair ensemble. The latter is not only due to Landé–factor and microwave field inhomogeneities, but also to distributions of spin–dipolar coupling strength within the pairs and makes the distinction of coherent dephasing and incoherence difficult. Thus, a rephasing that leads to an echo effect, the recombination echo, has to be introduced by means of microwave phase changes. The recombination echo decay then allows to measure the fastest incoherent process. Another conclusion from the theoretical considerations is that influences such as spin–dipolar and spin–exchange interaction, as well as spin relaxation, are not only non–negligible but may even be determining factors for TSR transients and EDMR spectra.

In the course of this study a new experiment, the time domain measurement of spin–dependent recombination (TSR), has been developed. Technical aspects of the experimental setup are explained in detail so that the reader of this book should be able to reproduce the experiment with the same or other semiconductor materials. The experiments carried out for the verification of the theoretically predicted effects were performed on hydrogenated microcrystalline silicon (μc-Si:H). The data confirmed the predictions and allowed to deduce accurately the time constants determining for the processes involved, e.g. recombination, spin relaxation and pair dissociation. The access to these

new parameters brings new insight about recombination in μc-Si:H. The spin–dependent recombination channels at the dangling bond (db) resonance, which had been known from previous EDMR studies, could be associated with two different recombination paths, the recombination between CE and db centres and a db direct capture process. It was verified that the latter is the dominant recombination path in μc-Si:H. Finally, it was shown that the investigation of recombination in hydrogenated amorphous silicon by means of TSR is possible, too, as well as the measurement of coherence times of spin–based qubits of solid state quantum computers.

This thesis is focused on the understanding of the dynamics of spin–dependent charge–carrier recombination and to find ways to access the predicted effects experimentally. Possible applications to material science and quantum computation go far beyond those few that have been shown. In principle, TSR can be applied to any device or material system on which EDMR has been carried out successfully. In this regard only some examples of very important materials shall be mentioned here, for whose understanding TSR could be of great advantage:

- **c-Si/ gate dielectric interfaces:** Recombination at interfaces such as c-Si/SiO_2 or c-Si/SiN_x:H is of great importance for the understanding of electronic losses in thin film transistors. The same applies for the new high-k materials whose electronic interface properties are still not fully understood. The c-Si/SiN_x:H interface is also of great importance for solar cell applications since silicon nitride is used as anti–reflection and surface passivation material.

- **Grain boundary recombination:** Recombination at grain boundaries of polycrystalline materials could be explored by means of TSR. The measurement of pulsed EDMR on well defined grain boundaries, for instance in bicrystals, could give new insight about their detrimental or beneficial impact on charge–carrier transport and recombination.

- **Staebler–Wronski effect in a-Si:H:** The ability of TSR to measure transition probabilities in distinctly manipulated recombination channels could lead to new information about photoconductivity degradation and its recovery through anneal. The challenge for such an investigation would be the implementation of a controlled degradation and anneal setup into a TSR experiment.

- **Devices:** The measurement of TSR in pn–junctions could bring further understanding to the recombination in space charge regions.

Beyond the applications of TSR to material science, the work on the experimental method itself needs to be continued: In principle, the PLD measurement should be able to work for an ODMR experiment just as well as for EDMR when sensitive and fast infrared photodetectors are used. The technological improvement of the electrically detected TSR will depend on the improvement of the current measurement. Due to the compromise between detection sensitivity and time resolution that has to be made in any case, improvement will be possible only by reduction of the current offset. Thus, another way to perform TSR experiments should be considered where the photocurrent exists only

temporarily, which means, only the spin dependent decay of a few charge carriers is observed that are produced by a short laser burst right before the ESR manipulation of the spin pairs takes place. The advantage of such an experiment is the absence of an offset current. The disadvantage of such an experiment would be that the spin–pair ensemble would not rest in a quasi steady state during the ESR excitation which would introduce a high degree of complexity into the theoretical description as well as the interpretation of experimental data. Finally, a comment on the theory of TSR for which an arbitrary amount of time could be spent: In the theory presented in chapter 3, little attention was dedicated to the influence of nuclear spins. Hyperfine interaction can have dramatic influences on electronic–spin states as discussed in section 7 about nuclear spin qubits. Thus, the development of an understanding of the impact of hyperfine coupling on TSR transients could open access to information about certain impurities (e.g. hydrogen) on recombination processes.

In conclusion, TSR seems to be a very promising but also experimentally and theoretically demanding way to access new, previously not accessible information about charge–carrier recombination in semiconductors. Because of its potential, the application to many materials and a further development of this method is recommended for the future.

Appendix A

Theory

A.1 Stochastic Liouville equations

The recombination rate of charge carriers out of intermediate pair states is a macroscopic observable which depends on an ensemble of identical, quantum mechanical systems. A mathematical formalism for the description of such an observable's dynamics has to take statistical indeterminacies due to the distributions of single pair states within the ensemble as well as the quantum mechanical indeterminacies due to pairs in non–eigenstates with regard to the observable into account. This double indeterminacy can be treated in the following way: Probability theory predicts an expectation value

$$\langle A \rangle = \sum_{w \in W} p\left(w\right) A\left(w\right) \tag{A.1}$$

when the probability that a microscopic single system of the ensemble has a contribution $A\left(w\right)$ to the macroscopic observable A is $p\left(w\right)$. In terms of quantum mechanics, w is one of a set of possible states W in which a single system can be found. Note that W does neither have to contain eigenstates nor mutually orthogonal states, nor does it have to be a base set of the single systems observable. The expectation value of a single system can then be written as $\langle w|\hat{A}|w\rangle$ which takes care of the quantum mechanical indeterminacy. By insertion of two identities written as completeness relations $\sum_{i \in \mathcal{H}} |i\rangle\langle i|$ of an arbitrary base into eq. A.1, the macroscopic observable becomes

$$\begin{aligned} \langle A \rangle &= \sum_{w \in W} p\left(w\right) \langle w|\hat{A}|w\rangle = \sum_{w \in W} \sum_{i} \sum_{j} p\left(w\right) \langle w|i\rangle\langle i|\hat{A}|j\rangle\langle j|w\rangle \\ &= \sum_{i} \sum_{j} \langle j| \sum_{w \in W} |w\rangle p\left(w\right) \langle w|i\rangle\langle i|\hat{A}|j\rangle \end{aligned} \tag{A.2}$$

which is the trace of the product of the observables' matrix element $A_{ij} = \langle i|\hat{A}|j\rangle$ with a second matrix that one can define to be

$$\rho_{ji} = \langle j| \sum_{w \in W} |w\rangle p\left(w\right) \langle w|i\rangle. \tag{A.3}$$

The latter is called a density matrix or Liouville matrix and its corresponding operator, the density operator $\hat{\rho}$, contains all the information of the mixed ensemble state. Under consideration of Schrödinger's equation $i\hbar\partial_t|w\rangle = \hat{H}|w\rangle$, the time derivative of $\hat{\rho}$ becomes

$$\begin{aligned}\partial_t\hat{\rho} &= \partial_t\left(\sum_{w\in W}|w\rangle p(w)\langle w|\right) = \sum_{w\in W}\left(\partial_t|w\rangle\right)p(w)\langle w| + |w\rangle p(w)\left(\partial_t|w\rangle\right)^\dagger \\ &= \sum_{w\in W} -\frac{i\hat{H}}{\hbar}|w\rangle p(w)\langle w| + |w\rangle p(w)\langle w|\frac{i\hat{H}}{\hbar} = \frac{i}{\hbar}\left[\hat{\rho},\hat{H}\right]^- . \end{aligned} \tag{A.4}$$

This differential equation is called the Liouville equation. Its solution describes the evolution of $\hat{\rho}(t)$, and by means of the equation

$$\langle A(t)\rangle = \mathrm{Tr}\left[\hat{\rho}(t)\hat{A}\right] \tag{A.5}$$

which is eq. A.2 in an operator representation, the dynamics of the macroscopic observable A can be obtained. External changes of the ensemble, which means creation and annihilation of ensemble constituents can be described by a stochastic addend as done in equation 3.1 of chapter 3.1. In these cases however, the factors $p(w)$ do not represent probabilities but products of probabilities and the number of ensemble constituents.

A.2 Spin–dipole interaction

The interaction of magnetic fields with magnetic moments or magnetic dipoles as well as the mutual dipole–dipole interaction is explained in the textbook literature such as in the book by Jackson [100]. The magnetic field $\mathbf{B}(\mathbf{r})$ of a magnetic dipole $\mu_\mathbf{a}$ located at the origin of a Cartesian position space has the form

$$\mathbf{B}(\mathbf{r}) = \frac{3\mathbf{r}(\mathbf{r}\cdot\mu_\mathbf{a}) - \mu_\mathbf{a}}{r^5} \tag{A.6}$$

and since the energy of a second magnetic moment $\mu_\mathbf{b}$ in a magnetic field is $-\mu_\mathbf{b}\cdot\mathbf{B}$, the Hamiltonian of the dipolar interaction becomes

$$\hat{H}_D = \frac{\hat{\mu}_\mathbf{a}\cdot\hat{\mu}_\mathbf{b} - 3(\mathbf{r}\cdot\hat{\mu}_\mathbf{a})(\mathbf{r}\cdot\hat{\mu}_\mathbf{b})}{r^5}. \tag{A.7}$$

When the two magnetic moments are induced by two spins $\mu_{a,b} = g_{a,b}\mu_B\mathbf{S_{a,b}}$, the spin–dipolar interaction can be written in a form

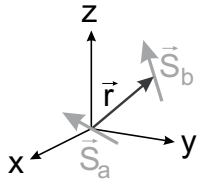

Figure A.1: The interaction between two dipoles with relative position $\mathbf{r}$ can be described in terms of the magnetic dipolar interaction of a spin $\mathbf{S_b}$ with the magnetic field $\mathbf{B}(\mathbf{r})$ induced by a spin $\mathbf{S_a}$ located at the origin of the coordinate system.

$$\hat{H}_D = \hat{\mathbf{S}}_\mathbf{a}\cdot\tilde{D}\cdot\hat{\mathbf{S}}_\mathbf{b} \quad \text{with} \quad \tilde{D}_{ij} = \frac{g_a g_b\mu_B^2}{r^5}\left(r^2\delta_{ij} - 3x_i x_j\right) \tag{A.8}$$

in which the dipolar interaction matrix $\tilde{D}$ is a tensor whose matrix representation by choice of a base of eigenvectors becomes

$$\tilde{D} = \begin{pmatrix} \frac{1}{3}D^D + D^E & 0 & 0 \\ 0 & \frac{1}{3}D^D - D^E & 0 \\ 0 & 0 & -\frac{2}{3}D^D \end{pmatrix}. \tag{A.9}$$

The elements of the matrix in eq. A.9 are called zero field parameters. They can be calculated, from the expectation values

$$D^D = \frac{3}{4} g_a g_b \mu_B^2 \left\langle \frac{r^2 - 3x_3^3}{r^5} \right\rangle \qquad \text{and} \qquad D^E = \frac{3}{4} g_a g_b \mu_B^2 \left\langle \frac{x_2^2 - x_1^2}{r^5} \right\rangle \tag{A.10}$$

when the distributions of the spins in the position space are known. In order to get an analytic term for the spin–dipole interaction, the Pauli spin matrices have to be plugged into eq. A.8, which leads to a complicated expression. However, by assuming the applicability of a high field approximation ($|\tilde{D}_{ij}| \ll |g_i \mu_B B_0|$), a simple matrix

$$\hat{H}_{SD} = \begin{pmatrix} D^d & 0 & 0 & 0 \\ 0 & -D^d & -D^d & 0 \\ 0 & -D^d & -D^d & 0 \\ 0 & 0 & 0 & D^d \end{pmatrix} \qquad \text{with} \qquad D^d = -\frac{D^D}{6} \tag{A.11}$$

can be obtained for the spin–dipole contribution $\hat{H}_D$ to the Hamiltonian in the product base.

A.3 Bloch's equations and quantum mechanics

Generally spoken, a Bloch equation is a system of inhomogeneous first order differential equations that can be written in the form

$$\dot{\mathbf{S}} = \boldsymbol{\Omega} \times \mathbf{S} - \hat{R}\,[\mathbf{S}] \tag{A.12}$$

in which $\mathbf{S}$ represents a three component observable and $\hat{R}\,[\mathbf{S}]$ is a linear functional on $\mathbf{S}$. Historically, Bloch's equation was formulated for the first time when Felix Bloch described the propagation of a nuclear induction in the presence of a constant magnetic field $\mathbf{B_0} = B_0 \hat{\mathbf{z}}$ and an electromagnetic radiation $\mathbf{B_1} = B_1 \hat{\mathbf{x}} e^{i\omega t}$ [6]. In a classical picture, the equation of motion of the magnetisation $\mathbf{m}$ of an ensemble of many nuclei could then be written as

$$\dot{\mathbf{m}} = [\mathbf{B_0} + \mathbf{B_1}] \times \mathbf{m} - \frac{\hat{\mathbf{z}}}{T_1} \left(m_z - m_z^0 \right) - \frac{m_x \hat{\mathbf{x}}}{T_2} - \frac{m_y \hat{\mathbf{y}}}{T_2} \tag{A.13}$$

under the assumption that the relaxation of each component of a non–equilibrium magnetisation is proportional to the difference of each component to its respective steady state value. The relaxation times T_1 and T_2 of this equation were chosen phenomenologically. They are different for the components parallel and perpendicular to the $\mathbf{B_0}$ field and are therefore referred to as transverse and longitudinal relaxation times.

The ingenuity of Bloch's approach to the description of magnetic resonance experiments has two important aspects: First, the semi–classical approach to the description of a macroscopic observable contained in the Bloch equation has proven to be in full accordance with quantum mechanical approaches. The $\hat{\mathbf{n}}$ component of the magnetisation of a macroscopic spin ensemble can be represented by an expression

$$m_n = g \mu_B \frac{\hbar}{2} \mathrm{Tr}\,(\sigma_n \rho) \tag{A.14}$$

wherein $g\mu_B\frac{\hbar}{2}$ stands for the magnetic moment of an ensemble constituent and ρ for the ensemble state. When ρ is then plugged into a Liouville equation as described in appendix A.1, the entire ODE system obtains the form of the Bloch equation. Impressive is in particular that this includes even the phenomenological relaxation part $\hat{R}[\mathbf{m}]$ in eq. A.12. As discussed in section A.5, the description of a random perturbation by a thermal bath which can be done by the introduction of a fluctuation Hamiltonian, leads to a modification of the Liouville equation that imposes the relaxation part on the Bloch equation. This does also lead to analytical expressions for the relaxation times [10].

The second important aspect of Bloch's equation lies in its generality with regard to many systems with non–degenerate energy eigenstates that are exposed to an oscillating perturbation. The Hamiltonians of bound electrons exposed to light, electron spins exposed to microwave radiation or nuclei exposed to radio frequency have all similar mathematical representations. Thus, practically all resonance phenomena can be expressed in one or the other way in terms of Bloch equations, which gives their theoretical description a universality that oftentimes has allowed the transfer of results in one field straight into another.

A.4 Bloch spheres and rotating frames

The most illustrative way for the description of magnetic resonance phenomena is the rotating reference frame picture which goes back to Erwin Hahn [9] who used it first for the explanation of spin–echo effects.
This approach describes a spin system from a viewpoint that rotates about the direction of the constant magnetic field $\mathbf{B_0}$. If the angular velocity of the rotating observer is equal to the frequency of an externally applied microwave radiation that is circular polarised in a plane perpendicular to $\mathbf{B_0}$, the magnetic radiation field $\mathbf{B_1}$ becomes constant. Figure A.2 illustrates the difference of the same spin system observed from the lab frame (left sphere) and the rotating frame (right sphere). In the lab frame, the spin $\mathbf{S}$ and the radiation field vector $\mathbf{B_1}$ rotate about the externally applied magnetic field $\mathbf{B_0}$ with the Larmor frequency ω_L and the microwave frequency ω, respectively. From the viewpoint of an observer who rotates

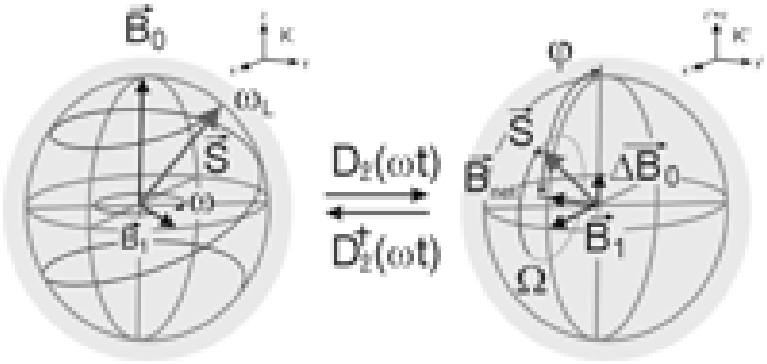

Figure A.2: Illustration of a spins magnetic moment on Bloch spheres that contain all possible spin states in a geometric, three dimensional coordinate system. The left sphere illustrates the situation from a lab frame perspective where both, the spin $\mathbf{S}$ and the radiation field vector $\mathbf{B_1}$ rotate about the externally applied magnetic field $\mathbf{B_0}$. The right sphere illustrates the viewpoint of an observer who rotates at the microwave frequency.

at the microwave frequency, the spin precesses at the Rabi frequency

$$\Omega = \sqrt{\left(\frac{1}{2}\frac{g}{\hbar}\mu_B B_1\right)^2 + (\omega - \omega_L)^2} \tag{A.15}$$

about the constant net magnetic field that consists of $\mathbf{B_1}$ fixed along the $\hat{\mathbf{x}}$ axis and the residual perpendicular field $\mathbf{\Delta B_0}$ in $\hat{\mathbf{z}}$ direction. The latter is different from the external magnetic field $\mathbf{B_0}$ since the spin precesses in the rotating frame not at the Larmor frequency but the difference of the rotation frequency ω and the Larmor frequency. The direction

$$\hat{\mathbf{n}}_{\mathbf{\Omega}} = \cos(\varphi)\,\hat{\mathbf{z}} + \sin(\varphi)\,\hat{\mathbf{x}} = \left[\frac{\omega - \omega_L}{\Omega}\right]\hat{\mathbf{z}} + \left[\frac{g\mu_B B_1}{2\hbar\Omega}\right]\hat{\mathbf{x}} \tag{A.16}$$

is also dependent on the Larmor- and the microwave frequency and the microwave–field strength B_1. Note that a rotation about the $\hat{x}$ axis takes place when $\mathbf{\Delta B_0}$ vanishes which means only when $\omega = \omega_L$. Thus, a 180^o spin flip of a spin system, originally aligned along the $\hat{\mathbf{z}}$ axis, is possible only at electron spin resonance. The major advantage of the rotating frame representation is that the perturbation Hamiltonian $\hat{H}_1$ in the Liouville equation 3.1 becomes time independent and, therefore, the algorithm for the solution of a system of ODEs with constant coefficient matrix as discussed in appendix A.6 can be used. Once a solution for the rotating frame has been found, the solution for the lab frame can be obtained by a simple transformation $\mathcal{D}^{\dagger}_{\hat{\mathbf{z}}}(\omega t)$ of this solution at a given time t.

Figure A.3 depicts the principle idea behind the Hahn spin–echo experiment [9], illustrated with the rotating Bloch sphere representation. Initially, the state of the spin ensemble rests in an equilibrium and is polarised along the $\hat{\mathbf{z}}$ axis, the direction of the external B_0 field. After a short and resonant (Larmor frequency is equal microwave frequency) microwave pulse whose length and intensity were chosen appropriately ($\frac{\pi}{2}$ pulse) was imposed onto the spin ensemble, a polarisation perpendicular to the $\hat{\mathbf{z}}$ axis is present. This polarisation is fixed in the rotating frame, which means it rotates at the Larmor frequency in the Lab frame and causes a detectable microwave radiation after the pulse is switched off. Due to the Larmor–frequency inhomogeneity within the ensemble, the spins then phase apart, causing a fast decline of the radiation intensity. This decline, solely due to coherent dephasing and not due to coherence decay, is called the "free–induction decay". When a second pulse is imposed onto the spin ensemble at time τ after the first pulse, all dephased spins are turned by an angle π about the same $\hat{\mathbf{x}}$ direction. Now all the spins are still dephased and also still in the $\hat{\mathbf{x}}$–$\hat{\mathbf{y}}$ plane, but those with higher Larmor frequencies precess behind those with lower Larmor frequencies. Thus, at time τ after the second pulse, a brief rephasing occurs exactly when the faster spins pass the slower ones.

The Hahn spin–echo experiment described above was the first experiment that proved the possibility of coherent rephasing of a dephased quantum ensemble. Note that this experiment is not a time reversal experiment, even though a phase reversal takes place: When the spins rephase at the time $t = 2\tau$, the polarisation of the ensemble points into the opposite direction than it does immediately after the initial $\frac{\pi}{2}$ pulse. The Hahn–echo experiment is dependent on the presence of polarisation within the ensemble before the pulse sequence is started. This condition is crucial for all radiation detected magnetic resonance experiments: Without polarisation there is no radiation absorbed or emitted

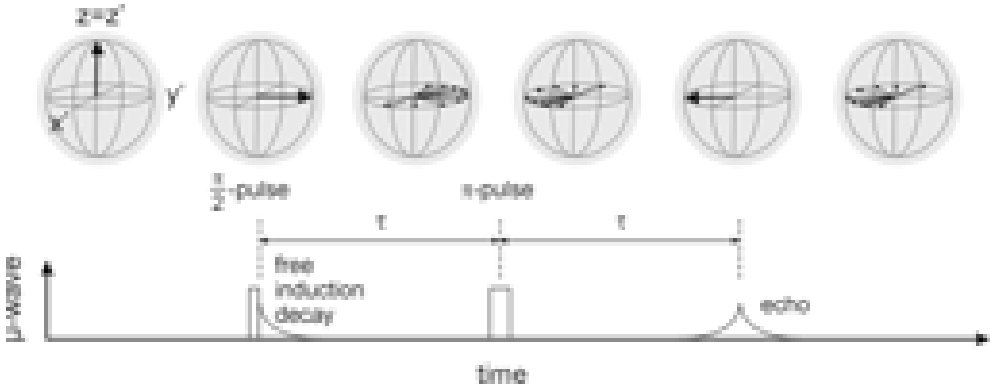

Figure A.3: Illustration of the Hahn spin–echo experiment. The Bloch spheres represent the moving frame in which the B_1 field is aligned along the $\hat{\mathbf{x}}$ axis during short an intensive pulses. The pulse sequence is a $\frac{\pi}{2}$–π echo sequence, the first and most simple way to obtain a coherent rephasing within a dephased spin ensemble. For details see text.

and thus, no signal will be detectable. This is a crucial difference from the recombination detected experiments presented in this book: Spin–dependent recombination is solely determined by the permutation symmetry of spin–pair states, polarisation does only play a minor role.

A.5 Redfield's theory of relaxation

The quantum mechanical theory of spin relaxation was developed by Redfield [58, 59] who applied his results first to the relaxation of nuclear–spin magnetisation. The motivation of Redfield's theory is the insufficiency of previous approaches in describing relaxation phenomena by simple rate equations. The latter, also known as Wangsness–Bloch theory, neglects the off–diagonal elements of density matrices. However, these contain phase information that may not necessarily cancel out immediately when relaxation takes place. The basic idea behind Redfields description of relaxation is the assumption that a thermal bath about an ensemble of microscopic systems imposes a fluctuation Hamiltonian $\hat{H}_{\mathrm{fl}}(t)$ that is added onto the unperturbed Hamiltonian $\hat{H}_{\mathrm{u}}(t) = \hat{H}_0 + \hat{H}_1(t)$ which describes the controlled influences by constant and oscillating magnetic fields B_0 and B_1 respectively. Plugged into the Liouville equation (eq.3.1, eq. A.4) one can separate the resulting expressions into a sum

$$\partial_t \hat{\rho}_{ij} = \frac{i}{\hbar}\left[\hat{\rho}, \hat{H}_{\mathrm{u}}\right]^{-}_{ij} + \tilde{R}_{ijkl}\left[\tilde{\rho}_{kl} - \tilde{\rho}^0_{kl}\right] \tag{A.17}$$

of the Liouville equation of the unperturbed Hamiltonian $\hat{H}_{\mathrm{u}}(t)$ and the Redfield relaxation term. This form already illustrates the physical truth behind a relaxation process: The system clearly tends to approach a diagonalised equilibrium state[1], but the rate at which each matrix element approaches this equilibrium state is not only proportional to its own

[1] when $\tilde{\rho}$ is represented in the eigenbase of $\hat{H}_{\mathrm{u}}$

difference from the equilibrium, but also on the differences of all other matrix elements. The Redfield matrix elements $R_{ijkl} = F\left[\hat{H}_{\mathrm{fl}}\right]$ are functionals

$$R_{ijkl} = \frac{1}{\hbar^2}\{j_{ikjl}\left(\omega_{ik}\right) + j_{ikjl}\left(\omega_{lj}\right) - \delta_{ik}\sum_p j_{lpjp}\left(\omega_{lp}\right) - \delta_{jl}\sum_p j_{ipkp}\left(\omega_{pj}\right)\} \tag{A.18}$$

in which

$$j_{ijkl}\left(\omega_{pq}\right) = \int_0^\infty G_{ijkl}e^{-i\omega_{pq}\tau}d\tau \tag{A.19}$$

is a functional called the spectral density which itself depends on $\omega_{ij} = \frac{1}{\hbar}\left(E_i - E_j\right)$, the difference between two eigenstates of the unperturbed Hamiltonian $\hat{H}_{\mathrm{u}}$ and the correlation function

$$G_{ijkl}(\tau) = \overline{< i\hat{H}_{\mathrm{fl}}(t-\tau)|j >< k|\hat{H}_{\mathrm{fl}}(t)|l >} \tag{A.20}$$

of the fluctuation Hamiltonian $\hat{H}_{\mathrm{fl}}$. A modern and detailed review of the exact derivation of eqs. A.18 to A.20 has been given by Atherton [10]. Note that the only assumption made therein is that the perturbation $\hat{H}_{\mathrm{fl}}$ is random, which means its covariance with the density matrix $\mathrm{cov}(\hat{\rho}, \hat{H}_{\mathrm{fl}}) =< i|\frac{i}{\hbar}\left[\rho(0), \hat{H}_{\mathrm{fl}}\right]|j >= 0$ vanishes in the interaction (Dirac) picture. While any fluctuation Hamiltonian $\hat{H}_{\mathrm{fl}}$ will be lengthy and not analytically available, one can take advantage of eqs. A.18 to A.20 nevertheless by deriving the following rules and relations that allow a connection between Bloch's phenomenologically defined spin relaxation times T_1 and T_2 and the elements of the Redfield matrix, especially under the assumption that the perturbation is sufficiently weak ($\partial\rho_{ij} \gg R_{ijkl}$ for all k, l):

- $R_{ijkl} = 0 \Leftrightarrow \omega_{ij} \neq \omega_{kl}$
- $R_{iijj} = R_{jjii} = \left(\frac{1}{T_1}\right)_{ij}$
- $\mathfrak{Re}(R_{ijij}) = -\left(\frac{1}{T_2}\right)_{ij}$
- $R_{iijj} = -\sum_{k\in\{1..n\}-\{j\}} R_{iikk}$.

The strength of Redfield's approach lies in a combination of accuracy and generality: It provides a link between phenomenological rate coefficients and exact quantum mechanics and can be utilised for the description of incoherence in spin ensembles, electronic states of atoms, semiconductors, superconductors or quantum well systems.

A.6 Analytic solution of an ODE

In order to find all solutions of a linear, inhomogeneous system of ordinary first order differential equations

$$\partial_t\tilde{\xi}\left(t\right) = \hat{A}\tilde{\xi}\left(t\right) + \tilde{b} \tag{A.21}$$

of a set of n unknown functions $\tilde{\xi}\left(t\right) = \left[\xi_i\left(t\right)\right]_{1\leq i\leq n}$ and with a constant coefficient matrix $\hat{A} = \left[A_{ij}\right]_{1\leq i,j\leq n}$ and an inhomogeneous part $\tilde{b} = \left[b_i\right]_{1\leq i\leq n}$, one has to add an arbitrary

solution to all solutions of the homogeneous ODE as shown in mathematical textbook literature [101]. One arbitrary solution of the inhomogeneous system is the steady–state solution that can be obtained from the system of linear equations

$$0 = \hat{A}\tilde{\xi}^S + \tilde{b}. \tag{A.22}$$

The general solution of the homogeneous ODE

$$\partial_t \tilde{\xi}(t) = \hat{A}\tilde{\xi}(t) \tag{A.23}$$

can be found with an Ansatz

$$\tilde{\xi}(t) = \tilde{v}_j \exp(\lambda_j t) \tag{A.24}$$

which, plugged into eq. A.23 yields a characteristic equation

$$\left[\hat{A} - \lambda_j \mathbb{I}\right] \tilde{v}_j = 0 \tag{A.25}$$

whose solution reveals a set of $m \leq n$ eigenvalues λ_j and n eigenstates $\tilde{v}_j$. The general solution to eq. A.21 is a linear combination of all the n orthogonal contributions

$$\tilde{\xi}(t) = \sum_{j=1}^{n} l_j \tilde{v}_j \exp(\lambda_j t) + \tilde{\xi}^S \tag{A.26}$$

whose coefficients l_j have to be chosen in a way such that the boundary conditions, which are the initial conditions $\tilde{\xi}^i = \tilde{\xi}(0)$, are matched. In order to do this, another system of linear equations

$$\tilde{\xi}^i - \tilde{\xi}^S = \sum_{j=1}^{n} l_j \tilde{v}_j \tag{A.27}$$

has to be solved. Note that the determinant of the coefficient matrix must not vanish in order to contain sufficient information for the calculation of a single solution. It is also important to be aware that the number n of unknown functions contained in $\tilde{\xi}(t)$ must match the number of available ODEs. This requirement does not seem to be fulfilled for the Liouville equation 3.1 since the 16 ODEs given correspond to 32 unknown functions ($\hat{\rho}$ belongs to a unitary vector space). This problem is resolved by the Hermiticity of $\hat{\rho}$ which imposes 16 constraints that reduce the number of independent functions by half.

Appendix B

Experiments

B.1 Continuous–wave electron spin resonance

The traditional and up to the present most widely used way to carry out ESR spectroscopy is the continuous–wave experiment (cw ESR). Figure B.1 depicts a block diagram of this experiment, which is usually carried out as a slow adiabatic sweep experiment where the intensity in a microwave resonator containing a given sample is measured versus the magnetic field. Throughout the measurement, the microwave generator continuously produces a radiation of constant intensity and constant frequency. When the external magnetic field reaches a value that together with the microwave frequency matches an electron spin resonance, microwave radiation is absorbed and thus, the intensity of the microwave radiation in the resonator is quenched. Note that the absorption increase can only remain in a steady state when the excited spins can release their energy with spin relaxation. Consequently, the on–resonance absorption of a given spin system is only proportional to the microwave intensity as long as the Rabi frequency is lower then the spin–lattice relaxation rate. Once the Rabi frequency exceeds $\frac{1}{T_1}$ (saturation regime), the absolute absorption does not increase with increasing intensity and, thus, the signal–to–noise ratio (SNR) deteriorates. Moreover, a quantitative interpretation of the signal intensity (e.g. for spin–density measurements) becomes difficult. For many spin systems in semiconductors, the T_1 times are in the range of μs to ms and hence, the intensity range of the microwave is in the μW to mW range. The sketch in fig. B.1 illustrates that noise reduction is implemented with a modulation lock–in method. Therefore, the magnetic

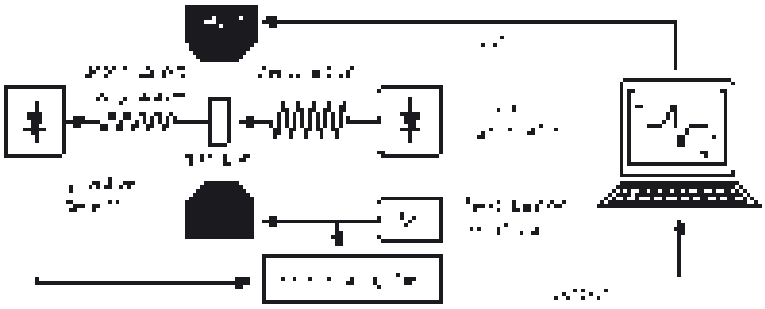

Figure B.1: Block diagram of a conventional cw ESR setup. The experiment is based on a slow adiabatic sweep of a magnetic field under constant exposure of the sample to weak microwave radiation. When spin resonance occurs, the microwave is absorbed and a decrease of the microwave intensity can be detected. For the purpose of noise reduction, lock–in amplification of the field modulated signal is carried out.

field is not only swept slowly but is also continuously modulated about its sweep position. Within a given spin resonance, this modulation leads to an oscillation of the signal intensity that is filtered out of the noise by a lock–in amplifier. The lock–in approach leads to a strong increase of the SNR but limits the resolution of the measurement to the amplitude of the magnetic–field modulation.

B.2 Continuous wave EDMR

Continuous–wave electrically detected magnetic resonance (cw EDMR) is based on the measurement of resonant changes of a material's photoconductivity under ESR excitation of paramagnetic centres that are involved in recombination or transport processes. Hence, the crucial difference between cw EDMR and cw ESR is the change of the observable — instead of the magnetic polarisation of a spin ensemble, the singlet or triplet content of a spin–pair ensemble is measured. Consequently, temperature, magnetic–field and microwave–intensity dependencies and the line shape of a detected signal are different. In addition to the contribution of relaxation processes to the homogeneous broadening as it is the case for cw ESR, electronic transition rates can also play a role for cw EDMR. In general, the results of EDMR experiments match ESR measurements only with regard to the Landé factors of detected spin centres. Note that saturation does not play a role for cw EDMR experiments since microwave radiation is not detected. While saturation causes the same limitation of the absolute magnitude for a detected resonance signal as it does for cw ESR, there is no deterioration of the SNR. Hence, cw EDMR is typically carried out at the highest available microwave intensity (200mW in the case of the cw mode of the Bruker E580 spectrometer).

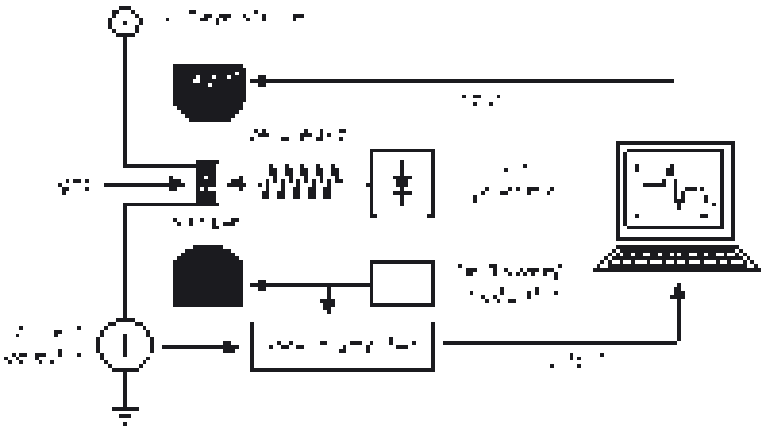

Figure B.2: Block diagram of a conventional cw EDMR setup.Unlike cw ESR, the resonance is not detected through the microwave absorption but the change of the photocurrent under constant exposure of the sample to a light illumination and voltage.

Since cw EDMR is a quasi static experiment similar to cw ESR, the same lock–in technology can be used in order to enhance the SNR. However, since electronic transitions that play a significant role for the measured recombination or transport processes may be much slower than the relaxation times, the modulation frequencies have to be many orders of magnitudes lower than comparable cw ESR measurements on the equivalent samples (Hz to kHz for cw EDMR instead of 10kHz to 100kHz for cw ESR). Cw EDMR is superior to cw ESR with regard to the increased sensitivity to the absolute number of spins that can be detected. While state of the art ESR has detection limits in the range

of 10^{11} spins contained in the microwave field of a given resonator (under assumption of a reasonable narrow line width, ≈.1G), cw EDMR is only limited by the detection limit of sample current changes. Sample currents however are strongly dependent on the sample's conductivity, photoconductivity and geometry. For actual measurements, this turns out to be an extraordinary advantage for the cw EDMR of thin–film semiconductor samples, were an increase of the absolute spin sensitivity by 8 to 10 orders of magnitude can be realised.

Beside the advantages, there are also various drawbacks and limitations of cw EDMR in comparison to the cw ESR experiment. Beside the obvious confinement of this method to semiconductor materials with spins that have an impact on conductivity, there is a strong limitation of the information that can be obtained from an EDMR scan. The high complexity of the line shapes on many different parameters makes it almost impossible to obtain quantitative data from cw EDMR line shapes (see also ref. [46]). Moreover, spin–density measurements are hardly possible since spin densities and signal intensities hardly correlate. Finally, EDMR measurements are technically difficult to perform: Subtle sample contacts have to be brought onto the small sample surfaces and wires have to connect these contacts with the outside of the resonator. This makes the technical implementation difficult and the metal of the contacts and wires also reduces the cavity quality factor that has to be as high as possible for cw experiments. Thus, under certain sample contact conditions, the cavity tuning for a cw EDMR experiment can pose quite a challenge.

B.3 Pulse Spell routines for TSR

In the following, three short PulseSpell scripts are displayed which are only examples for the many different routines that were actually used for all the experiments displayed in this book. However, these examples contain most of the commands from which any of the actually used pulse sequences can be made.

(A) Recording of real–time transients versus magnetic field

```
                          begin defs                for k=1 to n
; long term transient     dim s[1024,128]           bsweep y=1 to sy
;                         end defs                  shot i=1 to 2
; magnetic field sweep    ;                         p0 [+x]
; and pulse transient     begin lists               dig [sg1]
; recording after         asg1 +a                   next i
; single short pulse      bsg1 +b                   next y
;                         end lists                 scansdone(k)
; n :  number of scans    ;                         next k
; p0:  length of pulse    begin exp [quad trans]    end exp
```

The routine collects and averages `n` real–time transients after a `p0` long microwave pulse for each of the 128 magnetic field positions.

(B) Transient amplitudes versus pulse length and magnetic field

```
                          ;                          d0=d1
; short term transient     begin defs                 for x=1 to sx
;                         dim s[256,128]             shot i=1 to 1024
; magnetic field sweep     end defs                   p1 [+x]
; and pulse amplitude      ;                          d0
; recording with           begin lists                acq [sg1]
; increasing pulse         asg1 +a                    next i
; length                   bsg1 +b                    p1=p1+dx
;                          end lists                  d0=d0+dx
; n :  num.  of averages   ;                          next x
; p2:  initial p.-length   begin exp [intg]           next k
; dx:  increment of        bsweep y=1 to sy           next y
; pulse length             for k=1 to n               end exp
; d1:  collection time     p1=p2
```

This routine measures the pulse length dependence of the TSR signal amplitude. The photocurrent is measured at a time `d1` after the end of a microwave pulse whose lengths is altered in 256 steps, beginning with an initial pulse length `p2` which is increased by intervals of length `dx`. All pulse length dependence measurements are averaged 1024×`n`.

(C) Recording of real–time transients versus pulse length

```
                          begin defs                 for x=1 to sx
; short/long term meas.    dim s[1024,256]            shot i=1 to 2
; ; recording of pulse     end defs                   p3 [+x]
; length dependence of     ;                          d0
; real--time transient     begin lists                dig [sg1]
; after single pulse       asg1 +a                    next i
;                          bsg1 +b                    p3=p3+dx
; n :  number of averg.    end lists                  next x
; p4:  initial pulse       ;                          next y
; length                   begin exp [intg]           next k
; dx:  increment of        for k=1 to n               end exp
; pulse length             bsweep y=1 to sy
;                          p3=p4
```

This routine measures the pulse length dependence of the real–time transients for a given, fixed magnetic field. The transient is obtained from `n` averages measured after pulses of 256 different lengths between `p2` and 256×`dx`. Many pulse experiments such as the recombination echo sequences were obtained with routines (ii) and (iii) by insertion of additional pulse commands that had different pulse length and phase orientations. For instance, "`p5 [-y]`" stands for a pulse of length `p5` and a negative polarisation along the $mathbf{\hat{y}}$ axis). More details of PulseSpell are outlined elsewhere [102].

Bibliography

[1] Cordon Art, M.C. Escher, The Official Website, `http://www.mcescher.com`, 2002.

[2] H. J. Möller, *Semiconductor for Solar Cells* (Artech House, Boston, London, 1993).

[3] G. E. Moore, in *Proceedings of the SPIE - The international society for optical engineering* (SPIE, Santa Clara, CA, 1995), Vol. 2440, pp. 2–17.

[4] T. Mouthaan, *Semiconductor Devices Explained* (Wiley, New York, Weinheim, 1999).

[5] D. V. Lang, J. Appl. Phys. **45**, 3023 (1974).

[6] F. Bloch, Phys. Rev. **70**, 460 (1946).

[7] F. Bloch, W. W. Hansen, and M. Packard, Phys. Rev. **70**, 474 (1946).

[8] E. Zavoiski, J. Phys. USSR **9**, 211 (1945).

[9] E. L. Hahn, Phys. Rev. **80**, 580 (1950).

[10] N. M. Atherton, *Priciples of Electron Spin Resonance* (Ellis Horwood PTR Prentice Hall, Chichester, England, 1993).

[11] S. Geschwind, R. J. Collins, and A. L. Schawlow, Phys. Rev. Lett. **3**, 545 (1959).

[12] J. Brossel, S. Geschwind, and A. L. Schawlow, Phys. Rev. Lett. **3**, 548 (1959).

[13] J. Klein and R. Voltz, Phys. Rev. Lett. **36**, 1214 (1976).

[14] A. J. Hoff, E. J. Lous, and R. Vreeken, in *Pulsed EPR a new field of application*, edited by C. P. Keijzers, E. J. Reijerse, and J. Schmidt (North Holland, Amsterdam, 1989), Chap. 19, pp. 219–226.

[15] V. Weis, K. Möbius, and T. Prisner, J. magn. Res. **131**, 17 (1998).

[16] K. L. Purvis, S. P. Wiemelt, T. Maras, M. Blue, V. Melkonian, P. D. Ashby, S. A. Riley, L. S. Fifield, K. A. Martin, and A. M. Nishimura, J. Lumin. **71**, 199 (1997).

[17] E. van Oort and M. Glasbeek, in *Pulsed EPR a new field of application*, edited by C. P. Keijzers, E. J. Reijerse, and J. Schmidt (North Holland, Amsterdam, 1989), Chap. 19, pp. 227–231.

[18] B. M. Tadjikov, A. V. Astashkin, and Y. Sakaguchi, Chem. Phys. Lett. **283**, 179 (1998).

[19] R. Maxwell and A. Honig, Phys. Rev. Lett. **17**, 188 (1966).

[20] D. J. Lepine and J. J. Prejean, in *Proceedings of the 10th International Conference on the Physics of Semiconductors*, edited by S. P. Keller, J. C. Hensel, and J. Stern (US. Atomic Energy Commission, USA, 1970), p. 805.

[21] D. J. Lepine, Phys. Rev. B **6**, 436 (1972).

[22] M. Stutzmann, M. S. Brandt, and M.W. Bayerl, J. Non–Cryst. Solids **266-269**, 1 (2000).

[23] P. Kanschat, K. Lips, and W. Fuhs, J. Non–Cryst. Solids **266-269**, 524 (2000).

[24] B. Stich, S. Greulich–Weber, and J.-M. Spaeth, Appl. Phys. Lett. **68**, 1102 (1996).

[25] B. Stich, S. Greulich–Weber, and J.-M. Spaeth, J. Appl. Phys. **77**, 1546 (1995).

[26] H. Dersch, L. Schweitzer, and J. Stuke, Phys. Rev. B **28**, 4678 (1983).

[27] I. Solomon, J. Non–Cryst. Sol. **35&36**, 625 (1980).

[28] I. Solomon, D. Biegelsen, and J. C. Knights, Sol. Stat. Commun. **22**, 505 (1977).

[29] T. Eickelkamp, S. Roth, and M. Mehring, Mol. Phys. **95**, 967 (1998).

[30] I. Hiromitsu, Y. Kaimori, M. Kitano, and T. Ito, Phys. Rev. B **59**, 2151 (1999).

[31] I. Hiromitsu, Y. Kaimori, and T. Ito, Solid State Commun. **104**, 511 (1997).

[32] M. Dobers, K. v. Klitzing, J. Schneider, G. Weimann, and K. Ploog, Phys. Rev. Lett. **61**, 1650 (1988).

[33] C. F. O. Graeff, M. S. Brandt, M. Stutzmann, M. Holzmann, G. Abstreiter, and F. Schäffler, Phys. Rev. B **59**, 13242 (1999).

[34] I. Solomon, Sol. Stat. Commun. **20**, 215 (1976).

[35] R. Müller, P. Kanschat, S. von Aichberger, K. Lips, and W. Fuhs, J. Non–Cryst. Sol. **266–269**, 1124 (2000).

[36] K. Lips and W. Fuhs, J. Appl. Phys. **74**, 3993 (1993).

[37] F. C. Rong, G. J. Gerardi, W. R. Buchwald, E.H. Poindexter, M. T. Umlor, D. J. Keeble, and W. L. Warren, Appl. Phys. Lett. **60**, 610 (1992).

[38] J. H. Stathis, Appl. Phys. Lett. **68**, 1669 (1996).

[39] D. J. Lepine, V. A. Grazhulis, and D. Kaplan, in *Proc. 13th int. conf. on the Physics of Semiconductors, Rome* (North Holland, Amsterdam, 1976), Vol. 2440, p. 1081.

[40] V. S. L'vov, D. V. Tretyak, and I. A. Kolomiets, Sov.-Phys.-Semicond. **11**, 661 (1977).

[41] R. M. White and J. F. Gouyet, Phys. Rev. B **16**, 3596 (1977).

[42] W. Wosinski and T. Figielski, Phys. Stat. Sol. B **83**, 93 (1977).

[43] G. Mendz, D. J. Miller, and D. Haneman, Phys. Stat. Sol. B **20**, 5246 (1979).

[44] G. Mendz and D. Haneman, J. Phys. C:Solid St. Phys **13**, 6737 (1980).

[45] D. Kaplan, I. Solomon, and N. F. Mott, J. Phys. (Paris) – Lettres **39**, L51 (1978).

[46] P. Kanschat, Ph.D. thesis, Philipps Universität Marburg/ Lahn, 2000.

[47] B. E. Kane, Nature (London) **393**, 133 (1998).

[48] B. E. Kane, Fortschr. Phys. **48**, 1023 (2000).

[49] Z. Xiong and D. J. Miller, Appl. Phys. Lett. **63**, 352 (1993).

[50] B. Movaghar, B. Ries, and L. Schweitzer, Phil. Mag. B **41**, 159 (1980).

[51] L. S. Vlasenko, Yu. V. Martynov, T. Gregorkiewicz, and C. A. J. Ammerlaan, Phys. Rev. B **52**, 1144 (1995).

[52] K. Fukui, T. Sato, H. Yokoyama, H. Ohya, and H. Kamada, J. magn. Res. **149**, 13 (2001).

[53] K. Lips, *Spinabhängigkeit von Transport und Rekombination in Filmen und Solarzellen aus amorphem Silizium* (Cuviller Verlag, Göttingen, 1994).

[54] A. V. Barabanov, O. V. Tretiak, and V. A. L'vov, Phys. Rev. B **54**, 2571 (1996).

[55] A. V. Barabanov, O. V. Tretiak, and V. A. L'vov, Phys. Stat. Sol. (b) **207**, 419 (1998).

[56] A. V. Barabanov, V. A. L'vov, and O. V. Tretiak, Preprints of the Bogolyubov Institute for Theoretical Physics **ITP-93-68E**, 1 (1994).

[57] R. Haberkorn and W. Dietz, Solid State Commun. **35**, 505 (1980).

[58] A. G. Redfield, Adv. Magn. Reson. **I**, (1965).

[59] A. G. Redfield, IBM J. Res. Dev. **I**, 19 (1957).

[60] M. Stutzmann, Lokalisierte Zustände in amorphem Germanium und Silizium, 1983.

[61] J.-H. Zhou, S. Yamasaki, J. Isoya, K. Ikuta, M. Kondo, A. Matsuda, and K. Tanaka, Mat.Res.Soc.Symp.Proc. **452**, 821 (1997).

[62] N. A. Kurnit, I. D. Abella, and S. R. Hartmann, Phys. Rev. Lett. **13**, 567 (1964).

[63] W. Niggemeier, G. von Plessen, S. Sauter, and P. Thomas, Phys. Rev. Lett. **71**, 770 (1993).

[64] J. Sakurai, *Modern Quantum Mechanics*, revised ed. (Addison Wesley, Reading, 1994).

[65] C. Boehme and K. Lips, Appl. Phys. Lett. **79**, 4363 (2001).

[66] D. Will, C. Lerner, W. Fuhs, and K. Lips, Mat.Res.Soc.Symp.Proc. **467**, 361 (1997).

[67] P. Kanschat, H. Mell, K. Lips, and W. Fuhs, Mat. Res. Soc. Symp. Proc. **609**, A27.3.1 (2000).

[68] R. Carius, J. Müller, F. Finger, N. Harder, and P. Hapke, in *Photo- and dark conductivity of μc-Si:H thin films*, edited by J.M. Marshall, N. Kirov, and J.M. Maud (PUBLISHER, Varna, Bulgaria, 1998), pp. 157–165.

[69] M. Luysberg, P Hapke, R. Carius, and F. Finger, Phil. mag. A **75**, 31 (1997).

[70] M. Birkholz, B. Selle, E. Conrad, K. Lips, and W. Fuhs, J. Appl. Phys. **88**, 4376 (2000).

[71] P. Reinig, Ionenassistierte Magnetron–Sputterdeposition von kristallinen Siliziumschichten für Dünnschichtsolarzellen, 2002.

[72] B. I. Shklovskii, H. Fritsche, and S. D. Baranovskii, Phys. Rev. Lett. **62**, 2989 (1989).

[73] C. Boehme, P. Kanschat, and K. Lips, Nucl. Instrum. Methods B **186**, 30 (2002).

[74] F. Finger, C. Malten, P Hapke, R. Carius, F. Flückinger, and H. Wagner, Phil. mag. Lett. **70**, 247 (1994).

[75] K. F. Brennan, *The Physics of Semiconductors*, 1 ed. (Cambridge University Press, Cambridge, 1999).

[76] S. Brehme, P. Kanschat, K. Lips, I. Sieber, and W. Fuhs, Material Science and Engineering B **69–70**, 232 (2000).

[77] S. Brehme, personal communication (unpublished).

[78] R. Brüggemann and C. Main, Phys. Rev. B **57**, R15080 (1998).

[79] S. D. Baranovskii, M. Zhu, T. Faber, F. Hensel, P. Thomas, M. B. von der Linden, and W. F. van der Weg, Phys. Rev. B **55**, 16226 (1997).

[80] Z. Iqbal, F. A. Sarott, and S. Veprek, J. Phys. C: Solid State Phys. **16**, 2005 (1983).

[81] H. Kiess, V. Augelli, and R. Murri, Thin Solid Films **141**, 193 (1986).

[82] V. Augelli, H. Kiess, and R. Murri, J. Non–Cryst. Sol. **77–78**, 675 (1985).

[83] R. Brenot, P. Bulkin, P. Roca i Cabarrocas, B. Drevillon, and R. Vanderhaghen, J. Non–Cryst. Sol. **227–230**, 1001 (1998).

[84] D. L. Staebler and C. R. Wronski, Appl. Phys. Lett. **31**, 292 (1977).

[85] D. Monroe, Phys. Rev. Lett. **54**, 146 (1985).

[86] M. Stutzmann, W. B. Jackson, and C. C. Tsai, Phys. Rev. B **32**, 23 (1985).

[87] C. Tsang and R. A. Street, Phys. Rev. B **19**, 3027 (1979).

[88] M. Stutzmann, Phys. Rev. Lett. **47**, 21 (1985).

[89] H. Dersch, J. Stuke, and J. Beichler, App. Phys. Lett. **38**, 456 (1981).

[90] S. Heck and H. Branz, App. Phys. Lett. **79**, 3080 (2001).

[91] S. Heck, Ph.D. thesis, Philipps Universität Marburg/ Lahn, 2002.

[92] *Semiconductor Spintronics and quantum computation*, edited by D. D. Awschalom, D. Loss, and N. Samarth (Springer, New York, 2002).

[93] J. L. O'Brien, S. R. Schofield, M. Y. Simmons, R. G. Clark, A. S. Dzurak, N. J. Curson, B. E. Kane, N. S. McAlpine, M. E. Hawley, and G. W. Brown, Phys. Rev. B **64**, 161401 (2001).

[94] B. Koiller, X. Hu, and S. Das Sarma, Phys. Rev. Lett. **88**, 027903 (2002).

[95] B. E. Kane, N. S. McAlpine, A. S. Dzurak, R. G. Clark, G. J. Milburn, He Bi Sun, and Howard Wiseman, Phys. Rev. B **61**, 1023 (2000).

[96] S. M. Sze, *Physics of Semiconductor Devices*, 2 ed. (Wiley, New York, 1981).

[97] M. Winter, Web Elements, `http://www.webelements.com`, 2002.

[98] B. G. Svennson, *Crystalline silicon*, Vol. 20 of *emis datareviews* (INSPEC, London, 1999), Chap. 14.5, pp. 763–772.

[99] M. A. Nielsen and I. L. Chuang, *Quantum computation and quantum information*, 1 ed. (Cambridge University Press, Cambridge, 2000).

[100] J. D. Jackson, *Classical Electrodynamics* (Wiley, New York, 1975).

[101] W. Walter, *Gewöhnliche Differentialgleichungen* (Springer, Heidelberg, 1996).

[102] R. T. Weber, *Elexsys E580 User's Manual*, software version 2.1 ed., Billerica, MA USA, 2000.

List of Figures

List of constants, variables and conventions

Constants of nature

$c = 299792458\text{ms}^{-1}$	speed of light in vacuum
$k_B = 1.380662 \times 10^{23}\text{JK}^{-1}$	Boltzmann's constant
$\hbar = 1.054589 \times 10^{-34}\text{Js}$	Planck's constant ($h = 2\pi\hbar$)
$m_e = 9.109534 \times 10^{-31}\text{kg}$	electron mass
$e = 1.6021892 \times 10^{-19}\text{As}$	electron charge
$\mu_B = \frac{e\hbar}{2m_e} = 9.2741 \times 10^{-24}\text{JT}^{-1}$	Bohr's magneton
$\mu_0 = 4\pi \times 10^{-7}$	permeability of vacuum (defined)

Variables

A	arbitrary observable
A_l	cross section area of laser beam
$\tilde{A}$	arbitrary coefficient matrix of ODE system
a	universal fit variable
b	universal fit variable
$\tilde{b}$	arbitrary inhomogeneous contribution to ODE system
$\mathbf{B}$	magnetic field imposed on spin pair
$\mathbf{B_0}$	constant (or only adiabatically changed), strong external field
B_0	field strength of constant magnetic field
$\mathbf{B_1}$	radiation field induced by microwave radiation
B_1	field strength of microwave radiation
$B_1^{\max}$	maximum B_1 strength in presence of B_1 inhomogeneities
$\mathbf{B}_\text{net}$	net–magnetic field of spin in rotating frame
c	universal fit variable
d	dissociation probability of a single spin pair
D^d	high field approximation spin–dipolar coupling constant

D^D	spin–dipolar coupling matrix component D
D^E	spin–dipolar coupling matrix component E
D	dissociation rate of spin pairs
$\tilde{D}$	spin–dipolar interaction matrix
D_S	steady state dissociation rate of spin pairs
$\mathcal{D}_{\hat{\mathbf{n}}}(\phi)$	drehoperator
E_i	different energy levels in presence of magnetic field
f	universal fit variable in section 5.4.2
f_{th}	thickness of semiconductor thin film
F_{ijkl}	functional that described Redfield–matrix elements
g	Landé factor in general
$g_{e,h}$	Landé factors of electrons and holes, respectively
$g_{a,b}$	Landé factors of two arbitrary spin–pair partners, respectively
G	generation rate of spin pairs
G_{eh}	generation rate of excess charge carriers
$G_{1,2,3,4}$	generation rate of pair states $T+$, 2, 3 and $T-$, respectively
$G_{\mathrm{ijkl}}(\tau)$	correlation function of fluctuation Hamiltonian
$\tilde{G}$	generation vector of ODE in eq. 3.30
$\hat{H}$	Hamiltonian of single spin pair
$\hat{H}_0$	Hamiltonian of spin pair in absence of microwave radiation
$\hat{H}_1$	Hamiltonian of spin pair due to microwave radiation
$\tilde{H}_1^{\uparrow\downarrow}$	representation of $\hat{H}_1$ in the product base
$\hat{H}_D$	spin–dipolar interaction Hamiltonian
$\hat{H}_{\mathrm{fl}}$	random fluctuation Hamiltonian that causes spin relaxation
$\hat{H}_{\mathrm{SD}}$	Spin–dipolar interaction Hamiltonian in high field approximation
$\hat{H}_{\mathrm{u}}$	Hamiltonian of unperturbed spin pairs in absence of fluctuation fields
i, j, k, l	general index variables
I	sample current
I_{ph}	photocurrent
$j_{\mathrm{ijkl}}(\omega_{\mathrm{pq}})$	spectral density of fluctuation Hamiltonian
J	spin–exchange interaction constant
K	observer frame
K'	frame rotating at frequency ω
l	constant in general ODE solution that has inform. about init. conditions
$\mathbf{m}$	magnetisation of spin ensemble
$m_{\mathrm{x,y,z}}$	components of $\mathbf{m}$
$\tilde{M}$	coefficient matrix of ODE in eq. 3.30
$\hat{\mathbf{n}}_{\mathbf{\Omega}}$	unit vector in position space parallel to $\mathbf{B}_{\mathrm{net}}$
n	number of recombination steps for quantum read out
n_{db}	dangling bond density in material
$n_{e,h}$	density of free electrons and holes, respectively
n_{max}	maximum number of recombination steps
p	arbitrary probability
P	intensity of Ar^+ laser in TSR experiment

$P_{\mu\mathrm{W}}$	intensity of coherent microwave pulse in the TSR experiment
q_{TSR}	fraction of CE and db peak intensities in TSR–line shape
q_{echo}	fraction of CE and db peak intensities in echo line shape
r	distance between two spin–pair partners
$\mathbf{r}$	position vector between two spin–pair partners
$r_{S,T}$	recombination probability singlet and triplet states, respectively
$r_{2,3}$	recombination probability of state 2 and 3, respectively
R	recombination rate of spin pairs
R_S	steady state recombination rate of spin pairs
R_{ijkl}	Redfield matrix element
R_{res}	residual recombination rate due to all but the dominant rec. channels
$\mathcal{R}$	Redfield operator
$\mathbf{R}[\mathbf{S}]$	Relaxation rate of spin polarisation
$\mathcal{R}_{\mathrm{a,b}}$	Redfield operator of pair partner a and b, respectively
R_{sam}	Sample resistance
S	spin–quantum number
$\mathbf{S}$	arbitrary spin vector
$\mathbf{S_{a,b}}$	spin operators of the pair partners a and b, respectively
$S^z_{a,b}$	$\hat{z}$ components of spin operators
$\mathcal{S}$	stochastic changes of $\hat{\rho}$ due to spontaneous transitions
$\mathcal{S}_{an}$	annihilation part of $\mathcal{S}$ due to dissociation and recombination
$\mathcal{S}_{cr}$	creation part of $\mathcal{S}$ due to generation
t	time of photocurrent transient
$t_{\mu\mathrm{s}}$	time at which pulse length dependence of photocurrent is measured
t_0	begin of read out process
t_{read}	moment when read out result is detected
T	temperature
$T(\alpha)$	general transient function for Rabi oscillation
$T_{\mathrm{eff}}(\alpha)$	general transient function in presence of B_1 inhomogeneities
$T_{1,2}$	spin–lattice and spin–spin relaxation times, respectively
$T^{a,b}_{1,2}$	relaxation times of pair partner a and b, respectively
T_{3-9}	mixed relaxation rates within spin pair
T_M	dephasing time of spin ensemble ($\propto$ inverse of width of $\Delta\omega$ distribution)
$\tilde{U}$	transformation matrix from product base to base of energy eigenstates
$\tilde{v}_{\mathrm{j}}$	eigenvectors of ODE coefficient matrix
$\tilde{V}_{1,2}$	Transformation of spin–pair ensemble during short pulse excitation
w	element of probability space
W	general probability space
$x_{1,2,3}$	components of position vector between two pair partners
$\hat{\mathbf{x}}$, $\hat{\mathbf{y}}$, $\hat{\mathbf{z}}$	base vectors of Euclidean position space
α	absorption coefficient
$\delta\rho_{ij}$	Redfield contribution to the Liouville equation
$\mathbf{\Delta B_0}$	residual constant magnetic field in the rotating frame
$\Delta(\tau)$	relative change of density matrix elements
$\Delta^{\mathrm{eff}}(\tau)$	relative change that includes effects by g factor inhomogeneities

$\Delta^{u,v,w}(\tau)$	relative change of density matrix elements with spin–spin interactions
ΔD	dissociation rate change from steady state under ESR
ΔE	energy difference
ΔH	Magnetic field line width of TSR signal
$\Delta H_{\mathrm{V,L,G}}$	Widths of Voigtian, Lorentzian and Gaussian line shapes, respectively
ΔI_{ph}	change of photocurrent
ΔI_{echo}	differences of photocurrent changes on and off the recombination echo
$\Delta n_{e,h}$	density change from steady state of free electrons and holes, respectively
$\Delta\omega$	Larmor–frequency difference between two spins
ΔR	change of recombination rate from steady state under ESR
ΔR_{max}	maximum recombination change due to microwave pulse
ΔR_{bet}	recombination change that takes $\Delta\omega$ inhomogeneities into account
$\Delta\rho^1_{ij}$	change of matrix element during microwave interaction
$\Delta\sigma_{\mathrm{ph}}$	change of photoconductivity
$\Delta\sigma^*_{\mathrm{ph}}$	change of photoconductivity filtered by a current detection setup
ϵ	fraction of laser light that is reflected from cavity window
κ	parameter that stands for small (1) or large ($\frac{1}{2}$) Larmor separation
ν	microwave frequency (cycles per second)
ϕ	base shift angle of spin–pair energy eigenbase under spin–spin interaction
φ	angle between $\hat{\mathbf{n}}_{\boldsymbol{\Omega}}$ and $\hat{\mathbf{z}}$ in Bloch sphere
$\Phi(\Delta\omega)$	distribution of Larmor–frequency differences within spin–pair ensemble
$\Phi_{a,b}(\omega)$	distribution of Larmor frequency of spin a and b
$\Phi_{\mu\mathrm{w}}(B_1)$	arbitrary distribution of B_1 inhomogeneities
$\mu_{e,h}$	electron and hole mobility, respectively
ω	microwave frequency
ω_L	Larmor frequency of arbitrary spin
$\omega_{a,b}$	Larmor frequency of pair partner a and b, respectively
ω_0	sum of Larmor frequencies of pair partners
$\omega_{i,j}$	transition frequency between states $\lvert i\rangle$ and $\lvert j\rangle$
ω_Δ	half of the frequency split under influence of spin–spin interactions
Ω	Rabi frequency of arbitrary spin
$\Omega_{a,b}$	Rabi frequency of pair partners a and b, respectively
$\hat{\rho}$	state operator for spin–pair ensemble
$\hat{\rho}_0$	ensemble state in equilibrium
$\hat{\rho}^1$	ensemble right after microwave interaction
$\hat{\rho}^S$	ensemble in steady state
$\tilde{\rho}^E$	ensemble after microwave in energy eigenbase representation
$\tilde{\rho}^S$	matrix representation of $\hat{\rho}^S$
ρ^S	matrix elements ρ^S_{11} and ρ_{44} when both are equal in absence of polarisation
$\hat{\rho}_{\mathrm{ESR}}$	ensemble state under saturated, ESR excitation
$\rho^{\Delta\omega}_{ij}$	subensemble matrix element of spin pairs with Larmor separation $\Delta\omega$
ρ^{net}_{ij}	integrated ensemble matrix element
σ_{ph}	photoconductivity
$\hat{\sigma}_x$, $\hat{\sigma}_y$, $\hat{\sigma}_z$	Pauli's spinors
τ	length of microwave pulse

τ_{decay}	decay time of photoconductivity when fast recombination is present
τ_{flash}	lengths of laser pulse
τ_{hyper}	time required to switch hyperfine coupling on or off
τ_{life}	lifetime of spin pair when spin state allows recombination ($\tau_{\text{life}} = r_S^{-1}$)
τ_L	net lifetime of charge carrier
τ_{slope}	time required to switch exchange coupling on or off
τ_S	phenomenologically defined spin–relaxation lifetime
$\tau_{180^{\text{o}}}$	time of phase reversal in an echo experiment
τ_{f}	the "fast" time constant of the coherence decay during the pulse
$\tau_{\text{m,s}}$	the "medium" and "slow" time constants of quenching and enhancing decay

Substitutional variables

$\tilde{v}_i$	sections 3.3, 3.4.2
α_i	sections 3.3, 3.5, 3.5.1
β_i	section 3.3
ϵ_i	section 3.3
η_i	section 3.6
γ	sections 3.1.1, 3.5.1
λ_i	sections 3.3, 3.4.2
μ_i	section 3.6
ν_i	section 3.3
ξ_i	sections 2.1, 3.3, 3.4.2, 3.5.1
ζ_i	section 3.5.1

General symbol conventions

$\hat{\sigma}$	hats indicate operators
$\tilde{\sigma}$	tildes indicate matrices
σ_{ij}	indices indicate matrix elements
$\mathbf{E}$	boldface letters indicate vectors (usually elements of $\mathbb{R}^3$)
R	uppercase letters in rate equations indicate rates
r	lowercase letters in rate equations indicate rate coeff. (trans. probabilities)
i	indicator for imaginary part ($\mathfrak{Re}(i) = 0$, $\mathfrak{Im}(i) = 1$)
^{0}	"0" index of state variables always indicates an equilibrium state
^{S}	"S" index of state variables always indicates a steady state
$\overline{n}$	complex conjugate of n
$\mathcal{R}$	mathcal style indicates operator functionals.
$\|S\rangle$	elements of Hilbert space are written in bra–ket notation.
$\text{Tr}\,[\hat{\rho}]$	Trace of an operator or matrix
$\mathbb{I}$	unity operator or unity matrix
$\hat{\sigma}_a^x \otimes \hat{\sigma}_b^y$	element of product space
δ_{ij}	Kronecker's delta

The following publications have been released in connection with the preparation of this dissertation:

Boehme, C.; Kanschat, P.; Lips, K.
Quantum-beat recombination echoes
Europhys. Lett., **56** (5), 716 (2001)

Boehme, C.; Lips, K.
Time domain measurement of spin-dependent recombination
Applied Physics Letters, **79** (26), 4363 (2001)

Boehme, C.; Kanschat, P.; Lips, K.
Time domain measurement of spin-dependent recombination - a novel defect spectroscopy
Nucl. Instr. Meth. B, **186** (1-4), 30 (2001)

Boehme, C.; Kanschat, P.; Lips, K.
Time domain measurement of spin-dependent recombination in microcrystalline silicon
J. Non.-Cryst. Solids, **299-302**, 566 (2002)

Boehme, C.; Lips, K.
Light-intensity and temperature dependence of trap-dang bond recombination in hydrogenated microcrystalline silicon
Mat. Res. Soc. Symp. Proc., **715**, A16.2, (2002)

Boehme, C.; Lips, K.
Spin-dependent recombination - an electronic readout mechanism for solid state quantum computers
Phys. Stat. Sol. (b), **233** (3), 427 (2002)
also available in `arXiv: quant-ph/0208040`

Lips, K.; Boehme, C.
Recombination echoes in disordered silicon
to be published in J. Material Science

Other publications of the author:

Boehme, C.; Lucovsky, G.
Origins of silicon solar cell passivation by SiNx:H anneal
J. Non.-Cryst. Solids, **299-302**, 1157 (2002)

Boehme, C.; Lucovsky, G.
Dissociation reactions of hydrogen in remote plasma-enhanced chemical-vapor-deposited silicon nitride
J. Vac. Sci. Technol. A, **19** (5), 2622 (2001)

Boehme, C.; Lucovsky, G.
H loss mechanism during anneal of silicon nitride: Chemical dissociation
J. Appl. Phys. **88** (10), 6055 (2000)

Boehme, C.; Lucovsky, G.
Diffusion of hydrogen and deuterium in stack systems of SixNyHz/SixNyDz and crystalline Si
Mat. Res. Soc. Symp. Proc. **609**, A26.7.1, (2000)

Acknowledgements

I'd like to express my gratitude to those who have contributed to the successful accomplishment of my studies and my research:

Prof. Dr. Walter Fuhs, who has given me guidance, encouragement and freedom for the work at the Hahn–Meitner–Institut Berlin. His way to handle my work, his openmindedness with regard to new ideas and new ways have been a crucial ingredient for my success.

Dr. Klaus Lips, the advisor of my research studies. His commitment, enthusiasm, competence and energy are outstanding. Under his guidance I did not only learn to work on scientific problems but also how to present and to communicate the results to the scientific community and to the public. He has not only been a great advisor but also a good friend which is probably what made our work so productive and successful.

Prof. Dr. Sergei Baranovski, not only for his readiness to join my PhD–examination committee as the second evaluator but also and in particular for the enlightening discussions about quantum mechanics and the Drehoperators in Marburg as well as in Tsukuba, Japan.

All my coworkes at the department of silicon photovoltaics. In this regard I want to express my gratitudes especially towards Dr. Peter Kanschat, my predecessor in the ESR Lab. Dennis Schaffarzik who can really solve any problem of an experimentalists everyday life, Erhard Conrad and Dr. Mario Birkholz for the deposition of the hydrogenated microcrystalline silicon used in this work and Ina Sieber for taking the beautiful SEM picture of the hydrogenated microcrystalline silicon. Gisela Keiler for the creation of the sample contacts, Dr. Lothar Elstner, Dr. Sebastian Fiechter (SE3), Kerstin Jacob, Dagmar Patzek and Brunhilde Rabe for technical assistance. My office mates Dr. Peter Reinig and Dr. Rolf Stangl as well as Karsten Brendel and PD Dr. Norbert Nickel for the interesting and enlighting discussions.

Felice Friedrich, who did an awesome job on proofreading the thesis manuscript. For each typo that may have remained in this thesis there are 10 others that were found by her and also the two other proofreaders Klaus Lips and Kristie Durham.

Dr. Stefan Heck who gave me insight into the world of amorphous silicon and Dr. Brend Nelson from NREL for the supply of a-Si:H samples.

Prof. Dr. Gerry Lucovsky, the advisor of my Master studies at North Carolina State University. On the occasion of his 65th birthday celebrations in Raleigh, North Carolina, he introduced me to Prof. Fuhs — an encounter that led to my work at the HMI.

Andrea, Dietmar and Tim; Thorsten, Rudi, Daniel and many other friends.

My parents, who have always supported me throughout my education and my studies in Heidelberg, North Carolina and Berlin.

Last but anything beyond least, Kristie, whose advice on längvidsch ischuhs, computer graphics and most of all whose love were really great!

Beruflicher und wissenschaftlicher Werdegang des Autors

Schul- und Berufsausbildung

1987	Realschulabschluss, Realschule Oberkirch
1987–1990	Ausbildung zum Industrieelektroniker bei der BASF AG, Willstätt Besuch der Friedrich–August–Haselwander Berufschule, Offenburg
1990–1993	Besuch des Technischen Gymnasiums Offenburg, Abitur
1991	Arbeit als freier Autor für Computerzeitschriften

Ziviler Ersatzdienst

1993–1994	Individuelle Schwerbehindertenbetreuung beim Spastikerverein Offenburg

Studium und wissenschaftliche Arbeit

1994–2000	Studium der Physik an der Ruprecht–Karls–Universität Heidelberg Nebenfächer: Mathematik, Elektronik
1995	Arbeit als studentische Hilfskraft in der Gruppe von Prof. Dr. Dirk Schwalm am Max–Planck–Institut für Kernphysik in Heidelberg
1997–2000	Studium der Physik an der North Carolina State University, Raleigh, USA
1997–2000	Mitarbeiter der Gruppe von Prof. Dr. Gerald Lucovsky an der North Carolina State University, Untersuchung der Deposition von amorphen Siliziumnitridschichten und der Wasserstoffmigration darin
2000	Diplom an der Ruprecht–Karls–Universität; Titel der Diplomarbeit: “Diffusion von Wasserstoff und Deuterium in Schichtsystemen aus $Si_xN_yH_z$ und c-Si” Masters of Science degree an North Carolina State University, Titel der Master–Thesis: “Hydrogen loss mechanisms of ammonia rich remote plasma enhanced chemical vapor deposited silicon nitride”
2002	Gastaufenthalt an Joint–Research Center for Atomic Technology in der Gruppe von Dr. Satoshi Yamasaki in Tsukuba, Japan
2000–2002	Doktorand der Philipps–Universität, Marburg, Anfertigung der Dissertation als wiss. Mitarbeiter in der Abteilung SE1 am Hahn–Meitner–Institut Berlin unter Betreuung von Prof. Dr. Walther Fuhs und Dr. Klaus Lips

Stipendien und Auszeichnungen

1994	Erhalt des Hans–Böckler–Stipendiums
1997	Erhalt des Fulbright Stipendiums
1999	Wahl zur ΦΚΦ Society